PFC/RR-87-18 DOE/ID-01570-3

THERMAL DESIGN CONSIDERATIONS FOR PASSIVE SAFETY OF FUSION REACTORS

John E. Massidda and Mujid S. Kazimi

October 1987

Plasma Fusion Center
and the
Department of Nuclear Engineering
Massachusetts Institute of Technology
Cambridge, Massachusetts 02139 USA

*This work was supported by EG&G Idaho, Inc. and the U.S. Department of Energy, Idaho Operations Office under DOE Contract No. DE-AC07-76ID01570

THERMAL DESIGN CONSIDERATIONS FOR PASSIVE SAFETY OF FUSION REACTORS

by

JOHN E. MASSIDDA
MUJID S. KAZIMI

Massachusetts Institute of Technology
Plasma Fusion Center
Cambridge, Massachusetts 02139
October, 1987

Abstract

An analysis to develop thermal design guidelines for fusion reactor passive safety has been carried out. The purpose of the study is to develop a methodology, as well as establish guidelines, to analyze the passive safety potential of fusion reactors with respect to loss-of-cooling transients. The criteria for passive safety include protecting the public from radiological health risk by minizing the potential for radiation release, as well as protect the financial investment in the plant by minimizing the potential for damage to the plant. A number of variations of fusion blanket design were examined to determine their effect on the temperature response of the blanket following transients involving power/cooling mismatches. Loss-of-Flow (LOF), Loss-of-Coolant (LOC), and Overpower scenarios were considered. Reference blanket designs were selected both to represent the current stage of fusion blanket design, and to provide a range of design variations.

The allowable temperature limits of the structural materials were defined. The failure modes considered were acute structural failure, thermal creep rupture, and volatilization/oxidation of activated structural materials. Acute structural failure encompasses the possibility that structural damage may not occur, but changes in the microstructure of the material will prohibit its future use. Models were developed to predict failure by any of these modes given the post-accident temperature history.

The one-dimensional decay heat source in the reference blankets as a function of position and time was calculated. In terms of structural materials, the vanadium alloy V-15Cr-5Ti is found to yield the lowest level of decay heat density. This level decays by about an order of magnitude in one hour. A low-activation modified HT-9 also yields a low level of decay heat, which decays by an order of magnitude in about 24 hours. The structural steel Fe1422 has a high manganese content, which causes a high level of decay heat that doesn't decay by an order of magnitude for a number of months. The breeder materials liquid lithium and solid Li_2O both yield essentially no decay heat, assuming almost complete tritium removal. Liquid lithium-lead $Li_{17}Pb_{83}$ does generate a significant level of decay heat, but does not cause a substantial increase for the total blanket, since the structural materials dominate. A neutron multiplier, such as beryllium, will cause an increase in the decay heat level, due to the increase in the low energy neutron population. This increase can be significant.

The temperature history for the blankets following a LOF or LOC accident was calculated, using a heat transfer code developed for this purpose. The heat source in the undercooling transient analysis is primarily the decay heat, since rapid plasma

shut-off is assumed. The material limits models developed previously were then used in conjunction with the temperature histories to determine if and when failure will occur in each blanket. In this manner, elements of blanket design which increase or decrease the thermal safety margin, with respect to loss-of-cooling transients, were identified.

The results show that the maximum temperature rise in the first wall following the accident, ΔT_{max}, is almost linearly dependent on the neutron wall load Γ_n. With these results, maximum allowable wall loads to achieve passive safety in loss-of-cooling transients were defined for the blankets considered in this study. The Blanket Comparison and Selection Study (BCSS) level one Li/Li/V blanket is passively safe in both the LOF and LOC accidents at peak wall loads of up to 8 MW/m^2. The Li_2O/He/HT-9 blanket is subject to structural failure at peak wall loads of about 4 MW/m^2, depending on the first wall stress level. To maintain passive safety, high power density devices, such as the TITAN Reversed-Field-Pinch, may be limited to wall loads of 10 MW/m^2 or lower, again depending on the first wall stress level, and whether coolant can drain from the module. The D-D fuel cycle, because of its low neutron wall load, offers excellent inherent safety potential, but D-D blankets must be designed with safety in mind. Designs which solely maximize power output, by maximizing the blanket multiplication factor with the use of solid steel blankets, compromise the safety advantage of the low wall load and can be subject to structural damage.

The impact of natural convection on the temperature response to a LOFA was analyzed, using the assumption that the secondary cooling cycle remains availabe during the transient. It was found that helium is a poor natural convection medium. In liquid metal cooled blankets, the impact was found to depend heavily on the post-accident behavior of the magnetic field. If the magnetic field remains at its operational value, then only $Li_{17}Pb_{83}$ experiences sufficient natural convection to have an impact on the temperature response. Natural convection in liquid lithium is suppressed due to the high MHD pressure drop. If the magnetic field experiences rapid reduction, such as two orders of magnitude in 30 minutes, then the natural convection impact is substantial. In both liquid lithium and $Li_{17}Pb_{83}$ cooled systems, the temperature decreases rapidly and levels out at a quasi-steady state value which is well below the temperature limits. For this reason, it is important to design superconducting magnets such that they can experience a rapid field reduction.

Plasma overpower and continuation transients were also analyzed. In a plasma overpower transient, the plasma heat flux could increase well above the nominal level, with no corresponding increase in the cooling rate. In this case, there appears to be a threshold heat flux. Above this heat flux, the first wall will likely fail almost immediately. Below the threshold heat flux, the first wall will survive for some time. A plasma continuation transient occurs when cooling is lost but the plasma continues to burn. This can cause first wall failure in a matter of seconds. The heat transfer pathway from the first wall to the rest of the blanket has a large impact on the failure time. Both the overpower and continuation transients indicate the need for an automatic plasma shut-off mechanism.

Acknowledgements

This work was completed as part of the first author's Ph.D. dissertation for the Department of Nuclear Engineering at the Massachusetts Institute of Technology. There are a number of people who have assisted in the completion of this work. For their contributions, we would like to thank the following people: Professor John Meyer of MIT, for valuable input throughout the thesis, and especially regarding structural issues, such as the thermal creep model; Robert Krakowski of Los Alamos and Shahram Sharafat of UCLA, also for assistance in the Vanadium creep analysis; Ed Cheng of GA Technologies for assistance in the decay heat calculations; Boro Malinovic for providing and explaining the basis of the natural convection model; and Sandra Brereton for assistance with the D-D blanket analysis.

The first author is grateful to the Magnetic Fusion Energy Technology Fellowship Program, for providing the funding for his graduate studies at MIT.

This work was performed under appointment to the Magnetic Fusion Energy Technology Fellowship Program which is administered for the U.S. Department of Energy by Oak Ridge Associated Universities.

Table Of Contents

List of Tables

List of Figures

1. Introduction

Although fusion reactor design is still at a relatively early stage, it is important that safety concerns be included in the design process. Fusion energy appears to offer significant safety and environmental advantages over alternative sources of energy. This issue is especially important in light of recent developments in the fission nuclear reactor industry. Due to the potential of a large scale release of radioactivity during a severe accident, despite the low probability of these events, fission reactors require multiple safety systems, huge containment buildings, and plans for public evacuation. This last issue in particular has cast a serious shadow over the future of fission reactors as a commercial power source. Besides the threat to the public health, an accident at a fission plant could mean the loss of a huge capital investment due to damage sustained by the reactor, such as at Three Mile Island.

Considering these issues, there is clearly a strong incentive to design fusion reactors which are inherently safe. Ideally speaking, this means that in the event of a severe accident, such as a complete loss of cooling, no external intervention or other additional means of accident mitigation would be required to prevent either a radiological release or substantial plant damage. That is, plant personnel would be able to simply "walk away"from the accident. Repairs would only be required on the failed component which led to the accident, and the down-time of the plant would be minimized. Further, no evacuation of the public would be required. This

would mean that in the construction of the plant, there would be no need for the redundant cooling systems and "nuclear grade"construction, nor for the large containment structure, that is required at fission plants. These aspects of fission plant construction represent a significant fraction of both the capital cost and the construction time. Finally, the lack of a need for evacuation planning would eliminate the licensing snafus that have recently been a major obstacle for the fission industry. The potential for fusion reactors to be inherently safe from damage, even under severe accident conditions, will have a significant impact on whether a commercial fusion reactor is ever built.

1.1 Background and Results of Previous Studies

The issue of the potential hazards of fusion reactor operation has been the focus of a number of earlier studies. Many of these have concentrated on defining the risks associated with fusion [1.1,1.2,1.3]. The primary hazards of fusion plant operation are the use of tritium in the fuel cycle, coupled with the need to use lithium as a tritium breeder (for the D-T fuel cycle only), the activation of structural materials and the potential release of these activation products, and the presence of large magnets and high magnetic fields, resulting in a huge source of stored (magnetic) energy. These items have to be considered in any assessment of the safety of the plant.

Generally speaking, there are two levels of safety concern. The first level involves the risk to public health resulting from a release of radioactivity from the plant. This issue has received considerable attention recently [1.3, 1.4, 1.5, 1.6]. There are two sources of radiation in a fusion power plant: tritium and neutron activation products. Tritium is used as a fuel in the D-T fuel cycle, and is an unavoidable by-product in both the D-D and D-^{3}He fuel cycles, although the inventory of tritium in these advanced fuel cycles is far lower than in the D-T cycle. Neutron activation products are the result of neutron interactions with the first wall/blanket

structures surrounding the plasma. The total inventory of these activation products depends largely on the fuel cycle and the reactor materials. Comparison of the activity levels, as well as the general safety characteristics of the D-T, D-D, and D-^{3}He fuel cycles is made in reference [1.7].

These radiation sources only represent a threat to the public if they are released to the environment. There are a number of mechanisms for the release of radiation. Tritium handling and its associated dangers is fairly well understood, and continues to be the subject of analysis [1.8, 1.9, 1.10]. Almost all of the activation products are contained within the structure of the plant [1.11]. Thus, significant release can only occur if the structural integrity of the reactor is lost, and the radioative isotopes, whether in elemental or oxide form, are volatilized. The loss of structural integrity implies an accident condition. This could be the result of a natural disaster, such as earthquake or flood, or an off-normal condition in the reactor itself, which could lead to structural failure. Mobilization of the radioactive inventory occurs primarily through volatilization of the activation products. Previous studies [1.4, 1.12, 1.13] have shown that this will only occur to a significant degree if the temperature in the activated structure gets very high, well above the normal operating range.

In the past, studies have concentrated on quantifying the risks and consequences of a radiation release from a fusion power plant [1.1, 1.4, 1.5,1.14]. Many of these studies have attempted to reduce the consequence of such a release by minimizing the activation product inventory, primarily through the use of low activation materials [1.15, 1.16, 1.17, 1.18]. If the combination of risk and consequence of a radiation release can be reduced such that there is no threat (or a minimal threat) to the public safety, then the plant can be considered inherently safe with regard to this matter.

The second level of concern regarding plant safety involves damage to the plant itself. Note that the conditions required for the release of a significant part of the activation product inventory would almost always involve severe plant damage (a

tritium release could occur without such damage). However, damage to the reactor, such as a structural failure, does not necessarily imply a release of radioactivity. Plant damage can be caused by natural disasters such as stronger than expected earthquakes, but these phenomena are unavoidable, and at any rate, the risk is the same for all types of power plants. Damage to the reactor can also be the result of equipment and/or operator failure. These failures can generally be divided into three classes. The first involves the release of chemically-stored energy, such as a lithium spill and fire, which could cause extremely high temperatures and severe structural damage. The second involves the release of magnetically-stored energy, such as a magnet failure, which could generate excessive stresses in the reactor structures, also leading to structural damage. Both of these issues are of great importance to fusion plant safety. Finally, the third class of accidents that could cause plant damage is a power/cooling mismatch, which could also generate high temperatures and subsequent failure of structural components. This report concentrates on this third class of failure.

The problem stems from the fact that a loss-of-cooling or an increase in power would cause the temperature in the first wall/blanket region of the reactor to rise. If these temperatures get too high, the structural elements in the first wall/blanket will weaken and subsequently suffer structural failure and possibly melt. In severe cases, this could also lead to the release of some of the activation product inventory.

Methods of quantifying and/or minimizing the risk of plant damage have received far less attention than those involving radiation release. Radiation release is clearly a more severe problem than plant damage, but ideally speaking, inherent safety encompasses both concerns. Logan has defined inherent safety as the requirement that ". . . strictly passive means of shutdown and subsequent afterheat removal be sufficient to prevent significant damage or radioactivity release in the event of (Loss-of-Coolant) or (Loss-of-Flow) accidents, earthquakes, fire, floods, loss of electrical power, malfunction of control systems, or plant operator mistakes"[1.19]. Logan's argument is essentially that inherent safety will represent

an economic advantage for fusion over alternative energy sources, primarily for the reasons discussed in the beginning of this chapter.

Fetter [1.1] also makes a strong case for inherently safe fusion reactors, but essentially defines inherent safety as only the requirement that off-site doses resulting from an accident be low enough to avoid any early deaths.

The definition of inherent safety adopted for this study is taken to be that given by Logan. That is, only those blankets which passively cool themselves, after a loss-of-cooling transient, without sustaining any damage are considered inherently safe. This automatically includes the requirement that there be no significant release of radiation. Blankets which are likely to suffer damage in the event of an undercooling transient, but do not pose any threat of significant radiological release, are not considered inherently safe, but still represent a substantial advantage over current fission light-water-reactor technology. It must be pointed out that this study encompasses only loss-of-cooling transients, and its purpose is to identify design and operational guidelines which improve or assure safety with regard to these transients. A truly passively safe reactor must be protected against other potential failures as well, such as lithium fires, magnet failures, and tritium releases. Furthermore, the designs identified in this report as passively safe, that is, those designs that achieve the passive safety criteria, can be considered passively safe only with regard to loss-of-cooling transients. They cannot necessarily be considered passively safe with regard to the full range of accidents that must be considered at a fusion power plant.

This report investigates some of the thermal aspects of fusion reactor safety; in particular, the thermal and structural response of fusion blankets to power/cooling mismatches. There are essentially two types of power/cooling mismatches, both of which will result in elevated temperatures in the blanket. The first type involves loss-of-cooling, and is referred to as an undercooling transient. The second type involves an increase in the power level with no corresponding increase in the cool-

ing rate, and is referred to as an overpower transient. The purpose of this study is to determine whether blankets can be designed that will passively cool themselves without damage in the event of a power/cooling mismatch, and to identify elements of blanket design which enhance thermal safety. Design elements which hinder thermal safety are also identified, and suggestions for alternative approaches are given. The impact of some operational parameters is also examined, with the goal of developing operational guidelines to insure passive safety. Much of this work was carried out in conjunction with the study conducted by the Senior Committee on Environmental, Safety, and Ecomomic Aspects of Magnetic Fusion Energy (ESECOM) [1.4], and some of the results presented in this report have been used in the ESECOM work.

1.2 Approach and Outline of Analyses Performed

The basic approach to this investigation involves calculating the temperature response of a blanket to undercooling and overpower transients. Once the temperature response is known, a determination can be made as to whether the blanket will suffer structural damage, and whether there exists significant potential for the release of radioactivity. The temperature responses of a number of different blankets are then compared to determine which designs are better in terms of thermal safety. The sensitivity of the temperature response to a number of operational parameters is also determined through a series of parametric calculations, in order to establish operational guidelines.

1.2.1 Introduction to Reference Blanket Selection

In order to fulfill the purpose of this investigation, a number of reference fusion reactor blanket designs are required, on which the analyses are performed. A careful literature survey was conducted to identify conceptual blanket designs which are

appropriate for this purpose. As a result of this survey, a total of six different blanket designs were selected as the reference blankets. The blankets that were chosen are considered to represent the state-of-the-art in fusion blanket design. Also, the variations among them allow for interesting comparisons, for the purposes of identifying the design elements which affect thermal safety. The blankets selected include two self-cooled, liquid metal tokamaks, two helium-cooled, solid breeder tokamaks, a self-cooled liquid metal Reversed-Field-Pinch (RFP), and a helium-cooled, steel structure, D-D fuel cycle tokamak.

The blankets came essentially from three sources. The primary source was the Blanket Comparison and Selection Study (BCSS), which was coordinated by Argonne National Laboratory and completed in 1984 [1.20]. The BCSS represents the most complete examination of blanket design issues performed to date. In the study, a wide range of blanket options were evaluated on the basis of viability, cost, performance, and safety. Each option was ranked according to its merits as either a promising concept which deserves high priority attention (level one); a potentially attractive concept, with some modifications, deserving a low level research effort (level two); an unattractive concept which should not be considered further (level three). The BCSS blankets used in this study are all ranked level one or level two.

The second source of reference blankets was the ESECOM study [1.4], which also analyzed a number of blanket designs, on the basis of economic, safety, and environmental concerns. Some of the blankets used in the ESECOM study are slight modifications of the blankets identified by the BCSS as promising (level one). Many of the analyses presented in the following chapters were carried out simultaneously with the ESECOM study. In fact, the nature of some of these analyses was guided by ESECOM, and the results obtained herein will be published in the ESECOM report.

Finally, the third source of a reference blanket was a study comparing the economic and safety aspects of various fusion fuel cycles [1.7], carried out by Brereton

at MIT. A D-D fuel cycle blanket was taken from Brereton's work, such that the thermal safety aspects of this fuel cycle could be analyzed.

Blanket #1 was taken from the Blanket Comparison and Selection Study (BCSS) [1.20]. It is a self-cooled liquid lithium design, with vanadium alloy V-15Cr-5Ti structure. Blanket #2 also was taken from the BCSS, and is helium-cooled with solid Li_2O breeder. The structural material is HT-9 which has been modified for low activation [1.1]. This version of HT-9 is referred to as MT-9 throughout the remainder of this report. These two blankets, while BCSS designs, were chosen in parallel with ESECOM. Blanket #3 was also chosen in parallel with ESECOM [1.4], and is similar to the blanket design of the TITAN Reversed-Field-Pinch reactor [1.21]. It is also a self-cooled liquid lithium blanket with VCrTi structure. Blanket #4 is identical to Blanket #1, except it uses liquid lithium lead $Li_{17}Pb_{83}$ as the breeder/coolant. Blanket #5 is identical to Blanket #2, except beryllium has been added to improve the neutronic performance. Finally, Blanket #6 was taken from Brereton's study which compared the economic and safety aspects of different fuel cycles [1.7]. It is part of a D-D reactor, consisting of helium-cooled MT-9 structure. The blanket designs are discussed in detail in Chapter 2.

1.2.2 Introduction to Material Limits

A determination of the allowable temperature limits in the materials of interest is also required, in order to distinguish acceptable temperature responses from those which will result in damage. For this study, the materials of interest are two of the most widely considered fusion structural alloys, namely the vanadium alloy V-15Cr-5Ti, and a modified version of the ferritic steel HT-9. This version of HT-9, called MT-9 in this report, was proposed by Fetter [1.1], and is modified to reduce activation. The relevant failure mechanisms for these alloys at elevated temperatures are those of acute structural failure, thermal creep rupture, and oxidation/volatilization, which can lead to the mobilization of the radioactive

inventory. Acute structural failure occurs when the stress in a material exceeds the Ultimate Tensile Strength (UTS) of the material. This also refers to changes in the micro-structure of the material which may take place as a result of the elevated temperatures. These changes in micro-structure will prohibit the future use of the material. Thermal creep rupture occurs when the applied stress combines with high temperatures to cause excessive creep. The material limits models and assumptions are developed in Chapter 3.

The temperature limits presented in Chapter 3 and used in this study were taken from a number of sources. The primary sources of material limit information were the semi-annual reports published by the Alloy Development for Irradiation Performance (ADIP) program [1.22]. The thermal creep data for both HT-9 and VCrTi came largely from the UCLA materials effort headed by Nasr Ghoniem [1.23]. The analysis of thermal creep in vanadium structures was done in conjunction with the TITAN study [1.21], although the models used in TITAN are not necessarily the same as those used here. The oxide mobilization data was taken directly from the ESECOM study [1.4] and some of its supporting references [1.12,1.13].

For the structural materials used in this analysis, the available strength data are limited to temperatures below about 650 °C [1.20,1.22,1.23,1.24]. This necessitated that assumptions be made about the strength of these materials at higher temperatures, as well as extrapolation of the available data to the temperature range of interest in this study. The data on the effect of irradiation on the strength properties of the structural materials is even more limited. For this reason, the limits used in this study represent unirradiated strength property data.

1.2.3 Introduction to Decay Heat Analysis

It is clear that the temperature response of a blanket to a given power/cooling mismatch will depend on the magnitude and distribution of the heat source. In the undercooling transients, this heat source has two origins. First, there is the

plasma heat flux on the surface of the first wall, and the operational power density from neutron interactions within the volume of the blanket. As long as the plasma continues to burn, this heat source will exist. In most of the undercooling analyses performed in this study, it is assumed that the plasma shuts off rapidly, and this heat source turns out to be relatively small. The second origin of heat is the decay of radioactive isotopes within the blanket. These isotopes, usually referred to as activation products, are produced by neutron interactions with the blanket materials. Both the D-T and D-D fuel cycles represent large neutron sources, and consequently yield significant neutron fluxes in the reactor structures. The resulting decay heat distributions are calculated for each of the blankets, and comparisons are made to identify the materials and design aspects which yield the lowest decay heat levels. This analysis is discussed in detail in Chapter 4. In the overpower transient analyses, only the plasma burn heat source is considered.

The decay heat level and general activation characteristics of fusion reactors has been the subject of a large number of previous studies [1.1, 1.11, 1.15, 1.25]. Most of the low activation work done previously has sought primarily to reduce the long term activation problems, such as reducing the contact dose to maintenance workers and alleviating the waste disposal problem. Decay heat production is a short term concern, i.e., the time frame is measured in hours or at most days.

A number of tools exist for the calculation of the decay heat level in a fusion reactor. Unfortunately, the agreement between them is not always good, and all of them are subject to the uncertainties in neutron cross-section data [1.26]. In this study, the decay heat level is calculated through the use of the REAC activation/transmutation code developed at Hanford Engineering and Development Laboratory (HEDL) [1.27], in conjunction with the ONEDANT neutronics code, developed at Los Alamos National Laboratory (LANL) [1.28]. ONEDANT is used to calculate the operational neutron fluxes in the blanket. These fluxes are then used as an input to REAC, which calculates the specific activity of the radioactive isotopes that are produced.

1.2.4 Introduction to Undercooling Transient Analysis

In the past, the early stage of fusion reactor design has made accurate calculation of the temperature response of fusion blankets to undercooling transients very difficult. With the emergence of detailed conceptual designs such as STARFIRE, MARS, and the BCSS designs, these calculations can now be made. Piet [1.14] analyzed the blanket temperature rise after a Loss-of-Coolant Accident (LOCA) for a number of different blanket designs. Piet's goal, however, was to develop simple scaling laws which allow for easy comparison of the thermal safety margins of different materials. Piet was also plagued (as was this study) by a lack of strength data for the relevant materials, and thus had to heuristically define the temperature limit as a 300 °C rise above the operational value.

More recently, others have calculated the post-LOCA temperature rise in fusion blankets [1.19,1.25]. For the most part, the purpose and results of these previous analyses are similar to those of this study. Both the ESECOM and TITAN studies paid considerable attention to this issue, both in parrallel with this work.

In general, undercooling transients can be split into two groups, namely Loss-of-Flow Accidents (LOFA) and Loss-of-Coolant Accidents (LOCA). For the purposes of carrying out the analyses presented in this report, a number of assumptions are made to define the characteristics of each accident scenario. Further, a number of parameters are varied, such that there are a total of eight different undercooling transient cases. Each case is defined by a set of parameters and assumptions, which are outlined in Chapter 5.

The calculated heat source is an input into the model that calculates the temperature response to a specific undercooling transient. In Chapter 5, a model is developed to account for conductive and radiative heat transfer only, that is, the effects of convection are neglected. The temperature responses calculated with this model are analyzed with the material limits models developed in Chapter 3 to determine whether structural failure is likely to occur. The results of this analysis

for the different blankets are compared, to determine which of the blankets can be considered passively safe, and identify the elements of the designs that affect the thermal safety. The sensitivity of the temperature response to the operational neutron wall load, as well as a number of other parameters, is determined through a series of parametric studies.

1.2.5 Introduction to Natural Convection Analysis

The most common type of LOFA is a pump-failure accident, in which the coolant pump fails. The assumption used in the undercooling transient analysis presented in Chapter 5 is that in this case, the coolant immediately stops flowing, and remains stagnant for the duration of the transient. In reality, it is possible that the coolant would continue to flow at some reduced rate, due to the pressure head that arises from buoyancy effects in the flow loop. Assuming the secondary cooling cycle remains availabe and operational, the flowing primary coolant would transport heat out of the blanket, and could substantially limit the temperature rise in a LOFA. This phenomenon is known as natural convection. The impact that natural convection has on the LOFA temperature response is analyzed in Chapter 6. The results are used to identify and recommend design aspects which enhance the potential for natural convection cooling.

Earlier studies on the question of natural convection in fusion reactors have generally found that the strong MHD pressure drop will greatly inhibit natural convection flow [1.29, 1.30], especially in lithium cooled systems. Properly analyzing such thermal-hydraulic phenomena in a fusion reactor has been severely hindered by the lack of detailed designs. Recent design studies such as the BCSS have partially alleviated this problem.

1.2.6 Introduction to Plasma Overpower/Continuation Transient Analysis

Besides the decay heat, the other heat source that can result in temperature excursions is the plasma. This can happen in two ways. First, if the plasma power increases with no corresponding increase in the cooling rate, the temperature will rise. This is called a plasma overpower transient, or simply an overpower transient. Secondly, a temperature rise will result if the plasma continues to burn after cooling is lost. This is known as a plasma continuation transient. The plasma overpower/continuation transients differ from the decay-heat induced transients in that the primary heat source is the plasma heat flux on the surface of the first wall. Compared to the decay heat source, this plasma heat flux is very large, and can cause a rapid temperature rise in the first wall, as well as a large thermal gradient. The result is that first wall failure is likely to occur much more quickly in the plasma induced transients than in the decay-heat induced transients. The overpower/continuation transients are analyzed in Chapter 7.

Previous studies [1.2, 1.31] have indicated that a plasma overpower transient would terminate before first wall failure due to first wall ablation, which would increase the impurity level in the plasma and quench it. This remains somewhat uncertain, and at any rate, by the time the transient terminates, the amount of first wall material ablated may be excessive, requiring replacement of the first wall. To avoid these problems, Logan [1.19] has suggested a mechanism which would cause the plasma to quench before any damage has resulted. This concept involves a small canister of helium, which would escape into the plasma in the event of an overpower or plasma continuation transient, and thus quench it. This idea is partially the basis of the analysis presented in Chapter 7.

References for Chapter 1

[1.1] S. Fetter, Radioligical Hazards of Magnetic Fusion Reactors, Lawrence Livermore National Laboratory, LLNL MS#61485F, 1985.

[1.2] J.G. Crocker and D.F. Holland, Safety and Environmental Issues of Fusion Reactors, Proc. of the IEEE, Vol. 69, No. 8, pp. 968-976, August 1981.

[1.3] J.P. Holdren and S. Fetter, Contribution of Activation Products to Fusion Accident Risk: Part II. Effects of Alternative Materials and Designs, Nuclear Technology/Fusion, 4, pp. 599-617, November 1983.

[1.4] Report of the Senior Committee on Environmental, Safety and Economic Aspects of Magnetic Fusion Energy, Final Report, U.S. DOE, to be issued as a Livermore National Laboratory report, 1987.

[1.5] S. Fetter, A Calculational Methodology for Comparing the Accident, Occupational and Waste Disposal Hazards of Fusion Reactor Designs, Fusion Technology, 8, p. 1359, July 1985.

[1.6] S. Fetter, Radiological Hazards of Fusion Reactors: Models and Comparisons, Doctoral Dissertation, University of California, Berkeley, May 1985.

[1.7] S.J. Brereton and M.S. Kazimi, Safety and Economic Comparison of Fusion Fuel Cycles, PFC/RR-87-7, Massachusetts Institute of Technology, Plasma Fusion Center, August 1987.

[1.8] J.B Cannon, Background Information and Technical Basis for Assessment of Environmental Implications of Magnetic Fusion Energy, U.S Department of Energy, DOE/ER-0170, August 1983.

[1.9] J.E. Phillips and C.E. Easterly, Sources of Tritium, Nuclear Safety, 22, No. 5, p. 612, September-October 1981.

[1.10] D.K. Sze et al.. An Assessment of Problems Associated with Tritium Containment, Fusion Technology, 8, p. 1985, September 1985.

[1.11] E.T. Cheng, Radioactivation Characteristics for Deuterium- Tritium Fusion Reactors, Nuclear Technology/Fusion 4, 1983.

[1.12] S.J. Piet, et. al., Oxidation/Volatilization Rates in Air for Candidate Fusion Reactor Blanket Materials, PCA and HT-9, J. Nucl. Mater. 141 – 143, pp. 24-28, November/December 1986.

[1.13] R.M. Neilson, Volatility of V15Cr5Ti Fusion Reactor Alloy, Idaho National Engineering Laboratory, EG&G Idaho, EGG-M–25985, December 1986.

[1.14] S.J. Piet, M.S. Kazimi, L.M. Lidsky, Potential Consequences of Tokamak Fusion Reactor Accidents: The Materials Impact, PFC/RR-82-19, Massachusetts Institute of Technology, Plasma Fusion Center, June 1982.

[1.15] G. Hopkins, et. al., Low Activation Fusion Design Studies, GA Technologies, Inc., GA-A17389, October 1984.

[1.16] J.A. Blink and G.P. Lasche, The Influence of Steel Type on the Activation and Decay of Fusion Reactor First Walls, Nuclear Technology/Fusion, 4, p. 1146, September 1983.

[1.17] R.W. Conn and A.W. Johnson, Minimizing Radioactivity and Other Features of Elemental and Isotopic Tailoring of Materials for Fusion Reactors, Nuclear Tech–
nology, 41, p. 1146, December 1978.

[1.18] M.Z. Youssef and R.W. Conn, On Isotopic Tailoring For Fusion Reactor Radioactivity Reduction, Nuclear Technology/Fusion, 4, p. 1177, September 1983.

[1.19] B.G. Logan, A Rationale for Fusion Economics Based on Inherent Safety, Lawrence Livermore National Laboratory, UCRL-91761, November 1984.

[1.20] D.L. Smith et al., Blanket Comparison and Selection Study (BCSS) - Final Report, Argonne National Laboratory, ANL/FPP-84-1, September 1984.

[1.21] F. Najamabadi, N.M. Ghoniem, R.W. Conn, et al., The TITAN Reversed-Field Pinch Fusion Reactor Study, Scoping Phase Report, UCLA-PPG-1100, January, 1987.

[1.22] R.E. Gold and R. Bajaj, Mechanical Property Evaluation of Path C Vanadium Scoping Alloys, Alloy Development for Irradiation Performance - Semiannual Progress Report DOE/ER-0045/10, pp. 122-141, October 1983.

[1.23] R.J. Amodeo and N.M. Ghoniem, Development of Design Equations for Ferritic Alloys in Fusion Reactors, Nuclear Engineering and Design/Fusion, 2, p. 97, 1985.

[1.24] J.E. Chafey and J.B. Wattier, Estimation of Allowable Design Stress Values for 12Cr-1Mo-0.3V Steel, General Atomic Project 4230, GA-A14610, February 1978.

[1.25] D.K. Sze, J. Jung, Afterheating Calculations, Argonne National Laboratory, presented at Georgia Institute of Technology, Atlanta, Georgia, May 15-16, 1985.

[1.26] E.T. Cheng, J.A. Blink, B.A. Engholm, F.M. Mann, A.M. White, Activation Cross Section Library Comparison Study - Numerical Results, June 1984.

[1.27] F.M. Mann, Transmutation of Alloys in MFE Facilities as Calculated by REAC (A Computer Code System for Activation and Transmutation), Hanford Engineering Development Laboratory, HEDL-TME-81-37, August 1982.

[1.28] R.D. O'Dell et al., User's Manual for ONEDANT: A Code Package for ONE-Dimensional, Diffusion-Accelerated, Neutral- Particle Transport, Los Alamos National Laboratory, LA-9184-M, February 1982.

[1.29] P.J. Gierszewski, B. Mikic, and N.E. Todreas, Natural Circulation in Fusion Reactor Blankets, ASME Journal of Heat Transfer V. 80-HT-69, pp. 1-7, July, 1980.

[1.30] B. Malinovic, Natural Convection Characteristics of Liquid Metal Cooled Fusion Reactors, S.M. Thesis, Nuclear Engineering Department, Massachusetts Institute of Technology, 1986.

[1.31] C.C. Baker et al., STARFIRE - A Commercial Tokamak Fusion Power Plant Study, Argonne National Laboratory, ANL/FPP-80-1, September 1980.

2. Reference Design Selection and Verification

The analyses described in this work were carried out on some or all of six reference blankets, which were chosen from a variety of sources. The underlying assumptions behind the important design parameters of each blanket, such as operational neutron wall load and surface heat flux, operating temperature range, and blanket lifetime, were verified through a brief literature survey. The tritium breeding ratios and blanket multiplication factors were checked using the one-dimensional neutronics code ONEDANT [2.1] to ascertain that they are in the acceptable range. The six designs selected are described in detail in this chapter, along with a brief review of their important parameters. The elemental compositions of the materials used are given in Table 4.2.1, and their thermal and mechanical properties are discussed in Chapter 5 and Appendix C.

Each blanket is designated simply by a number, i.e., Blanket #1, Blanket #2, etc. The general features of the six blankets chosen are summarized in Table 2.0.1. Furthermore, throughout the course of this work, some variations were made to some of the blankets. Different variations of a particular blanket were used to examine the effect the variation would have on the thermal safety of the blanket. Most of these variations involved material substitutions, e.g. MT-9 for Fe1422 in the manifold region of Blankets #1 and #3. Others represented slight changes in the configuration of the blanket, usually as attempts to improve the heat transfer from the first wall to the heat sink. Because of these variations, it became convenient to

Table 2.0.1 General Features of Reference Blankets.

Blanket	Material Combinations (Breeder/Coolant/Structure)	Reactor Type	Total Thickness (Blanket + Shield, m)	Neutron Wall Load (MW/m^2)	Lifetime (Full Power Years)
#1	Li/Li/VCrTi	D-T Tokamak	1.280	5.0	3.0
#2	Li_2O/He/MT-9	D-T Tokamak	1.068	5.0	3.0
#3	Li/Li/VCrTi	D-T RFP*	1.055	15.0	1.0
#4	$Li_{17}Pb_{83}/Li_{17}Pb_{83}$/VCrTi	D-T Tokamak	1.283	5.0	3.0
#5	Li_2O/He/MT-9/Be†	D-T Tokamak	1.068	5.0	3.0
#6	He/MT-9‡	D-D Tokamak	0.910	1.17	12.5

* Reversed-Field-Pinch; This design uses copper magnets, and thus does not have a magnet shield. The coils are included in the blanket thickness.

† Beryllium neutron multiplier is added to improve neutronic performance.

‡ D-D fuel cycle does not require tritium breeding, thus this blanket consists of coolant and structure only.

develop a method of referring to each blanket and its variations. In this method, a two character code is used to designate a particular variation of a particular blanket. The first character is a letter that designates the blanket (i.e., Blanket #1 - #6). Each blanket has a letter that corresponds to it. The second character is a number that represents the variation of the blanket. These two characters, then, designate the blanket and the variation. The different variations are shown in Table 2.0.2.

The six blankets that were chosen were selected for two reasons. First, they represent the state of the art in current fusion blanket design, and second, the variations among them allow for comparisons that should yield indications as to which design elements improve (or hinder) thermal safety.

Four of the blankets (Blankets #1, #2, #4, and #5) are essentially designs developed during the Blanket Comparison and Selection Study (BCSS) [2.2]. For the most part, there is good agreement between the maximum temperature limits given in the BCSS and those given in the literature [2.3 - 2.7]. Some of the operating conditions and parameters of the BCSS blankets are given in Table 2.0.3. According to Adegbulugbe [2.3], to achieve a 3 year lifetime with a first wall (FW) of 4.5 mm thickness (average BCSS FW thickness), the first wall heat flux must be less than about 0.7 MW/m^2, a 30% discrepancy with the BCSS. Also, assuming a flawed first wall, due to the crack growth rate, Adegbulugbe states that the first wall heat flux must not exceed 0.6 MW/m^2 to achieve a three year life, given the plasma burn cycle assumed in the BCSS.

Yu [2.4] indicates that a 7.5 mm beginning-of-life (BOL) first wall thickness is needed to support the stresses at end-of-life, which is 25% higher than the 6 mm BOL thickness given in the BCSS. Yu's value is based on an erosion rate of 1.5 mm/yr, which is 50% higher than the BCSS-assumed erosion rate of 1.0 mm/yr. According to Yu's fatigue analysis, a 15 MW-yr/m^2 lifetime is attainable for a first wall under 15 mm thick, but Yu puts a 10 MW-yr/m^2 lifetime limit on the first wall due to the loss of ductility.

Table 2.0.2 Designation of Blanket Variations.

Blanket	Designation	Variation
#1	A0	VCrTi Manifold, Fe1422 Shield
	A1	Fe1422 Manifold, Fe1422 Shield
	A2†	MT-9‡ Manifold, Fe1422 Shield
	A3	MT-9‡ Manifold, MT-9‡ Shield
#2	D1	First Wall Includes Radial Fins
	D4†	Slab First Wall Design
#3	E1	Slab First Wall, Fe1422 Manifold
	E2	Slab First Wall, MT-9‡ Manifold
	E3	Tubular First Wall, Fe1422 Manifold
	E4†	Tubular First Wall, MT-9‡ Manifold
#4	F1†	As Described in Text
#5	G1†	As Described in Text
#6	H1†	As Described in Text

† Base blanket, as described in Text.

‡ Modified low activation HT-9 from Reference [2.10].

Table 2.0.3 Operating Conditions and Parameters of Blanket #1. Wall Load, Heat Flux, and Erosion Rate are the same for all BCSS Blankets.

Parameter	Value
Neutron Wall Load	5.0 MW/m^2
First Wall Heat Flux	1.0 MW/m^2
Blanket Lifetime	3 Full Power Years
First Wall Erosion Rate	1 mm/yr
BOL First Wall Thickness	6 mm
EOL First Wall Thickness	3 mm
Maximum Structural Temperature	750 °C
Maximum Interface Temperature	740 °C

Other references generally support the parameters given in the BCSS. Blanchard and Ghoniem [2.5] indicate a maximum lifetime of 3 years due to the 2% strain limit criterion. Maziasz [2.6] states that with some improvements, a 15 MW-yr/m^2 lifetime should be possible at 500 °C operation, and Bloom and Smith [2.7] come to similar conclusions.

2.1 Blanket #1 - BCSS Li/Li/VCrTi

This blanket was chosen in parallel with the work of the Environmental, Safety, and Economics Committee (ESECOM) [2.8], which looked into some of the same issues that are covered in this work. The design is essentially the self-cooled Lithium-Vanadium tokamak blanket described in Chapter 7 of the BCSS.

The important parameters for this blanket, as described in the BCSS, are shown in Table 2.0.3. The operational neutron wall load is 5 MW/m^2, with a surface heat flux of 1 MW/m^2. The assumption is that 20% of the plasma heat flux is radiated to the limiter. The blanket is designed for a lifetime of three full power years, i.e., 15 MW-yr/m^2. A review of the literature [2.3 - 2.7] shows that these are slightly optimistic but reasonable values. Table 2.1.1 shows the tritium breeding ratio (TBR) and blanket multiplication factor for this and all the blankets considered. As can be seen, the 1-D TBR and blanket multiplication factor are both adequate.

The basic Tokamak dimensions for Blanket #1 (as for Blankets #2, #4, and #5) were taken from the BCSS, and are the same as STARFIRE [2.9]. Figure 2.1.1 gives these dimensions. As can be seen, the major radius is 7.0 m, and the first wall radius is 2.14 m.

Both the neutronic and thermal analyses performed in this work were done in one dimension. Most of the thermal analysis was carried out assuming slab geometry. A one-dimensional slab representation of the basic design for the blanket

Table 2.1.1 Tritium Breeding Ratios (TBR) and Blanket Energy Multiplication Factors for the Reference Blankets.

Blanket #	TBR	Blanket Multiplication Factor
1	1.33	1.16
2	1.20	1.14
3	1.32	1.22
4	1.31	1.25
5	1.37	1.10
6	N/A	1.83

Figure 2.1.1 Reference Tokamak Dimensions. From Reference [2.2].

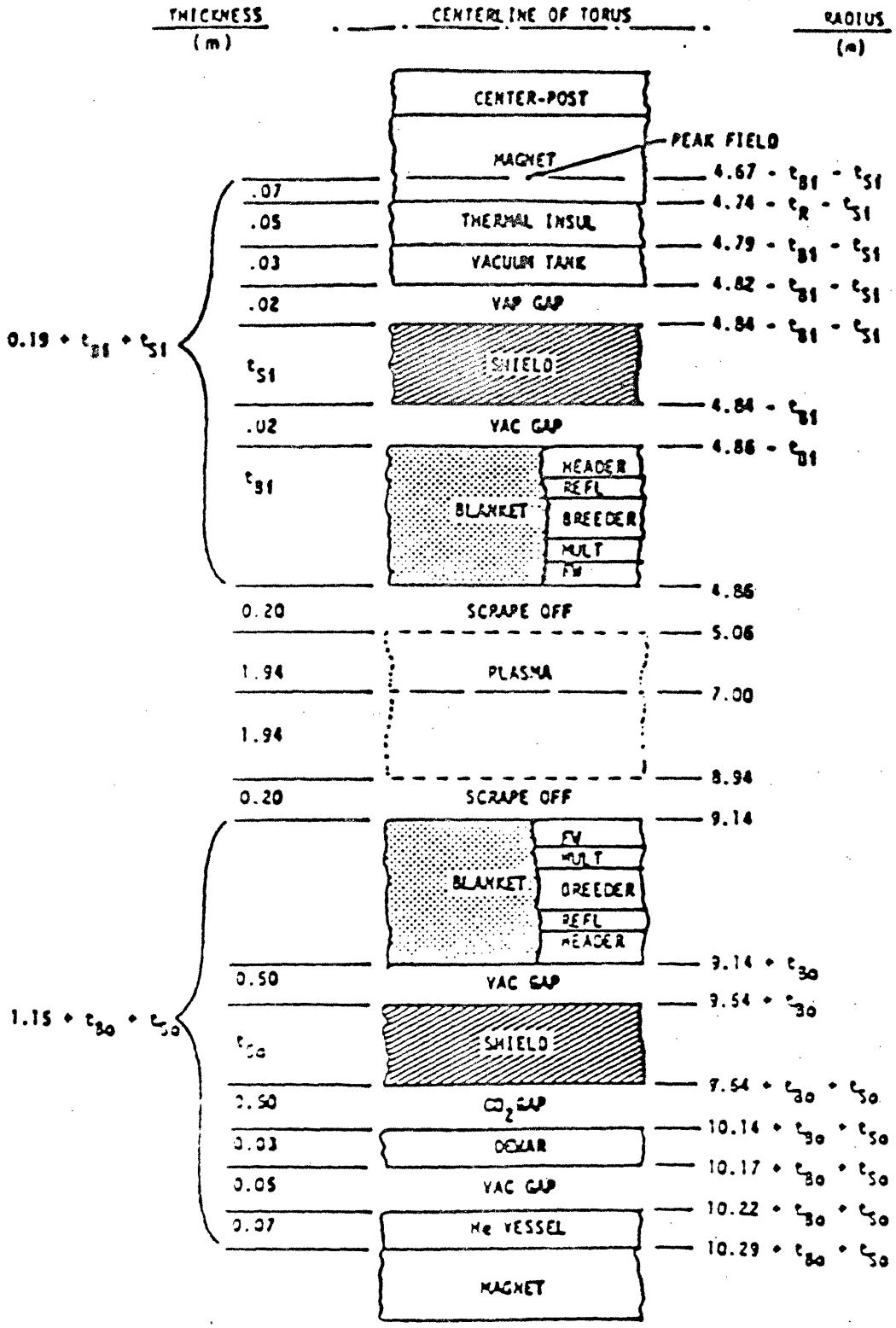

itself is shown in Figure 2.1.2. The vertical dashed lines delineate the "regions"of the blanket. For identification purposes, the regions of each blanket are numbered from left to right, i.e., in the case of Blanket #1, from 1 to 8. Region 1 is essentially the front face of the first wall, that is, that portion which receives the plasma heat flux. Region 2 is the first wall coolant channel, and consists of rectangular channels through which the lithium coolant flows. Region 3 is the back structural slab of the first wall. Region 4 is the main breeding region, consisting mostly of liquid lithium, with 7.5% VCrTi structure. Region 5 is the manifold region, where the lithium coolant enters and exits the blanket from the coolant headers. Region 6 is the second wall, a solid slab for structural purposes. Region 7 is the vacuum gap, which provides thermal insulation for the blanket, in order to minimize heat loss from the blanket during operation. The design of this gap turns out to be quite interesting from the standpoint of thermal safety, as is discussed in Chapter 5. Finally, Region 8 is the shield, which operates at low temperature and provides radiation and thermal shielding for the superconducting magnets.

The dimensions shown in Figure 2.1.2 correspond to the inboard side - the reason for analyzing the inboard side is given in Chapter 4. The actual first wall geometry is shown in Figure 2.1.3. This shape is modeled as shown in Figure 2.1.4 for the purpose of the one-dimensional slab analysis.

The material volume fractions were taken directly from the BCSS. While the BCSS design utilizes Fe1422 as the structural material in the manifold region (Region 5), Blanket #1 uses a modified version of HT-9 (MT-9), as a thermal safety improvement. This is discussed in Chapters 4 and 5. The HT-9 used is modified for low activation, as proposed by Fetter [2.10]. The material fractions in Region 2 (88.9% Li, 11.1% VCrTi) are calculated from the information given in Figure 2.1.4, where it is shown that the VCrTi "slabs"are 0.3 cm thick, and the Li channel is 2.4 cm thick; thus, the VCrTi is 11.1% (0.3/(0.3+2.4)) of the material in this region.

Figure 2.1.2 One-Dimensional Schematic of Blanket #1 for Neutronic and Thermal Analyses.

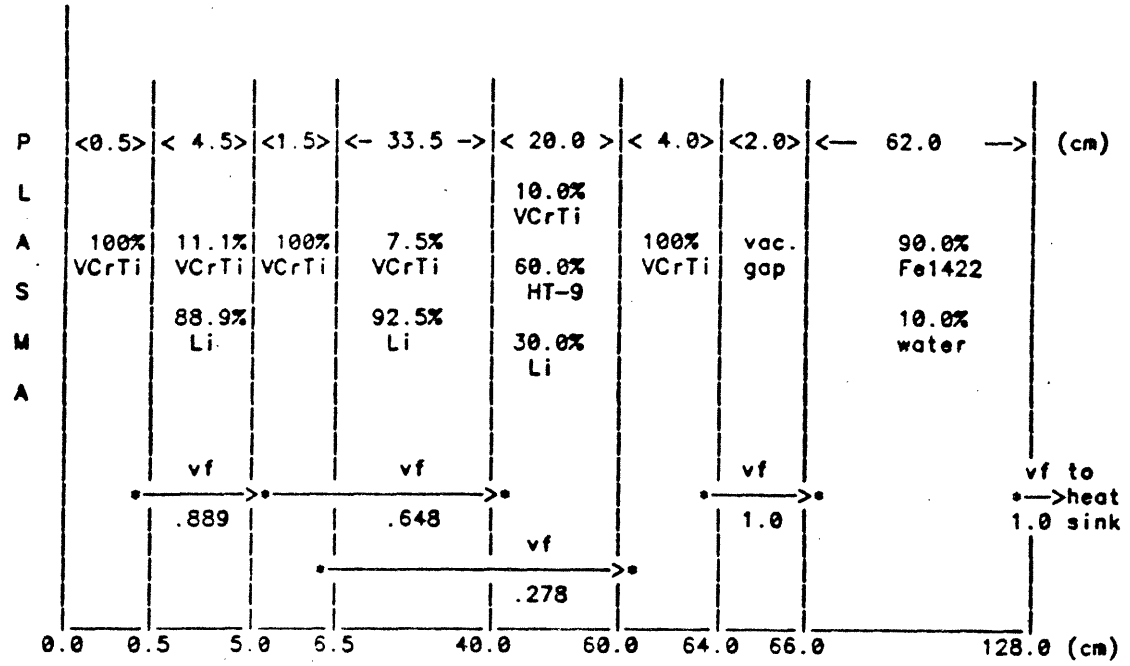

• Arrows connecting asterisks indicate thermal radiation paths in LOCA (complete Lithium drain) case. The vf parameters indicate the view factor for that particular radiation path.

Figure 2.1.3 Schematic of Blanket #1 Geometry. From Reference [2.2].

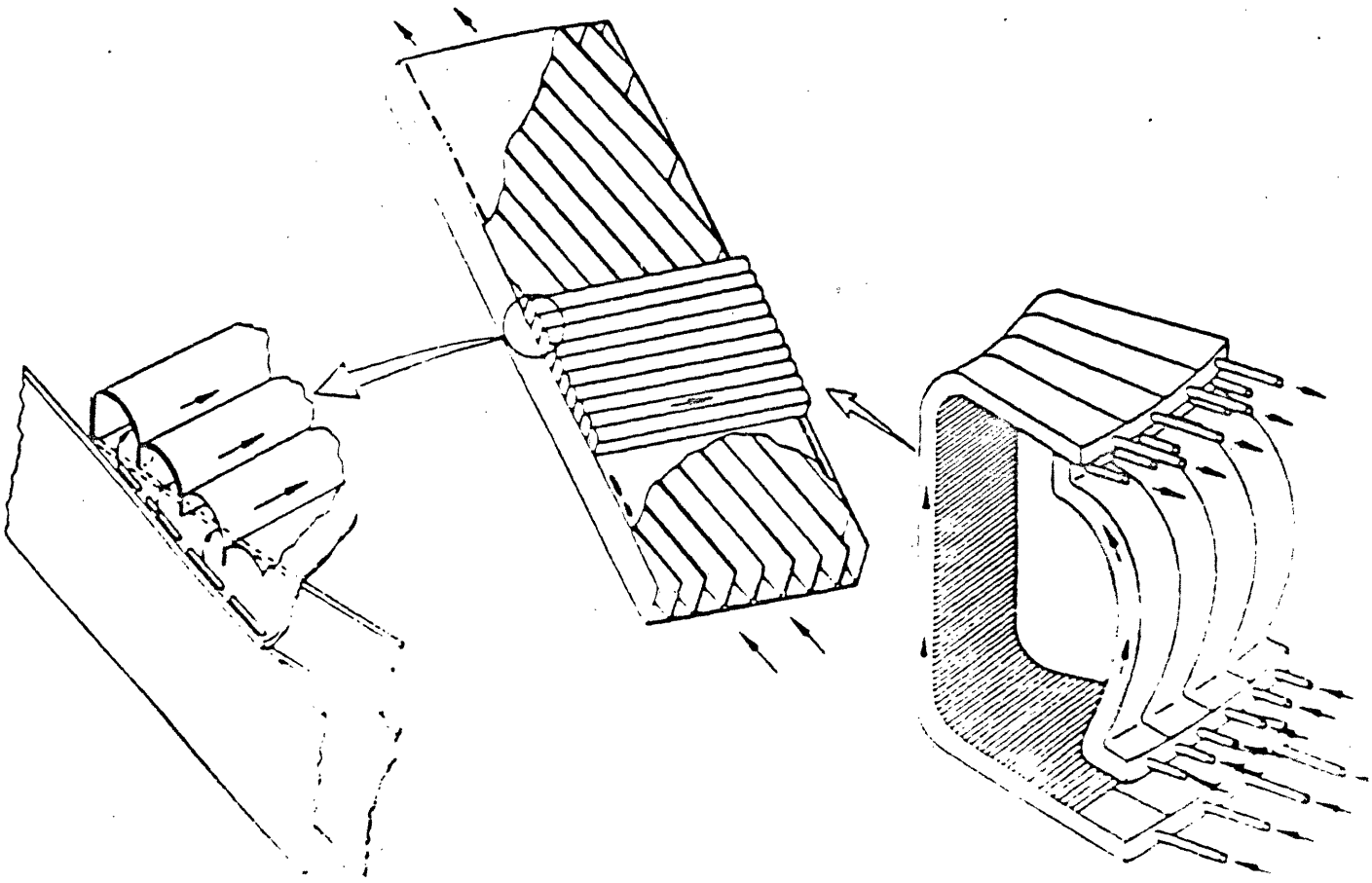

Figure 2.1.4 Cross-sectional View and Dimensions of Blanket #1. From Reference [2.2].

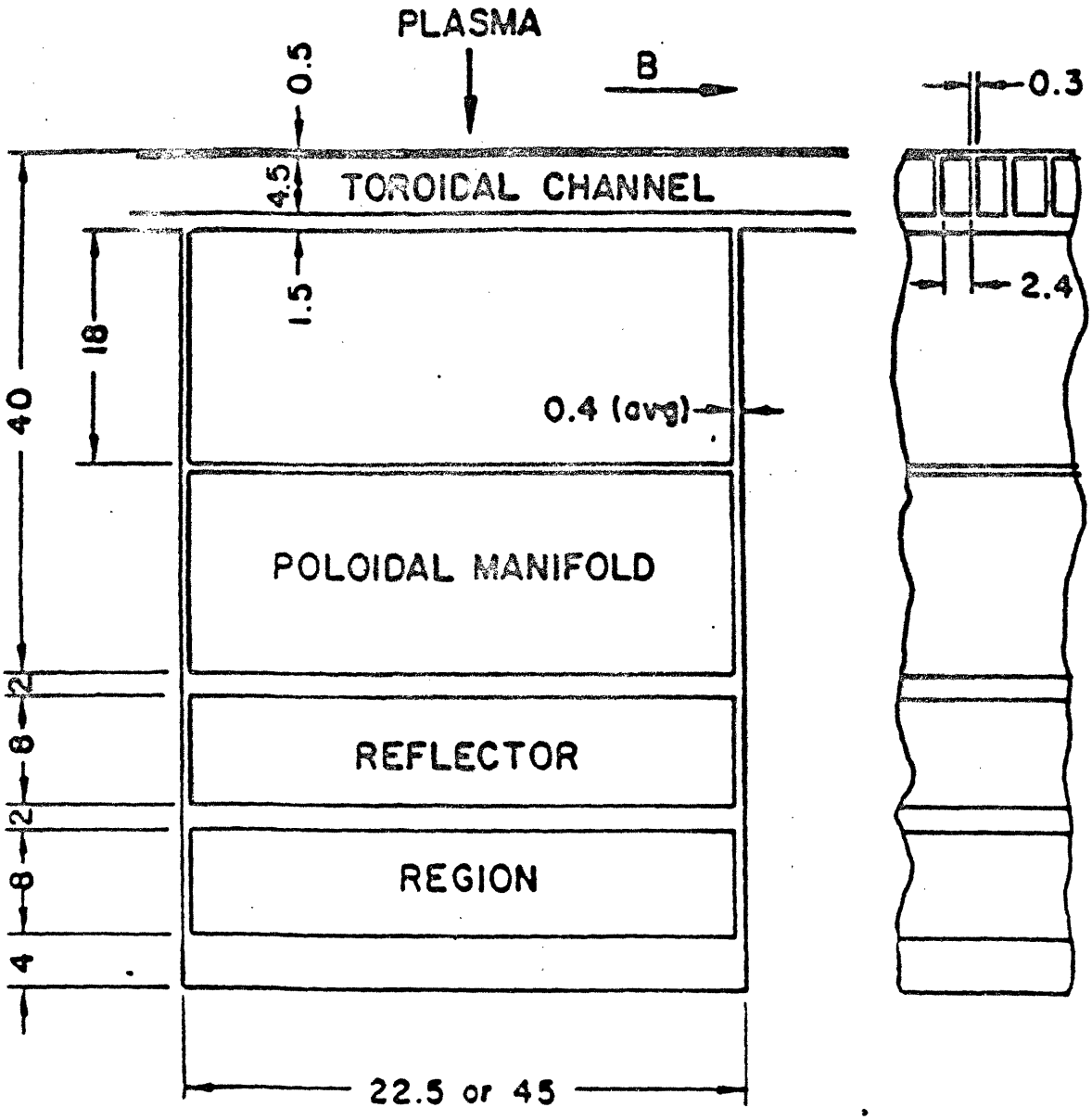

2.2 Blanket #2 - BCSS Li_2O/He/MT-9

Blanket #2 was also chosen in parallel with the ESECOM study, and also was taken from the BCSS (BCSS Chapter 8). It consists of a helium-cooled, solid Li_2O breeder with the ferritic steel MT-9, which is a version of HT-9 modified for low activation based on reference [2.10], as the structure. The one-dimensional geometry is shown in Figure 2.2.1, which is the slab representation of the actual blanket module shown in Figure 2.2.2. Region 1 is the front slab of the first wall. Region 2 is the coolant path for the helium coolant, and consists essentially of pure helium. Region 3 is the back slab of the first wall, and it provides structural support as well as defines the coolant flow path. Region 4 is the flow distribution region, where the coolant is distributed into the breeder channels. Region 5 is the main breeder region, consisting mostly of solid Li_2O. Region 6 is the second breeder region. Region 7 is the manifold region, where the coolant exits the blanket. Region 8 is the vacuum gap, and Region 9 is the magnet shield. All the material fractions were taken directly from the BCSS.

The important parameters for Blanket #2 are essentially the same as for Blanket #1 (see Table 2.0.3). The only differences are in the maximum allowed temperatures. For Blanket #2, these are about 200 °C less than for Blanket #1 [2.2,2.3]. As is seen in Table 2.1.1, the 1-D tritium breeding ratio for Blanket #2 is marginally acceptable. The TBR (and blanket multiplication) can be improved by adding beryllium to the blanket [2.2,2.9]. Blanket #5 is identical to Blanket #2 except that Blanket #5 has beryllium in the breeding region (see Section 2.5), in order to achieve adequate tritium breeding. The purpose for including both blankets is to determine the effect that beryllium has on thermal safety. This is discussed in Sections 4.2.3 and 5.4.1.3.

2.3 Blanket #3 - LANL Li/Li/VCrTi

Blanket #3 was also selected from the ESECOM study [2.8], and is similar

Figure 2.2.1 One-dimensional schematic of Blanket #2 for Neutronic and Thermal Analyses.

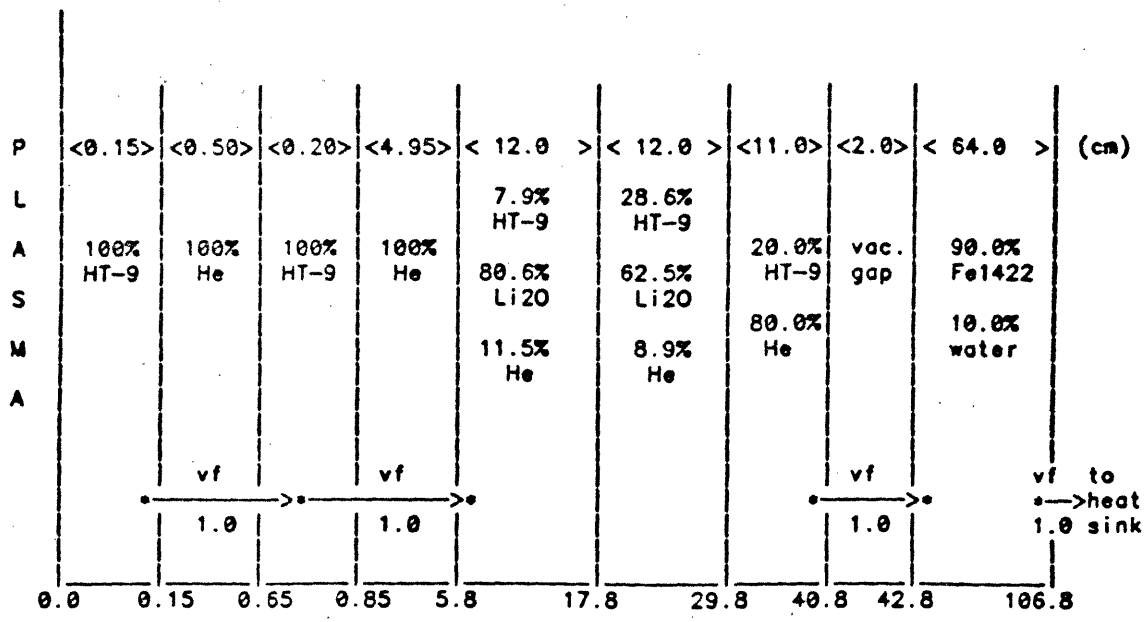

* Arrows connecting asterisks indicate thermal radiation paths. The vf parameters indicate the view factor for that particular radiation path.

Figure 2.2.2 Schematic of Blanket #2. From Reference [2.2].

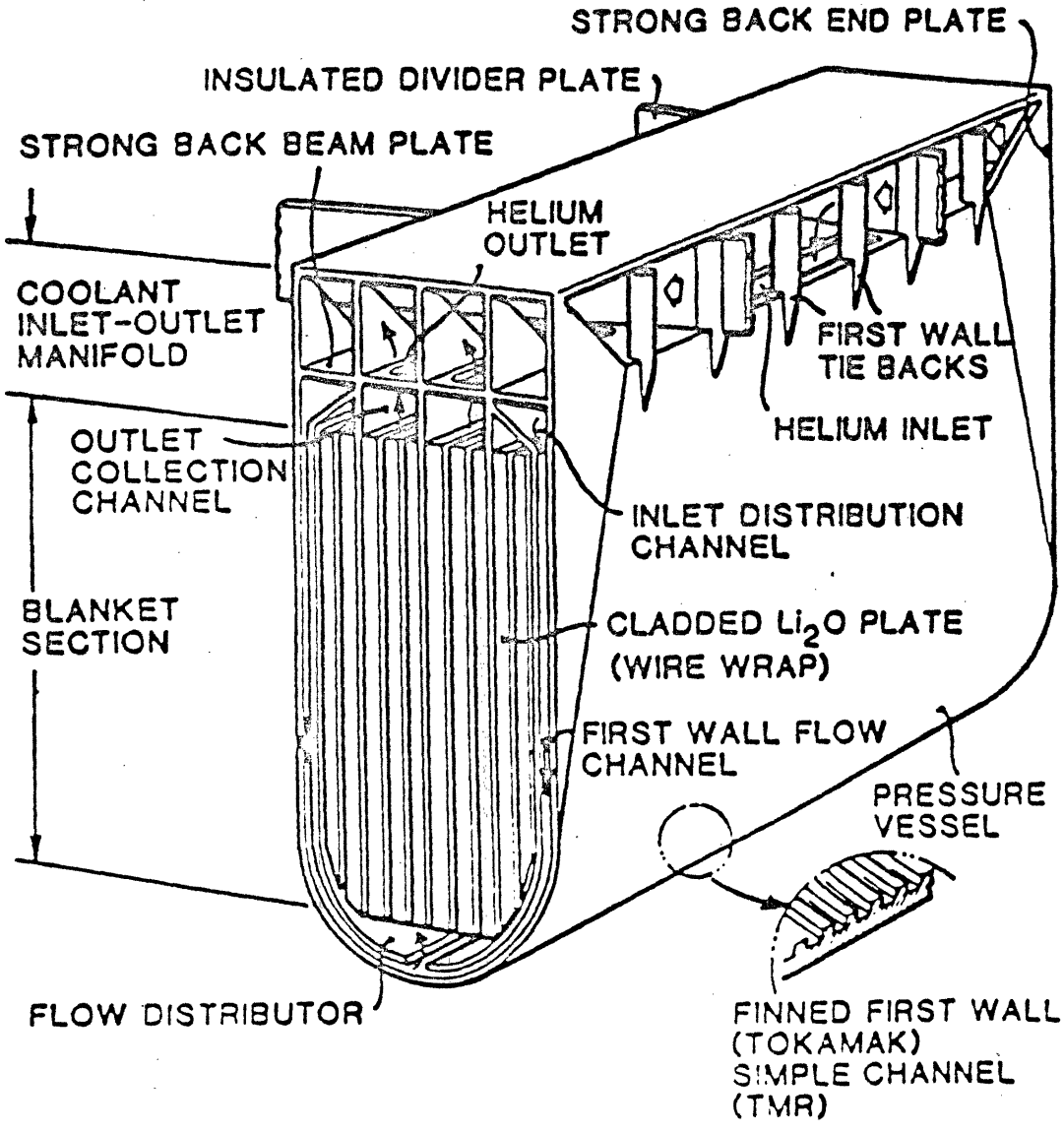

to the blanket of the TITAN Reverse-Field-Pinch (RFP) study [2.11]. The major radius of the RFP is 4.23 m, and the first wall radius is 0.65 m. Figure 2.3.1 shows the 1-D representation for Blanket #3. This blanket is similar to Blanket #1; the major differences are the overall size and, more significantly, the lack of a large shield. The RFP is a compact, high power density reactor with copper magnets, which eliminates the need for the large shield seen in Blankets #1 and #2. The lack of this shield has a significant impact on the temperature response to power/cooling mismatches, as is discussed in Chapter 5. Since there is no shield, the magnet regions are included in the analysis for Blanket #3. These are Regions 8 and 9 in Figure 2.3.1.

The TITAN RFP is designed for higher wall loads [2.11], perhaps as high as 20 MW/m^2, with a lifetime of the first wall/blanket components of about one year. Whether these wall loads are feasible on the basis of first wall material properties was not verified in our work. According to the information reviewed at the beginning of this chapter (references [2.2 - 2.7]), wall loads greater than 10 MW/m^2 may be too optimistic from the materials standpoint. The high wall load cases were included, in part, to examine the effect of wall load on the temperature response in the event of power/cooling mismatches. This issue is discussed in detail in Chapter 5.

The 1.0 cm thickness of the vacuum gap shown in Figure 2.3.1 was chosen arbitrarily. The actual thickness of this vacuum gap will have no effect on the results of the neutronic or thermal analyses, since both are treated in one dimensional forms.

The operating temperature of Blanket #3 is 600 °C, constant across the thickness of the blanket. This is higher than any of the BCSS blankets, but is still within the acceptable range of maximum structural temperature and maximum structure/coolant interface temperature for the materials being used [2.2,2.3]. Table 2.1.1 indicates that the TBR and blanket multiplication for Blanket #3 are both adequate.

Figure 2.3.1 One-dimensional schematic of Blanket #3 for Neutronic and Thermal Analyses.

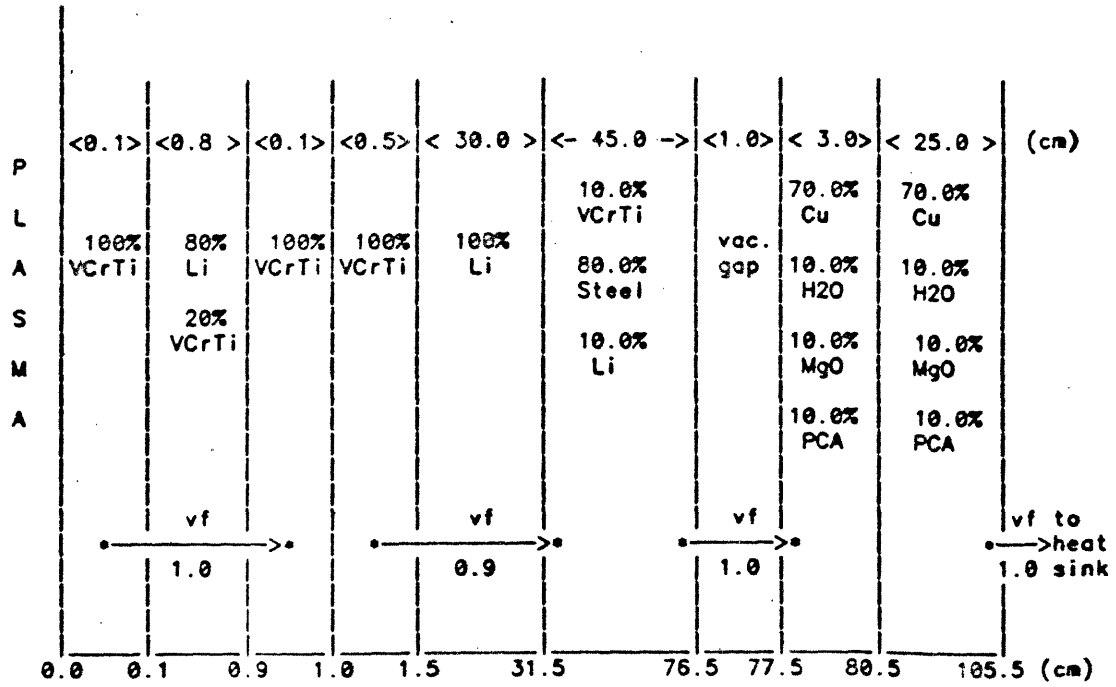

* Arrows connecting asterisks indicate radiation paths in LOCA (complete Lithium drain) case. The vf parameters indicate the view factor for that particular radiation path.

2.4 Blanket #4 - BCSS LiPb/LiPb/VCrTi

Blanket #4 was chosen to examine the effect of $Li_{17}Pb_{83}$ (also referred to as simply LiPb) instead of Li as the breeder material. It is identical to Blanket #1 except for the substitution of LiPb for Li, and the first wall is 50% thicker, to support the heavier LiPb. The ^6Li enrichment in the LiPb is 30% [2.2]. Otherwise, all other parameters are identical to Blanket #1, except the operating temperature, which is about 50 °C lower than for Blanket #1 [2.2].

Figure 2.4.1 shows the 1-D geometry for Blanket #4, which, as stated, is essentially identical to Blanket #1. Table 2.1.1 shows that the TBR and blanket multiplication for Blanket #4 are both adequate. While the TBR is slightly lower than that of Blanket #1, the blanket multiplication is slightly higher.

2.5 Blanket #5 - BCSS Li_2O/He/MT-9/Be

Blanket #4 was selected in conjunction with Blanket #1 to determine the relative thermal safety of LiPb vs. Li. Similarly, Blanket #5 was chosen in conjunction with Blanket #2 to determine the effect of a neutron multiplier, in this case beryllium, on the thermal response to an undercooling transient. Blanket #5 is identical to Blanket #2 except that in the first breeder region (Region 5), some of the Li_2O is replaced with Be. As is mentioned in Section 2.2, the inclusion of Be improves the TBR. As can be seen in Table 2.1.1, adding Be improved the marginal Blanket #2 TBR more than sufficiently. The question is, what effect will this have on the thermal safety.

Figure 2.5.1 shows the Blanket #5 geometry. Note that Be is 20% of the volume in the first breeder region. The beryllium density is 80% of theoretical density, which allows for the swelling which occurs during irradiation [2.2].

Figure 2.4.1 One-dimensional schematic of Blanket #4 for Neutronic and Thermal Analyses.

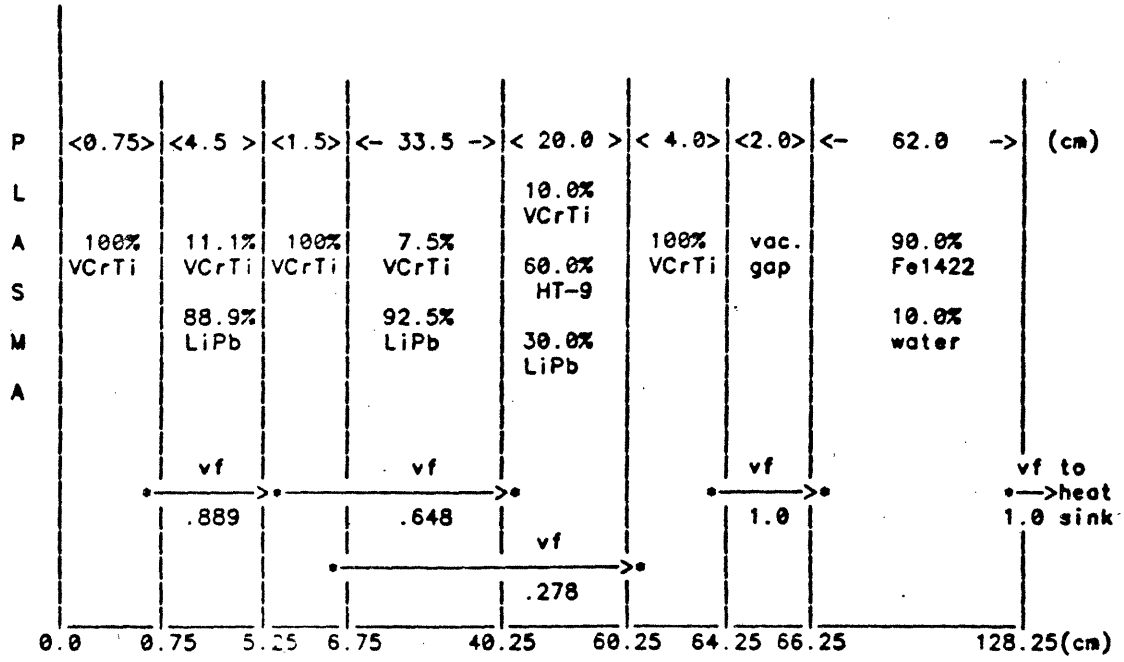

* Arrows connecting asterisks indicate radiation paths in LOCA (complete Lithium-Lead drain) case. The vf parameters indicate the view factor for that particular radiation path.

Figure 2.5.1 One-dimensional schematic of Blanket #5 for Neutronic and Thermal Analyses.

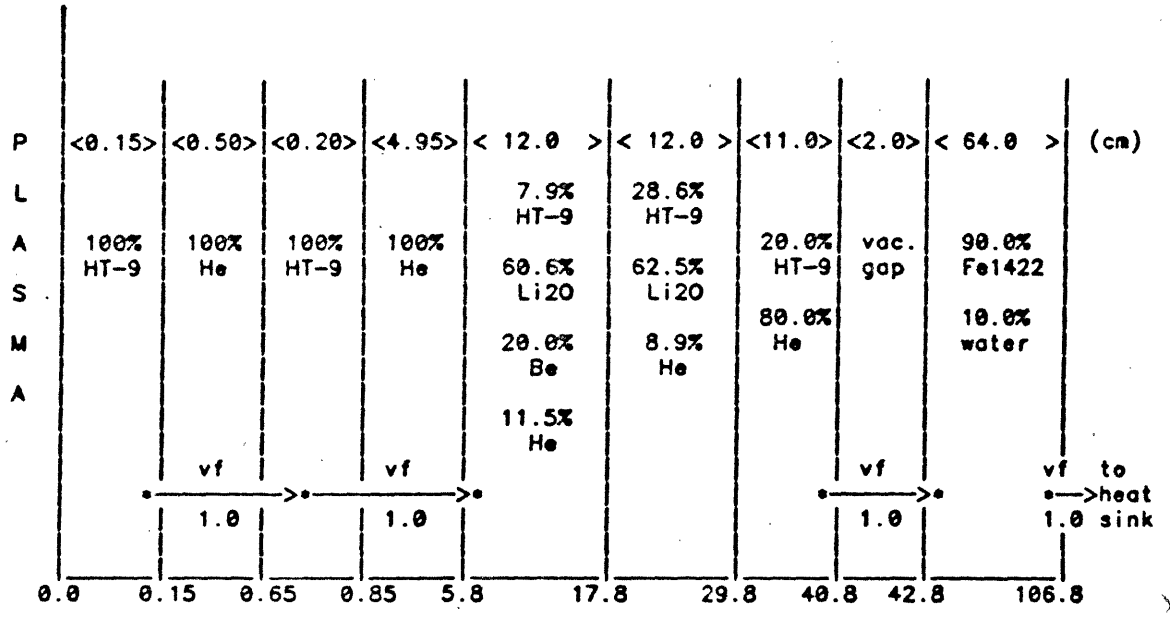

* Arrows connecting asterisks indicate thermal radiation paths. The vf parameters indicate the view factor for that particular radiation path.

2.6 Blanket #6 - SJB D-D MT-9/He

Blanket #6 was selected to examine the thermal safety of the D-D fuel cycle, and was taken from the work of Brereton [2.12] on safety and economic comparisons of fusion fuel cycles. The D-D fuel cycle is attractive for a number of reasons [2.12], including enhanced safety due to the absence of tritium. The geometry for Blanket #6 is shown in Figure 2.6.1. In this blanket, the first wall is incorporated into the blanket, such that Region 1 is simply a large slab of helium-cooled HT-9. The HT-9 used in this blanket is identical to that used in the other blankets, that is, the low activation version proposed by Fetter [2.10] and called MT-9. The blanket region is followed by a vacuum gap (Region 2). Regions 3 and 4 comprise the neutron shield. Region 5 is a second vacuum gap, and Region 6 is a stainless steel dewar [2.12].

Note the absence of a tritium breeder material. Since tritium breeding is not a requirement in the D-D fuel cycle, there is added flexibility in the design of the blanket. Thus the blanket can be designed to maximize the total power (i.e., blanket multiplication factor), or to improve thermal safety. The criterion used to choose the blanket thickness was that 94% of the neutron energy must be captured in the blanket, and the shield thickness was chosen to sufficiently attenuate the neutron flux for magnet protection [2.12]. The multiplication factor for the blanket shown is given in Table 2.1.1.

2.7 Summary

Six reference blankets were chosen for the purposes of carrying out the analyses described in this work. These blankets represent the current approach to tokamak blanket design, and differ from each other in ways that allow for interesting comparisons. The operating parameters of each blanket were verified through a survey of the literature. Some of these parameters, such as wall load and blanket lifetime, are perhaps somewhat optimistic but do not appear unreasonable when compared to earlier designs.

Figure 2.6.1 One-dimensional schematic of Blanket #6 for Neutronic and Thermal Analyses.

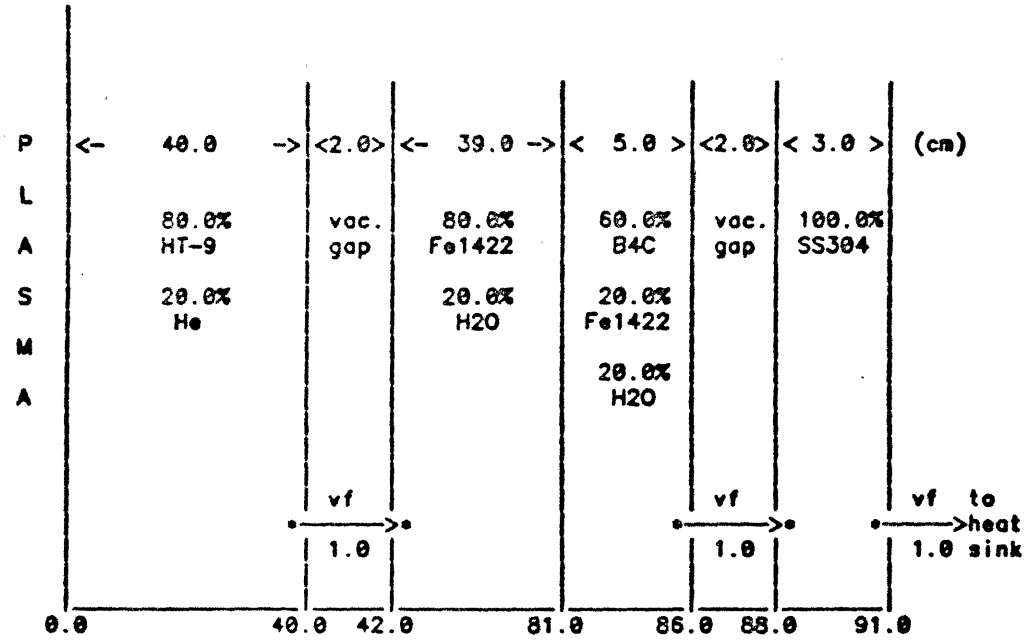

* Arrows connecting asterisks indicate radiation paths. The vf parameters indicate the view factor for that particular radiation path.

References for Chapter 2

[2.1] R.D. O'Dell et al., User's Manual for ONEDANT: A Code Package for ONE-Dimensional, Diffusion-Accelerated, Neutral- Particle Transport, Los Alamos National Laboratory, LA-9184-M, February 1982.

[2.2] D.L. Smith et al., Blanket Comparison and Selection Study (BCSS) - Final Report, Argonne National Laboratory, ANL-84-1, September 1984.

[2.3] O.A. Adegbulugbe, Structural Design Limits for Fusion First Walls, Doctoral Dissertation, Nuclear Engineering Department, Massachusetts Institute of Technology, 1981.

[2.4] G.P. Yu, Relationship of Material Properties in the Design of a Fusion Reactor First Wall, Doctoral Dissertation, Nuclear Engineering Department, Massachusetts Institute of Technology, 1981.

[2.5] J.P. Blanchard and N.M. Ghoniem, The Influence of Irradiation and Thermal Creep on Stress Redistribution in Fusion Blankets, J. Nucl. Mater., Vol. 122, 1-3, May 1984, pp. 101-105.

[2.6] P.J. Maziasz, ORNL, Swelling and Swelling Resistance Possibilities of Austenitic Stainless Steels in Fusion Reactors, Metals and Ceramics Division, CONF-830942–87, 1984.

[2.7] E.F. Bloom, ORNL, and D.L. Smith, ANL, Structural Materials for Fusion Reactor Blanket Systems, CONF-840570–12, 1984.

[2.8] Report by the Committee on Environmental, Safety and Economic Aspects of Magnetic Fusion Energy, Final Report, U.S. DOE, to be issued, 1987.

[2.9] C.C. Baker et al., STARFIRE - A Commercial Tokamak Fusion Power Plant Study, Argonne National Laboratory, ANL/FPP-80-1, September 1980.

[2.10] S. Fetter, Radioligical Hazards of Magnetic Fusion Reactors, Lawrence Livermore National Laboratory, LLNL MS#61485F, 1985.

[2.11] F. Najamabadi, N.M. Ghoniem, R.W. Conn, et al., The TITAN Reversed-Field Pinch Fusion Reactor Study, Scoping Phase Report, UCLA-PPG-1100, January, 1987.

[2.12] S.J. Brereton and M.S. Kazimi, Safety and Economic Comparison of Fusion Fuel Cycles, PFC/RR-87-7, Massachusetts Institute of Technology Plasma Fusion Center, August 1987.

[2.13] Y. Gohar, Design Analyses of Self-Cooled Liquid-Metal Blankets, Argonne National Laboratory, ANL/FPP/TM-208, 1986.

3. Material Limits

Material limits affect the thermal design of a fusion reactor in a variety of ways. In terms of normal operation, the lifetime of the blanket system is limited by the ability of the first wall material to withstand the neutron fluence, cyclic heat load, and erosion rate [3.1,3.2,3.3]. In an off-normal condition such as a Loss-of-Flow Accident (LOFA) or Loss-of-Coolant Accident (LOCA), the elevated temperatures experienced by the structural components can lead to damage and/or the release of radioactive isotopes [3.4,3.5,3.6]. Thus it is important to attempt to quantify the various limits that affect the thermal design, as well as the consequences of exceeding these limits. From the standpoint of this work, it is important to quantify the damage that may be caused by a particular transient, in order to identify means of minimizing such damage.

In this chapter, some of the limits based on material properties are discussed. This includes a brief discussion of blanket lifetime, followed by a more involved discussion on the temperature limits of the main structural materials (HT-9 and VCrTi). Note that the version of HT-9 used in this work, called MT-9, is assumed to have identical structural and thermal properties to the standard HT-9. A model for predicting the consequences of the elevated temperatures reached during LOFA and LOCA is presented. Details of the calculations presented in this chapter are

included in Appendix A.

3.1 Lifetime Limits

The usable lifetime of the first wall/blanket system will have a significant impact on the economics of a fusion reactor [3.7]. The assumed lifetime will also affect the decay heat analysis, as well as the waste management problem, since the buildup of radioactive isotopes increases with time. As briefly mentioned in Chapter 2, the factors that will affect the lifetime of the first wall include irradiation damage and erosion (physical sputtering) [3.1,3.2,3.3].

3.1.1 Erosion

Erosion is the removal of material on the plasma side of the first wall due primarily to physical sputtering from ion bombardment [3.1,3.8]. The erosion rate is determined by the magnitude of the flux and energy of the charge-exchange neutrals at the first wall, and thus is dependent on the wall load (i.e., plasma power density). The BCSS selected an erosion rate of 1.0 mm/yr to correspond to the 5 MW/m^2 neutron wall load used in that study. This value is more of a reasonable assumption than the result of a detailed calculation. Other references [3.2,3.3,3.8] predict a somewhat higher rate. It is this erosion rate that determines the lifetime of some blankets. The maximum first wall thickness is limited by thermal stress considerations. The thermal stress in the first wall is directly related to the temperature gradient across the first wall, which is linearly dependent on the product of the first wall thickness and the surface heat flux. Using Blanket #1 as an example, given the surface heat flux of 1.0 MW/m^2, the maximum first wall thickness turns out to be 6 mm. Given the maximum allowable primary stresses in the first wall, which are due to the coolant pressure, the minimum thickness of the first wall is determined. This is given in BCSS as 3 mm. The difference between the

maximum and minimum thicknesses is the amount of material that can be eroded away during the lifetime of the blanket. This is 3 mm for Blanket #1. Dividing this thickness by the erosion rate gives the usable lifetime of the first wall. For Blanket #1, then, this lifetime is three years of full power operation. Although the maximum and minimum first wall thicknesses are slightly different for the other BCSS blankets (Blankets #2, #4, and #5), the same three year life is assumed for these blankets, which have the same value of plasma heat flux and neutron wall load as Blanket #1. This is done so as not to bias any results on the basis of blanket lifetime.

3.1.2 Atomic Displacements

Besides the charged particle bombardment on the surface of the first wall, the first wall/blanket structure is subject to irradiation by neutrons, which penetrate into the structure and collide with lattice nuclei. The neutron irradiation fluence (flux × time, n/cm^2) of the first wall is commonly measured in displacements-per-atom (dpa) [3.9]. The dpa is the average number of times an atom is displaced from its lattice site by interactions with the neutron flux. The number of dpa accumulated by the first wall material depends primarily on the magnitude and energy spectrum of the neutron fluence. Available formulae for calculating dpa [3.9] are linearly dependent on the the product of the neutron fluence and the neutron energy. Because of this, the first wall lifetime in units of (MW-yr/m^2) can be translated directly into dpa. For both HT-9 and VCrTi under irradiation by 14.1 MeV D-T neutrons, one MW-yr/m^2 translates into 11 dpa [3.1]. Thus, three years of full power operation at 5 MW/m^2 gives a lifetime of 15 MW-yr/m^2, which translates into 165 dpa for both materials. Note that this 165 dpa is not lifetime limiting for these materials. The lifetime of the D-T tokamak blankets is determined by first wall erosion, as is discussed in Section 3.1.1. Discussion of the dpa limit for these materials is given below.

A number of studies have examined the effect of dpa on the strength properties of materials [3.1, 3.9, 3.10, 3.11]. Under irradiation, most materials experience hardening, i.e., an increase in the yield strength and a decrease in the ductility [3.9, 3.12]. They also experience swelling, due partly to helium production through (n,α) reactions. Both of these effects are highly temperature dependent.

The dpa can be the limiting factor in the lifetime of the first wall. According to the BCSS [Section 6.1], radiation induced swelling is the most restrictive limit on the dpa, based on a swelling limit of 5%. This leads to a limit of about 250 - 275 dpa for HT-9 [3.1].

Based on a limit of 275 dpa in the HT-9 first wall, at 11 dpa per MW-yr/m^2, a lifetime of 25 MW-yr/m^2 for a D-T reactor may be predicted †. In a D-D reactor, because the neutron spectrum is different than for a D-T reactor, it might be inappropriate to use the 11 dpa per MW-yr/m^2 "translation factor"mentioned above. There are two opposing ways to view the problem.

The first method is to use the approach of Olander [3.9]. Olander assumes that the dpa production is linearly dependent on the product of the neutron fluence and the average neutron energy. The fluence is found by multiplying the neutron wall load (MW/m^2) by the lifetime (yr) and *dividing* by the average neutron energy. Thus it is seen that the neutron energy will cancel out of the equation for dpa production rate, leaving only the product of wall load and time, i.e., MW-yr/m^2. Thus for a fixed dpa limit, there will be a fixed lifetime (MW-yr/m^2) limit, regardless of the average neutron energy. This means that D-T and D-D reactors, which have different average neutron energies, will nevertheless be subject to the same lifetime limit. In the HT-9 example above, this is 25 MW-yr/m^2 (based on the dpa limit of 275 and the translation factor of 11 dpa per MW-yr/m^2). equations (3.1) - (3.3)

† Again, note that the lifetime of 15 MW-yr/m^2 used both in the BCSS and in this study for the D-T tokamak blankets is based on a first wall erosion rate of 1.0 mm/yr.

show this approach mathematically.

$$dpa \propto (N_n)(E_n) \tag{3.1}$$

where

E_n is the average neutron energy (MeV), and

N_n is the neutron fluence (n/cm^2),

$$N_n = \frac{(\Gamma_n)(t)}{E_n} \tag{3.2}$$

where

Γ_n is the neutron wall load (MW/m^2), and

t is the time (yr),

such that $(\Gamma_n)(t)$ is the lifetime (MW-yr/m^2). Thus,

$$dpa \propto (\Gamma_n)(t) \tag{3.3}$$

It is seen from equation (3.3) that there is no dependence of dpa production on the average neutron energy. In this case, given a fixed dpa limit, which is a material property, the lifetime (MW-yr/m^2) will also be fixed, regardless of the neutron energy.

The alternate approach is to assume that the dpa production depends *only* on the neutron fluence, and not the average neutron energy, as long as the energy is above a certain threshold, e.g., 1 MeV. In both D-T and D-D fusion systems, almost all of the flux in the first wall will be above this threshold. In this approach, the

lifetime (MW-yr/m^2) is found by multiplying the fixed dpa limit by the average neutron energy, and converting to the appropriate units. Mathematically,

$$dpa \propto N_n \tag{3.4}$$

and, using equation (3.2),

$$dpa \propto \frac{(\Gamma_n)(t)}{E_n} \tag{3.5}$$

Given a fixed dpa limit, then, the lifetime is found by

$$(\Gamma_n)(t) \propto (dpa)(E_n) \tag{3.6}$$

It is seen in this approach that the lifetime (MW-yr/m^2) depends linearly on the average neutron energy. In a D-D reactor, the average neutron energy is about 8.2 MeV [3.7], and thus the lifetime of a D-D blanket will be 0.58 ($= \frac{8.2}{14.1}$) times as long as that for a D-T blanket. This is due to the fact that, because of the lower average neutron energy, there are more neutrons produced per megawatt in a D-D reactor than in a D-T reactor. Since it is assumed that the number of dpa depends *only* on the number of neutrons (and not their energy), for the same thermal power, the dpa rate in the D-D reactor will be higher than in the D-T reactor. This latter approach was used to determine the lifetime of Blanket #6 [3.7]. Instead of 25 MW-yr/m^2, the lifetime of Blanket #6 is thus 14.6 MW-yr/m^2. At a neutron wall load of 1.17 MW/m^2, this translates into a usable life of 12.5 full power years (FPY) [3.7].

Determining which of these two approaches is more correct is an important issue, especially in comparing the economics of D-D vs. D-T reactors [3.7]. The truth probably lies somewhere between these two approaches; dpa production scales

as neutron fluence times the average neutron energy raised to some fractional power. That is,

$$dpa \propto (N_n)(E_n)^{\alpha} \tag{3.7}$$

where $0 < \alpha < 1$.

There are a number of factors which will affect the value of α. Although this particular issue does not significantly impact the remainder of this work, it deserves further attention. A brief discussion of some of the relevant factors follows.

Atomic displacements are, for the most part, the result of scattering interactions of neutrons with nuclei [3.9]. As the neutron scatters off the nucleus, some of the neutron energy is imparted to the nucleus, and the nucleus is then "kicked"out of its lattice site. If the imparted energy is sufficient, the nucleus becomes a "primary knock-on atom"(PKA), and will knock more nuclei out of their lattice sites before it is finally stopped. Thus, the total number of displacements produced by the single scatter depends on the amount of energy that is transferred to the nucleus. Clearly, then, higher energy neutrons should produce more displacements than lower energy neutrons; in fact, the effect should be linear (α=1), as stated by Olander. This assumes that neutrons of different initial energies give up an equal fraction of their initial energy by scatter before they are captured or transport out of the first wall region. That is, if a 14.1 MeV neutron and a 2.5 MeV neutron both give up half their initial energy by scatter within the first wall, then the ratio of displacements produced will be $\frac{7.05}{1.25} = 5.64$, which is the same as the ratio of their initial energies, and α in equation (3.7) will equal one. It is unlikely that this will be the case, however.

At high energies, especially > 5 MeV, the elastic scattering process is highly forward peaked [3.13, 3.14]. That is, higher energy neutrons give up a smaller fraction of their energy per scatter than lower energy neutrons [3.14, 3.15, 3.16],

and experience a smaller change in their angular direction. Furthermore, the elastic scattering cross-section for many structural materials decreases significantly above 5 MeV. For iron, this cross-section goes from about 2 barn at 5 MeV to about 1 barn at 14 MeV [3.13]. The result is that 14 MeV D-T neutrons may actually experience fewer scatters within the first wall of a fusion reactor than 2.5 MeV D-D neutrons, before they transport through the first wall and into the blanket. This would mean that the 14 MeV neutron actually imparts *less* energy to the nuclei in the first wall, and thus produces *fewer* displacements, than the 2.5 MeV D-D neutron. This effect will work to reduce the value of α in equation (3.7). Determining the magnitude of this effect, and thus the value of α, requires a detailed neutronic analysis which is beyond the scope of this work.

3.2 Temperature Limits

The limits discussed in Section 3.1 are relevant in determining the normal operating lifetime of the first wall/blanket system. The goal of this work, however, is to quantify the structural damage that will occur as the result of an off-normal condition, and identify guidelines to prevent or minimize such damage. The relevant material limits in this instance involve the high temperature properties of the structural materials, since the transients considered in this work all involve elevated temperatures.

In the event of a major accident involving the blanket, the important temperatures of concern are those of the structural material. It is the structure that maintains the geometry of the reactor, and also contains the large majority of radioactive isotopes (except tritium; see Section 4.2). When dealing with elevated temperatures in the structure of a fusion reactor blanket, there are essentially three areas of concern. These are: 1) melting, 2) structural damage, and 3) radio-isotope release. All of these are functions of temperature, and the purpose of calculating the temperature response to power/cooling mismatches is to determine whether any

of these will occur, and how severe the problem will be. The temperatures at which these occur in the structural materials VCrTi and HT-9 is discussed in this section.

3.2.1 Structural Failure

At temperatures of about one-half the melting temperature and greater, most structural materials which have been irradiated exhibit a severe loss of ductility due to helium embrittlement [3.1], as well as a decrease in yield stress. Thus, it is possible that at some (elevated) temperature, the ultimate tensile strength (UTS) of a material will drop below the stress that it supports, and the material will suffer acute failure. Whether the structure will completely fail depends on the magnitude of the stress it supports. A detailed analysis to determine the post-accident stress distribution was considered beyond the scope of this work, however, a zeroth-order estimation of the stress is necessary. In general, there are two sources of stress in the first wall. There is the pressure stress, which is due to the presence of the (pressurized) coolant in the first wall coolant channel, and the thermal stress, which arises from the temperature gradient across the first wall. The magnitude of both of these stresses will be affected by the accident. During a Loss-of-Cooling Accident, the pressure stress on the first wall structure should decrease from that of normal operation. In both a pump-failure LOFA or any LOCA, there would be a decrease of coolant pressure, resulting in reduced pressure stresses in the first wall. Quantifying this stress is an important issue in fusion reactor accident analysis. The thermal stress is somewhat more complicated, since it depends on the details of the operational and post-accident first wall temperature gradient. A more detailed discussion of thermal stress is given in Chapter 7, in which the overpower transients are discussed. For the purposes of the analyses presented in Chapters 5 and 6, the total first wall stress level is treated rather heuristically. The reader is cautioned that the stress levels used in the calculations presented in these chapters are not the result of a detailed stress analysis.

Even if the applied stress never exceeds the yield stress, the material can still suffer structural failure due to thermal creep. At high temperatures, even relatively low values of applied stress can cause a material to creep excessively, until it ruptures (i.e., reaches tertiary creep) [3.1, 3.17, 3.18]. A discussion on the post-accident thermal stress in the first wall is included in the following section on HT-9 Temperature Limits. Again, quantifying the possibility of thermal creep rupture remains an important issue in fusion reactor accident analysis.

Given the stress level, it is possible to make an estimate of the time-to-rupture (t_r) due to thermal creep using the Larson-Miller Parameter [3.17]. The Larson-Miller parameter P is a function of t_r and temperature, and is constant for a given stress level in a given material. Specifically,

$$P = (T)(C + \log_{10} t_r) \tag{3.8}$$

where

P = Larson-Miller parameter, constant for a given material and stress level,

T = temperature (R),

C = constant (usually about 20 [3.17]), and

t_r = time to rupture or to reach a specified value of creep strain (h)

Using the available data from creep tests on VCrTi [3.1, 3.10], the value of P can be found at a specified stress. Then, knowing the temperature, the time-to-rupture t_r can be found with equation (3.8). If the time spent at a particular temperature is greater than the rupture time for that temperature, then the material is expected to fail due to creep rupture. Since the temperature is changing with time, the rupture time will also be changing. In this case, failure is assumed to occur when the cumulative fraction of time over rupture time exceeds one. This is handled by defining the *rupture fraction*, f_r. The rupture fraction is the time spent

at a particular temperature divided by the rupture time for that temperature. The rupture fraction is summed up over increments of time Δt; if it exceeds one, the material has failed. That is,

$$f_{r_i} = \frac{\Delta t_i(T)}{t_r(T)} \tag{3.9}$$

where

f_{r_i} = rupture fraction for time increment $\Delta t_i(T)$,

$\Delta t_i(T)$ = time spent at temperature T, and

$t_r(T)$ = rupture time for temperature T, as determined from equation (3.8).

Summing f_{r_i} over all the time increments $\Delta t_i(T)$ from time = 0 to the end of the transient gives the cumulative rupture fraction f_r for the transient;

$$f_r = \sum_{\Delta t_i(T)} f_{r_i} \tag{3.10}$$

If the cumulative rupture fraction f_r exceeds one, then the material has failed. The details of this calculation are given in Appendix A.

3.2.1.1 VCrTi Temperature Limits

The melting temperature of the V-15Cr-5Ti alloy is approximately 1890 °C [3.1]. This is the highest of the three candidate structural materials considered in the BCSS. A number of problems can result at temperatures far below this, however.

Above 1000 °C, VCrTi undergoes a change of phase, and components which reach these temperatures may not be re-usable [3.19]. As long as the temperature

does not reach 1200 °C, the VCrTi will not experience a significant decrease in yield strength. At 1200 °C, VCrTi experiences a drastic loss of strength [3.19]. Under these circumstances, there is a good chance that the VCrTi components will no longer be able to support the stresses on them, resulting in gross structural failure. While the stress levels are largely unknown, for the purposes of this work, it will be assumed that any VCrTi component that exceeds 1200 °C will fail. In Chapter 7, other assumptions are made to accomodate the analysis carried out in that chapter.

Regarding long term effects, such as thermal creep, the available data is limited to temperatures below 800 °C [3.1, 3.10]. At 800 °C, the stress required to cause 1% creep in 1000 hours is about 270 MPa [3.1]. Additional discussion on the available creep data is given in Appendix A. On the basis of the stress analysis for Blanket #1 given in the BCSS, it is assumed here that in a LOFA, the stress in the VCrTi first wall will remain at about 10 MPa, and in a LOCA, the stress will be about 1 MPa. In the LOFA case, it is assumed that the coolant remains in the blanket. The operational system pressure of the liquid lithium in Blanket #1 is about 3 MPa, which leads to a primary first wall stress of over 100 MPa. About 95% of the coolant pressure is supplied by the coolant pump, in order to overcome the MHD pressure drop of the liquid metal coolant as it flows through the blanket. Thus, when the pump fails, the coolant pressure will drop to about 5% of the operational pressure, leaving a first wall primary stress of about 5 MPa, which is conservatively estimated to be 10 MPa. Note that if the LOFA is caused by a flow blockage in which the coolant pump continues to function, the coolant pressure could remain high, and thus the first wall stress could remain at its operational value ($\sim$ 100 MPa or more). The reader must be cautioned that the stress levels given are not the result of a detailed stress analysis, but are merely guesses, based on the operational characteristics, and are used primarily for the purposes of illustration. Over the relatively long duration (many hours) of some undercooling transients, the stress level will change due to the mechanical strain (or creep), which is continuously occurring, and to changes in the temperature distribution. The data base for VCrTi

regarding thermal creep is extremely limited, and thus an accurate analysis of the post-accident thermal stress is impossible at this time. Determination of the Larson-Miller parameter as a function of stress is discussed in Appendix A.

3.2.1.2 HT-9 Temperature Limits

The melting temperature of the ferritic steel HT-9 is 1420 °C [3.1]. As for VCrTi, many problems arise at temperatures far below this.

The available data on yield strength vs. temperature for HT-9 is limited to temperatures up to 650 °C. Attempting to extrapolate to higher temperatures can lead to problems, but the lack of any hard data leaves no other option. The data given in reference [3.20] are shown in Figure 3.2.1. It is seen that the yield and ultimate tensile strengths of HT-9 experience a fairly substantial decrease at temperatures above 550 °C, which corresponds to about one-half the melting temperature. These data only go to 650 °C, and linear extrapolation to higher temperatures results in a yield stress of zero at 750 °C. This indicates that there must be a turnaround in the slope of the yield stress vs. temperature plot between 650 °C and 750 °C, and the yield stress levels out at some (low) value at temperatures above 750 °C. Thus for the purposes of the undercooling transient analyses, it will be assumed that any HT-9 component that exceeds 900 °C will fail. This failure could be in the form of structural damage, if the UTS drops below the stress in the material. Even if the applied stress is so low that this damage does not occur, HT-9 experiences a re-crystallization similar to that of VCrTi at about 900 °C. This process will cause a drastic, unrecoverable loss of ductility, and thus components which reach this temperature will not be re-usable. The requirement that such components be replaced would incur an economic penalty, and violate the criteria for inherent safety given in Chapter 1. In Chapter 7, a linear relation between Ultimate Tensile Strength and temperature is derived from these data and used to estimate the overpower transient failure time.

Figure 3.2.1 Yield and Ultimate Tensile Strength of HT-9 vs. Temperature. From Reference [3.20].

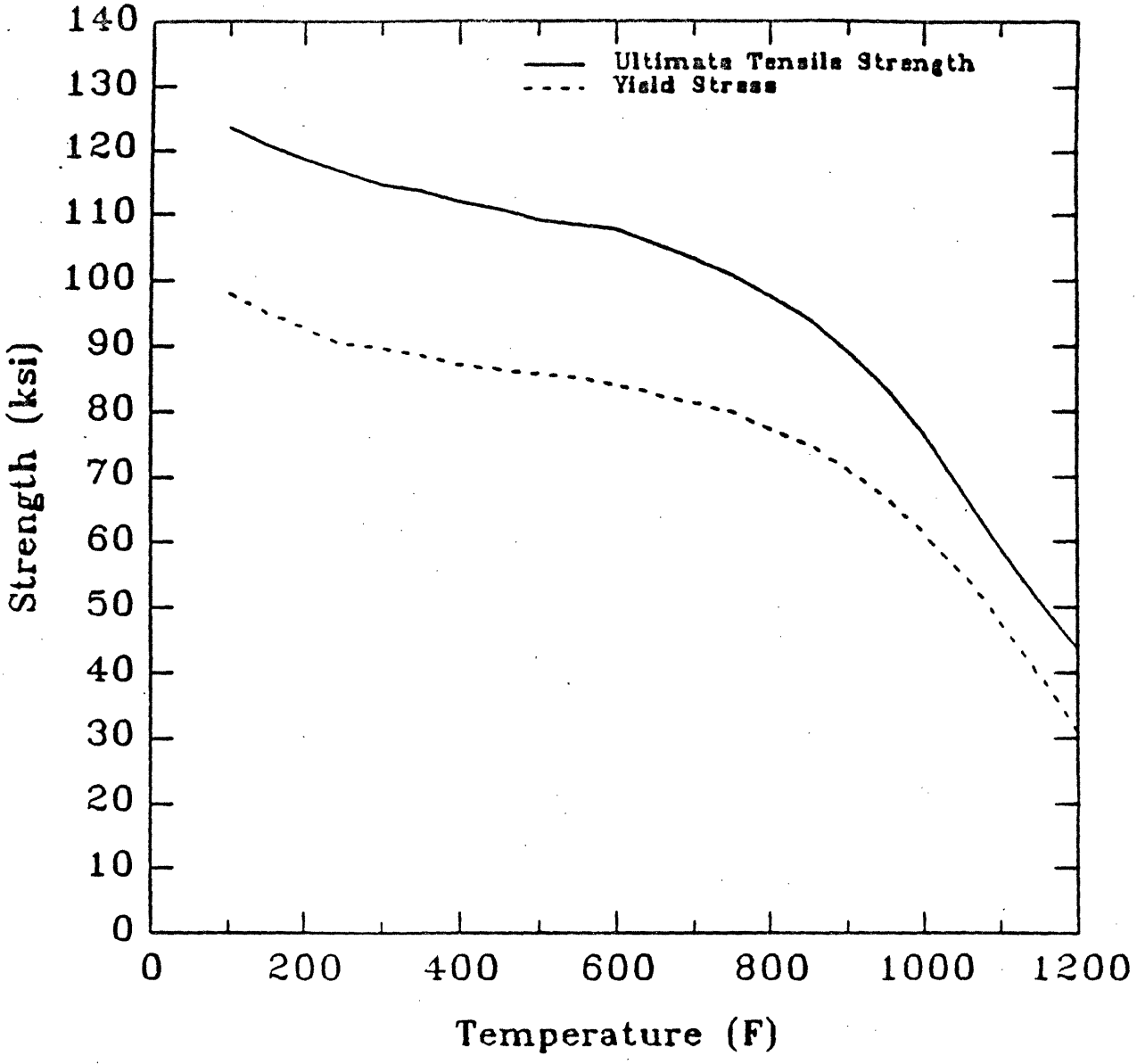

In terms of thermal creep, the published data [3.1, 3.10, 3.18, 3.20] again are limited to temperatures below 600 °C, and again, extrapolation is necessary. Unlike VCrTi, however, there do exist correlations for the creep strain rate [3.18], and thus an analysis on the post-accident thermal stress in the first wall can be carried out. A model for determining the thermal stress in an HT-9 first wall as a function of time following loss-of-coolant was created in conjunction with Brereton [3.7]. This model is described in detail in Appendix A (see also reference [3.7], Appendix G). Briefly, it is assumed that at accident initiation (t=0), the temperature gradient in the first wall goes to zero. This causes a thermal stress equal in magnitude (but opposite in sign) to the operational thermal stress, because of the relaxation strain which has occurred during operation. This post-accident stress will then begin to decrease due to strain relaxation again. Knowing the stress and temperature, the strain rate can be calculated from a correlation given in reference [3.18]. This can then be used to find the new stress level after a small time increment Δt has passed. This procedure is continued, resulting in a stress vs. time history for the duration of the transient.

The stress vs. time history is then used in conjunction with the temperature vs. time history, and the rupture fraction calculated with the method outlined in Section 3.2. The details of these calculations for the temperature histories given in Chapters 5 - 7 are given in Appendix A.

In the event of loss-of-flow, it is assumed that the coolant will remain at pressure. In the helium-cooled HT-9 structure blankets considered in this work (Blankets #2, #5, and #6), the helium pressure is 5 MPa. This coolant pressure will only be reduced by the pressure drop which is normally compensated for by the pump (which is assumed to have failed in a LOFA). This pressure drop is usually less than 10% of the system pressure. This means that in a LOFA, unlike a LOCA, the pressure stress in the first wall will remain high, and thus the post-accident stresses will be high. Based on the operational values of pressure stress given in BCSS, the post-accident stress for LOFA in the HT-9 blankets will be assumed to

remain constant at 120 MPa.

3.2.2 Radio-isotope Release

Other than causing structural damage to the reactor, the elevated temperatures caused by power/cooling mismatches can have another effect. Namely, due to oxidation and volatilization of various elements at elevated temperatures, radioactive isotopes can be mobilized and thus be released into the atmosphere [3.4, 3.21, 3.22]. For the structural materials at temperatures below melting, release of radionuclides can occur if the structural material comes in contact with oxygen (in air or steam). In this case, the structural elements will likely oxidize [3.21, 3.22, 3.23]. The vapor pressure of the oxides is much higher than the pure elements, and thus the oxide vapors will be released from the solid structure.

3.2.2.1 VCrTi Volatility/Oxidation

Oxidation of VCrTi can be an extreme problem at elevated temperatures. Above about 650 °C, vanadium oxidizes readily [3.22, 3.23]. At oxygen partial pressures of above 10^3 Pa, the most abundant oxide formed is V_2O_5, which has a melting temperature of about 670 °C [3.22, 3.24, 3.25]. Neilson [3.22] has quantified this effect with experiments, and some of his results are shown in Table 3.2.1. It is evident that at temperatures greater than 650 °C - 680 °C, the oxide V_2O_5 will form and melt. It is assumed that the liquid oxide layer will then slide off, thus exposing a new surface of solid VCrTi, which will then be oxidized. As is seen from Table 3.2.1, the total thickness of structure that can be removed by this process is highly dependent on the oxygen partial pressure as well as the exposure time. In any case, it appears that a significant fraction of the radioactive inventory could be mobilized through this process. Further, due to the loss of material, it is assumed that the first wall will suffer structural failure if it becomes oxidized.

Table 3.2.1 Time Required to form V_2O_5 Oxide as a Function of Temperature and Oxygen Partial Pressure. From Reference [3.22].

Oxygen Partial Pressure, Pa	Temperature, °C	Time at Temperature for Molten V_2O_5-Type Oxide Formation, h
2×10^4 (air)	650 - 680	0.2 - 0.25
10^4	650 - 680	0.2 - 0.25
10^3	650 - 750	$\geq$0.7
10^1	680	>24
10^1	680	>24

Based on the data from the EG&G experiment [3.21], The ESECOM Study [3.4] quantified the mobilization fraction of some of the elements present in a VCrTi structure after irradiation. Additionally, a threshold release fraction was defined, which is the minimum dose fraction that if released will cause a prompt whole-body dose of 200 rem at 1 kilometer from the release [3.4]. This prompt dose is defined as the total dose that would be received at the site boundary in the first seven days plus half the dose received from the eighth through the 30th days. ESECOM assumed no containment and the most pessimstic weather conditions. These results are shown in Table 3.2.2. Note in Table 3.2.2 that the dose release fraction for the Li/V tokamak in the worst case (case I-V) is 0.04. This means that at least 4% of the first wall must be released to cause the 200 rem dose. This is based on the ESECOM blanket first wall thickness and neutron wall load, which are 5 mm and 3.6 MW/m^2 respectively. The threshold release fraction scales linearly with both of these parameters. Note also in Table 3.2.2 that the dose fraction released (released is the same as mobilized, since no containment was assumed) if the first wall remains at 1500 °C for 10 hours is only 0.005, which is almost an order of magnitude less than the threshold. As will be seen in Chapters 5, 6, and 7, none of the transients considered in this work produce temperatures of 1500 °C for 10 hours.

It is appropriate to compare the 200 rem prompt dose limit to the Nuclear Regulatory Commission (NRC) 25 rem, two hour dose limit. This two hour dose includes the actual exposure received in the two hours following the initial release, plus the long term commitment received from inhalation of airborne radioactivity in those first two hours. Note that since the prompt dose includes exposure that occurs up to 30 days after initiation of the accident, it can be as much as two orders of magnitude higher than the two hour dose [3.26]. Thus, the 200 rem prompt dose limit is somewhat more stringent than the 25 rem two hour NRC limit.

Table 3.2.2 First Wall Threshold Release Fractions and Fractions Released for VCrTi and HT-9. Data from Reference [3.4].

First Wall Material	First Wall Thickness‡ (mm)	Neutron Fluence (MW/m^2)	Threshold Release Fraction*	Fraction Released† 1500 °C	1300 °C	1000 °C
VCrTi	10	20	0.04	5.0e-03	2.3e-04	3.3e-07
HT-9	10	20	0.03	1.2e-02	1.2e-03	1.0e-04

* Release Fraction required to cause 200 rem whole body dose at site boundary.

† Following 10 hours at the indicated temperature. Assumes no containment and most pessimistic weather and plume dispersion conditions.

‡ Equivalent thickness of pure structural material. That is, value given is total first wall thickness multiplied by volume fraction of structural material in the first wall.

3.2.2.2 HT-9 Volatility/Oxidation

The problem of oxidation in HT-9 does not appear to be as severe as it is in VCrTi, because the oxides of the elements comprising HT-9 do not melt at relatively low temperatures, the way V_2O_5 does. The volatility of these elements has been quantified by other studies [3.4, 3.21]. Piet et. al. [3.21] recommend some minor changes in the elemental composition of HT-9 in order to reduce the total activation product mobilization from HT-9 oxidation. The mobilization fraction of some of the elements in HT-9 are given by ESECOM [3.4]. These results are shown in Table 3.2.2. The total mobilization fraction is clearly quite sensitive to temperature.

Comparing the dose release fraction for the 1500 °C, 10 hour transient to the threshold release fraction in Table 3.2.2, it is seen that there is a safety margin of about 2.5. While this represents a release fraction that is much closer to the threshold than the vanadium case, all transients analyzed in this work lead to temperatures far below 1500 °C for 10 hours. Therefore, as for the vanadium cases, the critical dose at site boundary will not be a problem.

3.3 Summary

Material limits are an important aspect of fusion reactor design, for both operational and accident conditions. Some of these limits have been quantified to facilitate the analyses that follow in the remaining chapters.

The operating lifetime of the first wall/blanket system depends on physical sputtering (first wall erosion), atomic displacements, and helium induced swelling. Determining the operating lifetime of the first wall based on the atomic displacement limit (measured in displacements-per-atom, dpa) is somewhat uncertain due to the uncertainty in the dependence of the dpa rate on the neutron energy. This issue is important, particularly when comparing alternate fuel cycles, in which the neutron spectra are different from the D-T spectrum. There exist two conflicting viewpoints,

one which suggests that the dpa rate is linearly dependent on neutron energy [3.9], and one which suggests that there is no dependence of dpa rate on neutron energy [3.7]. The actual situation probably lies somewhere in between.

In the event of a transient which leads to elevated temperatures, the material limits of interest involve the dependence on temperature of the Ultimate Tensile Strength (UTS), creep resistance, and oxidation characteristics of the structural materials. Elevated temperatures in structural materials can cause melting, acute structural failure, thermal creep induced failure, and oxidation or volatization, all of which could lead to the release of radioactive isotopes.

Quantifying the structural response of the first wall requires determination of the post-accident stress level, which has a pressure component and a thermal component. This is a complicated problem, and is beyond the scope of this work. For this reason, heuristic estimates of the first wall stress were made, based on the operational conditions and the available data [3.1,3.18]. In the Loss-of-Flow (LOFA) scenario, it is assumed that the coolant remains in the coolant channel. In the liquid-metal cooled blankets (i.e., Li/Li/VCrTi Blanket #1), the non-flowing coolant pressure will be low, since most of the operating pressure is designed to overcome the MHD pressure drop. In this instance, the total post-accident stress (pressure + thermal) is assumed to remain constant at 10 MPa. In the helium cooled blankets (i.e., Li_2O/He/MT-9 Blanket #2), the non-flowing coolant pressure will be almost the same as the operating coolant pressure (5 MPa), and thus the post-accident first wall stress is assumed to be 120 MPa. In the Loss-of-Coolant (LOCA) scenario, there is only a thermal stress, since the coolant is no longer present. In the VCrTi blankets, since no data exists, this stress is assumed to be constant at 1 MPa. The improved data base for HT-9 allow for a more detailed calculation of the post-LOCA thermal stress based on thermal creep correlations [3.18].

The high temperature data base for the candidate structural materials VCrTi and HT-9 is quite limited, requiring extrapolation of the lower temperature data.

The UTS of the VCrTi alloy suffers a dramatic decrease above 1200 °C [3.19]. For this reason, it is assumed that VCrTi components which go above 1200 °C will suffer acute structural failure. Extrapolation of the HT-9 data [3.1, 3.10] indicate that the UTS will be very close to zero at 900 °C, and thus it assumed that HT-9 components which go to temperatures above this will also suffer acute structural failure. This actually depends heavily on the stress in the component. It is possible that this stress will be very low, and thus structural failure may not actually occur. However, at temperatures between 1100 °C to 1200°C for VCrTi, and 900 °C to 1000 °C for HT-9, re-crystallization of the material will occur, and thus the material will lose its ductility. This ductility will not be recovered upon cooling of the structure, and thus the component will not be re-usable. Further, the deformation and/or distortion that occurs may prohibit the simple removal of the damaged module. In either case, this would represent an economic penalty, since the affected modules would have to be repaired. This requirement violates the inherent safety criteria outlined in Chapter 1, and thus the acute failure temperature limits of 1200 °C for VCrTi and 900 °C for HT-9 are appropriate. In Chapter 7, a different approach is used to model the material strength. In that chapter, a relation between the UTS and temperature is derived for the purposes of estimating the failure time in plasma induced temperature excursions.

A model for analyzing the potential for thermal creep induced structural failure was developed, based on Larson-Miller theory [3.17]. This model is described in Section 3.2.1 and Appendix A.

A brief literature survey was conducted to estimate the potential for radioisotope release. The VCrTi alloy oxidizes readily above 650 °C [3.22 - 3.25], forming the liquid V_2O_5. This could result in severe structural damage. However, at temperatures of 1500 °C, the fraction of radioactivity mobilized in 10 hours are lower than that required to yield the threshold critical dose at the site boundary [3.4]. The release fraction for HT-9 under the same conditions is somewhat higher, but still has a reasonable safety margin.

References for Chapter 3

[3.1] D.L. Smith et al., Blanket Comparison and Selection Study (BCSS) - Final Report, Argonne National Laboratory, ANL/FPP-84-1, September 1984.

[3.2] O.A. Adegbulugbe, Structural Design Limits for Fusion First Walls, Doctoral Dissertation, Nuclear Engineering Department, Massachusetts Institute of Technology, 1981.

[3.3] G.P. Yu, Relationship of Material Properties in the Design of a Fusion Reactor First Wall, Doctoral Dissertation, Nuclear Engineering Department, Massachusetts Institute of Technology, 1981.

[3.4] Report by the Committee on Environmental, Safety and Economic Aspects of Magnetic Fusion Energy, Final Report, U.S. DOE, to be issued, 1987.

[3.5] S.J. Piet, M.S. Kazimi, L.M. Lidsky, Potential Consequences of Tokamak Fusion Reactor Accidents: The Materials Impact, PFC/RR-82-19, June 1982.

[3.6] B.G. Logan, A Rationale for Fusion Economics Based on Inherent Safety, Lawrence Livermore National Laboratory, UCRL-91761, November 1984.

[3.7] S.J. Brereton and M.S. Kazimi, Safety and Economic Comparison of Fusion Fuel Cycles, PFC/RR-87-7, Massachusetts Institute of Technology, Plasma Fusion Center, August 1987.

[3.8] D.L. Smith, Physical Sputtering Model for Fusion Reactor First Wall Materials, J. Nucl. Mater., 75, 20, 1978.

[3.9] D.R. Olander, Fundamental Aspects of Nuclear Reactor Fuel Elements, Technical Information Center, U.S. Department of Energy, TID-26711-PI, 1976.

[3.10] R.E. Gold and R. Bajaj, Mechanical Property Evaluation of Path C Vanadium Scoping Alloys, Alloy Development for Irradiation Performance - Semiannual Progress Report DOE/ER-0045/10, pp. 122-141, October 1983.

[3.11] R. Carlander, et al., Effects of Radiation on Substructure and Mechanical Properties of Metals and Alloys, American Society for Testing and Material publication ASTM-STP529, p. 399, 1973.

[3.12] B.A. Wilcox, Basic Strengthening Mechanisms in Refractory Metals, Refractory Metal Alloys, Metallurgy, and Technology, I. Machlin, et al., editors, Plenum Press, NY, pp. 1-40, (1968).

[3.13] M.D. Goldberg. et. al., Neutron Cross Sections, ENDF-B/V, Brookhaven National Laboratory, BNL-325, (1966).

[3.14] W.E. Meyerhof, Elements of Nuclear Physics, McGraw-Hill, Inc. (1967).

[3.15] A.F. Henry, Nuclear Reactor Analysis, The MIT Press, Cambridge, Massachusetts, 1975.

[3.16] A. Foderaro, The Elements of Neutron Interaction Theory, The MIT Press, Cambridge, Massachusetts, 1971.

[3.17] J.A. Collins, Failure of Materials in Mechanical Design, John Wiley & Sons, 1981.

[3.18] R.J. Amodeo and N.M. Ghoniem, Development of Design Equations for Ferritic Alloys in Fusion Reactors, Nuclear Engineering and Design/Fusion, 2, p. 97, 1985.

[3.19] D.K. Sze, Personal Commumication, July 1985.

[3.20] J.E. Chafey and J.B. Wattier, Estimation of Allowable Design Stress Values for 12Cr-1Mo-0.3V Steel, General Atomic Project 4230, GA-A14610, February 1978.

[3.21] S.J. Piet, et. al., Oxidation/Volatilization Rates in Air for Candidate Fusion Reactor Blanket Materials, PCA and HT-9, J. Nucl. Mater. 141 – 143, pp. 24-28, November/December 1986.

[3.22] R.M. Neilson, Volatility of V15Cr5Ti Fusion Reactor Alloy, Idaho National Engineering Laboratory, EGG-M-25985, December 1986.

[3.23] R.C. Weast, Editor-in-Chief, CRC Handbook of Chemistry and Physics, 65th Edition, CRC Press, Inc., 1984.

[3.24] Y.S. Touloukian, editor, Thermophysical Properties of High – Temperature Solid Materials, Thermophysical Properties Research Center, Purdue University, Volume 4-I, p. 524.

[3.25] Audiere, Madi, and Grenet, Electrical and Thermal Properties of V_2O_5, J. Mater. Sci., 17 [10], pp. 2973-2978, 1982.

[3.26] S. J. Piet, Safety and Environmental Requirements and Design Targets for TIBER-II, Informal Report, Idaho National Engineering Laboratory, EG&G-FSP-7848, September 1987.

[3.27] F. Holtzberg and A. Reisman, Reactions of the Group VB Pentoxides with Alkali Oxides and Carbonates II: Phase Diagram of the System $K_2CO_3V_2O_5$, J. Am. Chem. Soc., 78, pp. 1536-1540, 1956.

[3.28] G.K. Layden and J. McQuarrie, Effect of Minor Additions on Sintering MgO, J. Am. Ceram. Soc., 42(2), pp. 89-92, 1959.

[3.29] G.R. Rigby and P. Hutton, Action of Alkali and Alkali-Vanadium Oxide Slags on Alumina-Silica Refractories, J. Am. Ceram. Soc., 45(2), pp. 68-72, 1962.

[3.30] R.E. Gold and R. Bajaj, Mechanical Property Evaluation of Path C Vanadium Scoping Alloys, Alloy Development for Irradiation Performance - Semiannual Progress Report DOE/ER-0045/7, pp. 125-128, April 1982.

[3.31] M. Schirra, Creep and Creep-Rupture Behavior of Vanadium Based Alloys, United States - Euratom Fast Reactor Exchange Program, EURFNR-1449, 1977.

4. Decay Heat Analysis

The first step in calculating the temperature response to the various transients is to determine the heat source present within the system. With the plasma burning, this includes the surface heat flux on the front face of the first wall, and the volumetric power density from the interaction of the neutron flux with the blanket materials. This is the heat source for the transients considered in Chapter 7. In Chapters 5 and 6, however, it is assumed that a fairly rapid plasma shutdown can always be achieved in the event of an accident [4.1,4.2]. Thus, the bulk of the heat will come from the decay of the radionuclides which have been created in the blanket as the result of neutron interactions.

In this chapter, the origin of decay heat in fusion reactors is briefly discussed. This is followed by the presentation of the results of a fairly extensive analysis of the decay heat problem. This includes comparing the decay heating from different structural materials, breeder materials, and the impact of a neutron multiplier (Beryllium) on the overall decay heat density of a fusion blanket. The validity of a simplifying assumption commonly used in the calculation of decay heat density is assessed. The D-D and D-T fuel cycles are compared, as are the inboard and outboard sides of a D-T reactor.

For all the blankets outlined in Chapter 2, the one-dimensional decay-heat densities were calculated using the model described in the following section. The results are shown in Figures 4.0.1 through 4.0.6, which are plots of the decay heat

Figure 4.0.1 Decay Heat Density vs. Radial Distance for Blanket #1 (A2), Inboard, 5 MW/m**2

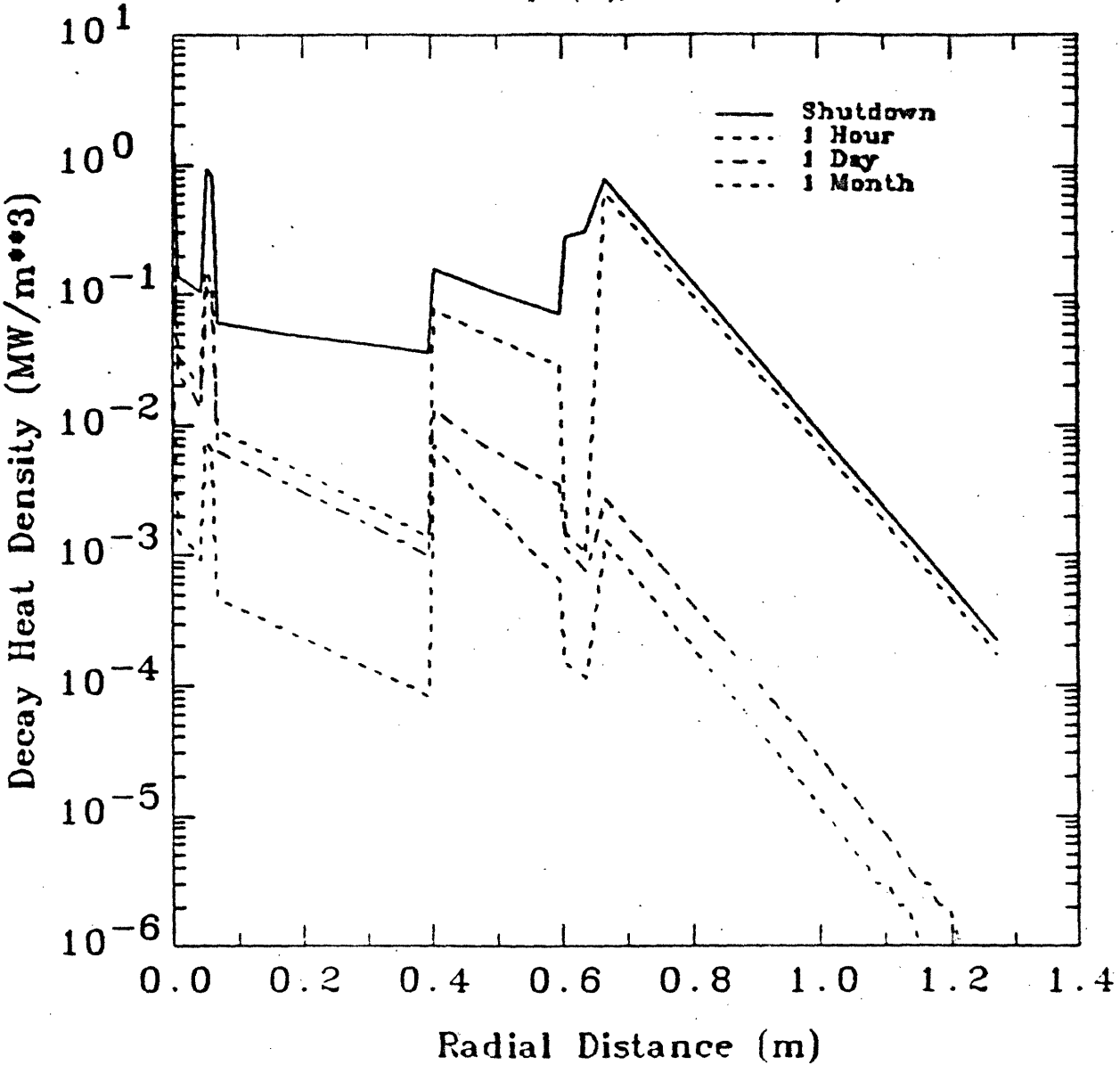

Figure 4.0.2 Decay Heat Density vs. Radial Distance for Blanket #2 (D4), Inboard, 5 MW/m**2

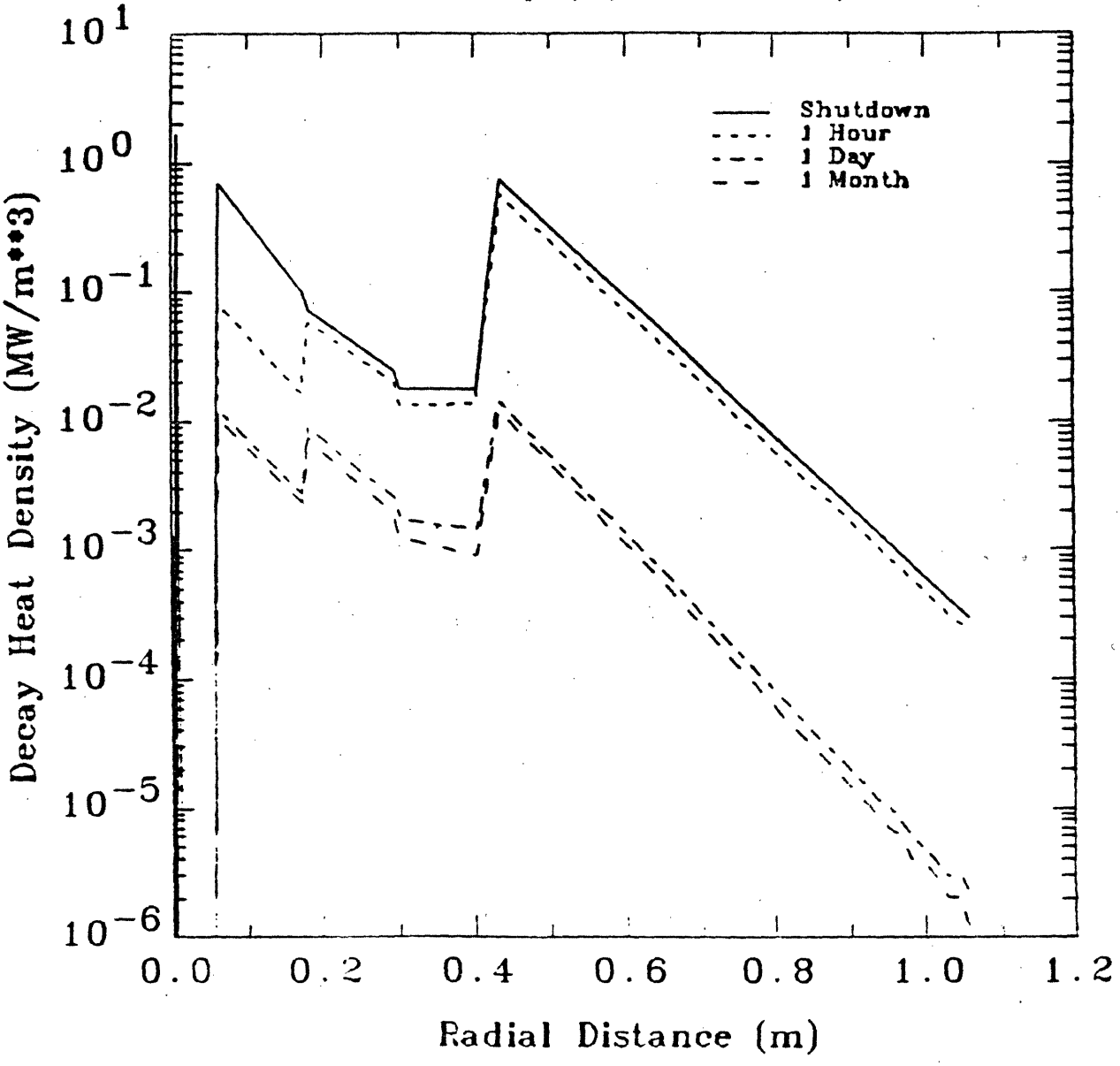

Figure 4.0.3 Decay Heat Density vs. Radial Distance for Blanket #3 (E2), Outboard, 5 MW/m**2

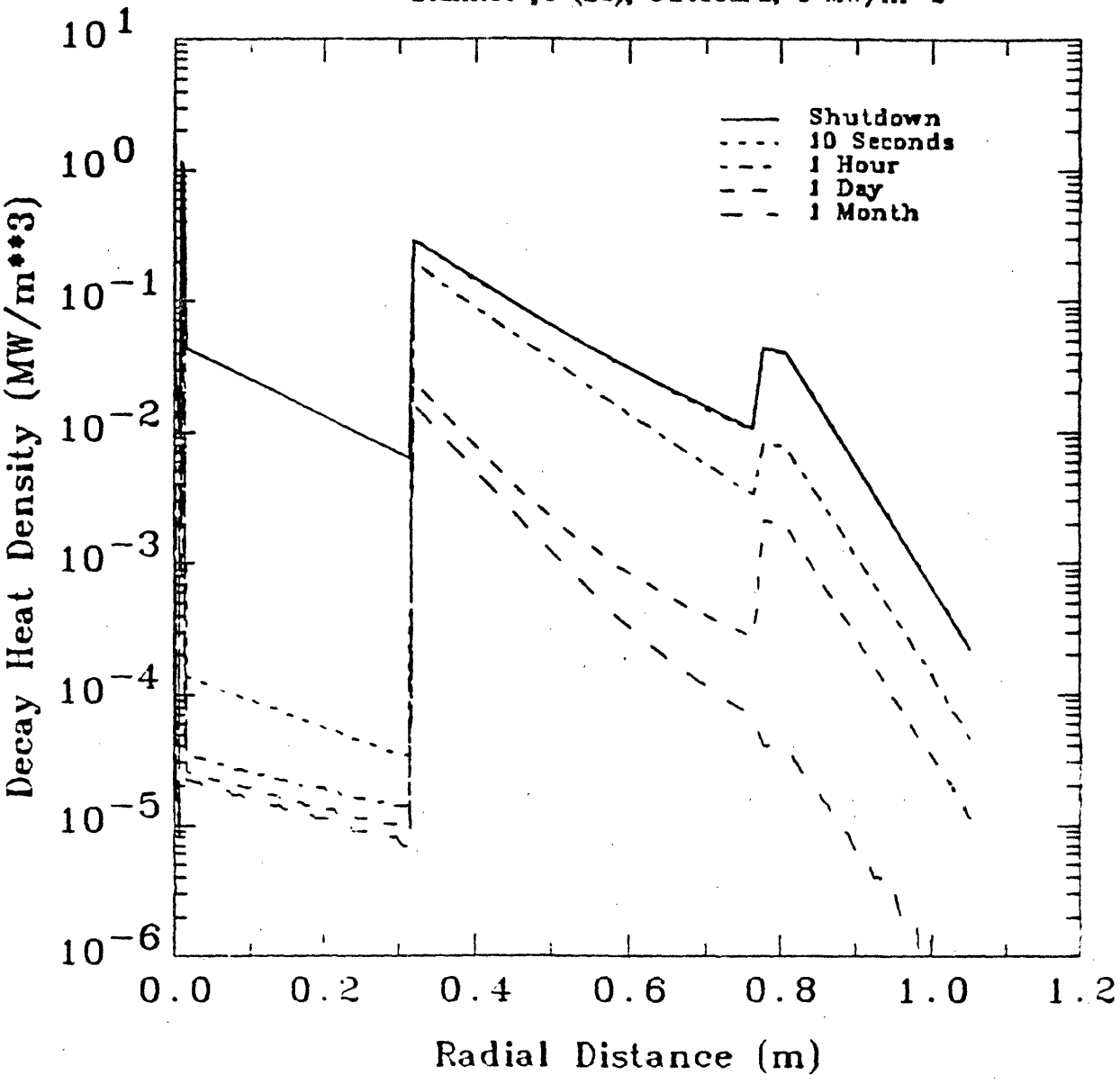

Figure 4.0.4 Decay Heat Density vs. Radial Distance for Blanket #4 (P1), Inboard, 5 MW/m**2

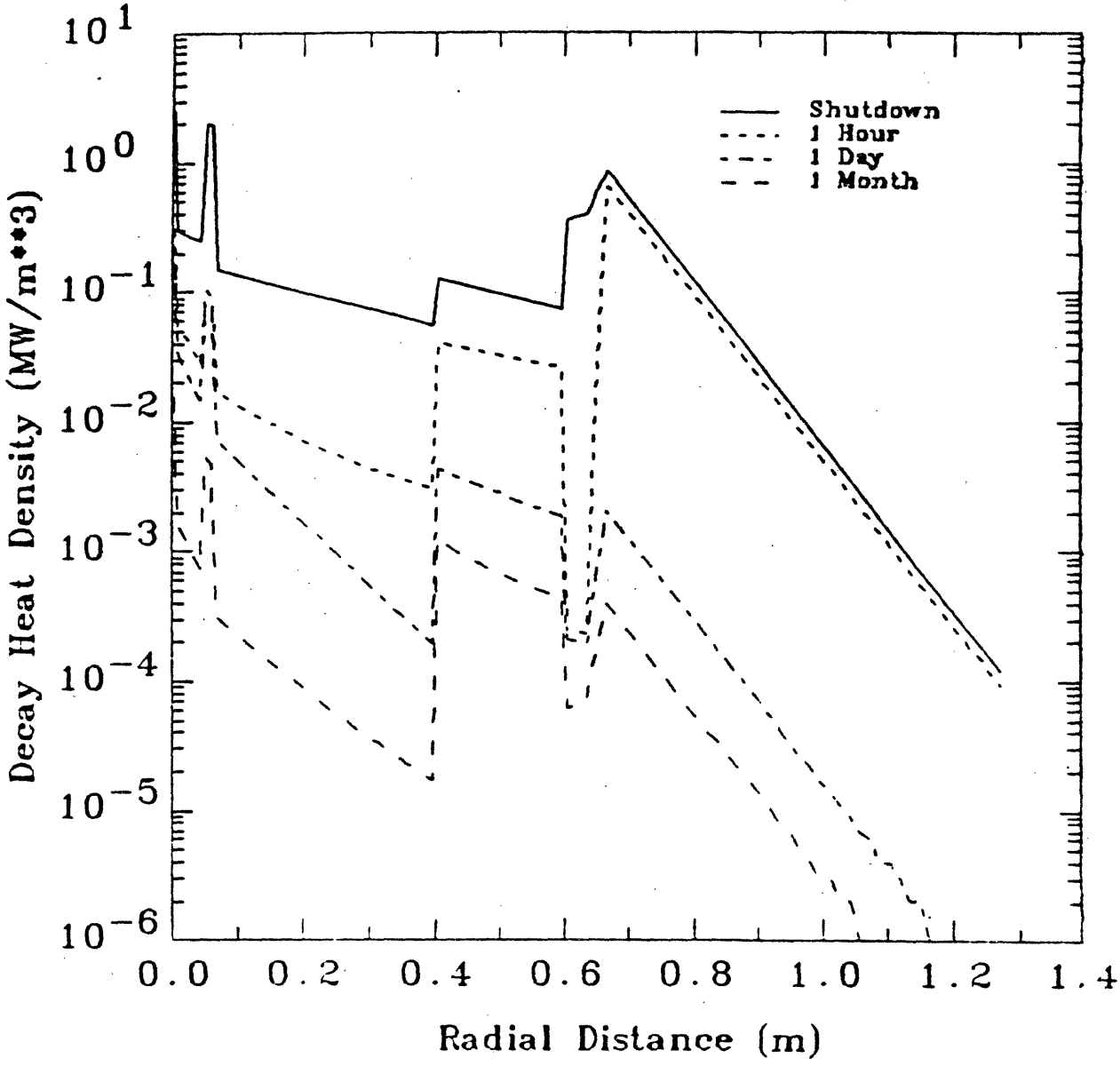

Figure 4.0.5 Decay Heat Density vs. Radial Distance for Blanket #5 (G1), Inboard, 5 MW/m**2

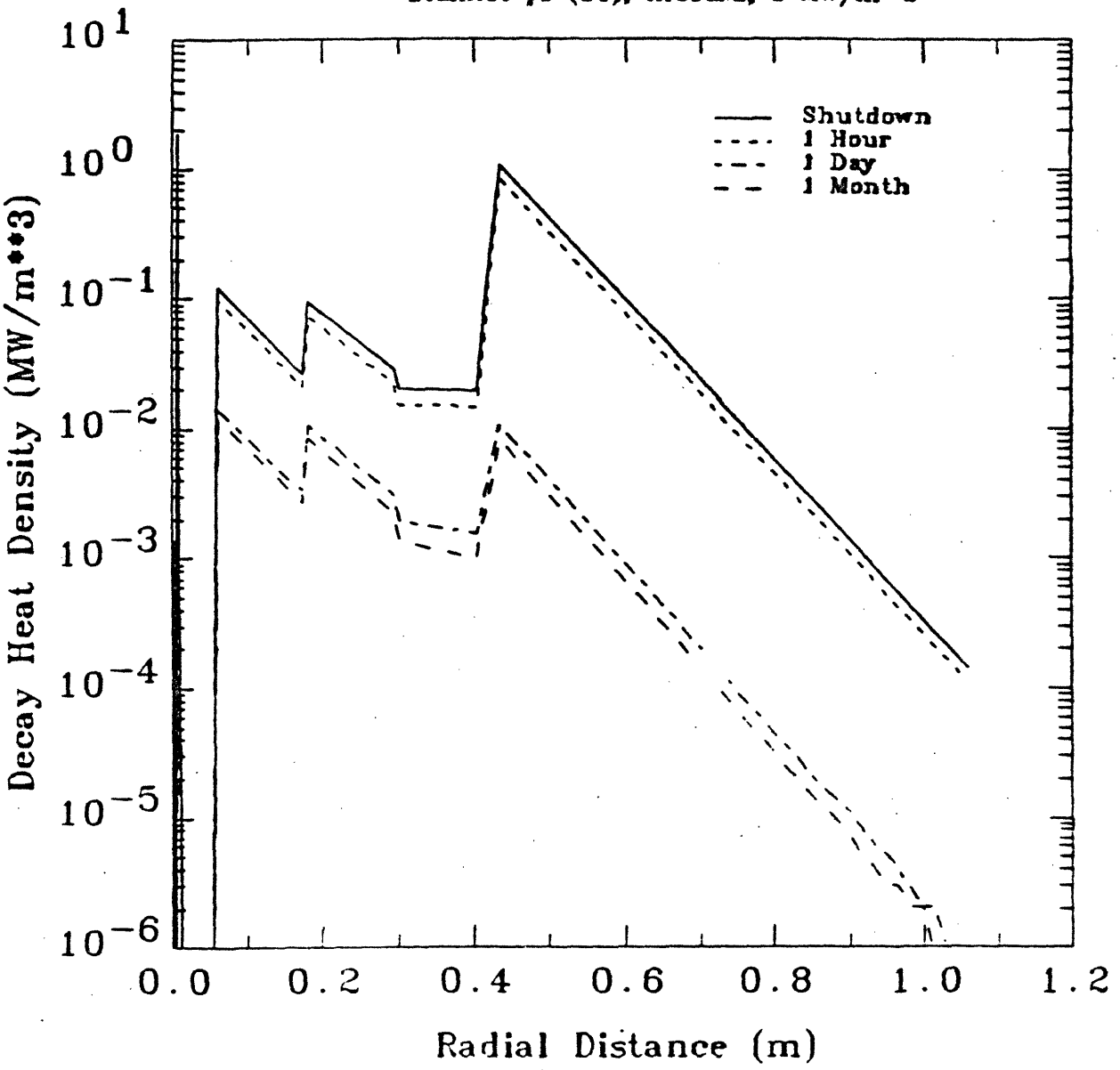

Figure 4.0.6 Decay Heat Density vs. Radial Distance for Blanket #6 (H1),Inboard, 1.17 MW/m**2

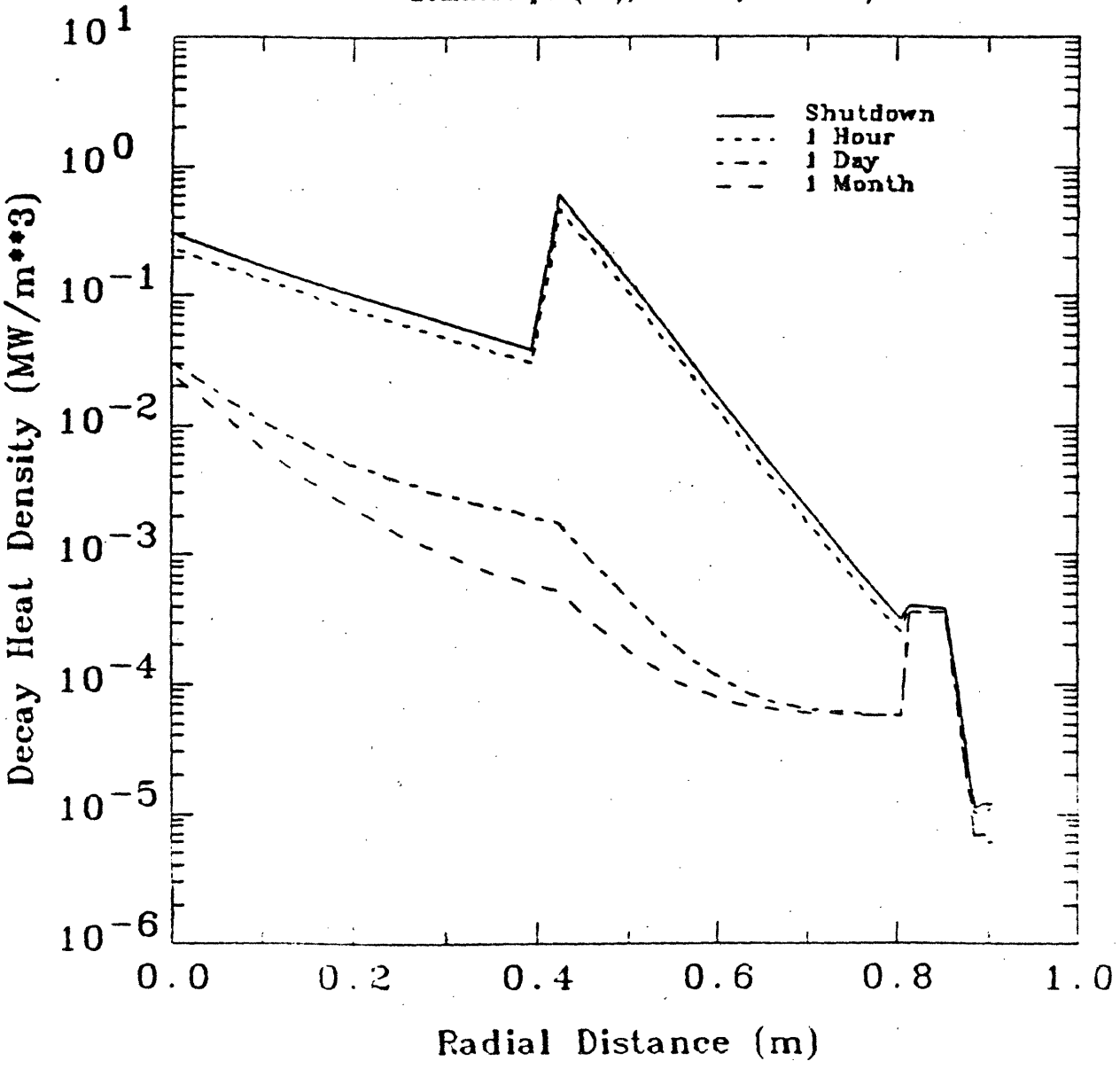

density (MW/m^3) vs. x, the distance from the first wall (m). These figures are discussed and compared throughout the rest of this chapter. For all the blankets, the decay heat analysis was done at the end of blanket life, since the decay heat density will be highest at this time [4.3], thus the case being analyzed will represent the most pessimistic case. As is discussed in Chapter 3, the lifetime of the D-T tokamak blankets (Blankets #1, #2, #4, and #5) is based on first wall erosion and and is assumed to be 15 MW-yr/m^2 (three full power years). For the Reversed-Field-Pinch Blanket #3, the lifetime is also about 15 MW-yr/m^2, which is one full power year. The lifetime of the D-D tokamak Blanket #6 is based on the dpa limit in the MT-9 first wall (see Section 3.1), and is about 14.6 MW-yr/m^2, which translates to 12.5 full power years [4.2,4.4,4.5].

4.1 Calculational Model

The mechanism for producing radionuclides within the blanket is neutron interactions with structural elements, the result of which is a radioactive nuclide. For instance, iron is a major element in many structural materials. Natural iron consists of ^{54}Fe, ^{56}Fe, ^{57}Fe, and ^{58}Fe [4.6]. These elements, in a fusion first wall/blanket which experiences a neutron flux, can undergo many reactions, including the following [4.6]:

$$^{56}\mathrm{Fe(n,p)}^{56}\mathrm{Mn}$$
$$^{57}\mathrm{Fe(n,d)}^{56}\mathrm{Mn}$$
$$^{54}\mathrm{Fe}(n,\gamma)^{55}\mathrm{Fe}$$
$$^{58}\mathrm{Fe(n,d)}^{57}\mathrm{Mn}$$

The isotopes ^{56}Mn, ^{55}Fe, and ^{57}Mn are radioactive, and will decay with a characteristic half-life. The decay energy thus released emerges as heat deposited in the location of the decaying isotope (for γ-decay this is not necessarily true; see Section 4.3).

From the example given above, it is seen that the amount of decay heat that

a given material produces will depend on a number of factors, including the cross-sections for reactions which produce radioactive isotopes, and the decay energy and half-life of those isotopes. Thus, while one material may be the source of a large amount of decay heat, another material may contribute only very little decay heat. So it is clear that materials selection has a major impact on the decay heat profile of a given blanket design [4.3,4.7]. This topic is discussed in detail in Section 4.2.

Determining the decay heat density ($\dot{q}'''_{decay}(x,t)$) in the first wall/blanket of a fusion reactor has been the subject of many studies [4.3,4.6,4.8]. However, a number of different calculational tools exist, and the agreement between them is not always good [4.9]. The differences exist primarily due to uncertainties in the value of the neutron cross-sections for the relevant reactions.

The first step in calculating $\dot{q}'''_{decay}(x,t)$ in the blanket involves finding the operational neutron fluxes. This is done using the one-dimensional neutron transport code ONEDANT [4.10], a discrete-ordinates code, using a P_3S_{12} approximation. One-dimensional cylindrical geometry is used to model the overall tokamak geometry (see Appendix B for further detail), with the dimensions and compositions of each blanket given in Figures 2.1.1 through 2.6.1. The fluxes calculated by ONEDANT are an input to the activation/transmutation code REAC [4.6]. For a given irradiation time, REAC calculates the the activity (Ci/cm^3) of the radionuclides produced at selected positions in the blanket for selected times after shutdown. REAC also calculates a 21 energy-group source distribution for decay γ's at the same selected blanket positions.

In the thermal analysis (Chapter 5), it was found in almost all cases that maximum temperatures were reached within 10 hours, and within 48 hours (two days), the temperatures had either leveled off or had begun to decrease. Thus, it was deemed sufficient to include only the isotopes which contribute significantly to the overall decay heat up to two days after shutdown. This is accomplished by calculating the amount of heat produced by every isotope given in the REAC output

within the first two days after shutdown. Then, only the isotopes that contribute 0.10% or more of the total are considered significant, and the rest are ignored. Table 4.1.1 shows some of the significant isotopes for some of the blanket materials.

The primary goal of the decay heat analysis is to determine the heat source $\dot{q}'''_{decay}(x,t)$ and represent it in a form which allows easy input into the thermal model. Thus, an equation for $\dot{q}'''_{decay}(x,t)$ is desirable. Using the decay constants of the respective isotopes, the decay heat density as a function of time for any position in the blanket can be expressed as:

$$\dot{q}'''_{decay}(t) = \sum_i a_i e^{-\lambda_i t} \tag{4.1}$$

where the sum is over all the significant isotopes present at that blanket position. Furthermore, the neutron flux decreases exponentially as the distance from the first wall (distance into the blanket) increases [4.11,4.12,4.13]. The activity calculated by REAC is a direct function of the neutron flux, and thus it can be assumed that the activity of each isotope will fall off exponentially with the distance from the first wall. This leads to the expression

$$\dot{q}'''_{decay}(x,t) = \sum_i a_i e^{-\lambda_i t} e^{-\mu_i x} \tag{4.2}$$

where x is the distance from the first wall. The parameters a_i and μ_i are found by manipulation of the data in the REAC output (a detailed discussion of this procedure is contained in Appendix B). The summation in equation (4.2) is over all the significant isotopes in the particular blanket region of interest. For a different region which contains different radioisotopes, the summation index will change to correspond to those isotopes. Equation (4.2) is used in the thermal model to calculate the decay heat source.

Throughout the remainder of this chapter, there are a number of references

Table 4.1.1 Isotopes contributing significantly to afterheat during the first 48 hours for the candidate structural and breeder materials.

VCrTi	MT-9	Fe1422	Lithium	Li_2O	$Li_{17}Pb_{83}$
^{52}V	^{54}Mn	^{56}Mn	^{3}H	^{3}H	^{203}Pb
^{51}Ti	^{56}Mn	^{54}Mn	^{6}He	^{16}N	^{209}Pb
^{48}Sc	^{58}Co	^{58}Co			^{3}H
^{47}Sc	^{99}Mo	^{59}Fe			
^{51}Cr		^{60}Co			
^{46}Sc					

to the *decay heat fraction*. The details of how the decay heat fraction is calculated are given in Appendix B. Briefly, the decay heat fraction is the total amount of decay power (MW) produced in the blanket (or one region of the blanket) divided by the total amount of power produced by the blanket during normal operation. This is similar to the decay heat fraction parameter used is assessing fission reactors, and is useful for comparing the decay heat levels in different blankets.

4.2. Materials Impact on Decay Heat Density

As was mentioned, the materials used in the First Wall/Blanket system will have a significant impact on the overall decay heat density [4.3,4.6,4.7,4.8]. An analysis was performed to compare the decay heat densities of some materials. In Chapter 5, the effect of the different decay heat densities on the blanket temperature response to undercooling transients is examined. The materials considered, with their elemental compositions, are listed in Table 4.2.1. Impurities were included in the decay heat analysis, but were found to have minimal effect, due to their small concentrations.

4.2.1 Structural Material

Most of the decay heat produced in a fusion reactor will come from the structural material [4.3]. This is because most of the high-Z elements typically used in structural materials are subject to transmutation reactions such as those given in Section 4.1. Thus, the choice of structural material will have a major impact on the overall decay heat density of the fusion reactor.

A number of different structural materials were analyzed in this work. In some cases, direct comparisons were made between candidate materials for the same application. In other cases, a comparison can only be made by comparing the decay heat densities of two blankets which use different structural materials.

Table 4.2.1 Candidate Structural and Breeder Materials and Their Constituent Elements. Number density (atom/barn-cm) of each material is listed below material name. Element concentrations are atomic fractions. Data from Reference [4.8].

	VCrTi	MT-9*	Fe1422	Lithium	Li_2O	$Li_{17}Pb_{83}$
Element	7.217×10^{-2}	8.483×10^{-2}	8.794×10^{-2}	4.514×10^{-2}	1.211×10^{-1}	3.381×10^{-2}
C	8.460×10^{-4}	9.210×10^{-3}	2.628×10^{-2}	5.766×10^{-6}	3.314×10^{-6}	negligible
N	1.813×10^{-3}	1.578×10^{-4}	7.379×10^{-4}	2.471×10^{-5}	1.421×10^{-5}	negligible
O	1.587×10^{-3}	- none -	- none -	- none -	3.325×10^{-1}	- none -
Al	7.520×10^{-5}	- none -	- none -	- none -	- none -	- none -
Si	5.440×10^{-4}	4.917×10^{-3}	4.453×10^{-3}	2.751×10^{-5}	1.416×10^{-5}	negligible
P	1.640×10^{-4}	- none -	2.634×10^{-4}	- none -	- none -	- none -
Ti	5.300×10^{-2}	- none -	- none -	- none -	- none -	- none -
V	7.953×10^{-1}	3.253×10^{-3}	- none -	4.070×10^{-7}	1.952×10^{-7}	negligible
Cr	1.465×10^{-1}	1.222×10^{-1}	2.102×10^{-2}	2.661×10^{-7}	1.912×10^{-7}	negligible
Fe	9.090×10^{-5}	8.431×10^{-1}	7.907×10^{-1}	1.239×10^{-6}	7.122×10^{-7}	negligible
Ni	8.650×10^{-6}	4.705×10^{-3}	1.797×10^{-2}	- none -	- none -	- none -
Nb	1.366×10^{-5}	1.189×10^{-5}	- none -	- none -	- none -	- none -
Mo	7.142×10^{-5}	5.757×10^{-3}	- none -	- none -	- none -	- none -
K	- none -	4.239×10^{-6}	- none -	3.539×10^{-5}	3.104×10^{-5}	5.308×10^{-6}
Mn	- none -	6.531×10^{-3}	1.386×10^{-1}	- none -	- none -	- none -
Cu	- none -	2.608×10^{-5}	- none -	- none -	- none -	5.445×10^{-6}
As	- none -	2.212×10^{-6}	- none -	- none -	- none -	- none -
S	- none -	- none -	3.392×10^{-5}	- none -	- none -	- none -
Li	- none -	- none -	- none -	9.998×10^{-1}	6.674×10^{-1}	1.701×10^{-1}
Na	- none -	- none -	- none -	9.022×10^{-5}	4.323×10^{-5}	1.354×10^{-5}
Ca	- none -	- none -	- none -	5.167×10^{-5}	2.481×10^{-5}	7.768×10^{-6}
Pb	- none -	- none -	- none -	- none -	- none -	8.269×10^{-1}

* Modifed for low activation, as presented in Reference [4.8]. Due to lack of cross-section data, the elements Barium and Bismuth are neglected, and Tungsten is replaced by Manganese. See discussion in Section 4.2.1.2.

4.2.1.1 Vanadium Alloy V-15Cr-5Ti

The vanadium alloy V-15Cr-5Ti is used as the structural material in blankets #1, #3, and #4. There are some regions in these blankets which are 100% VCrTi (see Figures 2.1.1, 2.3.1, and 2.4.1), and the decay heat density in these regions can be seen in Figures 4.0.1, 4.0.3, and 4.0.4.

The primary feature to note is that the decay heat density in VCrTi decays by almost one order of magnitude in one hour. This relatively rapid decay is one reason that makes VCrTi, in terms of decay heat, probably the best of the commonly considered structural materials (i.e., VCrTi, HT-9, PCA) [4.4]. The contribution of each isotope to the total decay heat produced in the VCrTi first wall region (Region 1) of Blanket #3 is displayed in Table 4.2.2. Shown are the isotopes that contribute to the total decay heat density, the individual decay heat density for each isotope at shutdown (broken down into contributions from β and γ decay and the total), the total heat each isotope contributes over a two day period, and the fraction (%) that each contributes to the two day total of all the isotopes. Recall that only those isotopes with a value in this column of at least 0.10 are considered significant.

At shutdown, the bulk of the decay heat from VCrTi comes from ^{52}V (see Table 4.2.2, column 4), which is produced in fairly large quantities from the ^{51}V(n,γ)^{52}V reaction. This reaction has a $\frac{1}{v}$ cross-section, and thus ^{52}V is produced primarily by slow neutrons. When it decays, ^{52}V emits a 1.07 MeV β particle and a 1.44 MeV γ ray [4.3]. The half-life of ^{52}V is only 3.75 minutes, thus, in less than one hour, the ^{52}V has essentially decayed away entirely. This is the main reason that the total decay heat from VCrTi reduces by an order of magnitude in one hour. The isotope ^{48}Sc, which has a half life of 43.7 hours, produces the most heat over the two day period.

Figure 4.2.1 plots the decay heat fraction in each region of Blanket #1, and the total, as a function of time. Note that, in the VCrTi first wall, the decay heat decays by a factor of about five in one hour. In the VCrTi second wall (Region 6),

Table 4.2.2 Isotopes contributing to decay heat in VCrTi first wall of Blanket #3.

Isotope	Half Life	DECAY POWER @ SHUTDOWN beta (W/cm**3)	gamma (W/cm**3)	total (W/cm**3)	Total Heat Produced in 2 Days (J/cm**3)	Percent of 2-Day Total Contributed by Isotope
Sc 48	4.37e+01 hr	0.278e-01	0.435e+00	0.463e+00	0.560e+05	86.516
Sc 46	8.38e+01 day	0.122e-02	0.223e-01	0.235e-01	0.402e+04	6.222
Cr 51	2.77e+01 day	0.137e-02	0.824e-02	0.961e-02	0.162e+04	2.506
Sc 47	3.35e+00 day	0.659e-02	0.453e-02	0.111e-01	0.157e+04	2.432
V 52	3.75e+00 min	0.115e+01	0.155e+01	0.270e+01	0.877e+03	1.356
V 48	1.60e+01 day	0.441e-03	0.622e-03	0.106e-02	0.176e+03	0.272
Ti 51	5.76e+00 min	0.204e+00	0.867e-01	0.291e+00	0.145e+03	0.224
Ca 47	4.54e+00 day	0.220e-03	0.685e-03	0.905e-03	0.135e+03	0.208
Ca 45	1.64e+02 day	0.388e-03	0.	0.388e-03	0.668e+02	0.103

Table 4.2.3 Isotopes contributing to decay heat in MT-9 first wall of Blanket #2.

Isotope	Half-Life	DECAY POWER @ SHUTDOWN beta (W/cm**3)	gamma (W/cm**3)	total (W/cm**3)	Total Heat Produced in 2 Days (J/cm**3)	Percent of 2-Day Total Contributed by Isotope
Mn 54	3.13e+02 day	0.858E-03	0.144E+00	0.145E+00	0.250E+05	50.688
Mn 56	2.60e+00 hr	0.464E+00	0.939E+00	0.140E+01	0.189E+05	38.403
Co 58	7.08e+01 day	0.337E-03	0.921E-02	0.955E-02	0.163E+04	3.313
Cr 51	2.77e+01 day	0.101E-02	0.608E-02	0.709E-02	0.120E+04	2.424
Mo 99	6.60e+01 hr	0.593E-02	0.229E-02	0.823E-02	0.112E+04	2.264
Fe 55	2.68e+01 yr	0.000E+00	0.212E-02	0.212E-02	0.367E+03	0.744
Co 57	2.70e+02 day	0.241E-03	0.146E-02	0.170E-02	0.294E+03	0.595
Co 60	5.27e+00 yr	0.457E-04	0.114E-02	0.119E-02	0.205E+03	0.416
Sc 48	4.37e+01 hr	0.735E-04	0.115E-02	0.122E-02	0.148E+03	0.300
Ni 57	3.61e+01 hr	0.880E-04	0.932E-03	0.102E-02	0.115E+03	0.233
Nb 92m	1.02e+01 day	0.297E-05	0.557E-03	0.560E-03	0.905E+02	0.183
V 52	3.75e+00 min	0.682E-01	0.917E-01	0.160E+00	0.519E+02	0.105

Figure 4.2.1 Decay Heat Fraction by Zone vs. Time for Blanket #1 (A2) Inboard, 5 MW/m**2, 3 Full Power Years

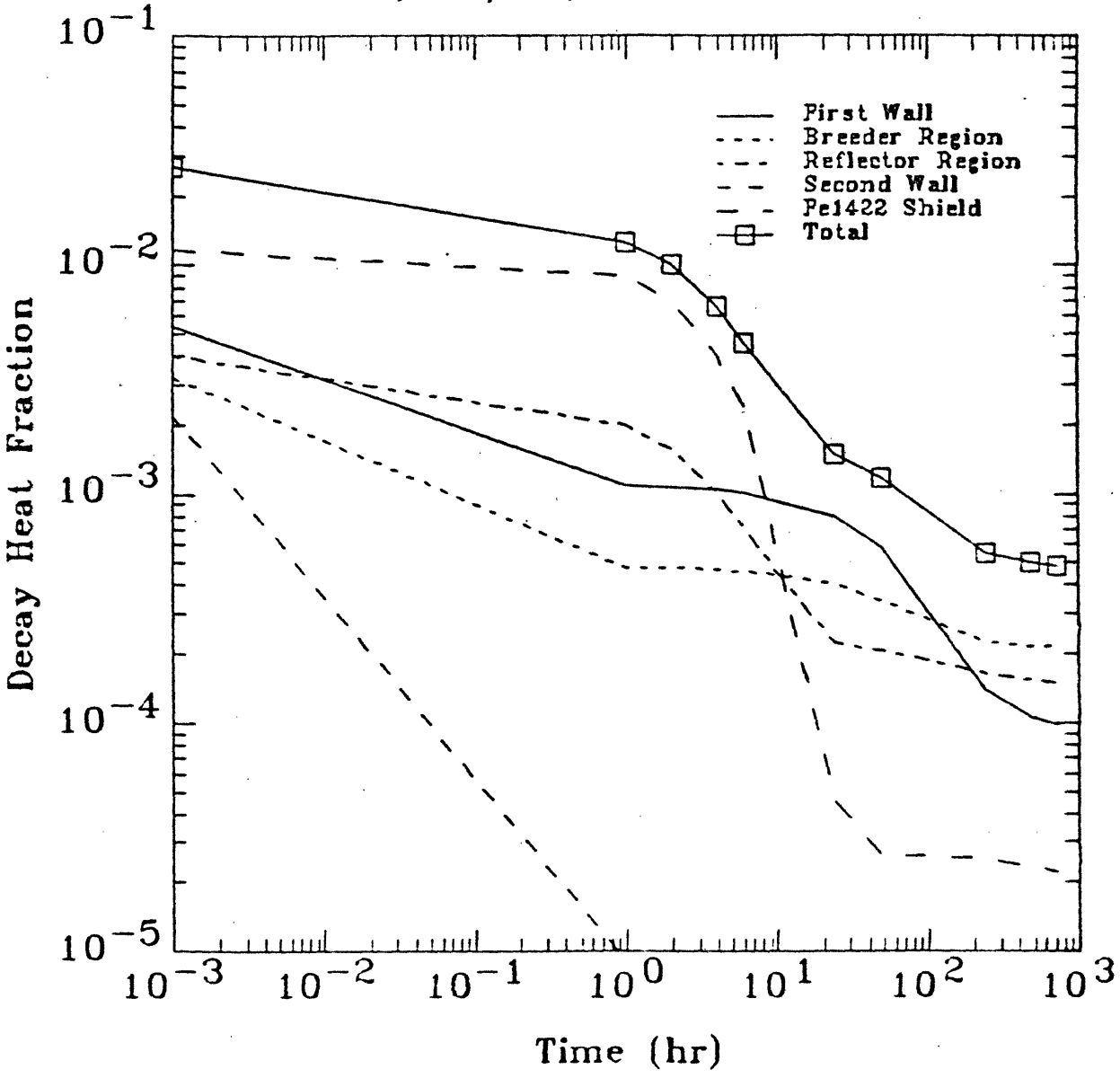

however, the decay heat decays by a factor of about 300 in one hour. This is because in the first wall, the flux is mostly fast, i.e., the neutron spectrum is hard. Thus, the slow-neutron induced $^{51}V(n,\gamma)^{52}V$ is less dominant, and other, longer lived isotopes, such as ^{48}Sc, which is formed primarily from the fast-neutron induced $^{51}V(n,\alpha)^{48}Sc$ reaction, play a more important role in the production of decay heat. The relatively long-life of these isotopes cause the total decay heat density in this region to decay more slowly. In the second wall, at the back of the blanket, the flux spectrum is much softer, and thus ^{52}V is by far the dominant isotope, producing over 99% of the decay power at shutdown. Thus, the total decay heat density in this region decays much more rapidly.

In summary, because the decay heat from VCrTi is dominated by the short-lived isotope ^{52}V, the decay power produced by VCrTi decays fairly rapidly in time. Thus, over a two day period, the total amount of decay heat produced by VCrTi is small compared to other structural materials. From the standpoint of decay heat production, then, VCrTi is the best candidate structural material.

4.2.1.2 Ferritic Steel MT-9

The ferritic steel MT-9 is used as the structural material in Blankets #2, #5, and the D-D Blanket #6. The HT-9 used throughout this study, referred to as MT-9, is a version proposed by Fetter [4.8], which has been modified to reduce the activation level. It should be pointed out that the HT-9 Fetter has proposed contains small amounts of tungsten, barium, and bismuth. The cross-sections for these elements were not available at the time the decay heat analysis was performed. The elements barium and bismuth were neglected, since the concentration of these elements is so small, and they don't lead to significant decay heat-producing isotopes anyway. Manganese was used to represent tungsten, since the decay heat behavior of these two elements is similar. MT-9 is also used as the bulk of the structural material in the manifolds of Blankets #1, #3, and #4. Check Figures 2.1.1 - 2.6.1 to

find the regions which contain only MT-9. The decay heat density in these regions can be seen in Figures 4.0.1 - 4.0.6.

Figure 4.2.2 shows the decay heat fraction for each region of Blanket #2 as a function of time. It takes 24 hours for the decay heat in the MT-9 first wall to decay by an order of magnitude, after which time it remains fairly constant up to a month after shutdown. Table 4.2.3 gives the isotopic breakdown of the decay heat in the first section of this first wall (Region 1 - see Figure 2.2.1). The dominant isotopes, both at shutdown and for the two day total, are ^{54}Mn and ^{56}Mn, which have half-lives of 313 days and 2.6 hours, respectively. At shutdown, ^{56}Mn contributes almost 90% of the decay power.

It should be noted that at the back of the blanket, where the flux is softer, ^{56}Mn does not become the highly dominant isotope the way ^{52}V does in VCrTi blankets. While it does contribute a higher fraction of the two-day total at the back, the effect is not nearly as pronounced as it is in Figure 4.2.1 for VCrTi. This is because ^{56}Mn is produced through a number of reactions, some from slow neutrons and some from fast neutrons [4.6]. Similarly, ^{54}Mn is produced by a few different reactions as well, and is not produced solely by fast neutrons, the way ^{48}Sc is from ^{51}V.

Despite the production of the long-lived isotope ^{54}Mn, MT-9 is still a good structural material in terms of decay heat. The overall decay heat level does decay by an order of magnitude in one day, and in areas where the flux is mostly slow, it will decay by significantly more than this in about eight to twelve hours.

4.2.1.3 Fe1422 Steel

Fe1422 steel is used as the shield material in all the blankets, and was proposed by the BCSS and ESECOM study as the manifold material in Blankets #1, #3, and #4. Fe1422 has good strength properties [4.4] and is significantly less expensive than HT-9 [4.5]. The "1422"notation indicates that the steel consists of 14% Mn,

Figure 4.2.2 Decay Heat Fraction by Zone vs. Time for Blanket #2 (D4)
Inboard, 5 MW/m**2, 3 Full Power Years

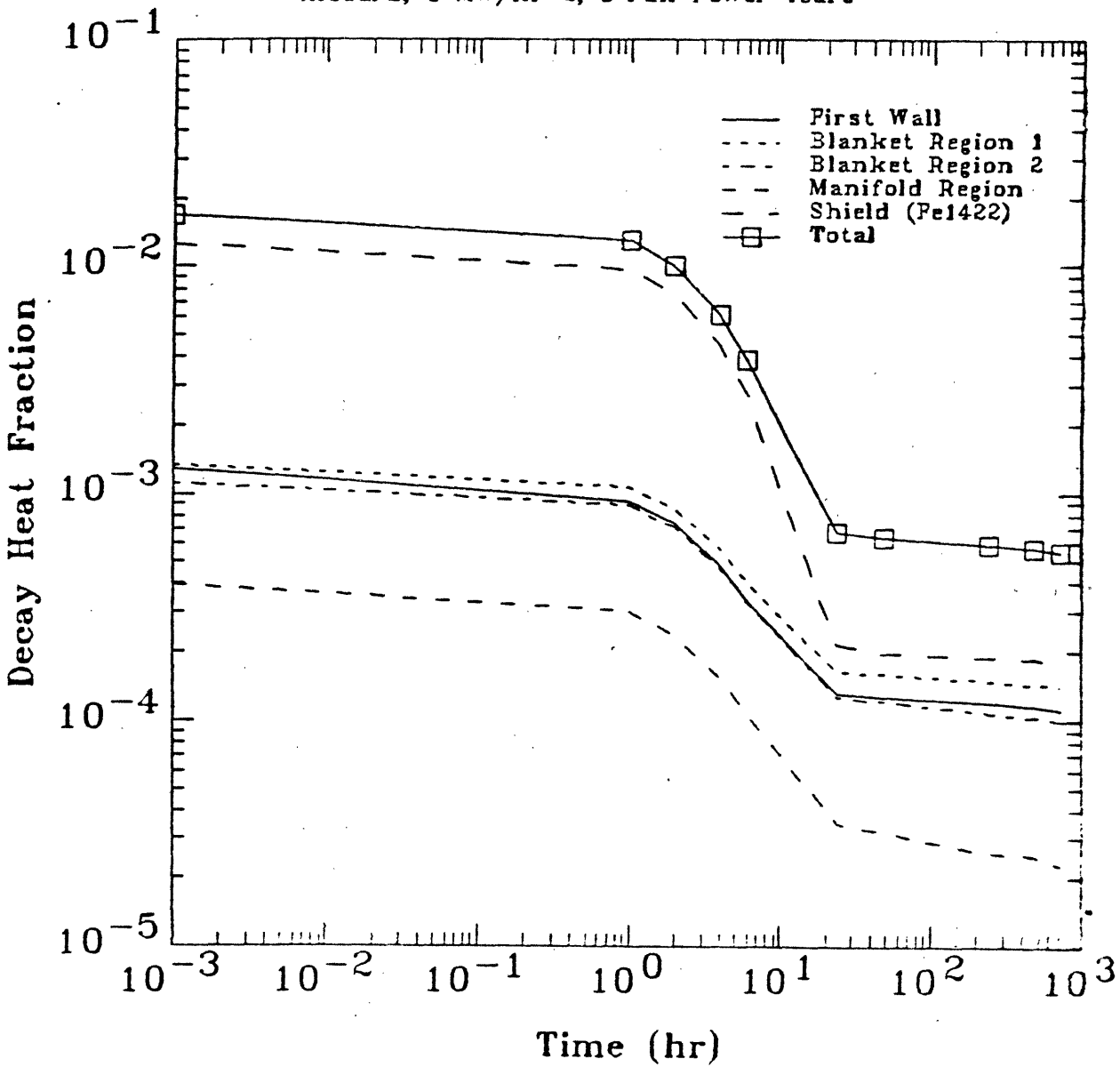

2% Ni, and 2% Cr. The remainder is Fe.

Figures 4.2.3 and 4.2.4 show the decay heat density vs. x for Blankets #1 and #3 with Fe1422 in place of the MT-9 in the manifold region (Region 5 in Blanket #1, Region 6 in Blanket #). Also, the decay heat density vs. time behavior for the Fe1422 shield region can be seen in Figures 4.2.1 and 4.2.2.

It is seen immediately from these figures that the decay heat density from Fe1422 is very high compared to VCrTi and MT-9. This is almost exclusively because of the large amount of manganese present, which produces both ^{54}Mn and ^{56}Mn. The decay heat density from Fe1422 does not decay significantly for a number of hours, until the ^{56}Mn (2.6 hour half-life) decays to a fraction of its initial concentration. Even then, ^{54}Mn (313 day half-life) continues to produce significant levels of decay heat for months.

Table 4.2.4 gives the isotopic breakdown of the decay heat production in the Fe1422 manifold region of Blanket #3. Note that ^{54}Mn produces over half of the two-day total, and produces about 12% of the decay power at shutdown. This means that the decay heat from Fe1422 will not be reduced by an order of magnitude until about three months have passed.

In Figures 4.0.1 - 4.0.6, it is seen that the decay heat density in the Fe1422 shields falls off quickly with x. This is due to the flux attenuation in the shield. Thus, in this region where the flux is low, and mostly thermal, using Fe1422 will not cause a significant problem in terms of decay heat.

Due to the large amount of manganese, the steel Fe1422 produces high levels of decay heat. Furthermore, a substantial fraction of this heat is produced by the long-lived isotope ^{54}Mn, and thus does not decay over a short time period. For these reasons, in terms of decay heat production, Fe1422 is a very poor structural material for use in the blanket/manifold region. In regions where the neutron flux is highly attenuated (i.e., the flux is small compared to the first wall, and the spectrum

Figure 4.2.3 Decay Heat Density vs. Radial Distance for Blanket #1, Pe1422 Manifold (A1), 5 MW/m**2

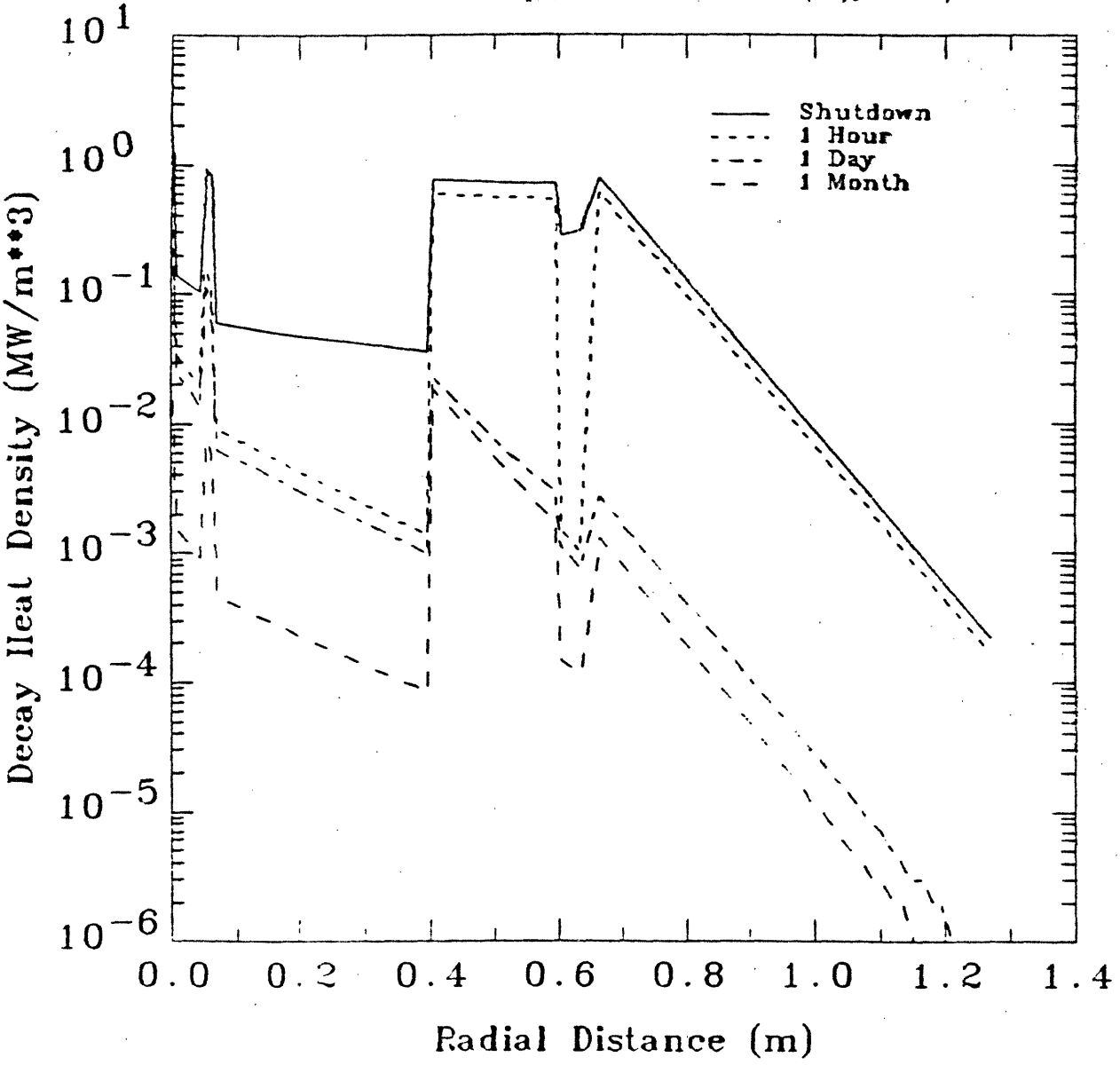

Figure 4.2.4 Decay Heat Density vs. Radial Distance for Blanket #3, Pe1422 Manifold (E1), 5 MW/m**2

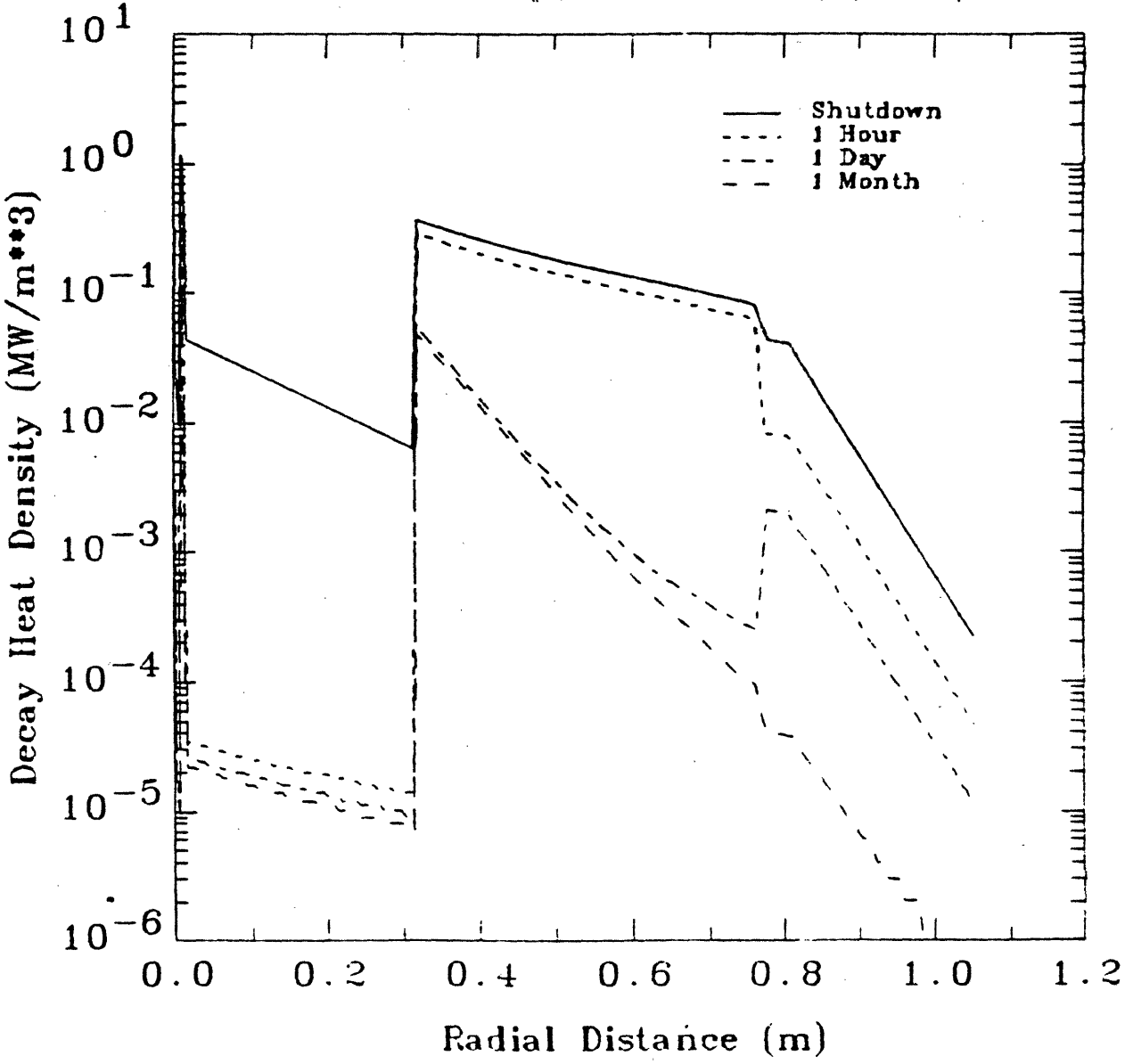

Table 4.2.4 Isotopes contributing to decay heat in Fe1422 Manifold in Blanket #3. Note that the decay heat in the interior of the manifold is found by an exponential interpolation of the endpoints.

FRONT OF MANIFOLD

Isotope	Half-Life	DECAY POWER @ SHUTDOWN beta (W/cm**3)	gamma (W/cm**3)	total (W/cm**3)	Total Heat Produced in 2 Days (J/cm**3)	Percent of 2-Day Total Contributed by Isotope
Mn 54	3.13e+02 day	0.275e-03	0.461e-01	0.464e-01	0.800e+04	53.889
Mn 56	2.60e+00 hr	0.104e+00	0.211e+00	0.316e+00	0.427e+04	28.727
Co 58	7.08e+01 day	0.329e-03	0.899e-02	0.932e-02	0.160e+04	10.746
Sc 48	4.37e+01 hr	0.289e-03	0.451e-02	0.480e-02	0.581e+03	3.913
Co 57	2.70e+02 day	0.732e-04	0.443e-03	0.517e-03	0.890e+02	0.600
Co 60	5.27e+00 yr	0.128e-04	0.320e-03	0.333e-03	0.575e+02	0.387
Sc 46	8.38e+01 day	0.164e-04	0.301e-03	0.317e-03	0.543e+02	0.366
Cr 51	2.77e+01 day	0.417e-04	0.250e-03	0.292e-03	0.492e+02	0.332
Fe 59	4.45e+01 day	0.256e-04	0.252e-03	0.277e-03	0.472e+02	0.318
Ni 57	3.61e+01 hr	0.212e-04	0.225e-03	0.246e-03	0.278e+02	0.187
Fe 55	2.68e+00 yr	0.	0.877e-04	0.877e-04	0.152e+02	0.102

BACK OF MANIFOLD

Isotope	Half-Life	DECAY POWER @ SHUTDOWN beta (W/cm**3)	gamma (W/cm**3)	total (W/cm**3)	Total Heat Produced in 2 Days (J/cm**3)	Percent of 2-Day Total Contributed by Isotope
Mn 56	2.60e+00 hr	0.264e-01	0.535e-01	0.800e-01	0.108e+04	96.927
Fe 59	4.45e+01 day	0.614e-05	0.604e-04	0.665e-04	0.113e+02	1.016
C 14	5.73e+03 yr	0.563e-04	0.	0.563e-04	0.972e+01	0.873
Mn 54	3.13e+02 day	0.256e-06	0.429e-04	0.432e-04	0.745e+01	0.668
V 52	3.75e+00 min	0.251e-02	0.338e-02	0.589e-02	0.191e+01	0.172
Co 58	7.08e+01 day	0.355e-06	0.970e-05	0.101e-04	0.172e+01	0.154
Cr 51	2.77e+01 day	0.641e-06	0.385e-05	0.449e-05	0.756e+00	0.068
Sc 48	4.37e+01 hr	0.252e-06	0.394e-05	0.419e-05	0.507e+00	0.045
P 32	1.43e+01 day	0.806e-06	0.116e-05	0.197e-05	0.324e+00	0.029
Fe 55	2.68e+00 yr	0.	0.101e-05	0.101e-05	0.175e+00	0.016

is mostly thermal), the decay heat problem is not so severe, and Fe1422 is an adequate material.

4.2.1.4 Direct Comparison: MT-9 vs. Fe1422

The steel Fe1422 is proposed as the structural material in the manifolds of Blankets #1, #3, and #4 [4.2,4.4]. The results shown in Section 4.2.1.3 and in Chapter 5, however, indicate that this is a poor choice. Ferritic steel MT-9 was substituted for the Fe1422 in these regions, and an analysis was done to find the impact on both the decay heat and the temperature response (see Chapter 5).

In Figure 4.2.5 the ratio of the decay heat density of the Fe1422 manifold over the MT-9 manifold of Blanket #1 is shown. At shutdown, this ratio is between five and ten, meaning that Fe1422 is producing between five and ten times as much decay heat as MT-9. Initially, the ratio increases with time, as ^{52}V which comes from the VCrTi present in the manifold, and ^{101}Mo which comes from MT-9, two short-lived isotopes that contribute significantly to the decay heat at shutdown, decay. After about 12 hours, however, the dominant isotopes become ^{54}Mn in Fe1422, and ^{54}Mn and ^{99}Mo in MT-9, and the ratio decreases. While there is substantially more ^{54}Mn from Fe1422, after one day, the ^{54}Mn and ^{99}Mo from MT-9 combine to produce almost as much decay heat, and thus the ratio approaches one. It should be noted that at longer times, the ^{99}Mo ($\tau_{\frac{1}{2}}$=66 hours) will decay, and the ratio will increase again, as ^{54}Mn becomes the only significant isotope for both materials. In this case, the decay heat ratio would approach about 2.75.

4.2.2 Breeder Material

There have been a number of lithium compounds that have been considered as potential breeder materials [4.1,4.4,4.13,4.14]. Three different breeder materials were considered in this work: Liquid Lithium, Solid Lithium-Oxide Li_2O, and Liquid

Figure 4.2.5 Ratio of Decay Heat Density vs. Radial Distance for Blanket #1, Fe1422/HT-9 Manifold (A1)/(A2)

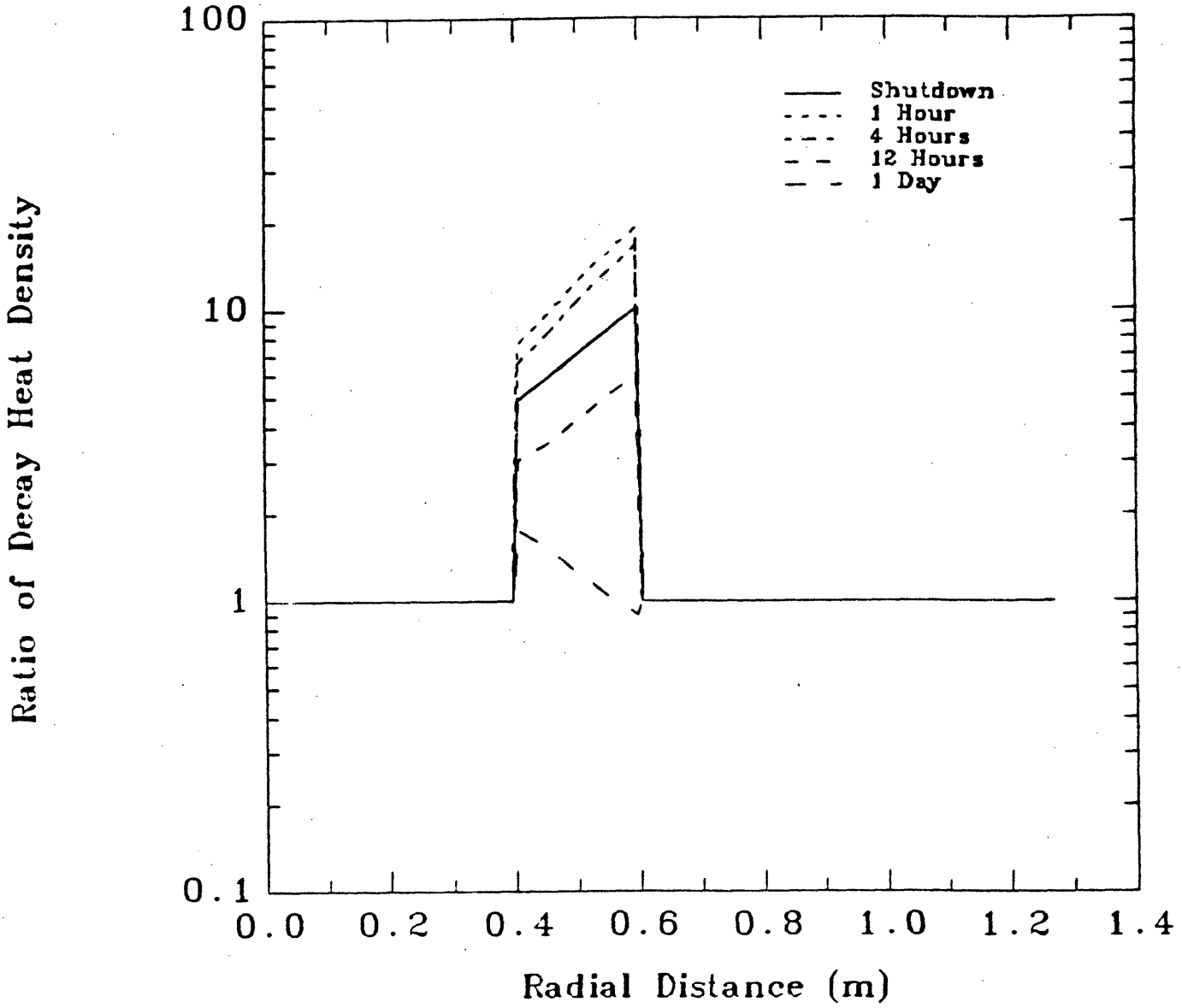

Lithium-Lead, $Li_{17}Pb_{83}$. In general, except for tritium, lithium itself does not produce any troublesome radioactive isotopes that contribute significantly to the overall decay heat in a blanket. Tritium can be a significant factor in the overall decay heat density, depending on the steady state concentration of tritium in the blanket.

For lithium compounds, the compound elements can produce isotopes that contribute significantly to the decay heat density. This is particularly true in the case of lithium-lead, where the lead produces some radioactive isotopes that are a major factor in the decay heat level of lithium-lead blankets.

The three breeder materials considered are analyzed from the standpoint of decay heat in this section. As in Section 4.2.1, some direct comparisons were made.

4.2.2.1 Liquid Lithium

Liquid lithium is used as the breeder material in Blankets #1 and #3. Figures 4.0.1 and 4.0.3, and Figures 4.2.1 and 4.2.6, show the decay heat behavior of these blankets. In particular, the breeder section (Region 5) of Blanket #3 (see Figure 2.3.1) is pure lithium. Table 4.2.5 gives the isotopic breakdown of the decay heat in this region. Compare the total amount of heat produced in two days in this region to that of the first wall regions in Tables 4.2.2 and 4.2.3. It is seen that liquid lithium produces relatively very little decay heat.

It should be noted that in calculating activity levels, REAC treats tritium as it does every other isotope. The code does not account for removal of tritium, but assumes that the tritium continues to accumulate for the duration of the irradiation time, which is the blanket lifetime. Thus, for the data presented in Table 4.2.5, the tritium concentration is reduced by a factor of 2000 from the concentration it would reach if no tritium was removed during normal operation [4.5,4.15]. That is, the activity calculated by REAC for the End-of-Life was reduced by a factor of 2000,

Figure 4.2.6 Decay Heat Fraction by Zone vs. Time for Blanket #3 (E4)
Outboard, 5 MW/m**2, 1 Full Power Year

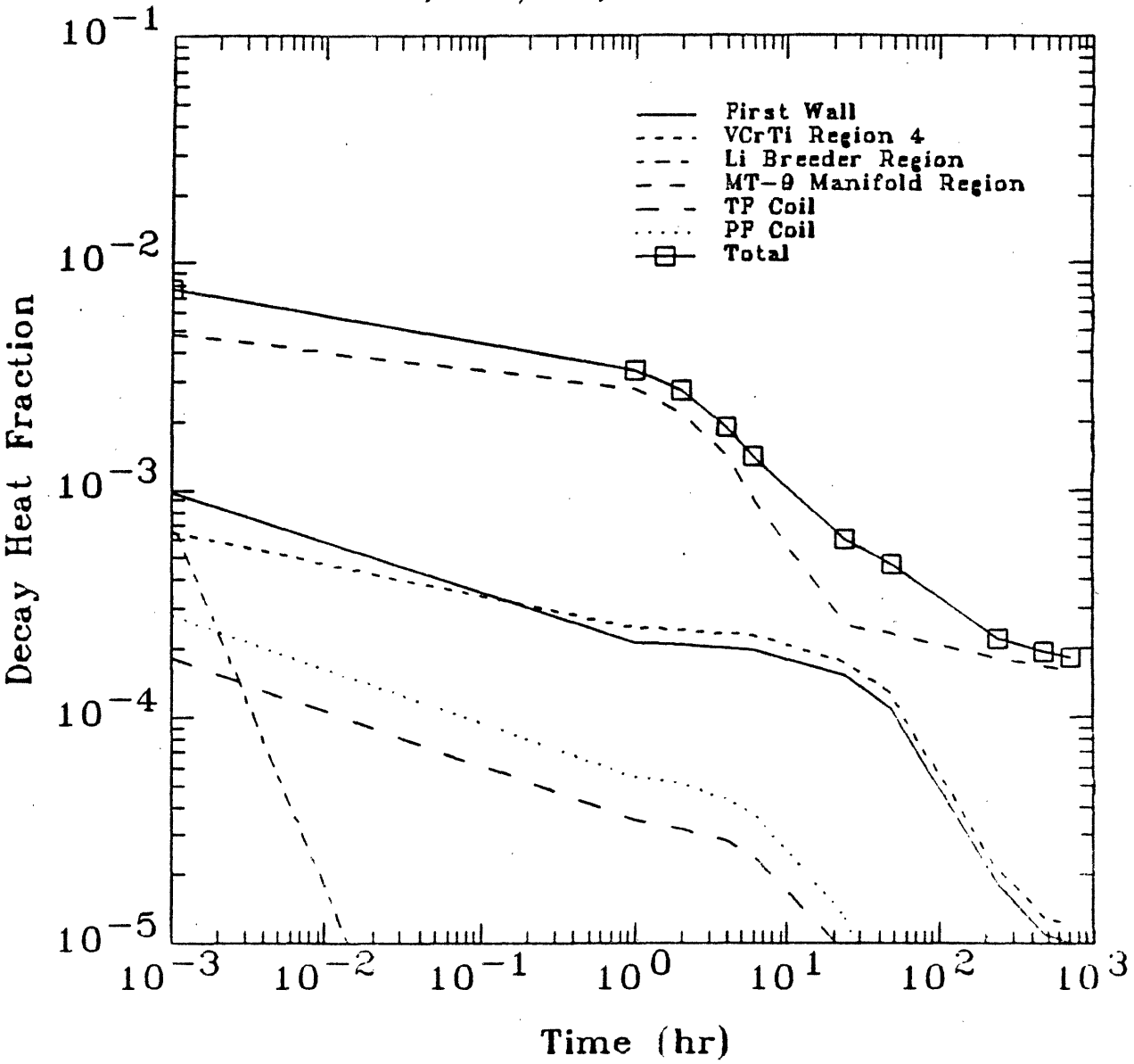

Table 4.2.5 Isotopes contributing to decay heat in liquid lithium breeder region of Blanket #3. Exponential interpolation is used for interior of region.

FRONT OF BREEDER REGION

Isotope	Half-Life	DECAY POWER @ SHUTDOWN beta (W/cm**3)	gamma (W/cm**3)	total (W/cm**3)	Total Heat Produced in 2 Days (J/cm**3)	Percent of 2-Day Total Contributed by Isotope
Na 22	2.60e+00 yr	0.506e-06	0.292e-05	0.343e-05	0.592e+00	32.278
Na 24	1.50e+01 hr	0.795e-06	0.595e-05	0.675e-05	0.469e+00	25.541
Zr 97	1.68e+01 hr	0.218e-05	0.843e-06	0.302e-05	0.227e+00	12.377
H 3	1.26e+01 yr	0.964e-06	0.	0.964e-06	0.166e+00	9.073
Ca 47	4.54e+00 day	0.237e-06	0.738e-06	0.975e-06	0.145e+00	7.916
He 6	8.00e-01 sec	0.450e-01	0.	0.450e-01	0.520e-01	2.832
K 42	1.24e+01 hr	0.516e-06	0.974e-07	0.613e-06	0.368e-01	2.004
Ar 41	1.83e+00 hr	0.571e-06	0.159e-05	0.216e-05	0.205e-01	1.119
Al 28	2.30e+00 min	0.414e-04	0.594e-04	0.101e-03	0.201e-01	1.094
Ar 37	3.50e+01 day	0.	0.109e-06	0.109e-06	0.184e-01	1.003
Mn 56	2.60e+00 hr	0.418e-06	0.846e-06	0.126e-05	0.171e-01	0.930
Cl 38	3.72e+01 min	0.243e-05	0.237e-05	0.480e-05	0.155e-01	0.843
Sc 48	4.37e+01 hr	0.583e-08	0.912e-07	0.970e-07	0.117e-01	0.639
Mn 54	3.13e+02 day	0.376e-09	0.631e-07	0.635e-07	0.109e-01	0.597
Ar 39	2.69e+02 yr	0.364e-07	0.	0.364e-07	0.630e-02	0.343

BACK OF BREEDER REGION

Isotope	Half-Life	DECAY POWER @ SHUTDOWN beta (W/cm**3)	gamma (W/cm**3)	total (W/cm**3)	Total Heat Produced in 2 Days (J/cm**3)	Percent of 2-Day Total Contributed by Isotope
Na 24	1.50e+01 hr	0.668e-06	0.500e-05	0.567e-05	0.394e+00	66.709
H 3	1.26e+01 yr	0.339e-06	0.	0.339e-06	0.586e-01	9.932
Na 22	2.60e+00 yr	0.415e-07	0.239e-06	0.281e-06	0.485e-01	8.215
Zr 97	1.68e+01 hr	0.253e-06	0.978e-07	0.350e-06	0.264e-01	4.466
Ca 47	4.54e+00 day	0.282e-07	0.879e-07	0.116e-06	0.173e-01	2.930
K 42	1.24e+01 hr	0.178e-06	0.336e-07	0.212e-06	0.127e-01	2.150
He 6	8.00e-01 sec	0.614e-02	0.	0.614e-02	0.709e-02	1.201
Ar 37	3.50e+01 day	0.	0.220e-07	0.220e-07	0.373e-02	0.632
Al 28	2.30e+00 min	0.738e-05	0.106e-04	0.180e-04	0.358e-02	0.607
Ar 41	1.83e+00 hr	0.958e-07	0.266e-06	0.362e-06	0.344e-02	0.583
Mn 56	2.60e+00 hr	0.714e-07	0.144e-06	0.216e-06	0.292e-02	0.494
Mn 54	3.13e+02 day	0.861e-10	0.145e-07	0.146e-07	0.251e-02	0.425
Cl 38	3.72e+01 min	0.285e-06	0.278e-06	0.563e-06	0.181e-02	0.307
Sc 48	4.37e+01 hr	0.752e-09	0.118e-07	0.125e-07	0.151e-02	0.256
Ar 39	2.69e+02 yr	0.708e-08	0.	0.708e-08	0.122e-02	0.207

to account for the fact that the tritium is constantly being removed during operation. This is arrived at by dividing the total amount of tritium (kg) that would accumulate if no tritium was removed for the lifetime of the blanket, by the actual steady state inventory (kg) of tritium in the blanket, as given by reference [4.15]. It is seen that tritium contributes about 10% of the total decay heat for the region, and at any rate, it is clear that the true decay heat level from pure liquid lithium is highly dependent on the actual steady-state concentration of tritium.

Note from Figure 4.0.3 that the decay heat density in this pure lithium region is well below that of the neighboring structural regions. At shutdown, the isotope ^{6}He, which has a very short half-life of 0.80 second, contributes over 99% of the decay heat from lithium. This isotope decays to insignificant levels within seconds, and thus the decay heat level at shutdown in the pure lithium region (Region 5) shown in Figure 4.0.3 is deceptive. Note that after only 10 seconds, this level decays by more than two orders of magnitude, and is almost four orders of magnitude less than the decay heat density in the adjacent MT-9 manifold region.

The conclusion is that from a decay heat standpoint, liquid lithium is an excellent choice of breeder material. If the tritium can be be effectively completely removed (i.e., $\geq$ 99% removal), then the amount of decay heat contributed by the lithium will be insignificant, and in the case of a Loss-of-Flow-Accident, the lithium in the blanket will act as a heat sink.

4.2.2.2 Solid Lithium-Oxide Li_2O

The ceramic lithium-oxide is used as the breeder in Blankets #2 and #5. Like liquid lithium, Li_2O produces no potentially troublesome radioactive isotopes except tritium. The fact that the tritium is constantly being removed eliminate it as a significant decay heat producing isotope. Since Li_2O is a solid ceramic, the steady state tritium inventory is a subject of concern [4.4]. The exact tritium inventory is a function of a number of parameters, such as pellet type and size, exact operating

temperature, and purge stream characteristics. Since the tritium concentration is a strong function of temperature, it is possible that, as the temperature rises in the course of the accident, some of the tritium will be driven out of the blanket, causing the concentration to decrease, although this could be offset by an increase in the tritium solubility at higher temperatures [4.16]. A detailed investigation of the exact tritium inventory before and during the accident was considered beyond the scope of this thesis. Thus, the concentration that would be reached if no tritium was removed during operation was reduced by an arbitrarily chosen factor. For Li_2O, this factor was chosen to be 10. According to reference [4.15], this factor should be more like 5000 in the helium-cooled Li_2O blankets, thus the factor of 10 is very conservative.

There are no regions in any of the blankets analyzed that contain pure Li_2O. Regions 5 and 6 of Blankets #2 and #5 contain Li_2O, but in these regions, the large fraction of the total decay heat produced in the first two days is from the MT-9 structure that is also present. Tritium is essentially the only isotope from Li_2O that contributes significantly at all, although ^{16}N, produced from $^{16}O(n,p)^{16}N$ reactions, is present in sufficient quantities to make a contribution at shutdown. The half-life of ^{16}N is very short (7.1 seconds), however, thus ^{16}N contributes very little over a two day period.

Since tritium is the only significant contributor to the decay heat from Li_2O, the overall decay heat in Li_2O blankets will depend on the amount and type of structure (see Section 4.2.1) and the steady-state tritium inventory in the blanket. Given that most of the tritium is removed during operation, the overall Li_2O contribution to the decay heat is small compared to that of the structure, even with the conservative reduction factor. Like liquid lithium, then, Li_2O is an excellent choice of breeder material from the decay heat standpoint.

4.2.2.3 Liquid Lithium-Lead $Li_{17}Pb_{83}$

Liquid lithium-lead is the breeder material in Blanket #4, which is essentially the same as Blanket #1 except for the breeder material. In Blanket #4, the tritium inventory was reduced by a factor of 100, since it is constantly being removed. This factor was chosen arbitrarily and is assumed conservative based on the results presented in Section 4.2.2.1 for liquid lithium.

The isotopic breakdown of the decay heat from the breeder region, Region 4, is shown in Table 4.2.6. Note that two isotopes of lead, ^{203}Pb and ^{209}Pb, are the most significant contributors to the decay heat in this region. Thus, unlike liquid lithium and Li_2O, $Li_{17}Pb_{83}$ does produce isotopes other than tritium that contribute significantly to the decay heat. In fact, note from Table 4.2.6 that because of these lead isotopes, the tritium contribution, while an order of magnitude higher than that of tritium in the breeder region (Region 5) of Blanket #3 (see Table 4.2.5), is only a small fraction of a percent of the total in the breeder region (Region 4) of Blanket #4. Given the conservative reduction factor of 100 that was used for Blanket #4, the indication is that in $Li_{17}Pb_{83}$, tritium is not a significant contributor to the decay heat, because of the high decay heat-producing lead isotopes ^{203}Pb and ^{209}Pb.

The decay heat problem with $Li_{17}Pb_{83}$ is pointed up in Figure 4.2.7, which shows the ratio of decay heat for Blanket #4 over Blanket #1. As was stated, these two blankets are identical except for the breeder material. Note that at shutdown and one hour, the decay heat in Blanket #4, especially in the first wall/breeder regions (where the decay heat is highest), is about a factor of two higher in Blanket #4 than in Blanket #1. This is due to the lead isotopes mentioned above. The decay heat in the shield is slightly lower in Blanket #4, due to greater flux attenuation in $Li_{17}Pb_{83}$.

At longer times, after the lead isotopes decay, it is seen that the ratio plotted in Figure 4.2.7 drops well below one, especially at the back of the breeder region. This is because in the $Li_{17}Pb_{83}$ system, the flux is much more thermalized than

Table 4.2.6 Isotopes contributing to decay heat in liquid lithium-lead/VCrTi breeder region of Blanket #4. Exponential interpolation is used for interior of region.

FRONT OF BREEDER REGION

Isotope	Half-Life	DECAY POWER @ SHUTDOWN beta (W/cm**3)	gamma (W/cm**3)	total (W/cm**3)	Total Heat Produced in 2 Days (J/cm**3)	Percent of 2-Day Total Contributed by Isotope
Sc 48	4.37e+01 hr	0.327E-03	0.511E-02	0.544E-02	0.658E+03	43.655
Pb203	5.20e+01 hr	0.151E-02	0.272E-02	0.423E-02	0.540E+03	35.833
Pb209	3.30e+00 hr	0.912E-02	0.000E+00	0.912E-02	0.156E+03	10.367
Sc 46	8.38e+01 day	0.155E-04	0.284E-03	0.300E-03	0.513E+02	3.405
V 52	3.75e+00 min	0.555E-01	0.746E-01	0.130E+00	0.422E+02	2.801
Cr 51	2.77e+01 day	0.213E-04	0.128E-03	0.149E-03	0.252E+02	1.670
Sc 47	3.35e+00 min	0.773E-04	0.531E-04	0.130E-03	0.185E+02	1.224
Hg203	4.66e+01 day	0.107E-04	0.297E-05	0.137E-04	0.233E+01	0.154
H 3	1.26e+01 yr	0.109E-04	0.000E+00	0.109E-04	0.188E+01	0.125
Ti 51	5.76e+00 min	0.243E-02	0.104E-02	0.347E-02	0.173E+01	0.115
Ca 47	4.54e+00 day	0.273E-05	0.850E-05	0.112E-04	0.167E+01	0.111
Mo 99	6.60e+01 hr	0.874E-05	0.338E-05	0.121E-04	0.165E+01	0.109
Nb 95	3.50e+01 day	0.416E-06	0.800E-05	0.842E-05	0.143E+01	0.095
Na 24	1.50e+01 hr	0.188E-05	0.141E-04	0.160E-04	0.111E+01	0.074
Nb 95*	8.67e+01 hr	0.000E+00	0.483E-05	0.483E-05	0.694E+00	0.046

BACK OF BREEDER REGION

Isotope	Half-Life	DECAY POWER @ SHUTDOWN beta (W/cm**3)	gamma (W/cm**3)	total (W/cm**3)	Total Heat Produced in 2 Days (J/cm**3)	Percent of 2-Day Total Contributed by Isotope
Pb209	3.30e+00 hr	0.338E-02	0.000E+00	0.338E-02	0.580E+02	55.767
V 52	3.75e+00 min	0.215E-01	0.290E-01	0.505E-01	0.164E+02	15.766
Sc 48	4.37e+01 hr	0.627E-05	0.980E-04	0.104E-03	0.126E+02	12.139
Pb203	5.20e+01 hr	0.295E-04	0.533E-04	0.828E-04	0.106E+02	10.168
Cr 51	2.77e+01 day	0.219E-05	0.131E-04	0.153E-04	0.258E+01	2.484
Sc 46	8.38e+01 day	0.331E-06	0.604E-05	0.637E-05	0.109E+01	1.051
H 3	1.26e+01 yr	0.380E-05	0.000E+00	0.380E-05	0.656E+00	0.631
Mo 99	6.60e+01 hr	0.293E-05	0.113E-05	0.407E-05	0.552E+00	0.531
Sc 47	3.35e+00 min	0.154E-05	0.106E-05	0.260E-05	0.368E+00	0.354
P 32	1.43e+01 day	0.756E-06	0.109E-05	0.185E-05	0.304E+00	0.292
Na 24	1.50e+01 hr	0.437E-06	0.328E-05	0.371E-05	0.258E+00	0.248
Nb 95	3.50e+01 day	0.692E-07	0.133E-05	0.140E-05	0.237E+00	0.228
Nb 95*	8.67e+01 hr	0.000E+00	0.805E-06	0.805E-06	0.115E+00	0.111

Figure 4.2.7 Ratio of Decay Heat Density vs. Radial Distance for Blanket #4 / Blanket #1 - (P1)/(A2)

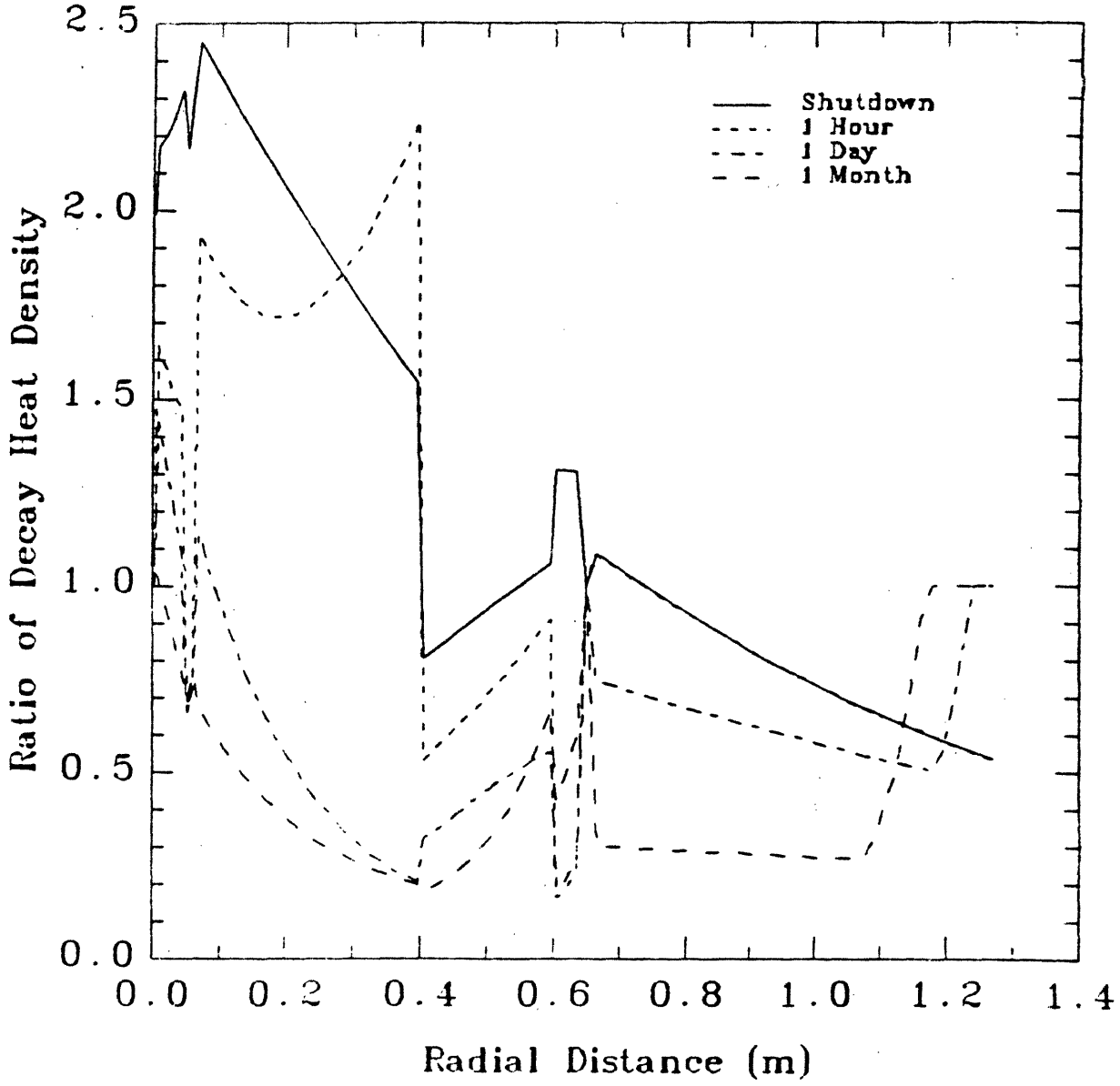

in the liquid lithium system. Longer lived isotopes such as ^{48}Sc, a product of the VCrTi structure, are produced primarily from fast neutron reactions. Thus these isotopes play a greater role in the (harder flux spectrum) liquid lithium blanket, so the decay heat in this blanket is higher at long times. It must be remembered, however, that the overall magnitude of the decay power at these longer times is much lower than at shutdown. The result is that over two days, the total amount of decay heat produced in the $Li_{17}Pb_{83}$ breeder region of Blanket #4 is about 20% higher than that produced in the liquid lithium breeder region of Blanket #1.

From purely a decay heat standpoint, $Li_{17}Pb_{83}$ is the least attractive of the three breeder materials considered in this work. This is because $Li_{17}Pb_{83}$ produces radioactive isotopes of lead which contribute relatively large amounts of decay heat compared to the other breeder materials.

4.2.3 Effect of Beryllium Neutron Multiplier

The use of a neutron multiplier has been considered in a number of blanket studies [4.1,4.4]. Through (n,2n) reactions, the neutron population, and thus the tritium breeding ratio, can be improved. The most attractive candidate for neutron multiplier is beryllium [4.4]. The neutron reaction of interest is $^{9}Be(n,2n)2\alpha$, which has a cross-section on the order of 0.5 barn and a threshold energy of about 2.2 MeV [4.17].

Because the $^{9}Be(n,2n)2\alpha$ reaction is endothermic, and the energy of the incoming neutron must be divided between the two outgoing neutrons, the effect of Be is to increase the less energetic flux. This can have a significant impact on the decay heat production. The isotopes that generally contribute significantly to the decay heat in a blanket can be roughly divided into two groups: those produced by slow neutrons (usually $\frac{1}{v}$ (n,γ) reactions), which will be referred to heretofore as group 1 isotopes; and those produced by fast neutrons (usually (n,p), (n,d), and (n,α) reactions), which will be referred to as group 2 isotopes. The group 1 isotopes

tend to have shorter half-lives than the group 2 isotopes. Thus, group 1 isotopes generally have a higher decay rate (and thus decay power) at shutdown, but they decay more quickly, that is, they "burn hotter for a shorter time." Table 4.2.7 breaks down some of the significant isotopes shown in Table 4.1.1 into groups 1 and 2, and gives their half-lives.

The split between groups 1 and 2 is very clear for VCrTi, with ^{51}Ti being the only exception. For MT-9, the split is much more fuzzy. ^{99}Mo, a group 1 isotope, has a half-life that is short compared to the other isotopes listed, but is not short for the purpose of this work, and ^{56}Mn is produced by fast and slow neutrons. It should be noted that in Fe1422, the slow neutron ^{55}Mn(n,γ)^{56}Mn reaction produces far more ^{56}Mn than the fast neutron ^{56}Fe(n,p)^{56}Mn reaction, and so ^{56}Mn is a valid group 1 isotope for Fe1422.

The point is that the isotopes that are produced, and the subsequent decay heat behavior of the system, are highly dependent on the flux spectrum, and since beryllium alters the spectrum by increasing the slow flux, there can be a significant difference in the decay heat between blankets that use beryllium and those which do not. This effect was analyzed by comparing the decay heat in Blanket #5 with that in Blanket #2. These two blankets are identical except for the presence of beryllium in the first breeder region (Region 5) of Blanket #5.

Figure 4.2.8 plots the ratio of the decay heat in Blanket #5 over the decay heat in Blanket #2. Note that in the breeder region, where the beryllium is located in Blanket #5, the ratio is just about 1.2, and decreases slightly with time. Table 4.2.8 displays the significant isotopes shown in Table 4.2.7 for the MT-9 in this breeder region, along with the decay heat that each isotope produces in two days. The ratio shown is the ratio of the total decay heat produced by the isotope in a two day period in Blanket #5 over Blanket #2. Note that the group 2 isotopes show the least differences (lowest ratios), while the group 1 isotopes show much greater differences (higher ratios). This is because the group 1 isotopes are produced by

Table 4.2.7 Comparison of Group 1 Isotopes vs. Group 2 Isotopes.

VCrTi

Isotope	Group	Primary Reaction	Half-Life
^{48}Sc	2	$^{51}V(n,\alpha)^{48}Sc$	43.7 hr
^{46}Sc	2	$^{47}Ti(n,n'p)^{46}Sc$	83.8 day
^{51}Cr	2	$^{52}Cr(n,2n)^{51}Cr$	27.7 day
^{47}Sc	2	$^{51}V(n,n'\alpha)^{47}Sc$, $^{48}Ti(n,d)^{47}Sc$	3.35 day
^{52}V	1	$^{51}V(n,\gamma)^{52}V$	3.75 min
^{51}Ti	2	$^{51}V(n,p)^{51}Ti$	5.76 min*

MT – 9

Isotope	Group	Primary Reaction	Half-Life
^{54}Mn	2	$^{54}Fe(n,p)^{54}Mn$	313 days
^{56}Mn	1	$^{56}Fe(n,p)^{56}Mn^*$, $^{55}Mn(n,\gamma)^{56}Mn$	2.6 hr
^{58}Co	2	$^{58}Ni(n,p)^{58}Co$	70.8 days
^{99}Mo	1	$^{98}Mo(n,\gamma)^{99}Mo$	66 hr
^{51}Cr	2	$^{52}Cr(n,2n)^{51}Cr$	3.35 days
^{59}Fe	1	$^{58}Fe(n,\gamma)^{59}Fe$	44.5 days*
^{55}Fe	2	$^{56}Fe(n,2n)^{55}Fe$, $^{58}Ni(n,\alpha)^{55}Fe$	2.68 yr

*Exception

Figure 4.2.8 Ratio of Decay Heat Density vs. Radial Distance for Blanket #5 / Blanket #2 - (G1)/(D4)

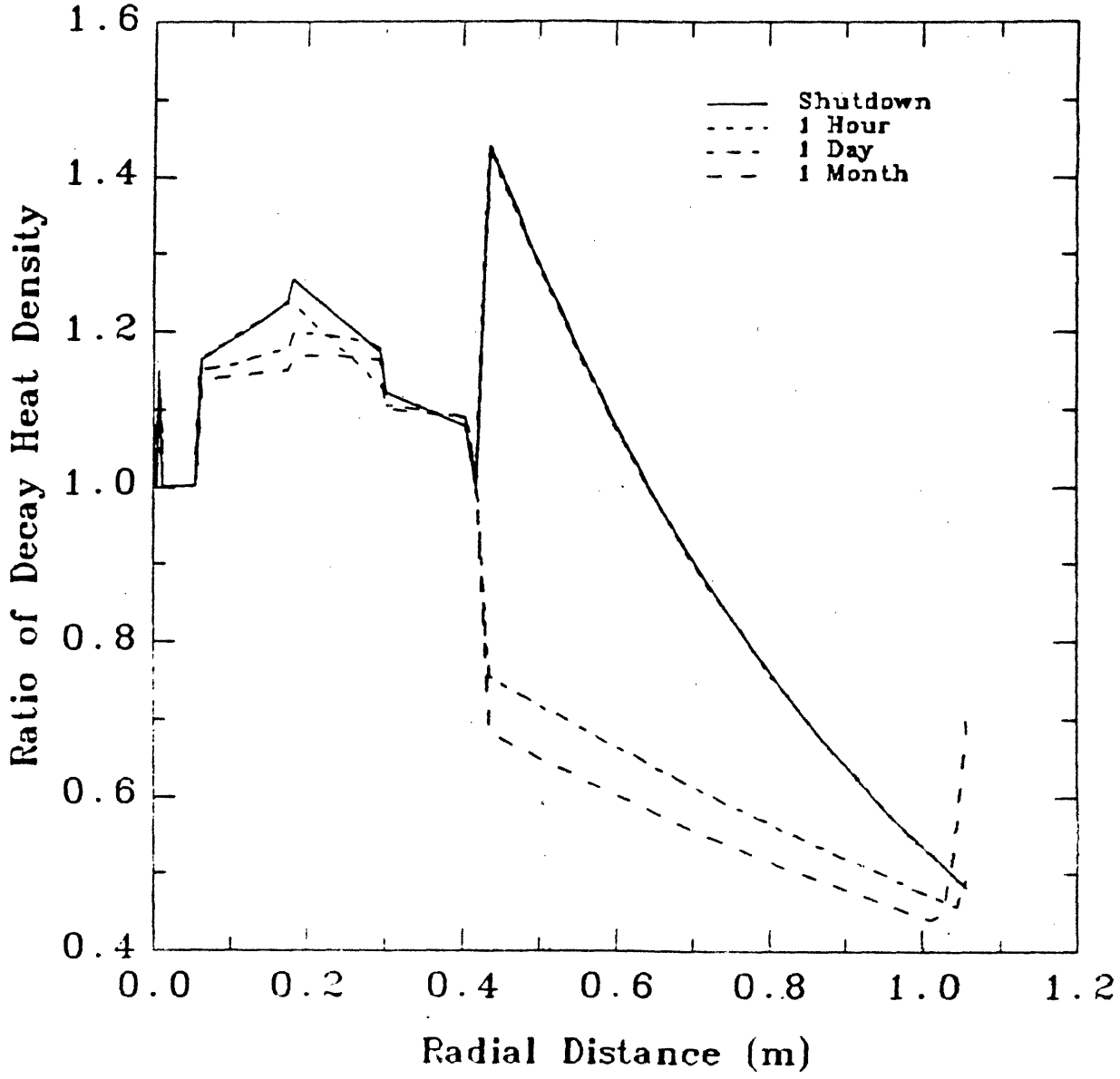

Table 4.2.8 Comparison of Decay Heat Produced in 2 Days by Isotopes in Blanket #5 vs. Blanket #2.

Isotope	Group	Blanket #5 (J/cm^3)	Blanket #2 (J/cm^3)	Ratio
^{54}Mn	2	2.227×10^3	1.966×10^3	1.133
^{56}Mn	1	1.750×10^3	1.491×10^3	1.174
^{58}Co	2	1.548×10^2	1.365×10^2	1.134
^{99}Mo	1	1.573×10^2	1.190×10^2	1.322
^{51}Cr	2	9.240×10^1	8.497×10^1	1.087
^{59}Fe	1	5.420×10^1	1.108×10^0	48.92
^{55}Fe	2	2.789×10^1	2.594×10^1	1.075
Total		4.684×10^3	4.027×10^3	1.163

the thermal flux, which is much higher in the beryllium system (Blanket #5). The group 2 isotopes are produced by the fast flux, which is only slightly higher in the beryllium system (due to the overall increase in the neutron population caused by the beryllium).

Note also in Figure 4.2.8 that the decay heat ratio in the front of the Fe1422 shield is 50% higher in Blanket #5 at shutdown. This again is due to the increase in the thermal flux, which produces a larger amount of ^{56}Mn, a group 1 isotope for Fe1422. Because thermal neutrons are attenuated more quickly (over a shorter distance) than fast neutrons, the mostly thermal flux in the shield of Blanket #5 falls off very sharply. The harder flux spectrum in the shield of Blanket #2 falls off less rapidly, and thus at the back of the shield, the decay heat is higher in Blanket #2.

At longer times, such as one day, after the ^{56}Mn has decayed away, the decay heat in the front of the shield of Blanket #5 is much lower than that of Blanket #2. This is because in this region, the fast flux in Blanket #2 is greater than that of Blanket #5, and so in Blanket #2, there is a greater production of longer-lived group 2 isotopes.

Overall, the total decay heat produced in Blanket #5 over a two day period is about 15% higher than that of Blanket #2. At shorter times, the difference is larger, because of the faster decay rate of the group 1 isotopes. After one hour, the total decay heat produced in Blanket #5 is about 25% greater than that of Blanket #2. This could be a significant difference, and could make a difference between inherent safety and non-inherent safety for this particular design. Other blanket systems might be even more adversely affected by the presence of beryllium. Note from Table 4.2.7 that there is a much greater split between the group 1 and group 2 isotopes in VCrTi than in MT-9. The indication is that for a VCrTi blanket, the inclusion of beryllium would result in a greater difference in the decay heat production. Note from the Fe1422 shield region of Figure 4.2.8 that the difference can indeed be very

large for some materials. The conclusion to be drawn is that the copious use of beryllium to increase tritium breeding ratios and blanket multiplication factors can lead to adverse affects with respect to decay heat, and some care should be taken to ensure that safety is not seriously compromised.

4.3 Effect of Transport of Decay Gamma Rays

In the Section 4.1, it was stated that the energy released when a radioactive isotope decays emerges as heat deposited in the location of the decaying isotope. For β emission decay, this is the case, since the charged β particle will be stopped almost immediately by the surrounding medium [4.18]. For γ emmission, the assumption that decay γ-rays also deposit their energy in the immediate vicinity of the decaying isotope was used for all the decay heat analyses presented thus far. In truth, however, decay γ's will instead transport through the blanket, depositing their energy along the way through pair-production and Compton scattering reactions, until finally, at low energies, the γ-ray is absorbed in the photo-electric effect [4.18,4.19].

Accounting for the transport of decay γ's could have a significant effect on the decay heat profiles presented in Figures 4.0.1 - 4.0.6. To examine this effect, the decay heat in Blanket #1 was calculated with γ-transport included, and the results compared to those obtained with the assumption that the γ's deposit their energy locally (Figure 4.0.1).

The decay heat density with allowance for γ-transport is calculated by making use of the 21 energy-group γ-source distribution which is given in the REAC output. The γ-source distribution is collapsed into 12 groups, and then used as the flux source input to a ONEDANT run. ONEDANT calculates the γ-heating distribution throughout the blanket that results from this γ-source distribution. The γ-heating distribution is added to the β-heating distribution calculated with the method described in Section 4.1. The total represents the true decay heat dis-

tribution, including the transport of decay γ's. Since ONEDANT calculates the γ-heating distribution only for a fixed γ-source, the decay heat calculated in this manner cannot be assumed to decay as $e^{-\lambda_i t}$, as is discussed in Section 4.1. Instead, for each time after shutdown at which a result is desired, the γ-source at that time, as calculated by REAC, must be input to ONEDANT, the resulting γ-heating distribution calculated, and this added to the β-heating distribution calculated for the same time.

The decay heat distribution in Blanket #1 with allowance for γ-transport is plotted in Figure 4.3.1, while Figure 4.3.2 plots the ratio of the decay heat in Blanket #1 with γ-transport over the decay heat with local γ deposition.

It is seen immediately in Figure 4.3.2 that the decay heat calculated with γ-transport is lower in the first wall, higher in the blanket and second wall, and lower in the shield, for the most part. In the manifold, it is higher at shutdown, lower at one hour, and about the same after that.

These results can be explained by noting in Figure 4.3.1 that accounting for γ-transport results in a smoother decay heat distribution. This is because γ-rays produced in high decay heat regions transport out of those regions, and deposit some of their energy in low decay heat regions. Thus, γ-rays produced in the first wall (primarily from ^{52}V) and the manifold region (primarily from ^{52}V, ^{54}Mn, and ^{56}Mn) transport out of their regions of origin and into the breeder region, increasing the decay heat density in the breeder region. Similarly, γ's produced in the shield (from ^{56}Mn and ^{54}Mn, both in large quantities due to the Fe1422 present) transport into the second wall and through into the manifold region, increasing the decay heat in both these regions while decreasing the decay heat in the shield.

After an hour, the ^{52}V has decayed away, and the dominant isotope in the VCrTi structure is ^{48}Sc, which is an even stronger γ-emitter than ^{52}V. Also, in the MT-9 and Fe1422 structure, ^{54}Mn contributes a greater fraction of the total decay heat, due to the faster decay of ^{56}Mn. Essentially all the decay energy emitted

Figure 4.3.1 Decay Heat Density Including Gamma-Transport vs. Radial Distan
for Blanket #1 (A2) Inboard, 5 MW/m**2

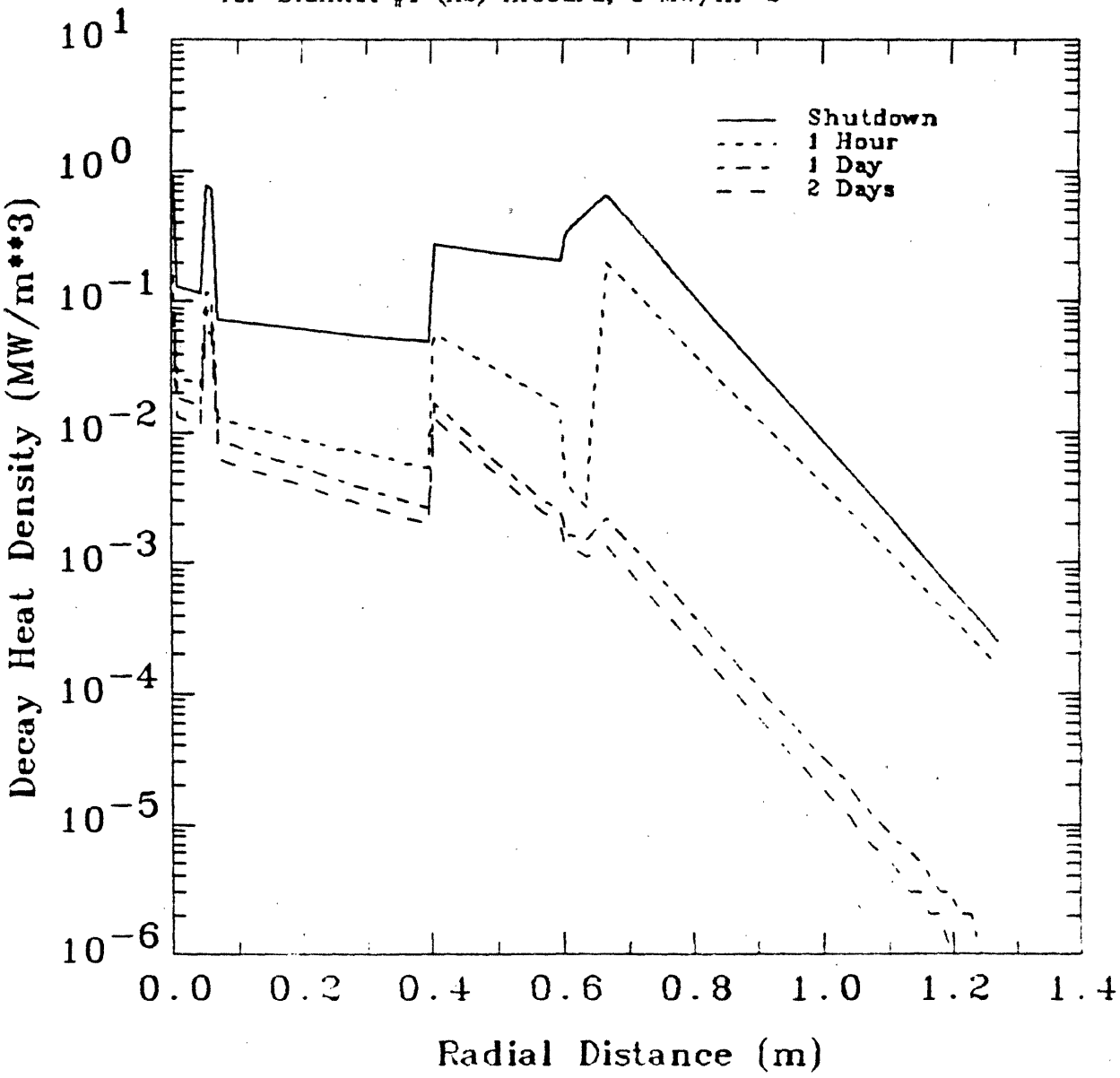

Figure 4.3.2 Ratio of Decay Heat Density vs. Radial Distance for Blanket #1 (A2) Gamma-Transport/Local Deposition

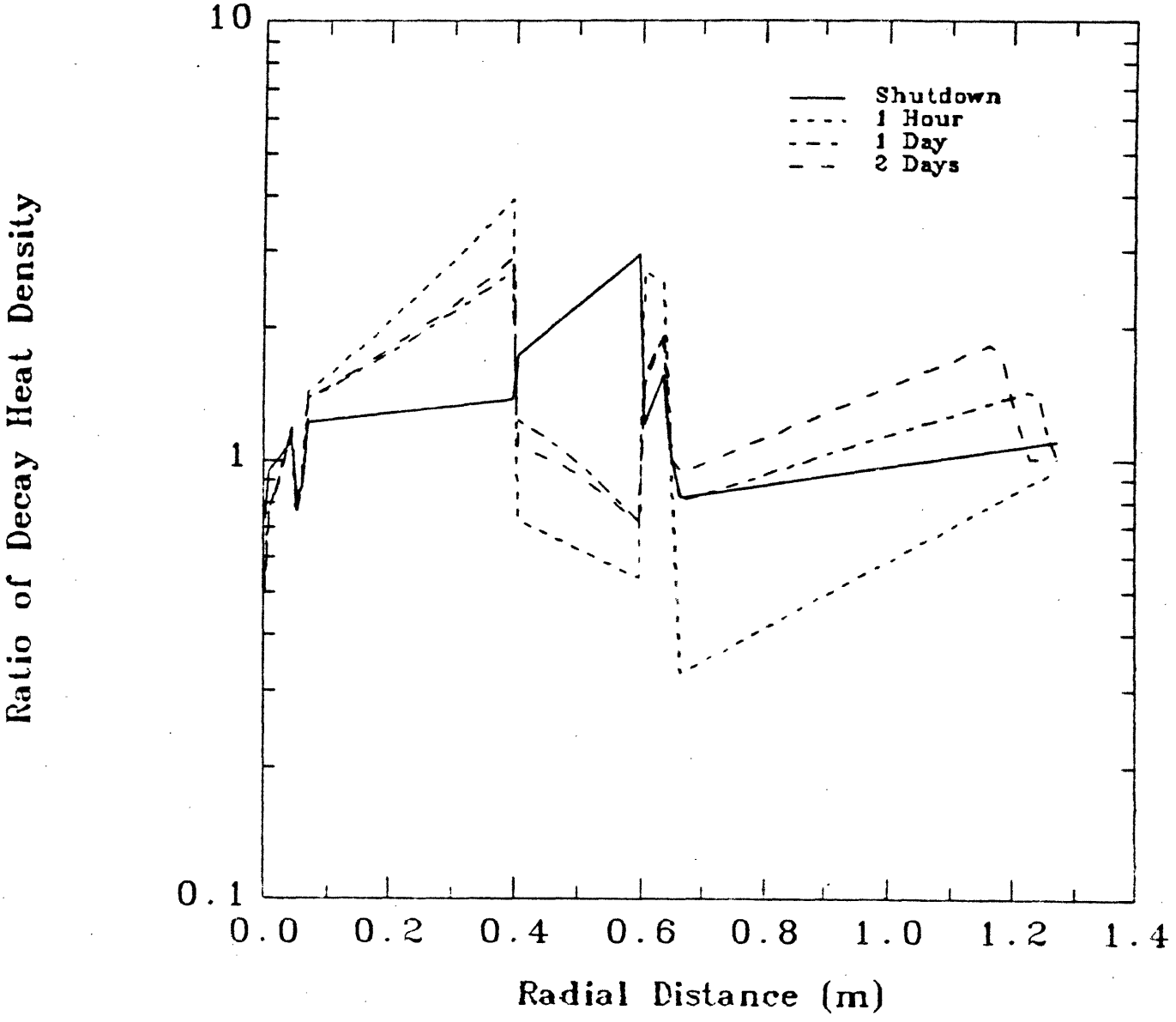

from ^{54}Mn is in the form of γ-rays. The result is that after an hour, the effect seen at shutdown is even more pronounced. The decay heat in the manifold is actually lower with γ-transport than without it, due to the fact that the γ's produced in the manifold region transport out and deposit their heat in other regions. The transport of decay γ's from the manifold into the breeder region results in the large ratio seen in Figure 4.3.2 at the back of the breeder region. At the front of the shield, the ^{54}Mn and ^{56}Mn produce γ's that transport into the second wall, boosting the heating rate in that region. At the same time, the ^{52}V in the second wall, which at shutdown produced γ's that deposited considerable heat in the front of the shield, has decayed away, thus, in the γ-transport case, the heating rate in the front of the shield reduces significantly in one hour. In the local-deposition case, the ^{52}V in the second wall does not affect the decay heat density at the front of the shield, and thus at one hour, the decay heat density at the front of the shield is still fairly high. This is the reason that at one hour, the ratio in Figure 4.3.2 at the front of the shield is small.

At one day and beyond, all the ^{56}Mn, a significant β-emitter, has decayed away, and the remaining dominant isotopes are ^{48}Sc from VCrTi, and ^{54}Mn from MT-9 and Fe1422. Since both these isotopes are almost pure γ-emitters [4.3], the effect is to "smooth out"the decay heat density distribution. Thus, in areas where the local-deposition decay heat (Figure 4.0.1) is low, the ratio will be greater than one (see Figure 4.3.2), and in areas where the local-deposition decay heat is high, the ratio will be less than one. This is seen in Figure 4.3.2.

The primary effect of accounting for the transport of decay γ's is that the decay heat density distribution appears smoother than it does when local deposition of decay γ's is assumed. Assuming local deposition, then, overestimates the decay heat in areas where the decay heat is highest, such as the first wall. The effect is dependent on the materials present, and the particular radioactive isotopes they produce. It should be noted that whether γ-transport is accounted for or not, the *total* decay heat produced is the same, assuming no γ escape out the back of the

shield, and since the decay heat is so low in this region, this is a good assumption. Thus, the effect of accounting for the transport of decay γ's on the temperature response to a LOCA or LOFA is minimal.

4.4 Decay Heat Behavior of D-D Blanket

In Chapter 2, it was mentioned that D-D blanket was chosen to analyze the inherent safety potential of this fuel cycle. In terms of decay heat, the primary difference between the D-T and D-D fuel cycles is in the spectrum of neutrons which emerge from the plasma. While each D-T reaction produces one 14.1 MeV neutron, the catalyzed D-D reactions produce about an equal number of 14.1 MeV and 2.5 MeV neutrons. The reactions involved in catalyzed D-D fusion are shown below.

$$D + D \longrightarrow T\ (1.01\ MeV) + H\ (3.02\ MeV)$$

$$D + D \longrightarrow {}^{3}He\ (0.82\ MeV) + n\ (2.45\ MeV)$$

$$D + T \longrightarrow {}^{4}He\ (3.5\ MeV) + n\ (14.1\ MeV)$$

$$D + {}^{3}He \longrightarrow {}^{4}He\ (3.6\ MeV) + H\ (14.7\ MeV)$$

The net result is that in D-D reactors, only 60% of the energy comes from neutrons, compared to 80% in D-T reactors [4.5]. D-D reactors operate at a much lower plasma power density, and thus neutron wall load, than D-T reactors. This could mean a lower decay-heat density in D-D blankets. However, D-D blankets are often optimized for blanket multiplication (see Table 2.1.1), in order to maximize the output energy for a given size reactor. This means that the D-D blankets often consist mostly of steel (see Figure 2.6.1), which produces more decay heat than the lithium breeder materials used in D-T designs.

The combination of the effects can be seen by comparing Figure 4.4.1 with Figure 4.2.2. Figure 4.4.1 is the decay heat fraction for the D-D Blanket #6.

Figure 4.4.1 Decay Heat Fraction by Zone vs. Time for Blanket #6 (H1)
Inboard, 1.17 MW/m**2 - 3 Full Power Years

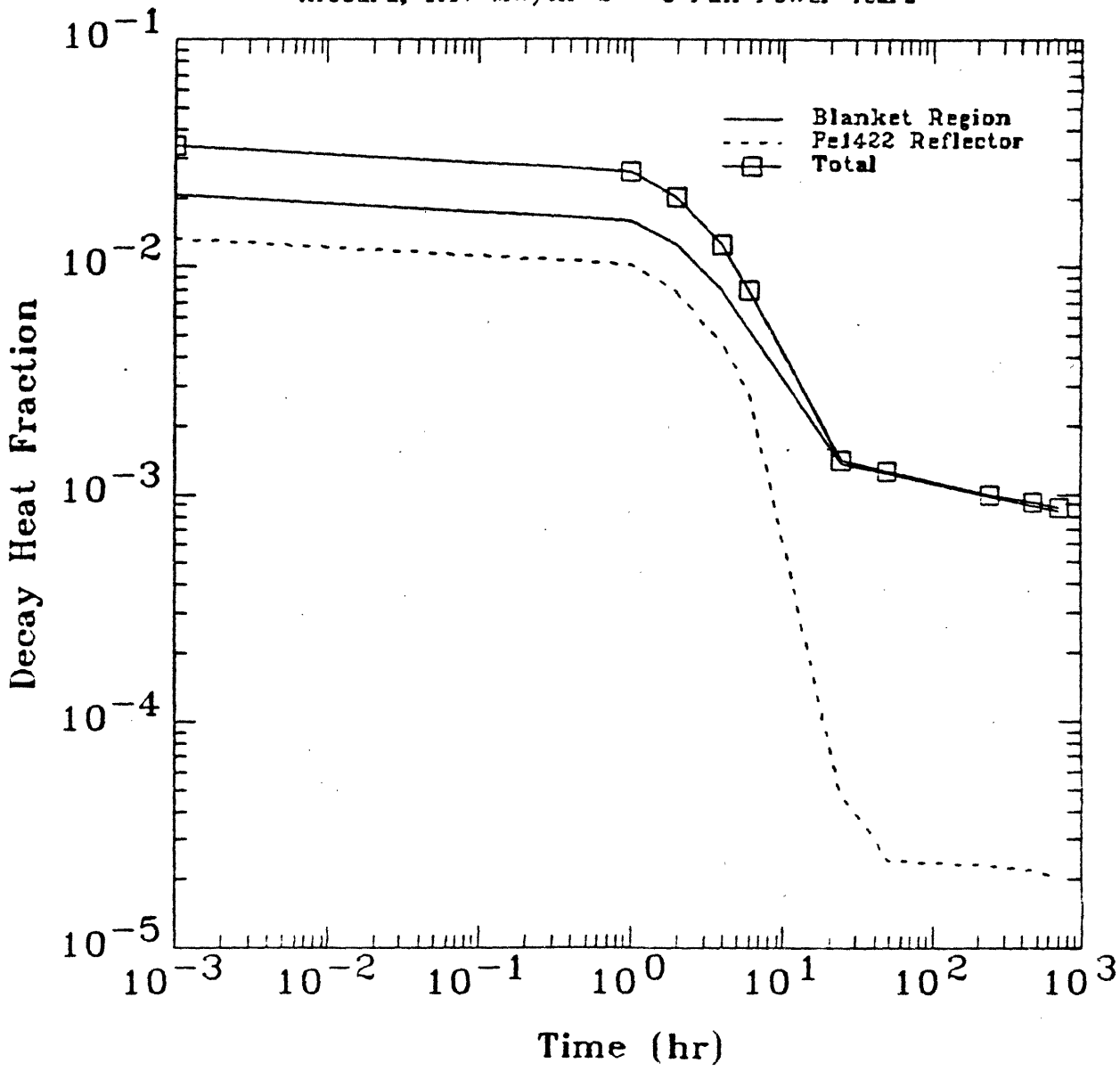

The decay heat fraction from the D-D Blanket #6 is higher, as is the total decay heat, than for Blanket #2, which consists of the same structural material (MT-9). The higher decay heat fraction in the D-D blanket is due primarily to the higher concentration of structural material. In fact, there is almost five times as much structure in the D-D inboard blanket as that of Blanket #2 (see Figures 2.2.1 and 2.6.1). However, it can be seen from Figures 4.2.2 and 4.4.1 that the decay heat fraction in the D-D blanket is only about a factor of two times higher than in Blanket #2. There are two contributing factors to this effect. First, as was mentioned, the fraction of the energy entering the blanket in the form of neutrons is lower in the D-D case. Second, the D-D blanket has a higher blanket energy multiplication factor. Both of these factors work to reduce the decay heat fraction of the D-D blanket (see Appendix C.2). Note that the decay heat from the B_4C and SS304 shield regions of Blanket #6 are not shown in Figure 4.4.1. This is because these regions do not contribute significantly to the decay heat from this blanket.

The conclusion is that, because of opposing effects, the overall decay heat in D-D blankets is very similar to that of D-T blankets. The increased design flexibility of the D-D blanket (e.g., no tritium breeder required) can be utilized to reduce decay heat levels and improve thermal safety by using low activation materials [4.3,4.5]. However, D-D designs which optimize only the energy multiplication (such as Blanket #6) will experience higher decay heat levels, and will therefore suffer a thermal safety penalty.

4.5 Decay Heat Level of Inboard vs. Outboard Blankets

In Chapter 2, it was stated that all of the analyses were performed on the inboard blankets (with the exception of the RFP Blanket #3), since this represents the more conservative case. To demonstrate this, the decay heat densities of the inboard and outboard versions of blanket #1 were calculated and compared.

Due to the geometric effects of toroidal geometry, the neutron flux in the out-

board first wall will be greater than that in the inboard first wall [4.13,4.20]. Thus, the decay heat density in the first wall will be higher on the outboard side. This will hold for the blanket as well; the decay heat density on the outboard side will be higher than the inboard side at the same radial position (i.e., at the same distance from the first wall). In all of the tokamak blankets considered in this work, however, as is the case in most tokamaks [4.1,4.4], the outboard blanket is considerably thicker than the inboard blanket. In particular, in the BCSS blankets considered here, the thickness of the shield is more than 50% greater on the outboard side than on the inboard side. Thus, because of the increased flux attenuation, the decay heat levels at the back of the outboard blanket will be very low compared to the inboard blanket. This will bring the *average* decay heat density (total decay heat over total volume) in the outboard blanket down. It is this average decay heat density that is important when considering the temperature rise due to afterheat during LOCA/LOFA.

To examine this issue, the outboard version of Blanket #1 was analyzed for both decay heat and temperature rise. The results of the decay heat analysis are presented here. Figure 4.5.1 shows the shutdown decay heat levels in the first wall of the inboard and outboard sides. Note that the decay heat density in the structural regions of the first wall is 15% - 20% higher on the outboard side, due to the higher neutron flux.

Figure 4.5.2 gives the shutdown decay heat densities in the entire blanket for the inboard and outboard sides. Note that for the first 40 cm, the two are very close. Actually, the outboard side is slightly higher (about 15%) due to the higher neutron flux. After 40 cm, the geometries of the two sides becomes different, although similar behavior is seen for the manifold and second wall regions (Regions 5 and 6) of each side. After the second wall in the outboard blanket, which is 85 cm from the first wall, there is a large (50 cm) vacuum gap. This accounts for the vertical lines in Figure 4.5.2. The primary difference is seen in the shield regions. While the attenuation of the decay heat in the shield is similar for both sides, note that the

Figure 4.5.1 Decay Heat Density vs. Radial Distance at Shutdown for Blanket #1 (A2) Inboard vs. Outboard, 5 MW/m**3

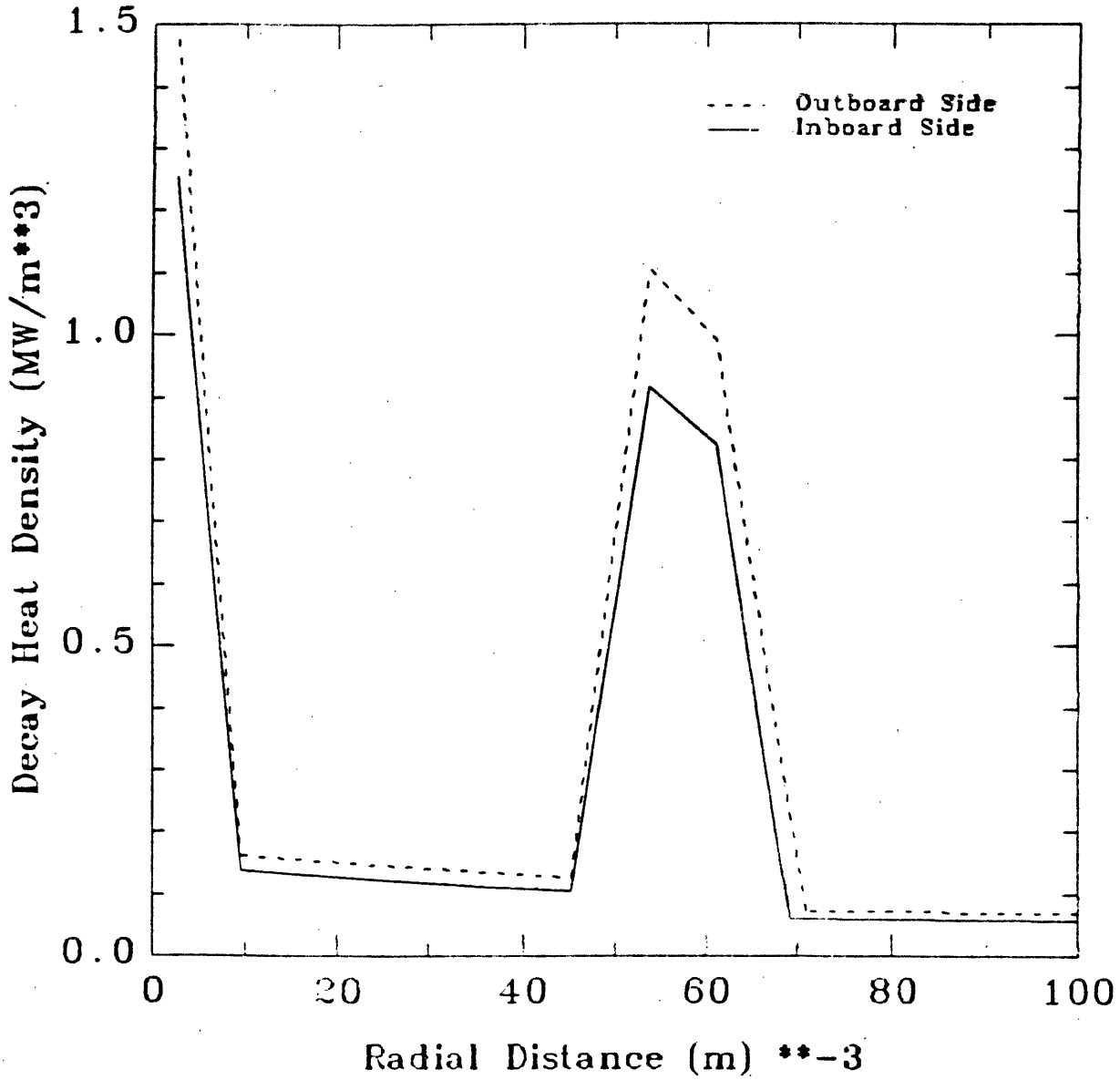

Figure 4.5.2 Decay Heat Density vs. Radial Distance at Shutdown for Blanket #1 (A2) Inboard vs. Outboard, 5 MW/m**3

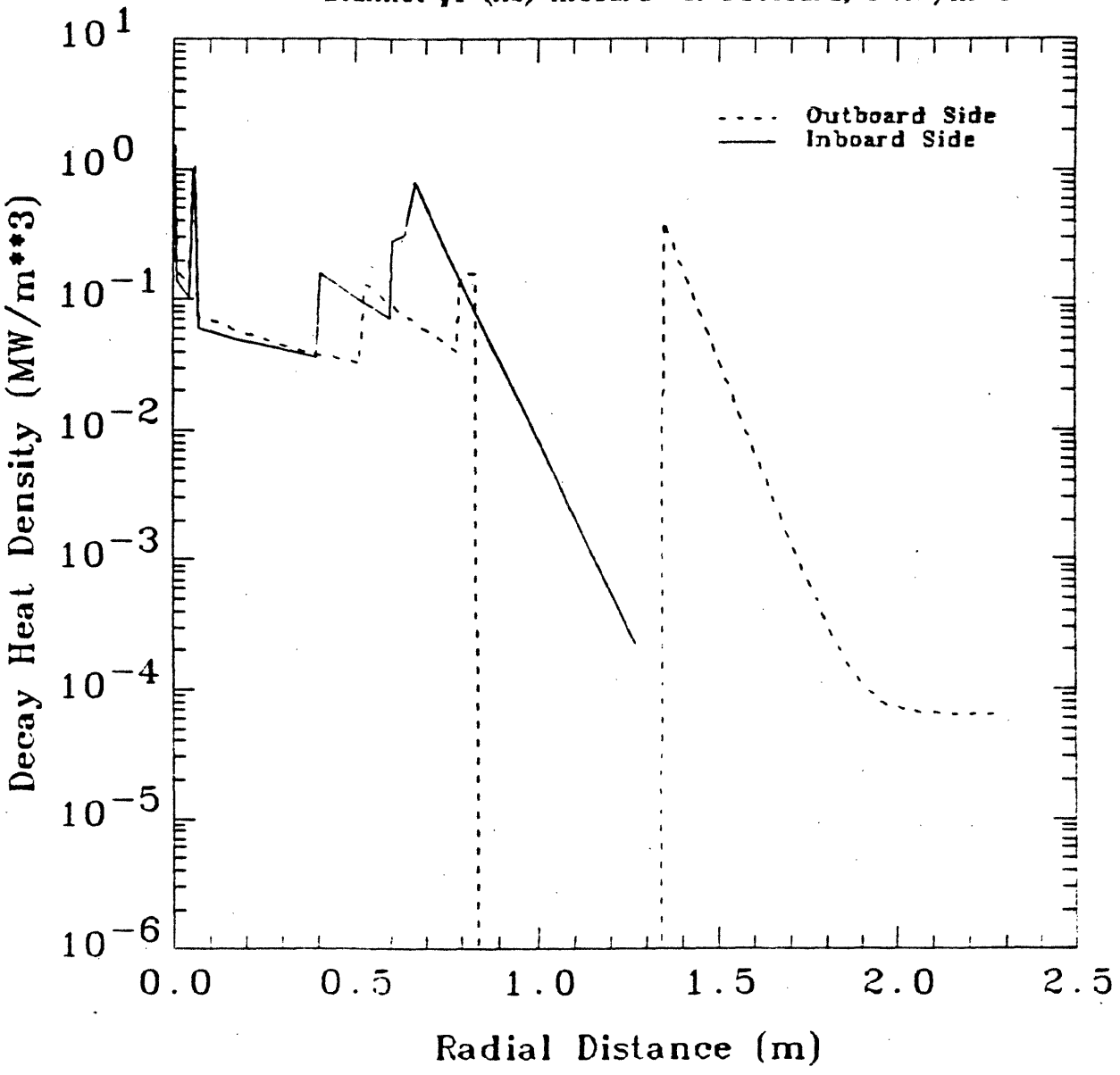

outboard shield has an additional 45 cm where the decay heat level is very low ($< 10^{-4}$ W/cm^3). This causes the *average* decay heat density in the outboard side to be lower than the average in the inboard side. At shutdown, the average decay heat density in the inboard blanket is 0.11 W/m^3. This average in the outboard side is 0.044 W/m^3. Thus, the average is 2.5 times greater in the inboard side, which puts the inboard blanket at greater risk in the event of a thermal transient such as LOCA or LOFA.

4.6 Summary

In both D-T and D-D fusion reactors, the neutrons produced in the plasma enter the first wall/blanket regions, where they interact with the various elements that comprise the blanket. Some of these interactions transform stable isotopes into radioactive isotopes. These radioactive isotopes then decay, and in the process deposit the decay energy in the form of heat. The heat thus produced is referred to as decay heat. For each of the six reference blankets described in Chapter 2, the post-shutdown decay heat density $\dot{q}'''_{decay}(x,t)$ (W/m^3), where x is the distance from the first wall and t is the time after shutdown, was calculated. The calculational tools used include the neutron transport code ONEDANT [4.10] and the activation/transmutation code REAC [4.6].

4.6.1 Structural Material

Due to the mechanism of decay heat production, the amount of decay heat produced is a highly material dependent property. In all of the blankets, it is the structural material which produces almost all of the decay heat. The vanadium alloy V-15Cr-5Ti yields a relatively low level of decay heat density at shutdown. Furthermore, most of this heat is produced by the short-lived isotope ^{52}V, which has a 3.75 minute half-life. This means that the total decay heat level of VCrTi

decays quickly, by as much as an order of magnitude or more in one hour, depending on the neutron flux spectrum. This makes VCrTi an excellent choice of structural material from the decay heat standpoint.

The ferritic alloy MT-9 also produces a fairly low level of decay heat at shutdown. Most of this heat, however, comes from the isotopes ^{54}Mn and ^{56}Mn, which have half-lives of 313 days and 2.6 hours, respectively. This means that the decay heat level of MT-9 will decay more slowly than that of VCrTi, e.g., it will take about 24 hours to decay by an order of magnitude. Beyond one day, however, the total decay heat level of MT-9 is also very low, making MT-9 another good choice of structural material from the decay heat standpoint.

The steel Fe1422 is much less expensive than HT-9 (MT-9), and has been proposed as a substitute for HT-9 for some applications. Unfortunately, the high (14%) manganese content of Fe1422 yields a very high decay heat level at shutdown. Furthermore, due to the relatively long life of the contibuting isotopes, this level decays quite slowly. It takes as long as three months for the decay heat level of Fe1422 to decay by an order of magnitude. For this reason, use of Fe1422 in the blanket is not recommended. In areas where the magnitude of the neutron flux is low and the spectrum is mostly thermal (i.e., the flux is highly attenuated), such as in the magnet shield of a superconducting tokamak, use of Fe1422 is acceptable.

4.6.2 Breeder Material

In the breeder materials, the decay heat level is not as important a factor, since these materials yield lower decay heat levels than the structural materials. In particular, both liquid lithium and the solid ceramic Li_2O yield only tritium as an isotope that could potentially contribute significant amounts of decay heat. Since the tritium that is produced in these breeder materials is constantly being removed, the maximum concentration of tritium in the blanket will be kept quite low, and thus its decay heat contribution will be minimal. The result is that both of these

breeder materials produce essentially no decay heat, and thus from the standpoint of decay heat, both are excellent choices for breeder material. Conversely, the eutectic $Li_{17}Pb_{83}$ yields two isotopes of lead, ^{203}Pb and ^{209}Pb, which contribute significant amounts of decay heat. The level of decay heat produced by $Li_{17}Pb_{83}$ is still lower than that of the structural materials, however, and thus, while LiPb is the least attractive of the three breeder materials considered, it should not present a particular problem in terms of decay heat.

4.6.3 Effect of Neutron Multiplier

Utilization of a neutron multiplier to improve the tritium breeding ratio in fusion blankets has been widely considered. The most attractive candidate neutron multiplier is beryllium. Beryllium increases the magnitude of the overall neutron flux, but especially of the lower energy flux, due to the physics of the multiplication reaction. The altered flux spectrum can have a significant impact on the decay heat level. The isotopes that produce decay heat can in general be divided into those produced by slow neutrons (group 1), and those produced by fast neutrons (group 2). Group 1 isotopes usually have shorter half-lives, thus decay more quickly, producing a higher decay heat level, but for a shorter time, than group 2 isotopes. The increased slow flux in systems which use beryllium results in a decay heat level that is about 25% higher in the first hour, and about 15% higher after one day. This effect is material dependent, but these values, which are specifically for the Li_2O/He/MT-9 system, should be representative.

4.6.4 Effect of Transport of Decay Gammas

One simplifying assumption used in the calculation of the decay heat level in a fusion reactor is that γ-rays emitted by decaying isotopes deposit their energy at the location they are produced. In reality, these γ's will transport through the

blanket and deposit their energy in a smeared fashion across the blanket. Including this effect in the calculation results in a decay heat density profile that is smoother, i.e., has a lower peak-to-average ratio, than when local deposition is assumed. This means that including the γ-transport effect will lower the calculated decay heat in regions where it is highest, and raise it in regions where it is lowest. The total decay heat will be the same in either case, however, and thus the impact on the temperature response to undercooling transients is expected to be minimal.

4.6.5 Decay Heat of the D-D Fuel Cycle

The different neutron spectrum and different neutron-to-thermal power ratio experienced in D-D vs. D-T reactors will have an impact on the decay heat level produced. In a D-D reactor, the neutron spectrum is softer, and a lower fraction of the energy comes from neutrons. This will result in a lower decay heat fraction. However, many D-D blankets are designed to maximize the blanket multiplication factor by using mostly steel. This high concentration of structural material results in a higher decay heat level. These opposing effects will cancel to a certain degree, and the final result will depend on the specific D-D design. It is recommended that the added design flexibility in the D-D reactor be used to minimize the activation level in the blanket, by constructing at least part of the blanket with a low activation material. If this is done, the D-D fuel cycle offers an excellent safety advantage in terms of decay heat.

[4.1] C.C. Baker et al., STARFIRE - A Commercial Tokamak Fusion Power Plant Study, Argonne National Laboratory, ANL/FPP-80-1, September 1980.

[4.2] Report by the Committee on Environmental, Safety and Economic Aspects of Magnetic Fusion Energy, Final Report, U.S. DOE, to be issued, 1987.

[4.3] E.T. Cheng, Radioactivation Characteristics for Deuterium- Tritium Fusion Reactors, Nuclear Technology/Fusion 4, 1983.

[4.4] D.L. Smith et al., Blanket Comparison and Selection Study (BCSS) - Final Report, Argonne National Laboratory, ANL-84-1, September 1984.

[4.5] S.J. Brereton, Safety and Economic Comparison of Fusion Fuel Cycles, Massachusetts Institute of Technology Plasma Fusion Center, PFC/RR-87-7, August 1987.

[4.6] F.M. Mann, Transmutation of Alloys in MFE Facilities as Calculated by REAC (A Computer Code System for Activation and Transmutation), Hanford Engineering Development Laboratory, HEDL-TME-81-37, August 1982.

[4.7] S.J. Piet, M.S. Kazimi, L.M. Lidsky, Potential Consequences of Tokamak Fusion Reactor Accidents: The Materials Impact, Massachusetts Institute of Technology Plasma Fusion Center, PFC/RR-82-19, June 1982.

[4.8] S. Fetter, Radioligical Hazards of Magnetic Fusion Reactors, Lawrence Livermore National Laboratory, LLNL MS#61485F, 1985.

[4.9] E.T. Cheng, J.A. Blink, B.A. Engholm, F.M. Mann, A.M. White, Activation Cross Section Library Comparison Study - Numerical Results, June 1984.

[4.10] R.D. O'Dell et al., User's Manual for ONEDANT: A Code Package for ONE-Dimensional, Diffusion-Accelerated, Neutral- Particle Transport, Los Alamos National Laboratory, LA-9184-M, February 1982.

[4.11] J.E. Massidda, Power Flattening in D-T Tokamak Fusion Reactor Blankets, Master's Thesis, Department of Nuclear Engineering, Massachusetts Institute of Technology, 1985.

[4.12] J.H. Huang and M.E. Sawan, Three-Dimensional Neutronics Analysis for the MARS Blanket, Trans. Amer. Nucl. Soc., 46, pp. 229-231, 1984.

[4.13] M. Abdou, Tritium Breeding in Fusion Reactors, Argonne National Laboratory, ANL/FTP/TM-165, October 1982.

[4.14] D.L. Smith et. al., Fusion Reactor Blanket/Shield Design Study, Argonne National Laboratory, ANL/FPP-79-1, July 1979.

[4.15] D.K. Sze, A.M. Hassanein, S.J. Piet, C.P.C. Wong, W.D. Bjorndahl, An Assessment of Problems Associated With Tritium Containment, Fusion Technology, Vol. 8, pp. 1985-1997, September 1985.

[4.16] D.R. Hanchar, Tritium Permeation Modelling of a Conceptual Fusion Reactor Design, Master's Thesis, Department of Nuclear Engineering, Massachusetts Institute of Technology, 1981.

[4.17] M.D. Goldberg, et. al., Neutron Cross Sections, ENDF-B/V, Brookhaven National Laboratory, BNL-325, (1966).

[4.18] W.E. Meyerhof, Elements of Nuclear Physics, McGraw-Hill, Inc. (1967).

[4.19] A. Foderaro, The Elements of Neutron Interaction Theory, The MIT Press, Cambridge, Massachusetts, (1971).

[4.20] J.V. Foley and J. Jung, A Comparative Multidimensional Nuclear Analysis of Candidate Blanket Designs for Tokamak and Tandem Mirror Reactor Concepts, ANL/FPP MS#49184D, November 1984.

[4.21] G.P. Lasche and J.A. Blink, The Dependence of Neutron Induced Radioactivity in Fusion Reactors on Geometric Design Parameters, UCRL-88212, April 1983.

[4.22] R.A. Krakowski, Parametric Results Using Generomak Model with Emphasis on Power Density Versus Inherent-Safety Tradeoffs, Memorandum to ESECOM, March 1986.

[4.23] G. Hopkins, et. al., Low Activation Fusion Design Studies, GA Technologies, Inc., GA-A17389, October 1984.

[4.24] R.W. Moir, et. al., Fission-Suppressed Hybrid Reactor - The Fusion Breeder, December 1982.

[4.25] D. Steiner and M. Tobias, Cross-Section Sensitivity of Tritium Breeding in a Fusion Reactor Blanket; Effects of Uncertainties of Cross-Sections of ^{6}Li, ^{7}Li, and ^{93}Nb, Nuclear Fusion 14, 1974.

[4.26] J.P. Holdren and S. Fetter, Contribution of Activation Products to Fusion Accident Risk: Part II. Effects of Alternative Materials and Designs, Nuclear Technology/Fusion 4, pp. 599-617, November 1983.

[4.27] D.K. Sze and A. White, Emergency Cooling of MARS, Nuclear Technology/Fusion 4, (2), pp. 775-779, September 1983.

[4.28] D. Steiner, The Neutron Induced Activity and Decay Power of the Niobium Structure of a D-T Fusion Reactor Blanket, ORNL-TM-3094, 1970.

[4.29] W.F. Vogelsang, G.L. Kulcinski, R.G. Loh, and T.Y. Sung, Transmutations, Radioactivity, and Afterheat in a Deuterium-Tritium Tokamak Fusion Reactor, Nuclear Technology, 22, p. 379, 1974.

[4.30] R.W. Conn, T.Y. Sung, and M.A. Abdou, Comparative Study of Radioactivity and Afterheat in Several Fusion Reactor Blanket Designs, Nuclear Technology 26, p. 391, 1975.

[4.31] R.Conn, K. Okula, and A. Johnson, Minimizing Radioactivity and Other Features of Elemental and Isotopic Tailoring of Materials for Fusion Reactors, Nuclear Technology 41, p. 389, 1978.

5. Analysis of Undercooling Transients

The most commonly considered transients which lead to a rise in temperature above the operational level are those which involve a loss-of-system-cooling. A number of different scenarios can lead to loss-of-cooling, including pump failure, flow blockage, loss-of-site power, and coolant tube rupture. These accidents can be divided into two general groups, namely, Loss-of-Flow Accidents (LOFA) and Loss-of-Coolant Accidents (LOCA). In a LOFA, the coolant, which normally is being pumped through the blanket and is thus removing the blanket heat via forced convection, stops flowing. This can arise because the coolant pump fails, or the coolant flow passage becomes blocked by some structural failure. The result is that the coolant remains in the blanket, but is no longer flowing. Thus, the heat being produced in the blanket (whether operational power or decay heat) is no longer being actively removed. This will lead to a temperature rise in the blanket. A LOCA can arise if a coolant tube or other coolant piping ruptures, thus allowing the coolant to leak out of the system. In this case, the coolant will drain out of the blanket, leaving a void in its place. This will obviously cause a termination of active cooling, and a blanket temperature rise.

In this chapter, the temperature response of a blanket to the undercooling transients (i.e., LOFA, LOCA) is analyzed with a simple, one-dimensional model that considers heat conduction and radiation only. The effects of natural convection blanket heat removal are put off for the next chapter. Comparing the temperature

response to these transients of the six blankets allows the identification of aspects of blanket design which assist in minimizing the maximum post-accident temperature. Analyzing the temperature responses with the temperature limit models given in Chapter 3 also allows the definition of operational limits which will insure passive thermal safety.

In the following sections, the physical basis for the model is described, followed by a brief summary of some of the assumptions used both in the development of the model and its applications. Following this, the results of the analysis for the (six) blankets are given, along with the results of an investigation into the sensitivity of the temperature responses to various parameters such as wall emissivity, plasma shut-off time, and neutron wall load.

5.1 Model For Thermal Transport

This section describes the development of the model used to calculate the temperature response to the undercooling transients.

5.1.1 Heat Transport Model

The model for the transport of heat in the blanket starts with the basic assumption that there are no moving fluids to be considered. Thus the appropriate equation for heat transport takes the form:

$$\rho(\mathbf{r})c_p(\mathbf{r},T)\left(\frac{\partial T(\mathbf{r},t)}{\partial t}\right) = \dot{q}'''_{decay} + \nabla\cdot k(\mathbf{r},T)\nabla T(\mathbf{r},t) \qquad (5.1)$$

The first simplification involves the approximation that the blanket geometry resembles that of a slab, with variations only in the x-direction. Thus, equation

(5.1) for a one-dimensional slab becomes:

$$\rho(x)c_p(x,T)\left(\frac{\partial T(x,t)}{\partial t}\right) = \dot{q}'''_{decay} + \left(\frac{\partial}{\partial x}\right)\left(k(x,T)\frac{\partial T(x,t)}{\partial x}\right) \qquad (5.2)$$

The blanket "slab"is broken up into a fine mesh to obtain a numerical solution to equation (5.2). Each mesh point has a temperature T_i, which is assumed constant with respect to x over a small volume Δx_i. Figure 5.1.1 displays this modeling. Equation (5.2) is then integrated over Δx_i, and the resulting equation for T_i(t) becomes:

$$\Delta x_i \rho_i c_{pi}(T)\left(\frac{dT_i}{dt}\right) = \int_{\Delta x_i} \dot{q}'''_{decay}(x,t)dx + \int_{\Delta x_i}\left(\frac{\partial}{\partial x}\right)\left(k_i(T)\left(\frac{\partial T_i(t)}{\partial x}\right)\right)dx$$

$$-\dot{q}''_{rad}(t)|_{x=x+\left(\frac{\Delta x}{2}\right)} - \dot{q}''_{rad}(t)|_{x=x-\left(\frac{\Delta x}{2}\right)} \qquad (5.3)$$

Equation (5.3) is a heat balance for the slab of thickness Δx_i around the mesh point i. This must include the heat flux leaving or entering mesh zone i at the zone boundaries due to radiative heat transfer. This radiation term is:

$$\dot{q}''_{rad} = \sigma\epsilon_{ij}\left(T_i^4 - T_j^4\right) \qquad (5.4)$$

$$\epsilon_{ij} = \left(\left(\frac{1}{\epsilon_i}\right) + \left(\frac{1}{\epsilon_j}\right) - 1\right)^{-1}$$

where σ = Boltzmann's constant

Since $\dot{q}'''_{decay}(x,t)$ can be approximated by a simple exponential function of x (see Section 4.1), it is easy to evaluate this integral in closed analytical form. The

Figure 5.1.1 Schematic of fine mesh approximation for one-dimensional slab geometry.

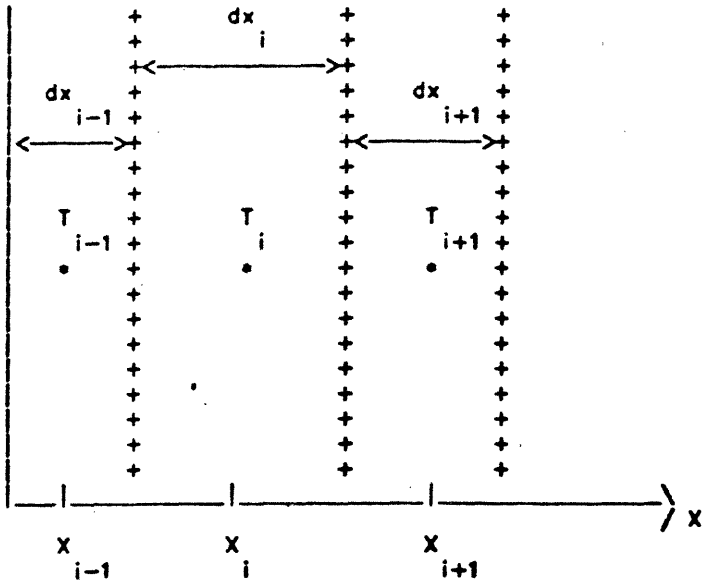

temperature gradient integral, however, involves some approximation to simplify its form. The temperature integral in equation (5.3) can be evaluated as -

$$\int_{\Delta x_i} \left(\frac{\partial}{\partial x}\right)\left(k_i(T)\left(\frac{\partial T_i(t)}{\partial x}\right)\right) dx = k\left(\frac{\partial T}{\partial x}\right)|_{x=x_i+\frac{\Delta x_i}{2}}$$

$$-k\left(\frac{\partial T}{\partial x}\right)|_{x=x_i-\frac{\partial x_i}{2}} \tag{5.5}$$

The value of dT_i/dx at the two zone interfaces can be approximated in finite difference form as $(T_{i+1}-T_i)/(x_{i+1}-x_i)$ and $(T_i-T_{i-1})/(x_i-x_{i-1})$ respectively. The second integral in equation (5.3) thus becomes

$$\int_{\Delta x_i} \left(\frac{\partial}{\partial x}\right)\left(k_i(T)\left(\frac{\partial T_i(t)}{\partial x}\right)\right) dx = k\left(x = x_i + \frac{\Delta x_i}{2}\right)\left(\frac{T_{i+1}-T_i}{x_{i+1}-x_i}\right)$$

$$-k\left(x = x_i - \frac{\Delta x_i}{2}\right)\left(\frac{T_i - T_{i-1}}{x_i - x_{i-1}}\right) \tag{5.6}$$

The problem is to evaluate k at the zone interfaces. This is done by linearly weighting the thermal resistance, i.e., $1/k$, between the two respective zones. Thus,

$$\Delta k_i = k\left(x = x_i + \frac{\Delta x_i}{2}\right) = \left(\frac{\left(\frac{1}{k_i}\right)\left(\frac{\Delta x_i}{2}\right) + \left(\frac{1}{k_{i+1}}\right)\left(\frac{\Delta x_{i+1}}{2}\right)}{\left(\frac{\Delta x_i}{2}\right) + \left(\frac{\Delta x_{i+1}}{2}\right)}\right)^{-1} \tag{5.7}$$

Using this expression, equation (5.3) becomes

$$\Delta x_i \rho_i c_{p_i}(T)\left(\frac{dT_i}{dt}\right) = \int_{\Delta x_i} \dot{q}'''_{decay}(x,t)dx + \Delta k_i\left(\frac{T_{i+1}-T_i}{x_{i+1}-x_i}\right)$$

$$-\Delta k_{i-1}\left(\frac{T_{i-1}-T_i}{x_i-x_{i-1}}\right)+\dot{q}''_{rad}(t)\Big|_{x=x_i-\frac{\Delta x_i}{2}}^{x=x_i+\frac{\Delta x_i}{2}} \tag{5.8}$$

where Δk_i is given in equation (5.7). With some algebraic manipulation, this becomes

$$\left(\frac{dT_i}{dt}\right)=\left(\frac{1}{\Delta x_i\rho_i c_{p_i}(T)}\right)\left[\int_{\Delta x_i}\dot{q}'''_{decay}(x,t)dx+\Delta k_i\left(\frac{T_{i+1}-T_i}{x_{i+1}-x_i}\right)\right.$$

$$\left.-\Delta k_{i-1}\left(\frac{T_i-T_{i-1}}{x_i-x_{i-1}}\right)+\dot{q}''_{rad}(t)\Big|_{x=x_i-\frac{\Delta x_i}{2}}^{x=x_i+\frac{\Delta x_i}{2}}\right] \tag{5.9}$$

There are several ways to solve equation (5.9), including implicit and explicit methods. The details of these solutions are provided in Appendix D. The final form of the equation for T_i, in implicit form, is as follows:

$$T_i^n=T_i^{n-1}+\left(\frac{1}{\Delta x_i\rho_i c_{p_i}(T)}\right)\left[\int_{\Delta t}dt\int_{\Delta x_i}\dot{q}'''_{decay}(x,t)dx+\left(\Delta k_{i-1}\left(\frac{T_{i-1}^n-T_i^n}{x_i-x_{i-1}}\right)\right.\right.$$

$$\left.\left.-\Delta k_i\left(\frac{T_i^n-T_{i+1}^n}{x_{i+1}-x_i}\right).+\sum_j\epsilon_{ij}\sigma\left[(T^n)_j^4-(T^n)_i^4\right]\delta_{ij}\right)\Delta t\right] \tag{5.10}$$

where

$\epsilon_{ij}=\left[\left(\frac{1}{\epsilon_i}\right)+\left(\frac{1}{\epsilon_j}\right)-1\right]^{-1}$,

superscript n refers to the time-step,

Δk_i given in equation (5.7),

$\delta_{ij}=1$ if there is a radiation path between points i and j,

$\delta_{ij} = 0$ if there is no radiation path between points i and j.

5.1.2 Material Property Modeling

All of the parameters in equation (5.10), i.e., x_i, ρ_i, $C_p(T)$, $k_i(T)$, ϵ_i, Δ_{ij} are inputs to the code, which is called THIOD (Transient Heating In One Dimension). The material properties ρ and ϵ are assumed to be constant with temperature. The specific heat and thermal conductivity, c_p and k, are assumed to be linear functions of temperature. The material properties used are given in Appendix C. This representation is assumed valid over the temperature range being observed in this analysis.

For regions which contain more than one material, or in which there may be some vacuum (due to coolant drain), the region is homogenized, and the volumetric heat capacity ρc_p for the region is found by a volumetric average of the materials present. The thermal conductivity for each region is found by weighting the conductivity of each conduction path by its area. This is valid, since the conduction paths within each region of the blankets considered in this work are radial, that is, they are homogeneous in the x direction. Further detail on the calculation of the zone-averaged thermal conductivity is given in Appendix C.

5.1.3 Description of Accidents

As mentioned in the brief discussion at the beginning of this chapter, the undercooling transients considered in this work are divided into two groups, Loss-of-Flow Accidents (LOFA) and Loss-of-Coolant Accidents (LOCA). In this section, the assumptions used to define these accidents are discussed, as well as the variations that were considered. In this discussion, and in the discussion of the results presented later in this chapter, time equals zero refers to the initiation of the accident.

5.1.3.1 Immediate Plasma Shut-Off vs. Continued Plasma Burn

Immediately following accident initiation, that is, the time at which the pump fails or the coolant tube ruptures, there is some question as to how the plasma will behave. There are essentially two scenarios to consider. The first scenario is referred to as immediate plasma shut-off, and the second is referred to as continued plasma burn.

In the case of immediate plasma shut-off, it is assumed that the plasma completely terminates at time equals zero (i.e., at accident initiation). The plasma heat flux to the first wall and the volumetric heating due to neutron interactions in the blanket both go immediately to zero. The only heat source in this case is the decay heat in the blanket, and for this reason, this scenario is referred to with the designation (DC), for Decay Heat only.

In the case of continued plasma burn, there is a question as to how long the plasma will continue to burn, and at what power level. This issue is discussed further in Chapter 7, but for the purposes of the analyses carried out in Chapters 5 and 6, an assumption was used to define the post-accident plasma burn rate vs. time behavior. This assumption was taken directly from the ESECOM [5.2] study. This behavior is shown in Figure 5.1.2. As is seen, the plasma is assumed to burn at full power for one full second, after which it ramps linearly down to zero power after five seconds. The continued plasma burn results in both a heat flux to the first wall and a volumetric heating due to neutron interactions within the blanket. The designation (PL) is used to refer to the continued plasma burn scenario.

In many of the cases analyzed, the continued plasma burn results in a peak first wall temperature being reached within five seconds of accident initiation. After this peak is reached, the temperature begins to decrease immediately. Later it increases again and reaches a second peak due to decay heating. The continued plasma burn impact on the temperature response is discussed in detail in Section 5.4.6.

Figure 5.1.2 Plasma Shutdown Mode After LOFA/LOCA

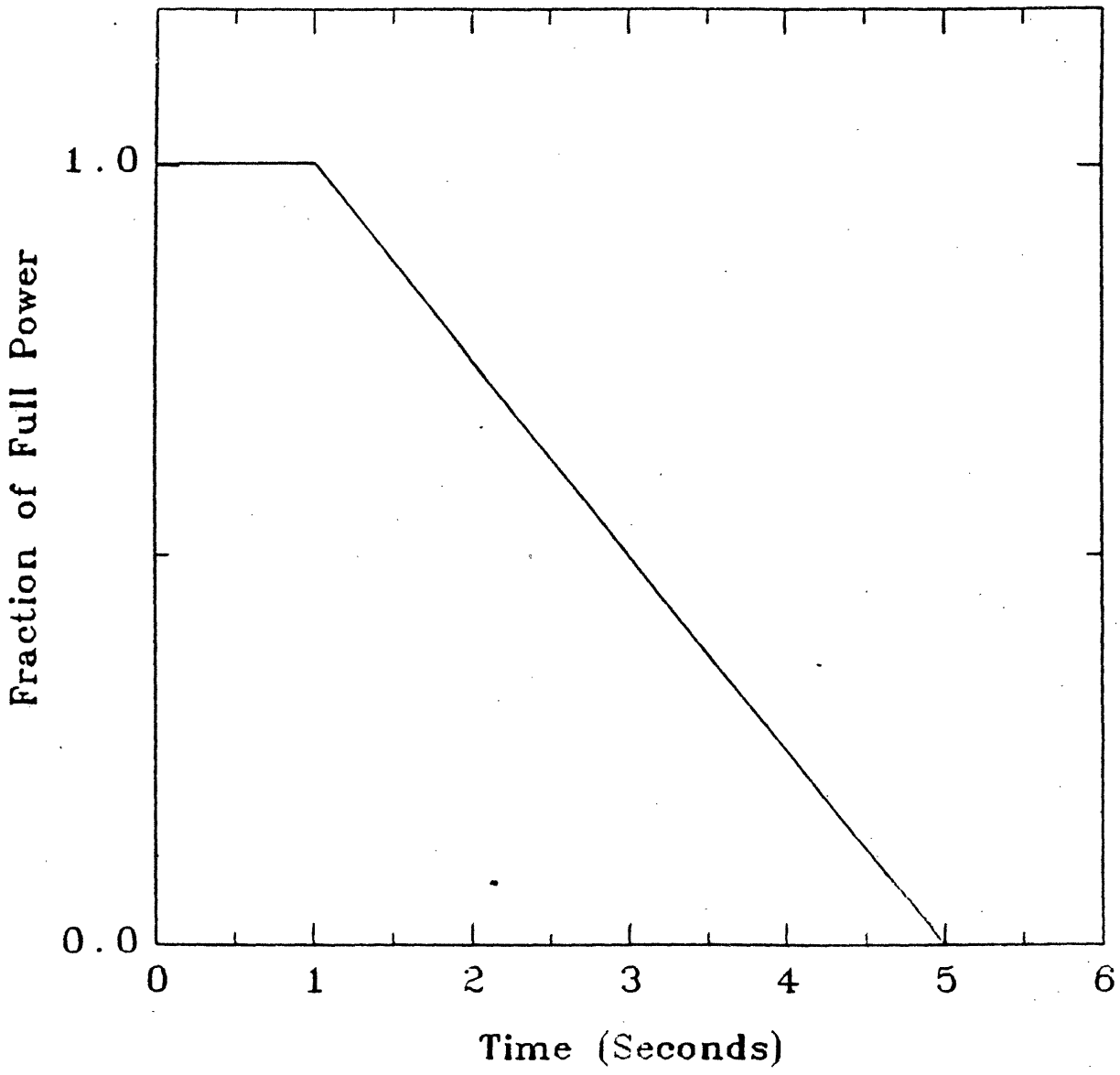

5.1.3.2 LOFA vs. LOCA

The two basic undercooling transients that were considered in this study are: 1) Loss-of-Flow Accident (LOFA), and 2) Loss-of-Coolant Accident (LOCA). For the analysis presented in this chapter, no consideration was given to the transient time in which the flow velocity reduces to zero (LOFA) or the coolant drains from the blanket (LOCA).

In the Loss-of-Flow case, the coolant velocity is assumed to go immediately to zero at accident initiation. The coolant then remains in the blanket as a stagnant liquid which is able to conduct heat as though it was a solid. Precisely speaking, this scenario is better described as a flow blockage than a pump failure, and in any case, this is a conservative approximation to the actual transient. In Chapter 6 pump failure events are described more realistically so that the coolant can still flow and remove heat by natural convection.

In the Loss-of-Coolant case, it is assumed that all of the coolant is lost at accident initiation, leaving a void in its place. Heat can be radiated across the void space left by the coolant loss, but no conduction or convection is assumed, except conduction along radial structural elements. In this scenario, there are no blowdown or time-to-drain effects. Allowing for finite coolant drain time should result in a smaller temperature rise, since the draining coolant would enhance the heat transfer from the first wall to the back of the blanket.

Piet [5.3] calculated the time-to-drain in a LOCA for a number of different scenarios. The results are highly dependent on the blanket module configuration and the location of the pipe or manifold break. In general, however, Piet found that high pressure coolants (such as helium) drain very rapidly ($t_e \leq 0.1$ second), while liquid metal coolants may take several seconds or even minutes to drain, depending on MHD factors. Thus, including time-to-drain effects in the helium cooled blankets (Blankets #2, #5, and #6) would have negligible impact on the LOCA temperature rise.

For the liquid metal cooled blankets (Blankets #1, #3, and #4), this is not the case. The plasma-induced peak temperature reached within the first five seconds would be reduced because of the enhanced heat transfer and increased heat capacity during the coolant drain time. According to Piet, the maximum coolant drain time, including MHD effects, is about 15 minutes. Thus, the decay heat induced peak, which is not reached for a number of hours, probably would not be affected.

5.2 Temperature Response of Blankets

The model described in the Section 5.1 was applied to the six blankets to determine the temperature response of these blankets to the undercooling transients considered (i.e., LOFA and LOCA). The heat source in this analysis includes the decay heat densities which are discussed in detail in Chapter 4, and the plasma and neutron heating rates in the continued plasma burn cases explained above.

The following four sections discuss the temperature response to the base case LOFA and LOCA of Blankets #1, #2, #3, and #6. These four blankets encompass the range of design variations considered in this work. The materials impact within similar designs is discussed in Section 5.4, with the use of Blankets #4 and #5. Blankets #4 and #5 are identical to Blankets #1 and #2, respectively, except for materials differences. The four blankets being discussed here include:

Blanket #1 - Self-cooled liquid metal (Li/Li/V) tokamak.

Blanket #2 - Helium-cooled solid breeder (Li_2O/He/MT-9) tokamak.

Blanket #3 - self-cooled liquid metal (Li/Li/V) Reversed-Field-Pinch, a compact, high power density machine.

Blanket #6 - Helium-cooled (He/MT-9) D-D fuel cycle tokamak.

5.2.1 Base Case Parameters

For all the blankets, one set of parameters is defined as the "base case". The results of the base cases are the basis of comparison for the results obtained when one or more of the parameters is varied from its base case value. For the most part, the values of the base case parameters are those which are given in the references as the operational values for the particular blanket (see Chapter 2, Table 2.0.3). The base case parameters for each blanket are presented in Table 5.2.1. A discussion of the values in Table 5.2.1 follows.

5.2.1.1 Radiative Emissivities

Impurities in the flowing coolant can cause a number of adverse effects, including corrosion and oxidation of structural surfaces which are in contact with the coolant [5.4]. For this reason, it is assumed that all the materials within the blanket will be relatively impurity-free. This means that the structural surfaces inside the blanket will be free of oxides. The radiative emissivity (ϵ) of such "shiny"(non-oxidized) surfaces is usually very low [5.5,5.6,5.7]. Thus, the value selected was ϵ=0.10.

All of the blanket designs considered in this work (see Chapter 2) have vacuum gaps separating the blanket and the shield (or coil), and the shield (or coil) and the heat sink. It is assumed that these surfaces could be exposed to air or other cover gas, which would result in the formation of an oxide layer. This oxide layer will increase the radiative emissivity [5.6,5.7]. The value chosen under this assumption is ϵ=0.50.

5.2.1.2 Heat Sink Availability

The blanket systems considered include only the blanket and shield combina-

Table 5.2.1 Base Case parameters for the undercooling transients of the six blankets.

Blanket	LOFA/ LOCA	Emissivity in Blanket	Emissivity Across Gaps*	Heat Sink Availability	Neutron Wall Load	Continued Plasma Burn**
#1	LOFA	0.10	0.50	100 °C Coil	5 MW/m^2	yes
	LOCA	0.10	0.50	100 °C Coil	5 MW/m^2	no
#2	LOFA	0.10	0.50	100 °C Coil	5 MW/m^2	no
	LOCA	0.10	0.50	100 °C Coil	5 MW/m^2	yes
#3	LOFA	0.10	0.50	20 °C Wall	15 MW/m^2	yes
	LOCA	0.10	0.50	20 °C Wall	15 MW/m^2	no
#4	LOFA	0.10	0.50	100 °C Coil	5 MW/m^2	yes
	LOCA	0.10	0.50	100 °C Coil	5 MW/m^2	no
#5	LOFA	0.10	0.50	100 °C Coil	5 MW/m^2	no
	LOCA	0.10	0.50	100 °C Coil	5 MW/m^2	yes
#6†	LOFA	0.10	0.50	100 °C Coil	1.17 MW/m^2	no
	LOCA	0.10	0.50	100 °C Coil	1.17 MW/m^2	yes

* From back of blanket to shield, and from back of shield to heat sink.
** Continued Plasma Burn behavior is discussed in Section 5.1.3.1.
† D-D blanket.

tion, except in the RFP Blanket #3, where the copper magnet coils are directly behind the blanket. For purposes of defining the boundary condition, it was assumed that behind the shield are the magnet coils, which, because they are cooled separately, do not lose cooling. Thus, the coils essentially represent a constant temperature heat sink, to which the shield can radiate heat. The coil temperature is assumed to remain at 100 °C. This is obviously much higher than the operational superconducting magnet temperature. The assumption is that the cryogenic cooling system will be shut off during the accident, but normal cooling will continue. In the case of the RFP blanket #3, where the coils are included, the heat sink is assumed to be the structure behind the coils, which is assumed to remain at room temperature, i.e., 20 °C.

5.2.1.3 Neutron Wall Load

The base case neutron wall load for each blanket is given in Table 5.2.1. These values are discussed in Chapter 2.

5.2.1.4 Post-Accident Plasma Burn History

The behavior of the plasma after accident initiation is discussed in Section 5.1.3.1. Essentially there are two cases: immediate plasma shut-off, and continued plasma burn. The continued plasma burn history assumed is shown in Figure 5.1.2. The effect of continued plasma burn vs. immediate plasma shut-off is discussed in Section 5.4.6. Additional discussion on the continued plasma burn issue is given in Chapter 7. In the liquid metal cooled blankets, i.e., Blankets #1, #3, and #4, the coolant suffers a substantial pressure drop during operation due to MHD effects, which are a result of the magnetic field [5.4,5.8,5.9]. As is seen in Chapter 6, the flow rate decreases very rapidly after pump failure because of these MHD effects. Thus, it is reasonable to assume in a LOFA that the flow stops at time=0.0, when

the pump fails. The time to reach "zero"flow is very short, and the amount of heat removed by the flowing coolant during this short time is negligible. For this reason, the base case LOFA for the liquid metal cooled blankets includes continued plasma burn. In the helium cooled blanke s (Blankets #2, #5, and #6), there is no MHD pressure drop. The operational flow loop pressure drop is only about 10% of the system pressure, and the time to reach "zero"flow after pump failure will not be as short. The heat removed by the flowing coolant between the time the pump fails and the time the coolant stops flowing can be significant. It is assumed here that this effect will exactly negate the effect of continued plasma burn, with the result being, effectively, that the LOFA is initiated at the same time that the plasma turns off. Thus, the base case LOFA for the helium cooled blankets assumes immediate plasma shut-off.

Conversely, in the LOCA cases, the time to drain for the helium coolant will be very short [5.3], and the heat removed during this short blowdown time will be negligible. Therefore, continued plasma burn represents the base case LOCA for the helium cooled blankets. The liquid metal coolants will have a significant drain time, due in part to the same MHD effects that cause the flow to go to zero so quickly in the LOFA case. This time-to-drain effect of the liquid metal coolants is also assumed to exactly negate the effect of continued plasma burn. Therefore, the base case LOCA for the liquid metal cooled blankets assumes immediate plasma shut-off.

5.2.1.5 Inboard vs. Outboard Blanket

For all of the tokamak blankets (all blankets except Blanket #3), the analysis considered only the inboard side. As is discussed in Section 4.5, due to effects of toroidal geometry, the neutron flux in the first wall and blanket of a tokamak will be slightly higher on the outboard side, depending on the aspect ratio [5.10,5.11]. Thus, it would be expected that the decay heat density in the first wall should be

somewhat higher on the outboard side, making the outboard side the more conservative (higher temperature rise) case. However, in all the tokamaks considered, the outboard blanket is considerably thicker than the inboard blanket. Thus, the decay heat density will be higher at the back of the inboard blanket than at the back of the outboard blanket, due to the increased attenuation from the thicker outboard blanket (see Section 4.5). Note that if high attenuation materials are used in the inboard blanket to further reduce the overall thickness, the decy heat density my become even higher than measured here. Overall, the average decay heat density is higher in the inboard blanket. This is why the inboard blankets were considered in both the decay heat and temperature response analyses. Note that Blanket #3 belongs to a Reversed-Field-Pinch reactor, which has equal blanket thicknesses on both the inboard and outboard sides. Thus, the analysis for Blanket #3 considered the outboard blanket. This issue is discussed further in Section 5.5.

5.2.1.6 Designation of Cases

In the course of this work, a number of variations were made to the input parameters discussed in this section (5.2.1) and in Section 5.1.3. For instance, cases were run for Loss-of-Flow (LOF) vs. Loss-of-Coolant (LOC), continued plasma burn (PL) vs. decay heat only (DC), as well as variations made in the radiative emissivity of various surfaces. To keep track of these cases, a bookkeeping scheme was devised to allow for quick reference to each different case. This scheme is described here.

Each case is referred to by a six-character name, such as A2C1PL. The six characters are broken down as follows: the first two characters designate the blanket and the variation, as discussed in Chapter 2 and displayed in Table 2.0.2.

The third character in the six-character name is always the letter C, and the fourth is a number; these two in combination designate the Case #, as given in Table 5.2.2. As can be seen, there are eight different cases, each one representing a different combination of the parameters discussed in Sections 5.1.3 and 5.2.1, such

Table 5.2.2 Summary of Different Cases Analyzed.

Case #	LOFA/LOCA	Emissivity in Blanket	Emissivity Across Gaps*	Heat Sink Available
C1†	LOFA	0.10	0.50	yes
C2‡	LOCA	0.10	0.50	yes
C3	LOFA	0.10	0.10	yes
C4	LOFA	0.10	0.50	no
C5	LOFA	0.10	0.10	no
C6	LOCA	0.50	0.50	yes
C7	LOCA	0.10	0.50	no
C8	LOCA	0.10	0.10	no

* From back of blanket to shield, and from back of shield to heat sink.
† Base Case LOFA
‡ Base Case LOCA

as LOFA vs. LOCA, high wall emissivity vs. low wall emissivity, etc. The fifth and sixth characters are either PL, which designates continued plasma burn (as discussed in Sections 5.1.3.1, 5.2.1.4, and 5.4.5), or DC, which designates decay heat only (immediate plasma shut-off).

The example given above is A2C1PL. This is broken down as follows. The 'A'represents Blanket #1, and the '2'represents the second variation of Blanket #1, which means the manifold material is MT-9 (see Table 2.0.2). The first variation of Blanket #1 (designated A1) used Fe1422 in the manifold, which is the way the blanket is proposed in the BCSS. In this study, the A2 (MT-9 manifold) blanket is the base Blanket #1 as described in Chapter 2. The 'C1'designates Case 1. From Table 5.2.2, it is seen that this is the base case LOFA. Note that the parameters given in Table 5.2.2 for Case 1 are the same as those given in Table 5.2.1 for the base case LOFA for Blanket #1. Finally, the 'PL'designates the continued plasma burn option, as opposed to the decay heat only option 'DC', as discussed in Sections 5.1.3.1 and 5.2.1.4. Tables 2.0.2 and 5.2.2 should be referred to when distinguishing between the different cases.

5.2.2 Blanket #1, Li/Li/V Tokamak

The design for Blanket #1, the Li/Li/VCrTi tokamak blanket from the BCSS [5.4], is discussed in detail in Section 2.1. The one-dimensional geometry and the decay heat source shown in Figures 2.1.1 and 4.0.1, respectively, are inputs to the code THIOD, which calculates the transient temperature response. The initial temperature distribution for this blanket was taken from the BCSS, and is shown in Appendix C. The other input parameters are discussed in Section 5.2.1. The code was run for the LOFA and LOCA scenarios outlined in Section 5.1.3.

For the LOFA case (designated A2C1PL), Figure 5.2.1 gives the temperature time history for the first wall and the front of the shield for the first 48 hours of the accident. Figure 5.2.2 shows the temperature vs. radial distance profile at

Figure 5.2.1 Temperature History Following LOFA in First Wall and Shield for Blanket #1 (A2C1PL), 5 MW/m2

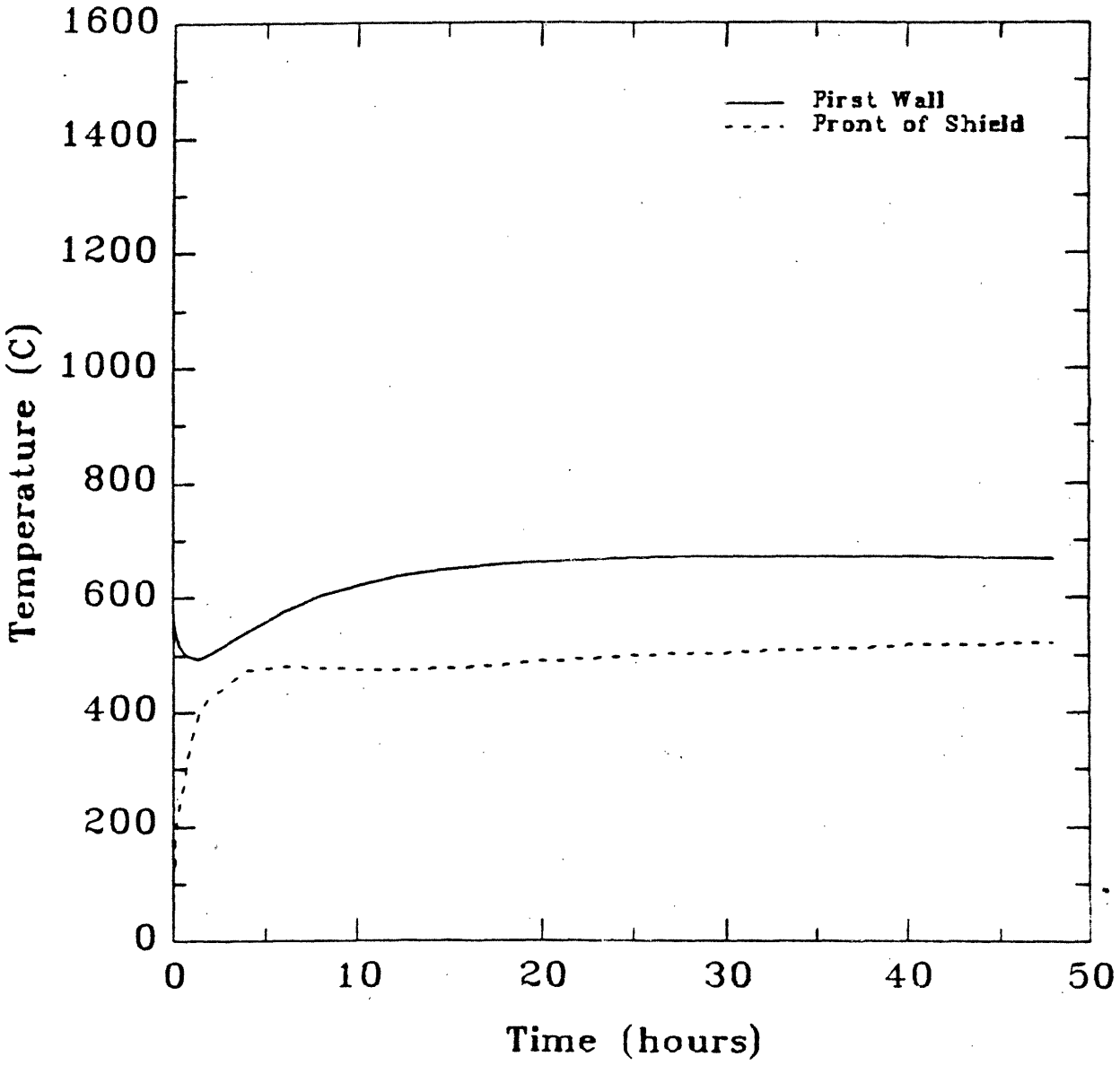

Figure 5.2.2 Spatial Temperature Distribution Following LOFA for Blanket #1 (A2C1PL), 5 MW/m2, at Shutdown, 1 Day, and 2 Days

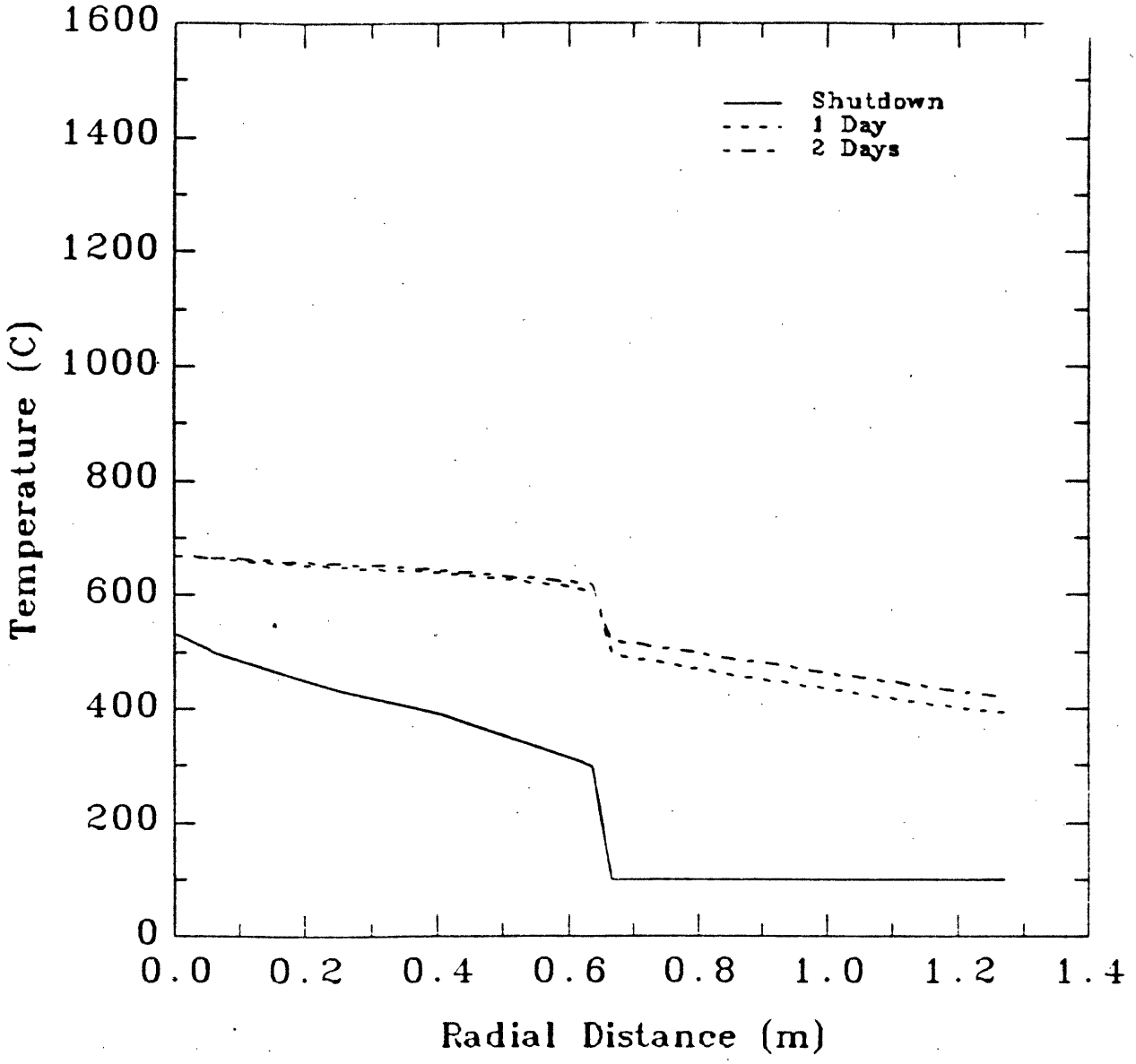

shutdown, one day and two days after accident initiation.

The most important feature to note from Figure 5.2.1 is that the temperature of the first wall does not exceed 700 °C at any time in the first 48 hours. The temperature levels off after about 30 hours, and at the 48 hour mark is actually decreasing slightly. Furthermore, from Figure 5.2.2, it is seen that the first wall is at the hottest temperature of any point in the blanket, as expected, since this region has the highest decay heat density (see Figure 4.0.1) and is farthest from the heat sink. This means that in the event of a LOFA under the base case conditions stated above, the entire blanket will remain well below the short term limits for VCrTi (see Section 3.2.1). Also, according to the information presented in Section 3.2.1 on thermal creep behavior, there should be no problem even if the 700 °C temperature is maintained for a very long time (10^3 hours). Since the temperature is decreasing after 48 hours and will continue to decrease, creep failure is not likely. Table 5.2.3 summarizes the results of the creep-rupture analysis, described in Section 3.2.1, of this scenario. Note that after 48 hours, the rupture fraction is negligible.

Regarding radio-isotope release, the temperature reached in the first wall is just about that which is required to cause oxidation. This is only a problem in an oxygen atmosphere, and since there will be no structural failure, there should be no pathway for oxygen to come in contact with the first wall. Thus, with regard to the base case LOFA, Blanket #1 can be considered to be inherently safe, as no radioactivity mobilization is expected to occur.

The response to the base case LOCA (A2C2DC) is shown in Figure 5.2.3. Note that the temperature of the first wall exceeds 900 °C after about 8 hours, and remains at this level for another 24 hours. This temperature does not pose an immediate threat to the structural integrity of the first wall. After 48 hours, the rupture fraction, given in Table 5.2.3., is only about 1.6e-04. This is based on a constant first wall stress of 10 MPa, which could be an overestimation. According to the extrapolation method used for VCrTi thermal creep behavior, at 1.0 MPa,

Table 5.2.3 Rupture Time/Fraction for Various Cases Analyzed.

Blanket #	Case	Wall Load (MW/m2)	Max Temp(C)	stress (MPa)	rupt time (hours)	rupt fract @ 48 hrs
1	A1C1PL	5.0	1115.6	10.0	>48	2.15e-01
1	A2C1PL	5.0	672.0	10.0	>48	<1.0e-08
1	A2C1PL	10.0	983.6	10.0	>48	4.04e-03
1	A2C1DC	5.0	668.9	10.0	>48	<1.0e-08
1	A2C2DC	5.0	925.1	10.0	>48	1.55e-04
1	A2C2DC	7.5	1116.7	10.0	>48	6.49e-01
1	A2C2DC	5.0	925.1	1.0	>48	1.07e-04
1	A2C2DC	7.5	1116.7	1.0	>48	4.71e-01
1	A2C2PL	5.0	926.9	10.0	>48	1.68e-04
1	A2C2PL	7.5	1118.8	10.0	>48	6.98e-01
1	A2C2PL	10.0	1281.5	10.0	6.090	——
2	D4C1DC	5.0	840.6	120.0	0.480	——
2	D4C1PL	5.0	864.9	120.0	0.003	——
2	D4C2PL	5.0	1001.7	*	>48	1.43e-02
2	D4C2PL	7.5	1142.1	*	0.005	——
2	D4C2DC	5.0	981.9	*	>48	2.61e-03
3	E4C1PL	15.0	1055.1	10.0	>48	7.21e-02
3	E4C1PL	15.0	1055.1	100.0	20.0	——
3	E4C1PL	20.0	1203.3	10.0	8.261	——
3	E4C2DC	5.0	941.2	10.0	>48	1.52e-04
3	E4C2DC	10.0	1154.4	10.0	10.200	——
3	E4C2DC	15.0	1325.4	10.0	1.460	——
3	E4C2DC	15.0	1325.4	1.0	1.560	——
3	E4C2PL	15.0	1776.6	10.0	0.001	——
5	G1C1DC	5.0	850.0	120.0	0.423	——
5	G1C2PL	5.0	1023.8	*	>48	2.24e-02
6	H1C1DC	0.585	573.2	120.0	>48	1.70e-04
6	H1C1DC	1.17	732.4	120.0	6.089	——
6	H1C2PL	1.17	741.5	*	>48	3.42e-06

* First Wall Stress is calculated based on thermal creep rate; see Appendix E.

Figure 5.2.3 Temperature History Following LOCA in First Wall and Shield for Blanket #1 (A2C2DC), 5 MW/m2

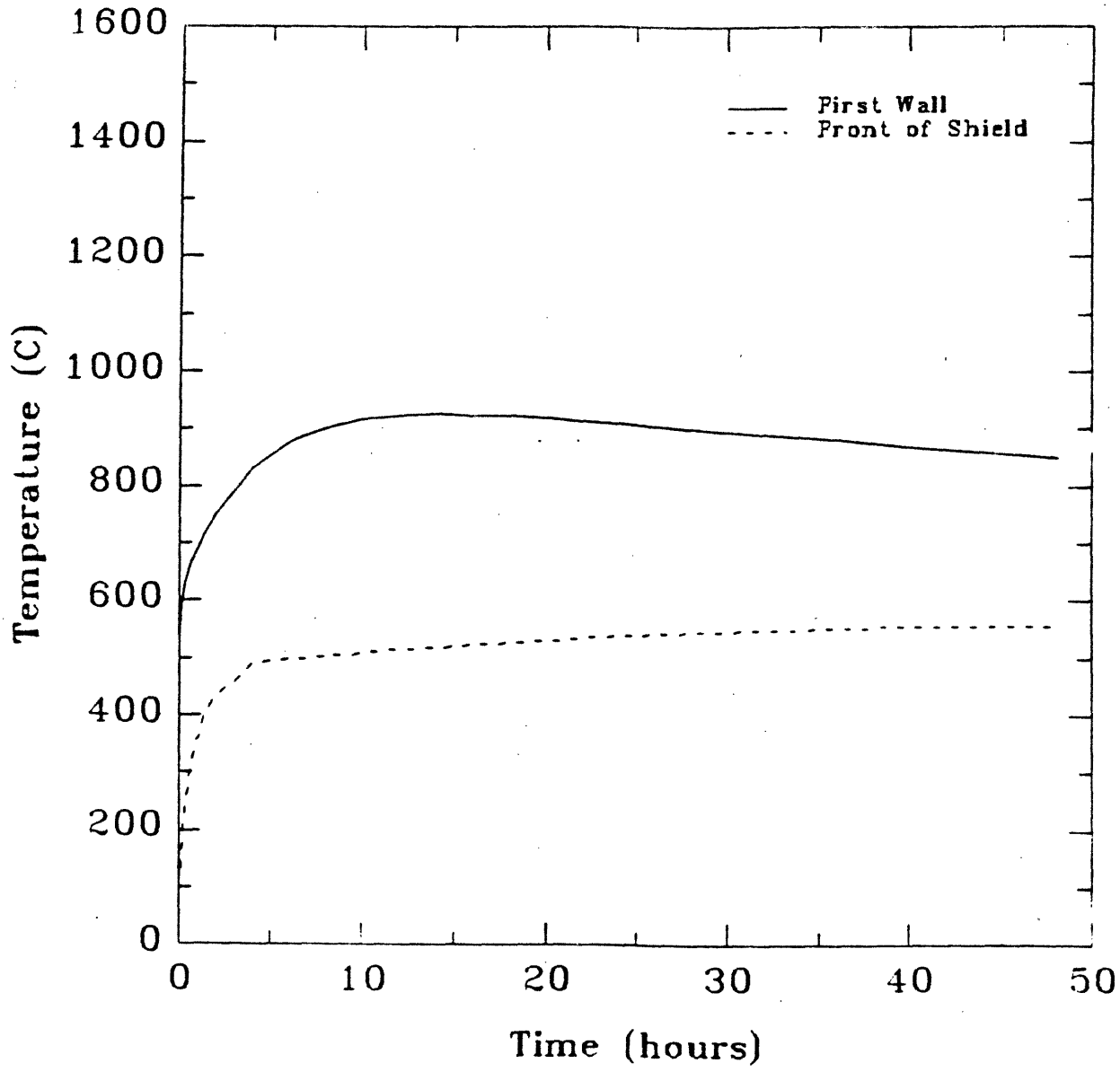

the rupture fraction is about 33% less than that at 10 MPa, or 1.1e-04. This should be in the range of any reasonable safety margin that might be imposed. At higher neutron wall loads, the rupture fraction increases significantly. Note from Table 5.2.3 that at 7.5 MW/m^2, which could be reached due to the poloidal variation of the wall load (i.e., 1.5 peak-to-average ratio - see Section 5.3), the rupture fraction reaches 0.7 after 48 hours. This is dangerously close to rupture, and would exceed the safety margin.

In the event of an oxygen leak into the vacuum chamber, possibly due to structural failure, the result would be disastrous. At 900 °C, vanadium oxidizes quite rapidly, forming liquid V_2O_5 [5.12]. In this case, it can be assumed that the entire first wall would be liquefied, and its possible that a fraction of the radioactive inventory would be mobilized.

If the possibility of an oxygen leak is excluded, then Blanket #1 does have the potential to be inherently safe with regard to the base case LOCA. Given some of the conservative assumptions regarding this transient (see Section 5.1.3.2), the analysis indicates that the first wall would survive, and no replacement or repair would be necessary. There is a reasonable safety margin at the nominal wall load, however, at higher wall loads, even those within the range of the poloidal variation, the temperature response results in conditions close to therml creep rupture.

5.2.3 Blanket #2, Li_2O/He/MT-9 Tokamak

The features of Blanket #2 are discussed in Section 2.2, and the decay heat source is given in Figure 4.0.2. The initial temperature distribution was assumed to be the same as that of Blanket #1. Actually, the operational temperature of Blanket #2 would be lower than that of Blanket #1, due to the more stringent temperature limits on HT-9 vs. VCrTi [5.4,5.13,5.14]. The same temperature distribution was chosen so as not to bias results of the accident analyses in favor of a blanket which operates at a lower temperature.

The response to the base case LOFA (D4C1DC) is given in Figure 5.2.4. The temperature rises steadily due to the decay heat, reaching a maximum of about 840 °C after an hour and a half. Then, because of the heat sink, the temperature decreases to under 700 °C after 48 hours.

This relatively rapid rise to 840 °C may cause serious problems in the MT-9 (HT-9) first wall. As is mentioned in Section 3.2.1.2, the temperature at which HT-9 is assumed to experience acute failure is 900 °C. This figure, however, represents only an educated guess based on an extrapolation of HT-9 strength properties at lower temperatures. It is possible that acute failure occurs at temperatures below 900 °C, in which case the first wall will likely fail after only 1.5 hours.

The thermal creep analysis indicates that creep rupture will occur after only 30 minutes (see Table 5.2.3). This is due to the relatively high pressure stress in the first wall (120 MPa - see Section 3.2.1.2) from the coolant pressure, which is assumed to remain near the operational level. The temperatures reached will not release substantial amounts of radioactivity, but the structural failure will represent a loss of capital investment.

Figure 5.2.5 displays the temperature response to the base case LOCA for Blanket #2 (D4C2PL). The continued plasma burn results in a peak temperature being reached within five seconds. After this, the first wall temperature decreases slightly, as the temperature gradient in the blanket flattens out somewhat. The temperature then rises, due to decay heat, reaching a maximum of 1000 °C in just over an hour. In just less than half an hour, the temperature reaches 900 °C, which is the temperature at which acute failure is assumed to occur in HT-9 (see Section 3.2.1.2).

The rapid temperature rise can be attributed to design of the first wall of this blanket (see Section 2.2, Figure 2.2.1). The first wall consists of a slab of MT-9, which is backed by a region of pure helium coolant (which is not present in the LOCA), followed by another slab of MT-9, and then another region of pure helium

Figure 5.2.4 Temperature History Following LOFA in First Wall and Shield for Blanket #2 (D4C1DC), 5 MW/m2

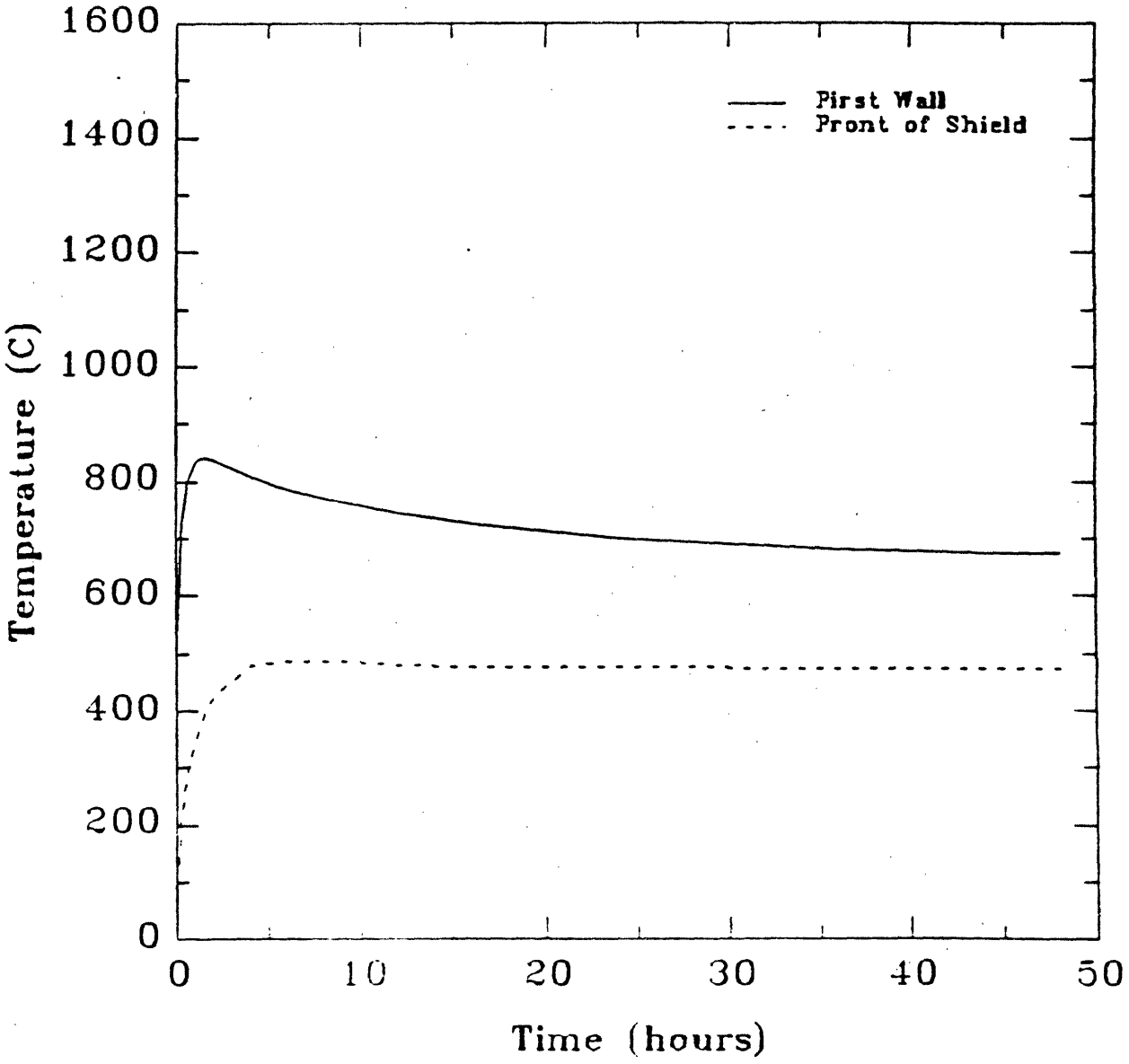

Figure 5.2.5 Temperature History Following LOCA in First Wall and Shield for Blanket #2 (D4C2PL), 5 MW/m2

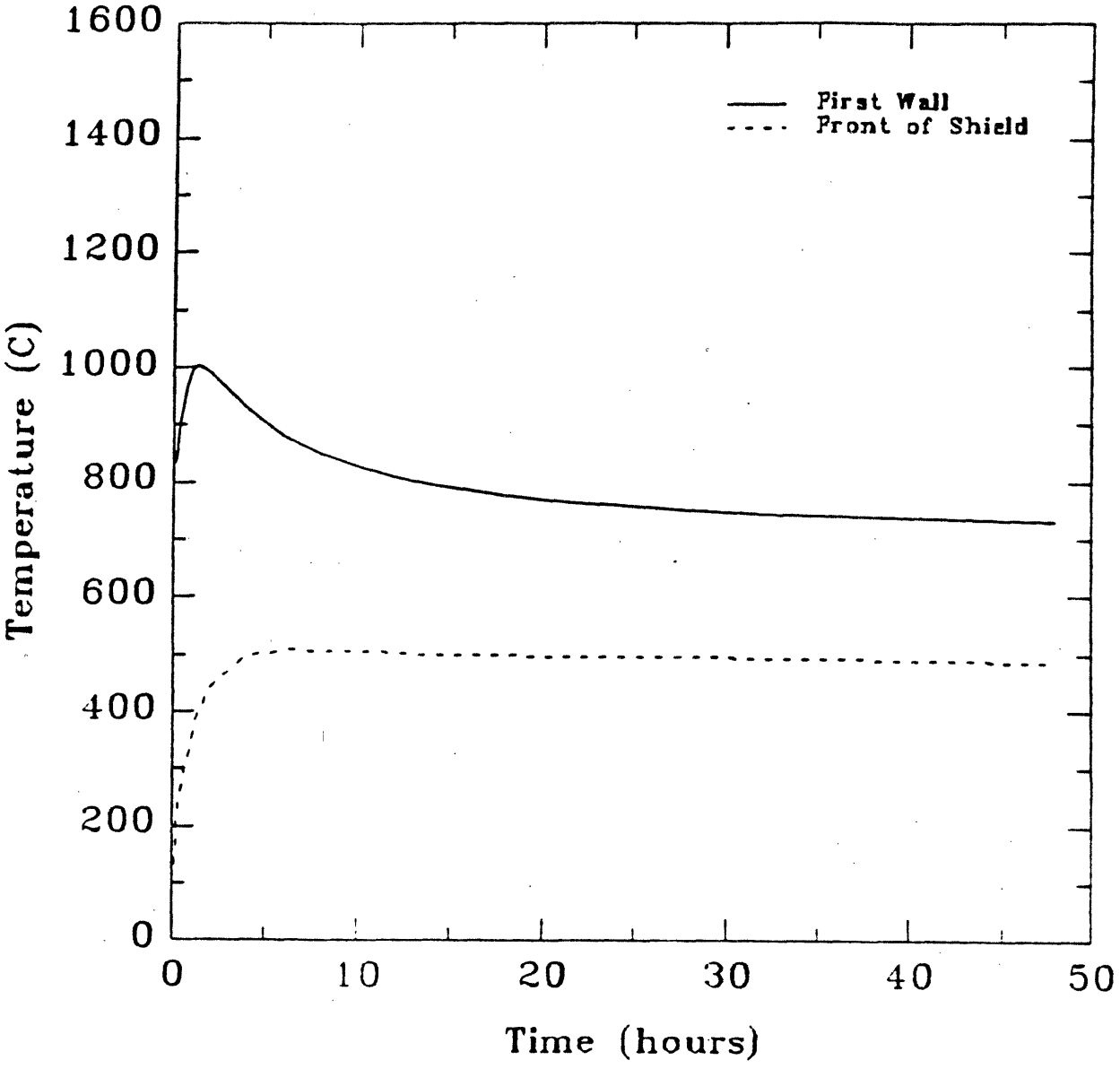

(again, a vacuum in the LOCA). Thus, the only available mechanism for removing heat from this first slab is via radiation to an equally hot second slab, which can only radiate to the bulk of the blanket. Recall that the radiative emissivity of these in-blanket surfaces is assumed to be low (ϵ=0.10, see Section 5.2.1.1 and Table 5.2.1). At these low emissivities, radiative heat transfer between two surfaces is only effective at very high temperatures, and when the temperature difference between the two surfaces is large. Thus, the first wall is essentially insulated until it becomes rather hot, at which time the heat removal rate due to radiation will overtake the decay heat source, and the first wall temperature will begin to decrease. The maximum temperatures that are reached in the early stages of the transient can be sufficient to cause gross structural failure. This could represent a generic problem with helium-cooled designs. The "tubes"that comprise the first wall of Blanket #1 (see Figure 2.1.4) provide a conduction path for removal of heat from the first wall even in a LOCA. The slab first wall design of Blanket #2 (see Figure 2.2.2) provides no such path. If the heat transport properties of helium are inadequate to allow for a tubular first wall design, then it should be recognized that from a safety standpoint, helium-cooled blanket designs are at a disadvantage. Otherwise, the conclusion to be made is that the first wall (of any blanket) should be designed with radial conduction paths that will not be degraded during a LOFA or a LOCA. That is, there should always be a solid structural member connecting the first wall to the remainder of the blanket, to facilitate first wall heat removal in the event that active cooling is lost.

5.2.4 Blanket #3, Li/Li/V RFP

The design of Blanket #3 is given in Figure 2.3.1, and the decay heat source is shown in Figure 4.0.3. This blanket was designed for a Reversed-Field-Pinch (RFP) reactor. For the purposes of this work, the RFP is the same as a tokamak except 1) the inboard and outboard blankets are the same, and 2) the magnets are copper (as opposed to superconducting). Copper magnets do not require the large shield

that superconducting magnets require, thus the overall blanket/shield thickness is less in the RFP. Instead of a steel shield behind the blanket, there are the copper poloidal and toroidal field coils. The initial temperature distribution is assumed to be flat across the blanket, at 600 °C, while the coils are assumed to be at room temperature (20 °C) [5.15].

The temperature response to the base case LOFA (E4C1PL) is given in Figure 5.2.6. The continued plasma burn causes a peak temperature of over 1050 °C in about 3 seconds, which falls off rapidly to 865 °C after 10 seconds. It continues to drop as the plasma-induced gradient flattens out, until after about 30 minutes it begins to rise again. The temperature reaches a second peak of 1050 °C after about 12 hours. It is unlikely that these temperatures will cause acute structural failure in the VCrTi first wall. The thermal creep analysis, as shown in Table 5.2.3, for the nominal 15 MW/m^2 wall load indicates that creep induced first wall structural failure will not occur within 48 hours. The rupture fraction at this time is about 0.07, which is small but significant. This significant value of the rupture fraction indicates that just a small increase in the temperature could lead to structural failure. Note in Table 5.2.4 that at 20 MW/m^2, which is in the range of the poloidal variation, the first wall will fail due to thermal creep after about 8 hours. Any oxygen that might leak into the system would severely aggravate the problem, due to oxidation.

The temperature response of Blanket #3 to the base case LOCA (E4C2DC) is shown in Figure 5.2.7. Assuming immediate plasma shut-off in this case (see Section 5.2.1.4) eliminates the first temperature peak seen for the LOFA in Figure 5.2.6. However, in the LOFA case, the stagnant liquid lithium acts as both a heat sink and a heat transfer medium. The lack of this liquid lithium in the LOCA case results in fairly rapid temperature rise in the first wall. The temperature reaches 1200 °C in less than an hour, at which time the first wall is assumed to suffer acute failure. Thermal creep analysis indicates creep rupture in about 1.5 hours. In the event of oxidation, these temperatures are high enough to result in significant mobilization

Figure 5.2.6 Temperature History Following LOFA in First Wall and Coil for Blanket #3 (B4C1PL), 15 MW/m2

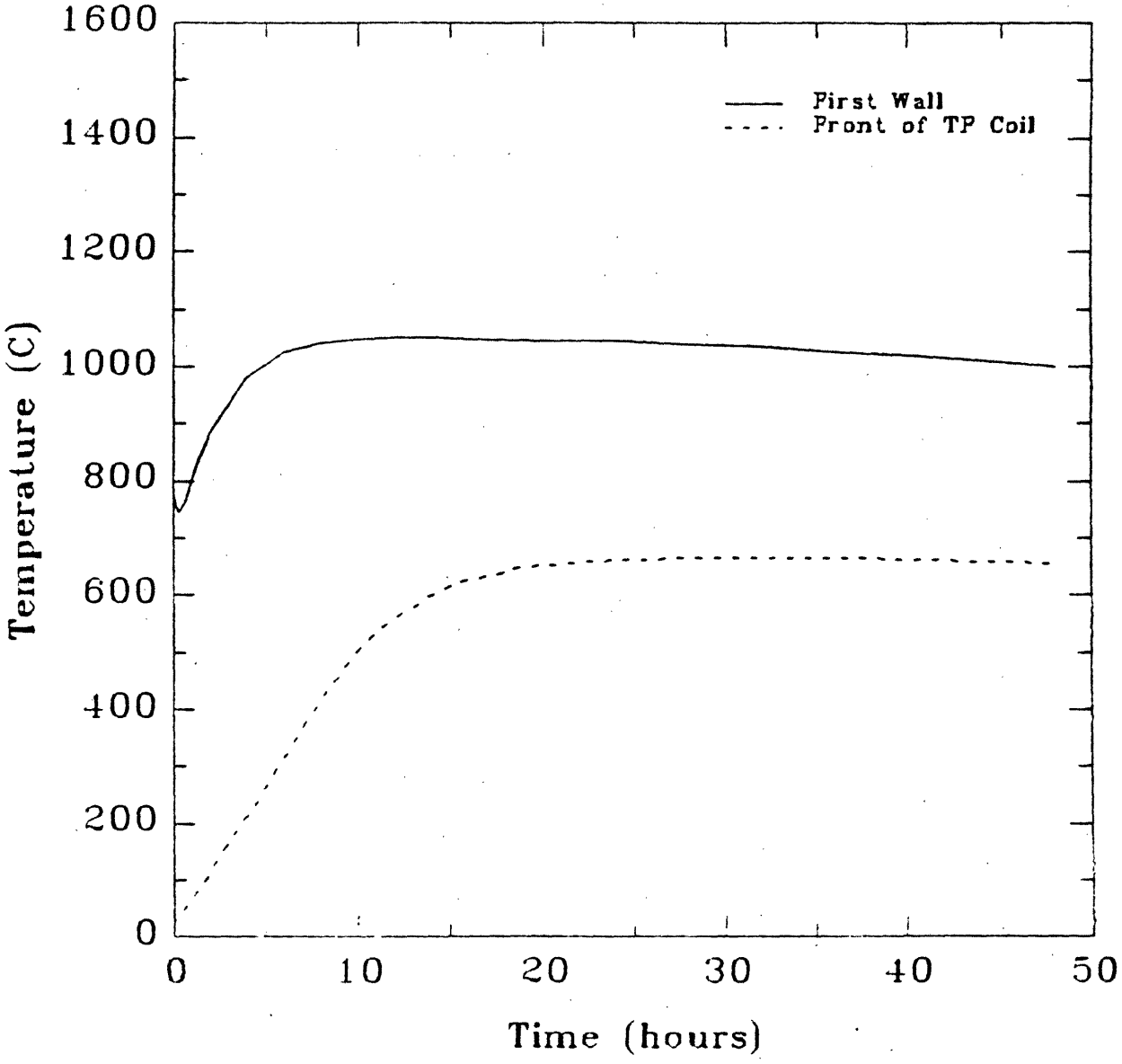

Figure 5.2.7 Temperature History Following LOCA in First Wall and Coil for Blanket #3 (E4C2DC), 15 MW/m2

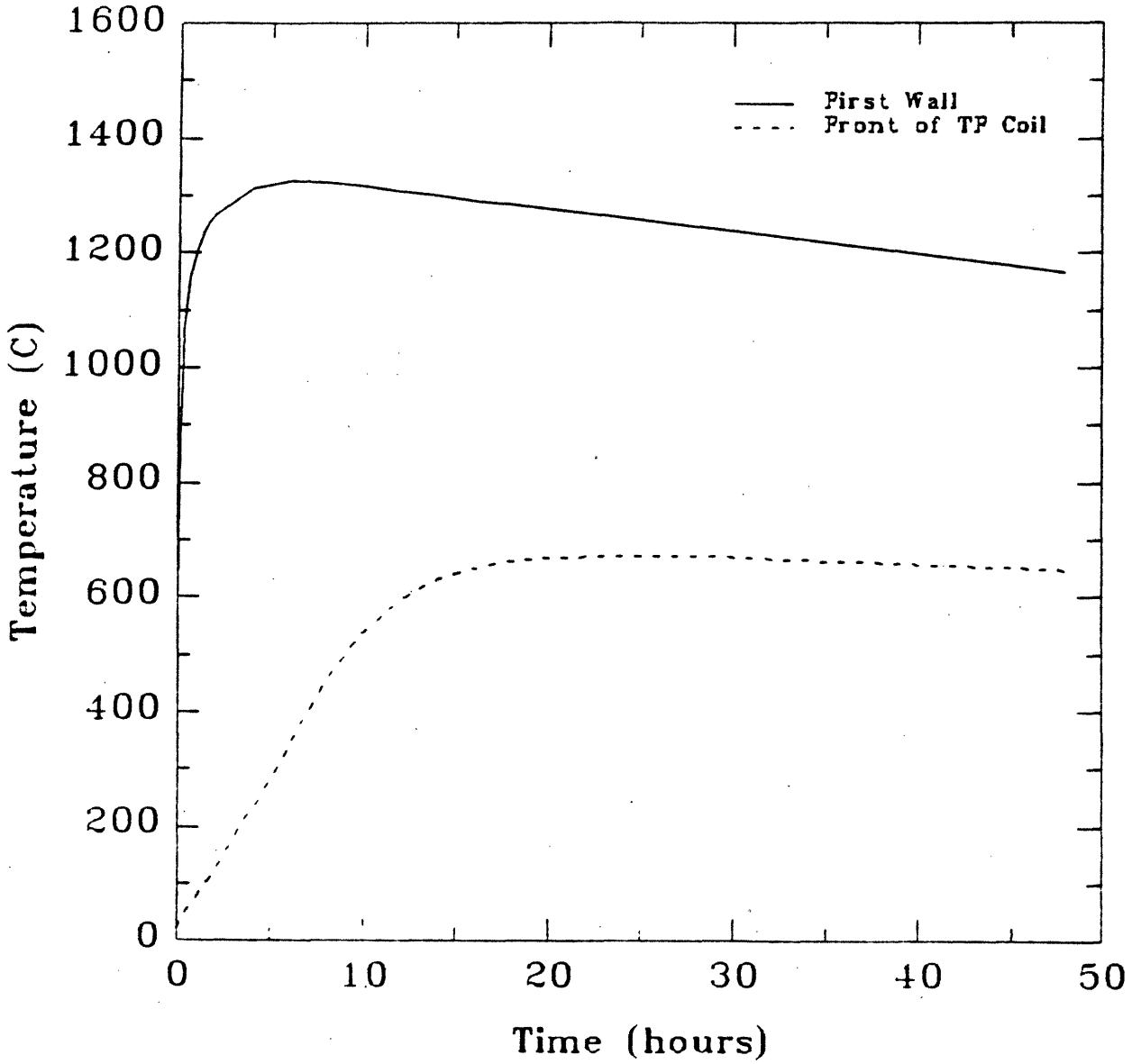

of the radioactive inventory (see Table 5.3.2). It is clear that a base case LOCA may lead to at least a loss of capital investment.

It is conceivable that liquid metal cooled blankets can be designed such that complete coolant drain from the blanket module is an improbable event. This is the approach taken in the TITAN study [5.15]. In the TITAN blanket, the lithium coolant enters and exits the blanket modules from the top. Thus, even in the event of a double-ended pipe break, the lithium that is within the blanket module will remain, due simply to gravity. This makes a LOCA, as it is defined in this study (i.e., complete coolant drain from the entire module), unlikely. This approach is highly recommended, given the results presented here. If such a design is feasible, then the maximum credible accident involving loss-of-cooling would be a LOFA, or a LOCA which results in only partial coolant drain. In either case, the continued presence of the lithium in the module would greatly limit the first wall temperature rise. This effect can be noted by comparing the temperature history of the LOFA (Figure 5.2.6) with that of the LOCA (Figure 5.2.7).

The high temperatures experienced by Blanket #3 are the result of the high wall load (15 MW/m^2) at which the RFP operates, and serve to illustrate the problem with high power density machines. As is discussed in Section 5.3, the maximum temperatures reached following LOFA or LOCA scale linearly with the operational wall load. This is attributed to the fact that the decay heat density also scales linearly with neutron wall load. This is an important consideration given the recent interest in compact, high power density machines. It would appear based on the above results that the economic advantage of very high power densities may be offset by a safety penalty. This issue is discussed further in Section 5.3.

5.2.5 Blanket #6, He/MT-9 D-D Tokamak

The D-D Blanket #6 is described in Section 2.6 and shown in Figure 2.6.1. The decay heat density of Blanket #6 is discussed in Section 4.4 and is given in

Figure 4.0.6. Blanket #6 has the same initial temperature distribution as Blankets #1 and #2.

The temperature response to the base case LOFA (H1C1DC) is given in Figure 5.2.8. Note that the first wall temperature actually declines at the start, as the temperature gradient across the blanket flattens out. The temperature then increases steadily, reaching a maximum of about 730 °C after 8 hours, before decreasing to below 690 °C at 48 hours. This maximum is very manageable in terms of acute failure and radiation release. The thermal stress analysis, however, indicates thermal creep failure of the first wall after 6 hours, as is shown in Table 5.2.3. This is due to the fairly high stress in the first wall, due to the presence of the coolant, which is assumed to remain at system pressure.

The response to the base case LOCA (H1C2PL) is given in Figure 5.2.9. There is an immediate temperature rise here, due to the plasma continuation assumed in helium-cooled LOCAs (see Section 5.2.1.4). The maximum temperature reached is about 740 °C, at about 8 hours. This is very similar to the LOFA case, as is expected, since the only difference between the LOFA and the LOCA in this blanket, except for the continued plasma burn, is the presence of helium. Since helium has low thermal conductivity and low volumetric specific heat, it has a small effect on the temperature response. Again, this temperature should not cause any problem with respect to acute structural failure or radiation release. The thermal creep analysis indicates also that the first wall will not approach failure due to thermal creep. The difference between this and the LOFA case is the stress assumed in the first wall. The details of the thermal stress/creep calculation for the LOCA are discussed in Appendix A. Since there is only a thermal stress, which is fairly small and relaxes with time, the elevated temperatures do not pose a problem.

This is in contrast to the LOFA results presented above. Again, the difference is in the first wall stress that exists in the LOFA (high stress) vs. the LOCA (low stress). The recommendation is that in the event of a LOFA, it would be advisable

Figure 5.2.8 Temperature History Following LOFA in First Wall and Dewar for Blanket #6 (H1C1DC), 1.17 MW/m2

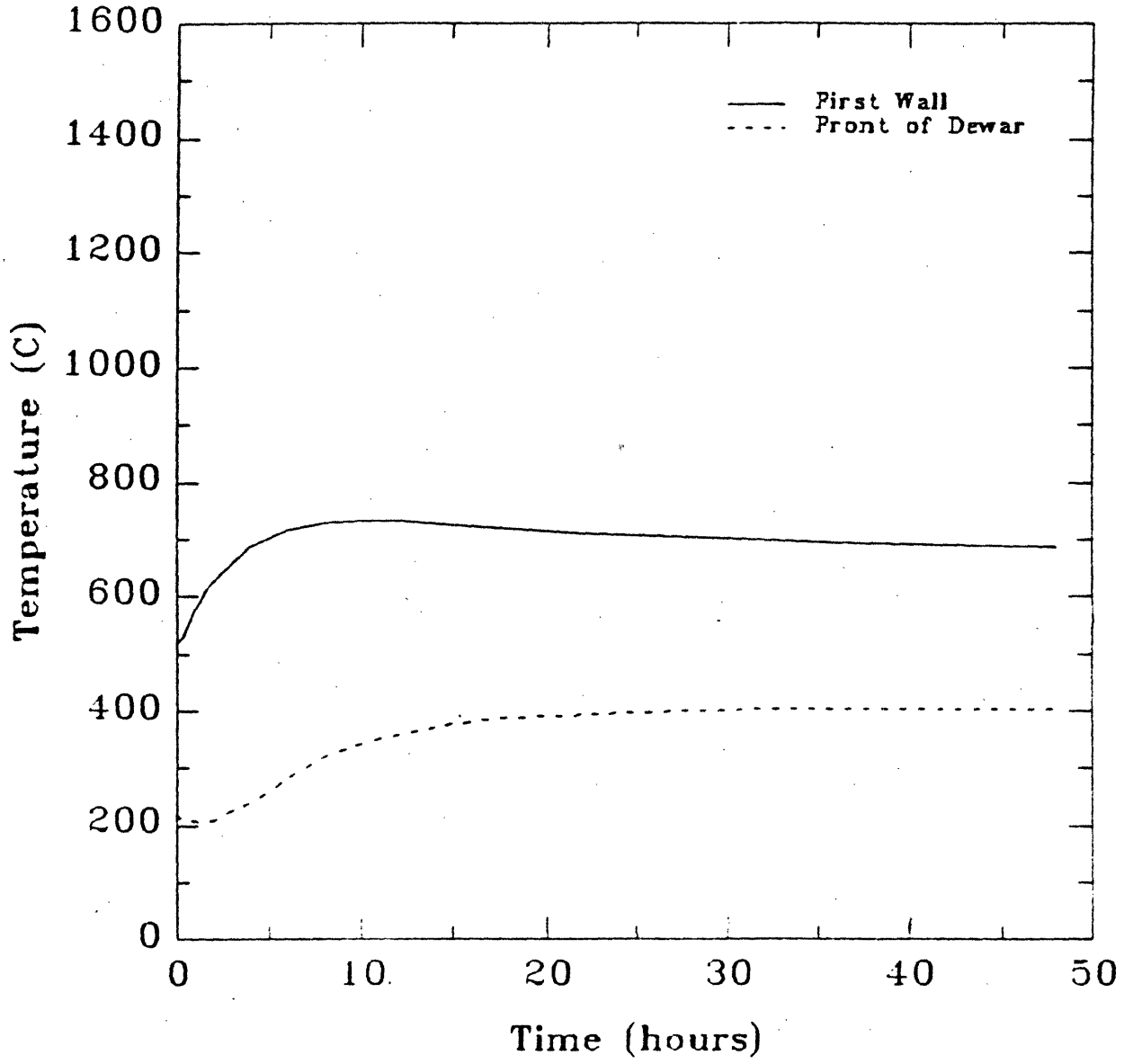

Figure 5.2.9 Temperature History Following LOCA in First Wall and Dewar for Blanket #6 (H1C2PL), 1.17 MW/m2

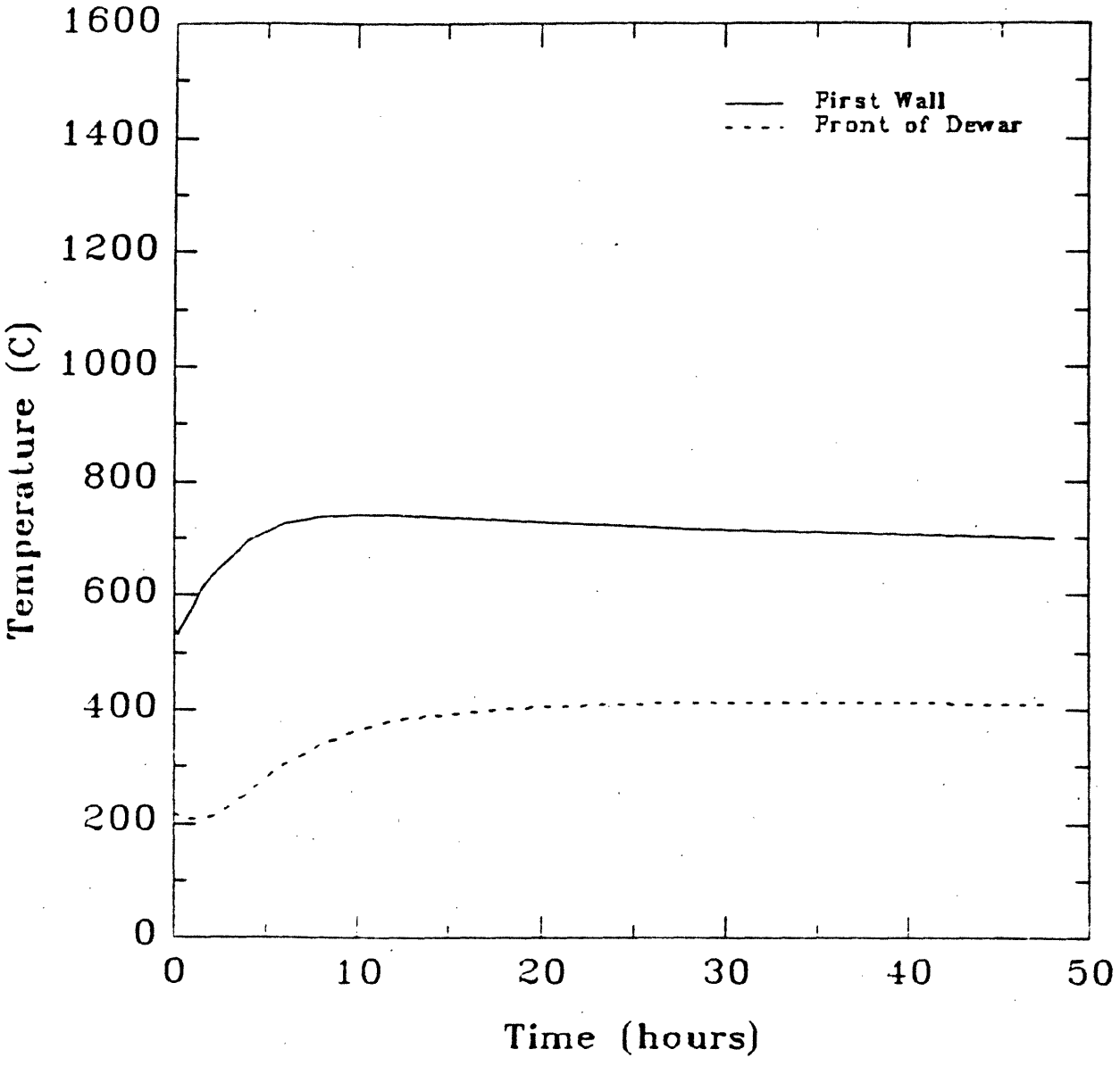

to de-pressurize the system by removing the coolant. In essence, this would mean turning a LOFA into a LOCA. In a LOFA, the presence of the helium coolant may mitigate the temperature rise of the first wall due to natural convection. The added pressure that the coolant exerts on the first wall, however, may cause thermal creep rupture, as is demonstrated above.

For the most part, the temperature rise in the D-D blanket is manageable. Assuming the coolant pressure can be relieved, the blanket is inherently safe with respect to both LOFA and LOCA. This is due to the low wall load at which the D-D machine operates. More discussion of the D-D safety performance is contained in Section 5.3.

5.3 Impact of Wall Load Variations

The thermal analysis of all the blankets was carried out for a number of different neutron wall loads, in order to determine the sensitivity of the post-accident temperatures to the operational wall load as well as develop guidelines for the maximum allowable wall load from the perspective of inherent safety. The results of this analysis are presented in this section.

Figures 5.3.1 and 5.3.2 give the maximum temperatures reached in the first wall of the six blankets following the base case LOFA and LOCA as a function of the operational neutron wall load. The maximum temperatures plotted in these figures are only those due to the decay heat. The peak temperature that may be reached within the first few seconds as a result of the continued plasma burn is a separate effect, and is examined in greater detail in Section 5.4.6.

Note that in all the cases, the maximum temperature is almost linearly dependent on wall load. This is due to the fact that the decay heat density is exactly linearly dependent on wall load [5.16,5.17]. The non-linearity in the maximum temperature is due to the fact that at higher temperatures (higher wall loads), the

Figure 5.3.1 Maximum First Wall Temperature Following LOFA vs. Wall Load for All Blankets, Base Case LOPA (Case 1)

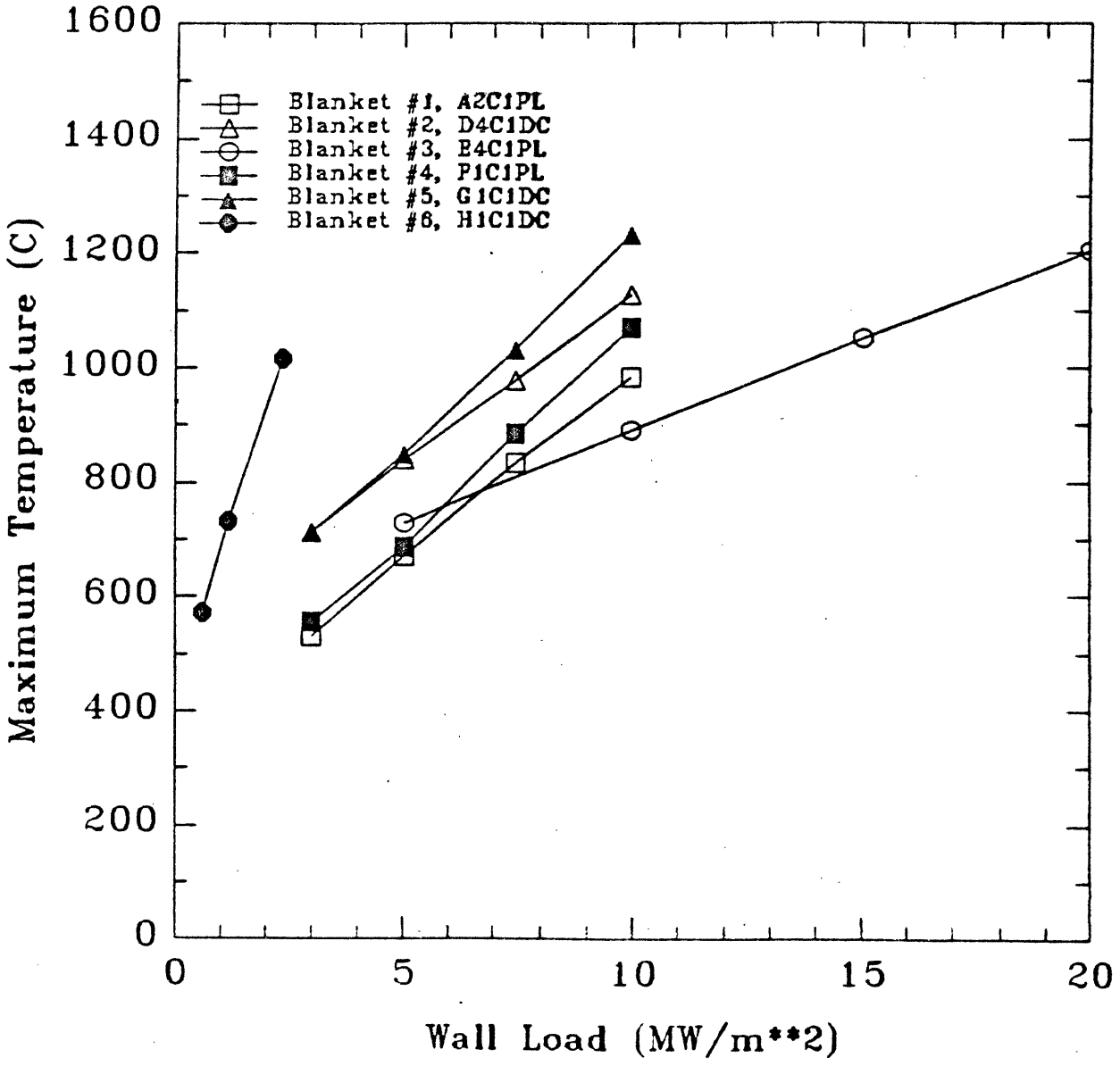

Figure 5.3.2 Maximum First Wall Temperature Following LOCA vs. Wall Load for All Blankets, Base Case LOCA (Case 2)

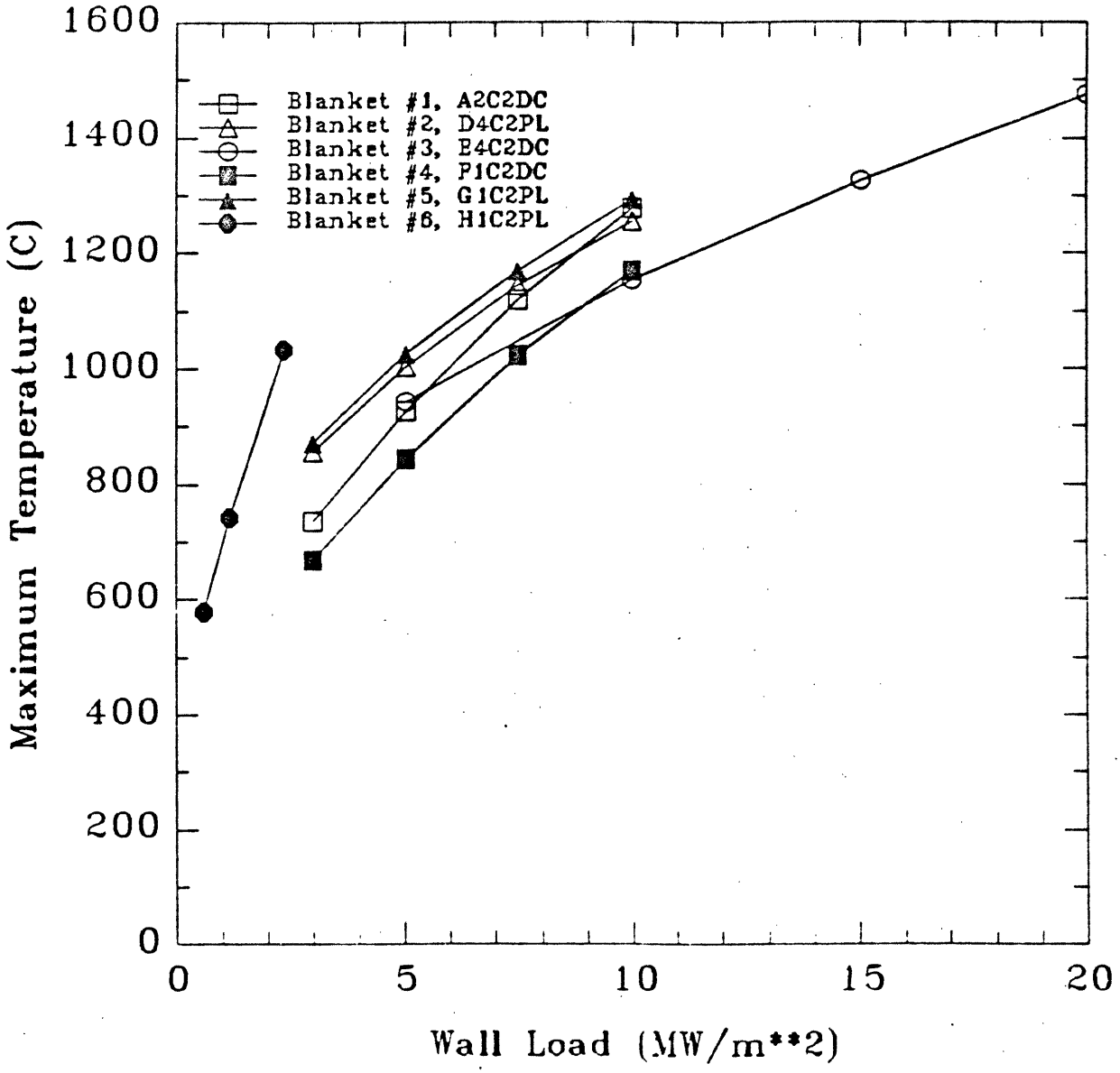

radiative heat transfer to the heat sink is more effective. This means that in the higher wall load cases, a higher fraction of the heat is transferred to the heat sink, resulting in a slightly less than linear dependence of maximum temperature on wall load. In most cases, this is a small effect, and can hardly be noticed in Figures 5.3.1 and 5.3.2.

It is interesting to note that the slope of maximum temperature (T_{max}) vs. Wall Load (Γ_n) is different for each blanket. (The reasons for this are primarily discussed in Section 5.4, which examines the effect of the different variations that each blanket represents.) To examine this effect, it is convenient to define the *temperature rise*, ΔT, as

$$\Delta T = T_{max} - T_o \tag{5.11}$$

where T_o is the initial temperature of the first wall.

The linear dependence of T_{max} on Γ_n allows us to express ΔT as

$$\Delta T = a\Gamma_n - b \tag{5.12}$$

where a and b are constants.

Table 5.3.1 gives the values of a and b for the blankets given in Figures 5.3.1 and 5.3.2 for the LOFA and LOCA base cases. These values of a and b were found for each blanket by simply substituting the data given in Figures 5.3.1 and 5.3.2 into equation (5.12).

The formulation in equation (5.12) allows for comparison of the temperature response of the various blankets in an interesting manner. The temperature rise in the blanket is related to three parameters: 1) the total heat produced, 2) the total heat storage capacity of the blanket, and 3) the amount of heat that is transferred

Table 5.3.1 Values of a and b for equation (5.12).

$$\Delta T = a\Gamma - b \tag{5.12}$$

LOFA

Blanket	a	b
#1	64.9	195.5
#2	59.3	-3.24
#3	31.8	31.8
#4	77.7	186.7
#5	74.5	41.0
#6	252.4	104.5

LOCA

Blanket	a	b
#1	77.9	30.0
#2	57.4	-152.3
#3	35.6	-162.9
#4	71.5	27.9
#5	60.4	-159.7
#6	259.2	104.0

to the heat sink. The total heat produced is defined as Q_{tot}, such that, in one dimensional slab geometry,

$$Q_{tot} = \int_0^{2\text{days}} dt \int_X \dot{q}'''_{decay}(x,t)dx \tag{5.13}$$

where X is the total thickness of the blanket. The total heat storage capacity of the blanket is defined as

$$C_{tot} = \int_X \rho c_p(x)dx \tag{5.14}$$

and the heat transferred to the heat sink is

$$Q_{HS} = \int_0^{2\text{days}} \dot{q}''_{\text{heat sink}}(t)dt \tag{5.15}$$

The amount of heat that goes toward heating the blanket is equal to the total amount of heat produced minus the amount that is transferred to the heat sink, i.e., Q_{tot} - Q_{HS}. Using these parameters, the temperature rise in the blanket can then be represented as

$$\Delta T = \frac{Q_{tot} - Q_{HS}}{C_{tot}} \tag{5.16}$$

Now, as was stated above, the decay heat density, and thus Q_{tot}, is linearly dependent on the operational neutron wall load. This allows the expression

$$Q_{tot} = q_t \Gamma_n \tag{5.17}$$

where q_t is the value Q_{tot} would equal if the neutron wall load was 1.0 MW/m^2. Substituting this into equation (5.16) results in

$$\Delta T = \frac{q_t}{C_{tot}} \Gamma_n - \frac{Q_{HS}}{C_{tot}} \tag{5.18}$$

Note that equation (5.18) has the same form as equation (5.12) if a and b from equation (5.12) are defined as

$$a = \frac{q_t}{C_{tot}} \tag{5.19}$$

$$b = \frac{Q_{HS}}{C_{tot}} \tag{5.20}$$

The representations given in equations (5.19) and (5.20) give insight into the physical significance of the values a and b given in Table 5.3.1. The parameter a is the ratio of the decay heat density over the heat storage capacity of a given material or combination of materials. It is primarily a material property, although different neutron spectra, i.e., D-D vs. D-T, can influence its value. The parameter b is more a function of the design of the blanket. It is essentially a numerical representation of the thermal coupling between the first wall and the heat sink. Blankets which have good conduction paths and high wall emissivities will have high values of b, whereas blankets which rely on thermal radiation or low conductivity materials (such as the helium cooled Blanket #2) will have lower values of b.

Ideally, a should be as low as possible, and b should be as high as possible. Comparisons of the values of a and b for the different blankets and their variations are made in the Sections 5.4 - 5.6. The following subsection will define maximum allowable wall loads for four of the blankets thus far considered.

5.3.1 Maximum Allowable Wall Loads

To define the maximum allowable wall load, it is first necessary to define the maximum allowable temperature rise. In Chapter 3, assumptions were made, based

on the available material data, regarding the temperatures at which VCrTi and HT-9 would experience acute structural failure. Also, a model for analyzing the potential for thermal creep rupture was presented. This was followed by a brief discussion on the potential for radioactive isotope release. On this basis, the minimum wall loads required to cause 1) thermal creep rupture, 2) acute structural failure, and 3) radioactive release were determined for each of the four blankets. From these numbers, maximum allowable wall loads for each blanket can be defined.

The range of wall loads considered for each blanket depends on the operational value as given by the references and shown in Table 5.2.1. For all the blankets with a base case wall load of 5 MW/m^2, the range considered is 3 MW/m^2 - 10 MW/m^2. The range for the RFP Blanket #3 (high power density machine) is 5 MW/m^2 - 20 MW/m^2, and for the D-D Blanket #6, it is 0.585 MW/m^2 - 2.34 MW/m^2 (0.5 - 2.0 times the operational value).

Examining a range of wall loads for each design is important for a number of reasons. First, the cost-of-electricity (COE) generally scales inversely with the wall load [5.18], thus defining a maximum wall load from a safety perspective will define the optimum economic design for a given blanket. That is, for the purpose of comparing different blanket designs on an economic basis, it is useful to know the maximum allowable wall load for each design. Secondly, the operational wall loads given in Table 5.2.1 represent an *average* over the entire area of the first wall. It is known, however, that because of geometric and plasma shaping effects [5.27], the wall load will not be constant with respect to the poloidal angle θ. In fact, the peak-to-average wall load ratio could be as much as 1.5 due to these poloidal effects, or perhaps even higher, depending on the plasma elongation and the aspect ratio [5.8]. The high aspect ratio in the RFP could result in a lower peak-to-average wall load ratio in that design. No analysis was performed to calculate the peak-to-average wall load ratio, and a value of 1.5 is assumed for all the blankets. This means that with a nominal wall load of 5 MW/m^2, there could exist local "hot spots"which see a wall load of 7.5 MW/m^2. To properly examine the effect of these poloidal wall

load variations would require at least a two-dimensional analysis, and is considered beyond the scope of this thesis. A conservative approach, however, is to carry out the 1-D analysis at the peaking factor of 1.5 (i.e., wall load of 7.5 MW/m^2 in the above example). This assumes no transverse heat transfer from a region of peak wall load to adjacent regions of lower wall load, but essentially comprises a fusion equivalent to the "hot channel factor"analysis used in fission reactor design [5.19], and is useful in assessing the true maximum allowable wall load.

The results of the maximum allowable wall load calculations are summarized in Table 5.3.2, which gives the maximum wall load permissible to avoid the specified failure in the particular accident scenario, i.e., LOFA or LOCA. Again, the three failure mechanisms are thermal creep rupture, acute structural failure, and critical radioactive release. It is important to note that the wall loads given for the structural damage failure modes (thermal creep rupture and acute structural failure) apply to the *peak* wall load of the reactor. This peak is equal to the average times the peak-to-average ratio, which could be as high as 1.5. Thus, if the wall load given in Table 5.3.2 is 10 MW/m^2, then the maximum permissible *average* wall load to avoid a local structural failure at the hot spot is $\frac{10}{1.5} = 6.7$ MW/m^2. Conversely, the wall loads given for the critical radioactive release apply to the average for the reactor. This is because the amount of radioactivity released depends on the radioactive inventory in the entire first wall, which in turn depends on the *average* wall load. Considering this, it is clear from Table 5.3.2 that the passive safety criterion of preventing structural damage is far more limiting in terms of operating wall load than the radiation release criterion.

In terms of thermal creep rupture, the wall loads given in Table 5.3.2 represent estimates at best, since the thermal creep analysis was based on large assumptions of the actual stess levels and materials data (see Section 3.2 and Appendix A). To examine the sensitivity of the thermal creep rupture maximum wall load on the first wall stress, a parametric study varying the stress level was carried out for two of the cases. These cases are the LOCA in Blanket #3, and the LOFA in Blanket

Table 5.3.2 Maximum Allowable Peak Wall Loads to Avoid Structural Failure and Radioactive Release.

Blanket #	LOFA/ LOCA	Wall Load (MW/m^2) to Exceed Temperature Limits: Thermal Creep Rupture*	Acute Structural Failure*	Radioactive Release**
1	LOFA	>10†	>10†	≫10‡
	LOCA	~8	8.8	>10
2	LOFA	~3	6.1	>10
	LOCA	~6	3.6	>10
3	LOFA	~17	20	>20
	LOCA	~7	11	~20
6	LOFA	~1	1.8	>2.5
	LOCA	>2.5	1.8	>2.5

* These wall loads correspond to peak of reactor, which could be 1.5 times the average.

** Excluding effects of possible lithium fire (Blankets #1 and #3 only). These wall loads correspond to average of reactor, and are based on a limit of 200 rem at the site boundary under adverse release condition.

† Wall Load Required is 2 - 5 MW/m^2 greater than maximum analyzed.

‡ Wall Load Required is at least 5 MW/m^2 greater than maximum analyzed.

#6, because, as is seen from Table 5.3.2, it is the thermal creep failure mechanism that limits the wall load for these cases. This means that the wall load limit for these cases may be sensitive to the actual first wall stress level. In the other cases shown in Table 5.3.2, the wall load is most limited by the acute structural failure mechanism, which was assumed not to be a function of the stress level.

Figure 5.3.3 shows the wall load required to cause thermal creep rupture as a function of first wall stress for the Blanket #3 LOCA (E4C2DC) and the Blanket #6 LOFA (H1C1DC). Note that the relationship between the failure wall load and the first wall stress is linear for the VCrTi first wall of Blanket #3, and exponential for the MT-9 first wall of Blanket #6. This arises because the dependence of the Larson-Miller parameter on stress is linear for VCrTi, and exponential for MT-9 (see Appendix A). The results in Figure 5.3.3 show that the maximum allowable wall load in Blanket #3 from thermal creep considerations in 10 MW/m^2, regardless of the stress. In Blanket #6, the maximum wall load is about 2.5 MW/m^2. These wall loads apply to the peak for the reactor, which may be 1.5 times higher than the average, due to the poloidal variation.

The wall loads given for acute structural failure are merely the wall loads required to cause a maximum temperature which exceeds the limits for acute structural failure given in Section 3.2. These temperature limits were found from extrapolation of limited data bases for both VCrTi and HT-9. As such, the numbers in Table 5.3.2 should not be taken so literally as they should be used for comparison between designs and for comparison with the nominal values given in Table 5.2.1. Comparison between designs is largely discussed in Section 5.4. Conclusions based on the maximum allowable wall loads for each design are given below. It should be pointed out that for the liquid lithium cooled Blankets #1 and #3, the possibility and consequences of a lithium fire were not considered in this study. In the event of a lithium spill, e.g., in a LOCA, exposure of the lithium to air could result in a chemical fire which might lead to temperatures which exceed those presented here. In this case, the lithium fire would be the limiting event in terms of thermal safety.

Figure 5.3.3 Wall Load to cause thermal creep rupture of first wall as a function of stress level in first wall; Blanket #3 LOCA (E4C2DC) and Blanket #6 LOPA (H1C1DC).

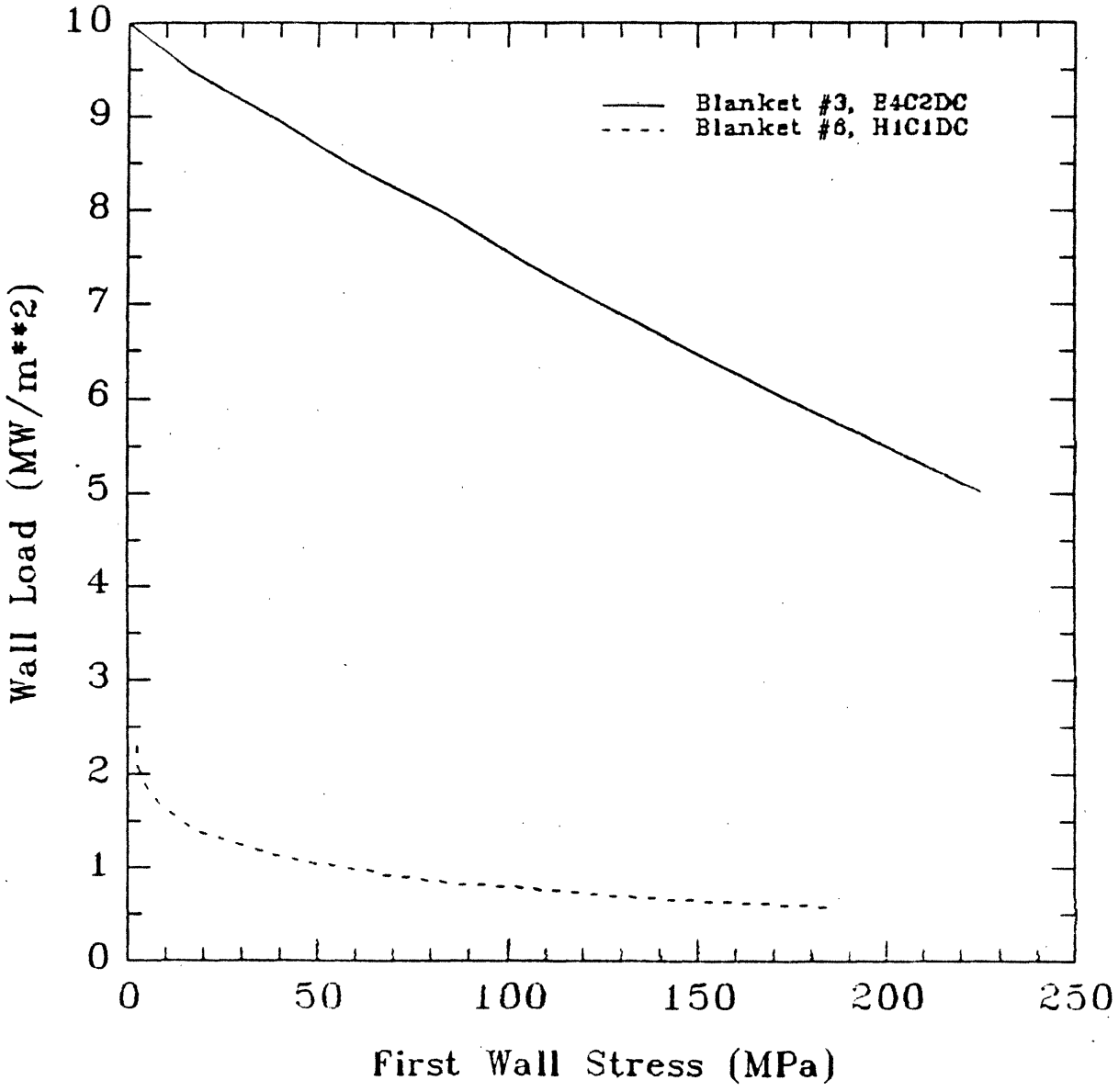

According to Table 5.3.2, Blanket #1 does meet the criteria for inherent thermal safety at the nominal wall load of 5 MW/m^2 for both LOFA and LOCA. Given the local hot spot factor of 1.5, resulting in a peak wall load of 7.5 MW/m^2, it is seen that a LOCA could lead to thermal creep rupture. This should be a localized occurrence, however, perhaps contained within one module. This assumes that no oxidation is allowed to occur. In the event of an oxygen leak into the system, there is the possibility of severe structural damage, even at low wall loads, due to the formation of the liquid V_2O_5 oxide (see Section 3.2.2.1). As for radiation release, it is seen that Blanket #1 could be operated at wall loads much higher than the nominal ($\sim$10 MW/m^2) without significant danger of violating the 200 rem criteria. The general conclusion to be drawn is that Blanket #1, the Li/Li/VCrTi tokamak, has excellent inherent safety potential at 5 MW/m^2.

Regarding Blanket #2, the indication from Table 5.3.2 is that the blanket could survive a LOFA at the nominal wall load of 5 MW/m^2 if the helium coolant could be sufficiently de-pressurized to eliminate the high pressure stress in the first wall, without being completely removed. Completely removing the helium would eliminate the conduction path from the first wall, and would essentially constitute a LOCA. Reliance on a system that depressurizes the coolant in the event of a LOFA does not constitute inherent safety unless the system operated passively, in which case no operator intervention would be required to prevent damage. At local hot spots, it is likely that acute failure would occur in a LOFA. In the LOCA, it is interesting to note that the wall load required to cause acute failure is lower than that required to cause thermal creep rupture. This is purely the result of the assumptions made about the first wall stress level and the temperature at which acute failure occurs. In any case, the indication is that gross acute structural failure would occur. This is largely due to the first wall design of Blanket #2. More discussion on this issue is given in Section 5.2.3. As for radiation release, Blanket #2 should be able to operate at higher wall loads ($\sim$10 MW/m^2) without danger. The conclusion to be drawn here is that, in terms of radiation safety, Blanket #2 can be

considered inherently safe at wall loads significantly above the nominal 5 MWm/^{2}. In terms of plant protection, however, because of the potential for structural failure, Blanket #2 does not meet inherent or passive safety criteria at the nominal wall load, or at wall loads significantly below the nominal value.

Given its high nominal wall load (15 MW/m^2), Blanket #3 can have serious safety problems. The indication from Table 5.3.2 is that thermal creep rupture will occur at wall loads only slightly above the nominal value in the LOFA scenario, and significantly below the nominal in the LOCA scenario. With the assumed local hot spot factor of 1.5, it is seen that a LOFA can also lead to acute structural failure. A LOCA will almost certainly lead to severe structural damage, even at wall loads well below the nominal. Finally, considering the existence of local hot spots, it is seen that a LOFA, and especially a LOCA, can result in a substantial radiological release. This is the only case considered in this study which has significant potential for large scale radiation release, and represents a statement of caution the case for high power density machines. The conclusion is that Blanket #3 is not inherently safe, and that the effort to assess the viability of high power density machines should include a substantial safety program to define both design approaches and limiting conditions for passive safety.

In contrast to Blanket #3, the D-D Blanket #6 operates at a low nominal wall load (1.17 MW/m^2). Table 5.3.2 indicates that at this wall load, a LOFA will lead to thermal creep rupture, but, as for Blanket #2, this depends on the ability to depressurize the coolant in the first wall. If this problem can be solved, then even with a local hot spot factor of 1.5, Blanket #6 should survive both LOFA and LOCA. The safety margin for this is small, however, and thus operation at higher wall loads is not advisable. This shows that, because of its low power density and hence low operational neutron wall load, the D-D fuel cycle offers a significant safety advantage. The safety performance of Blanket #6 is severely hindered by the fact that the blanket is optimized for blanket multiplication by consisting primarily of steel (see Sections 2.6 and 4.4). This results in a high decay heat density, and thus

a high maximum temperature after both LOFA and LOCA, considering the low wall load. Note in Table 5.3.1 that Blanket #6 has by far the highest value of the parameter a, which represents the ratio of decay heat to thermal capacity of the blanket. From an inherent safety viewpoint, it would be advantageous if some of the blanket multiplication capability was traded for increased safety by using less steel and more low activation material in the blanket. The lower temperature rise would allow for operation at higher wall loads and perhaps better economic performance. The conclusion is that the D-D blanket is inherently safe at the nominal wall load, but could be redesigned with the goal of an increased thermal safety margin.

5.4 Impact of General Variations

In Sections 5.2 and 5.3, the temperature responses of the four blankets which represent four different design approaches were examined. In this section, the impact on the temperature response of a number of general variations is analyzed. This includes the effect of different materials, different reactor types, and variations of the base case parameters presented in Table 5.2.1. The purpose of this section is to examine the effect of these variations in order to develop generic design guidelines to keep the temperatures reached in the event of LOFA or LOCA as low as possible.

The variations of the base case parameters presented in Table 5.2.1 are given in Table 5.2.2, which outlines the different cases analyzed. Note that Case 1 and Case 2 are the base case LOFA and LOCA respectively. Most of the analysis involves these cases. In later sections, the variations include the wall emissivities and the availability of the heat sink. Table 5.2.2 will prove convenient in distinguishing the different cases for the purposes of comparison.

5.4.1 Materials Impact

A significant amount of work has been done to quantify the impact of mate-

rials choice on fusion safety [5.2,5.3,5.20,5.21]. This subsection examines the issue further in attempt to add to the overall understanding of the materials impact. The materials impact on the decay heat density, which is an important aspect of the safety analysis, is discussed in Chapter 4.

5.4.1.1 Fe1422 vs. MT-9

In Section 4.2.1.4, the decay heat behavior of the structural steels Fe1422 and MT-9, both of which are considered for the bulk material in the manifold region of Blankets #1 and #3, are compared, with the conclusion that Fe1422 produces decay heat levels that are as much as an order of magnitude higher than MT-9. The indication is that using Fe1422 instead of MT-9 as the manifold material will result in a more adverse temperature response to LOFA/LOCA events. It is useful and illustrative to quantify this effect.

Figure 5.4.1 displays the temperature vs. time response of the first wall of two variations of Blanket #1, one with an Fe1422 manifold (A1) and one with an MT-9 manifold (A2), to a base case LOFA. The MT-9 case is the same as that shown in Figure 5.2.1 and discussed in Section 5.2.2. In this case (A2), the temperature never exceeds 700 °C, and this represents an inherently safe response to this accident. As is seen in Figure 5.4.1, the temperature response of the blanket with the Fe1422 manifold (A1) is markedly different. The temperature exceeds 1100 °C in less than 10 hours, and the thermal creep rupture fraction at 48 hours (see Table 5.2.3) is about 0.22, which is significantly high. This dramatic difference is due solely to the additional decay heat produced by the Fe1422. As is discussed in Section 4.2.1.3, Fe1422 has a high manganese content, and it is this element that is the source of most of the decay heat. Recommendations regarding the use of Fe1422 are made in Sections 4.2.1.3 and 4.2.1.4. It is clearly not suited for any application within the blanket itself, where it will be subject to high neutron fluxes. On the basis of these results, the economic penalty incurred by using MT-9 in the place of Fe1422

Figure 5.4.1 Effect of Manifold Material on First Wall Temperature History Following LOPA for Blanket #1, (A1C1PL) vs. (A2C1PL)

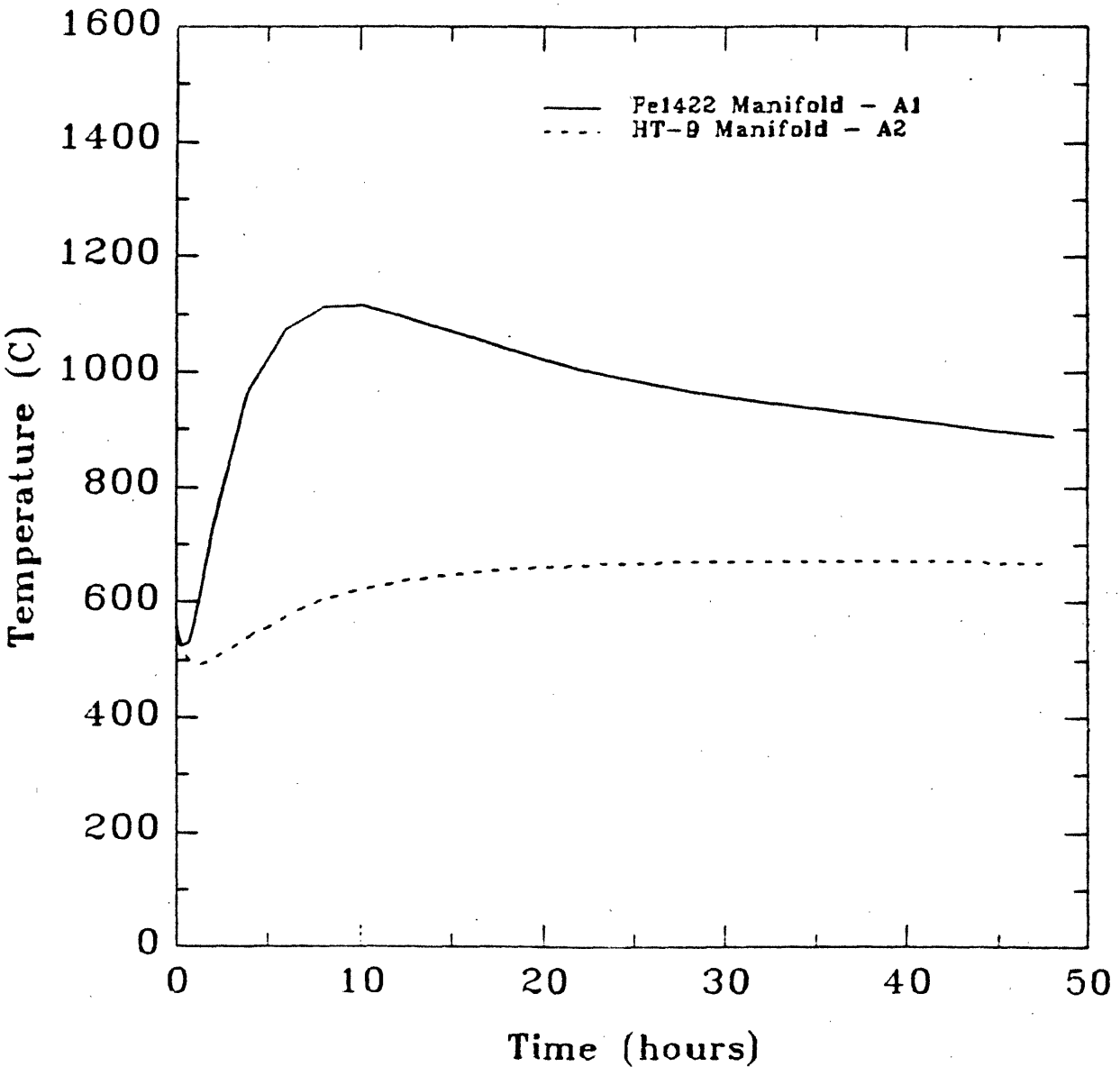

is justified.

5.4.1.2 Li/Li/V vs. LiPb/LiPb/V (Blanket #1 vs. Blanket #4)

As is discussed in Sections 2.4 and 4.2.2, Blankets #1 and #4 are identical except for the breeder material, and the fact that the first wall thickness of Blanket #4 is 0.25 cm greater than that of Blanket #1 to accomodate the heavier LiPb. The effect of this thicker first wall on the temperature response should be negligible, since it represents a very minor increase in the overall structure content of the blanket. and thus comparing these two blankets should give a good indication of the relative thermal safety of liquid lithium and lithium-lead.

The decay heat behavior of these breeder materials is discussed in Section 4.2.2. Briefly, assuming essentially complete tritium removal [5.22], liquid lithium contributes virtually no decay heat to the overall system. Lithium-Lead, on the other hand, produces isotopes of lead which do contribute significantly to the overall decay heat of the blanket. Furthermore, the volumetric heat capacity (ρc_p) of lithium is ~50% higher than that of LiPb in the temperature range of interest [5.4], and the thermal conductivity of lithium is as much as a factor of three higher than LiPb [5.23].

The combination of these three effects can be seen in Table 5.3.1 by noting the values of a and b for Blankets #1 and #4 in the LOFA case. The increased decay heat and decreased heat capacity lead to a higher value of a for Blanket #4 (about 20% higher), whereas the lower conductivity leads to a lower value of b. The difference in the value of b is small, mainly because the limiting heat transfer path in the LOFA for both of these blankets is the radiation from the blanket to the shield and the shield to the heat sink, thus the breeder material conductivity has only a small effect.

Figure 5.4.2a gives the temperature vs. time response of the first wall to the

Figure 5.4.2a Effect of Breeder Material on First Wall Temperature History Following LOPA, Blanket #1 (A2C1PL) vs. Blanket #4 (P1C1PL)

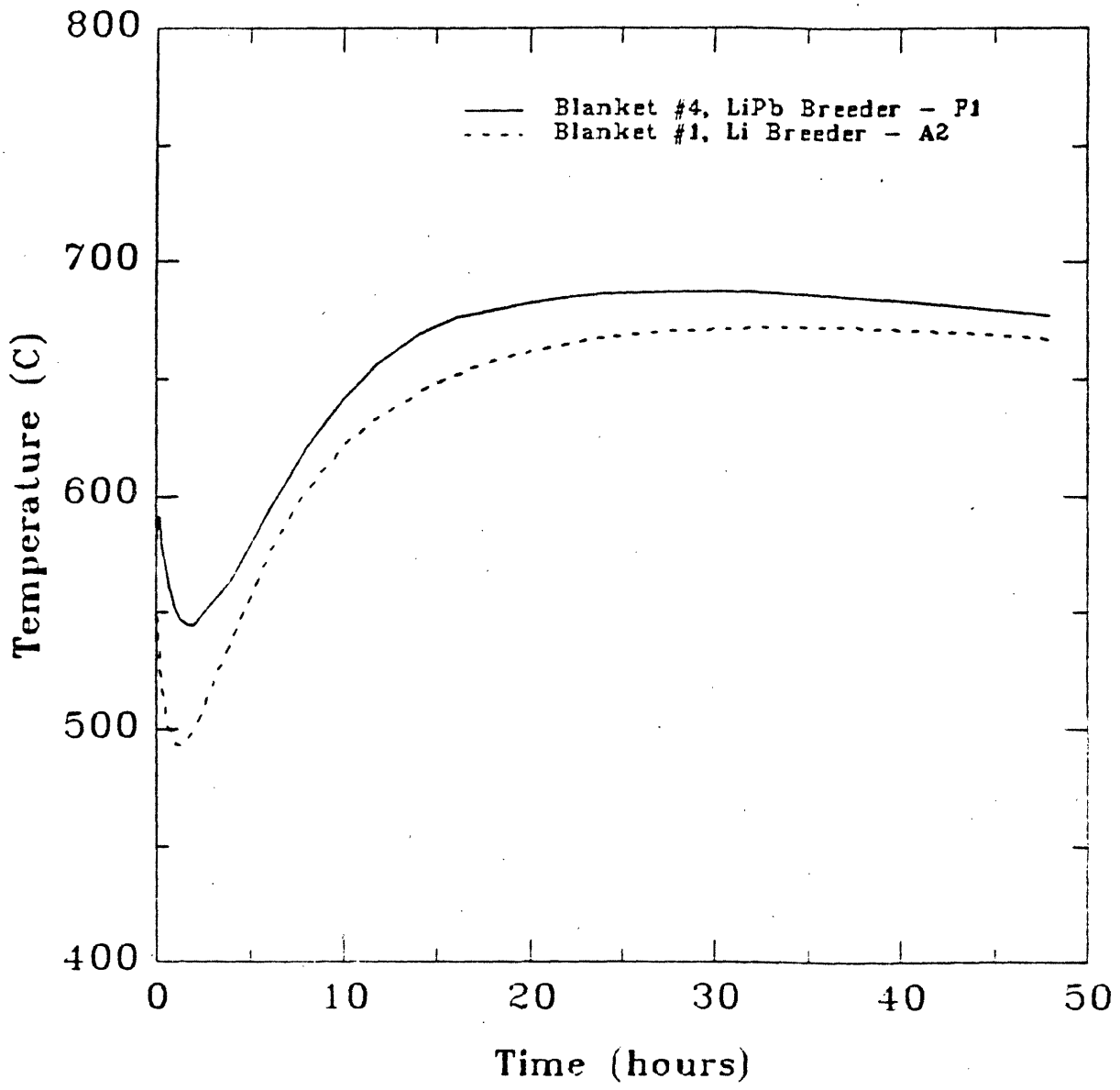

base case LOFA for Blankets #1 and #4. Note that, as expected, the Blanket #4 temperature is higher, but the difference is small. However, the higher value of a in Table 5.3.1 indicates that at higher wall loads, the difference will be more pronounced. For both the base case LOFA and LOCA, the maximum temperature vs. wall load for these two blankets is given in Figure 5.4.2b. Note that in the LOFA case, the difference in the maximum temperatures increases with wall load, with Blanket #4 experiencing the higher temperatures.

Comparing the temperature responses of Blankets #1 and #4 to the LOCA reveals an interesting effect. Note from Figure 5.4.2b that the maximum temperatures reached in the LOCA are actually lower in Blanket #4. Since the LOCA assumes a complete coolant drain, the LiPb is not present, thus does not contribute to the decay heat. During operation, however, the 30% ^{6}Li enriched LiPb in Blanket #4 captures more thermal neutrons than does the natural enrichment liquid lithium in Blanket #1. The effect is that in Blanket #4, less neutrons are captured by the VCrTi and MT-9 structure, since more are captured in the breeder material. Thus the decay heat contribution of the structural material is actually less in Blanket #4 than in Blanket #1. Note in Table 5.3.1 that the value for a in the LOCA case is less in Blanket #4 than in Blanket #1. The higher T_{max} vs. Γ_n slope this implies for Blanket #1 is visible in Figure 5.4.2b and is due to the higher decay heat in Blanket #1 in the LOCA case. This has a potentially important impact on thermal safety, particularly in blankets which use a structural material where most of the decay heat comes from slow neutron-induced group 1 isotopes (see Section 4.2.3), such as VCrTi. Increasing the ^{6}Li enrichment will increase the slow neutron absorption in the breeder material (and increase the tritium breeding ratio), and thus *decrease* the (n,γ) capture rate in the structural material. This will result in a lower decay heat, especially in a LOCA, where the coolant/breeder material is assumed to have drained. The lower decay heat leads directly to a lower temperature rise. This idea was originally proposed by Cheng in the TITAN study [5.15,5.24], and deserves further review for its potential impact on thermal safety.

Figure 5.4.2b Effect of Breeder Material on Maximum First Wall Temperature vs. Wall Load, Blanket #1 (A2) vs. Blanket #4 (P1)

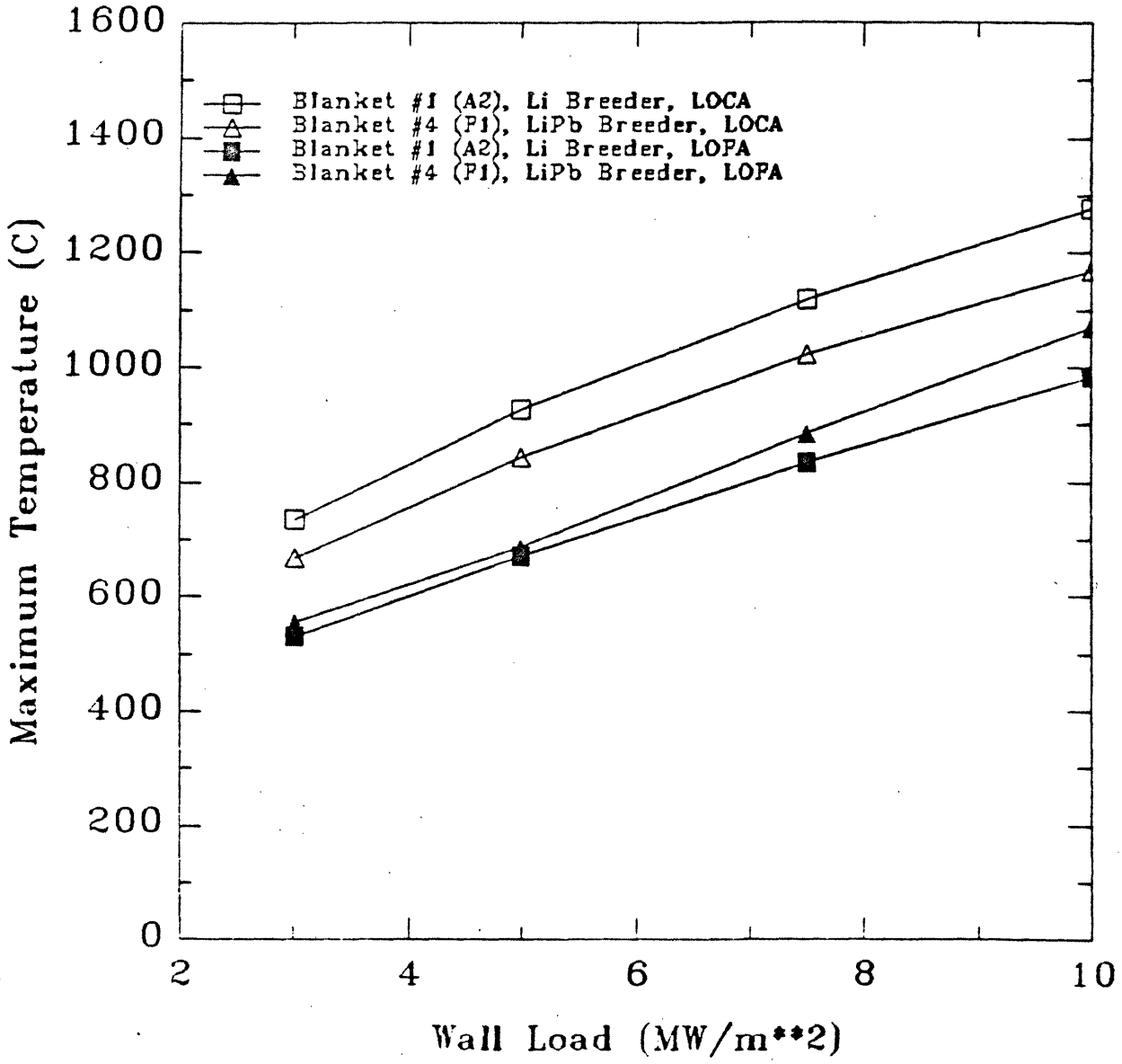

The conclusion is that, in the event of a LOFA, the lead isotopes produced by LiPb will increase the decay heat, and thus the maximum temperature reached, over that of a liquid lithium blanket. However, due to neutronic effects, the decay heat level in the structure of the LiPb blanket will be less than that of the lithium blanket, and thus the temperature rise in the event of a LOCA will be lower in the LiPb blanket. The lower structural decay heat level can be realized in lithium blankets as well, by increasing the ^{6}Li enrichment.

5.4.1.3 Effect of Neutron Multiplier (Li_2O/He/MT-9 vs. Li_2O/He/MT-9/Be)

Blanket #5 is identical to Blanket #2 except for the inclusion of beryllium in the first breeder region. As mentioned in Section 2.5, this is to improve the marginal tritium breeding ratio of Blanket #2. The impact of the inclusion of beryllium on the decay heat density is discussed in Section 4.2.3. Briefly, due to an overall increase in the neutron flux, especially the lower-energy flux, the multiplier causes about a 15% increase in the decay heat produced over two days. The increase over shorter periods is even greater (~25% after one hour). The effect that the inclusion of beryllium has on the temperature response to LOFA/LOCA is discussed here.

The values of a in Table 5.3.1 for Blankets #2 and #5, for the LOFA case, give an indication of the effect of the increased decay heat density in Blanket #5. The value of a for Blanket #5 is fully 25% higher than that of Blanket #2. This effect is seen graphically in Figure 5.3.1. Note in Table 5.3.1 that the value of b for Blanket #5 is higher than that of Blanket #2. There are two reasons for this. First, the higher temperatures reached in Blanket #5 make the radiative heat transfer mechanism more effective. Second, the high thermal conductivity of beryllium improve the overall conductivity through the main breeder region of Blanket #5.

Note from Table 5.3.1 that in the LOCA case, neither of the above effects are seen. The value of a for the two blankets are very similar, and the value of b is lower

for Blanket #5. The values of a and b in the LOCA case for these two blankets are misleading, due to the non-linear dependence of maximum temperature on wall load at the high temperatures reached in these blankets. This non-linear behavior can be seen in Figure 5.3.2. The value of a is calculated by drawing a straight line through the two endpoints in Figures 5.3.1 and 5.3.2. It is seen that in the LOCA case of both Blankets #2 and #5, this underestimates the value of a, and hence overestimates the value of b. While some insight can still be gained by examining the values of a and b in these cases, care must be taken not to interpret their exact values too literally.

For the most part, the maximum temperatures reached in Blanket #5 are similar to those reached in Blanket #2. The difference becomes significant at high wall loads in the LOFA case. Due to the greater sensitivity of maximum temperature to wall load of Blanket #5, the minimum wall load required to exceed the acute structural failure temperature limit in the base case LOFA is only 5.7 MW/m^2, vs. 6.1 MW/m^2 for Blanket #2. This difference is small but potentially significant, given the poloidal variation of the wall load discussed in Section 5.3. As in Section 4.2.3, the conclusion is that the use of beryllium in the breeder region to improve blanket performance will have a negative impact on the safety margin of the blanket. This point should be considered when assessing the viability of blankets that require a neutron multiplier.

5.4.1.4 Li/Li/V vs. Li_2O/He/MT-9 (Blanket #1 vs. Blanket #2)

Blankets #1 and #2 are different both in terms of the materials and their geometric configurations. In particular, the first wall design of Blanket #2 allows only for radiative cooling during a LOCA, which results in a high maximum first wall temperature (see Section 5.2.3 for additional discussion). In a LOFA, however, all the materials are present, and while the geometric differences affect the results, it is useful to compare the temperature responses of these two blankets to examine

the materials impact.

The maximum temperature vs. wall load during a LOFA for both of these blankets is plotted in Figure 5.3.1, while the values of a and b from equation (5.12) are given in Table 5.3.1. Note that a, which represents the ratio of decay heat produced over total heat capacity, is similar for both blankets. While MT-9 produces more decay heat per unit volume (J/cm^3) than VCrTi, the volumetric heat capacity (ρc_p) of MT-9 is almost a factor of two higher than that of VCrTi at the temperatures of interest. The result is that the value of a for Blanket #2 is slightly lower than that of Blanket #1. The real difference between these blankets is in the thermal coupling between the first wall and the heat sink.

During a LOFA, the primary pathway in both blankets for heat to go from the first wall to the back of the blanket is via conduction. In Blanket #1, the conduction medium is liquid lithium and VCrTi in the first wall and blanket regions, MT-9, VCrTi, and lithium in the manifold region, and finally a pure VCrTi second wall (see Figure 2.1.1). All of these materials have good thermal conductivities [5.4]. In Blanket #2, the conduction medium is pure helium in the first wall region, which has poor thermal conductivity [5.5], then MT-9, helium, and Li_2O throughout the remainder of the blanket. Of these, only MT-9 has good thermal conductivity, and the volume fraction of MT-9 in the blanket is fairly low (see Figure 2.2.1). The thermal conductivity of Li_2O is a subject of concern and is much lower than that of liquid lithium.

Figure 5.4.3 shows the temperature gradient across Blankets #1 and #2 following a LOFA at the time that the first wall reaches its maximum temperature. This is 34 hours for Blanket #1 and 1.5 hours for Blanket #2. Note that both blankets have the same initial temperature distribution. Figure 5.4.3 also gives the temperature gradient across Blanket #1 at 1.5 hours for comparison with that of Blanket #2. Note that the gradient across Blanket #1 at 1.5 hours is relatively flat, as it is at 34 hours. Immediately after the LOFA initiates, the temperature

Figure 5.4.3 Effect of Blanket Materials on Spatial Temperature Distribution Following LOPA, Blanket #1 (A2C1PL) vs. Blanket #2 (D4C1DC)

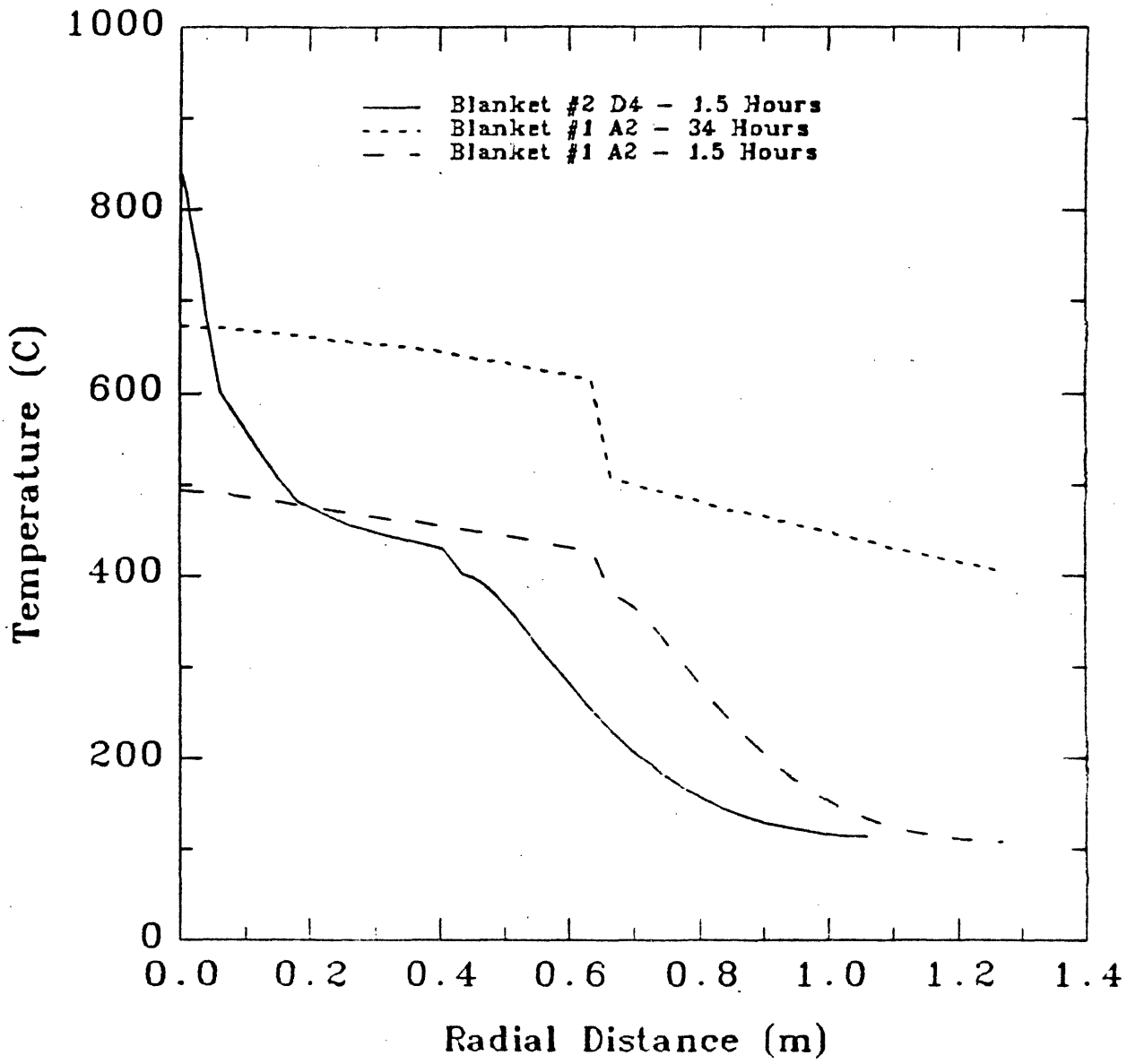

gradient across Blanket #1 flattens out, due to the good thermal coupling from front to back. The temperature of the entire blanket then begins to rise almost uniformly due to decay heating, until it reaches its maximum (at 34 hours), at which time it begins to decrease. Blanket #2 clearly exhibits very different behavior. The poor conductivity of helium leaves the first wall almost thermally insulated, so the first wall temperature rises sharply after initiation of the LOFA. Note the steep gradient across the first six centimeters of Blanket #2, followed by another region of moderate gradient. This second region is primarily Li_2O, which also has fairly poor thermal conductivity.

The poor thermal coupling between the first wall and heat sink in Blanket #2 is exhibited by the low value of b in Table 5.3.1. The result is that the first wall of Blanket #2 reaches a much higher maximum temperature than that of Blanket #1. For this reason, the maximum allowable wall loads to avoid the structural failure are much lower in Blanket #2 (see Table 5.3.2). In fact, note from Table 5.3.2 that either thermal creep rupture or acute structural failure will occur in Blanket #2 at the nominal wall load after a LOFA or LOCA. The apparent solution to the poor thermal coupling problem is to include conduction paths between the first wall and the bulk of the blanket. These could consist of perforated steel plates connecting the two first wall slabs (see Figure 2.2.2) to each other and to the breeder plates in the blanket region. Whether such plates would introduce problems regarding the operation of this blanket, such as restricting the coolant flow or introducing high thermal expansion-induced stresses, is unclear, and should certainly be analyzed. If it turns out that these problems would exist, then from the viewpoint of thermal safety, the recommendation is that helium-cooled blankets with designs similar to Blanket #2 should be avoided.

Comparing the response to the base case LOCA of these two blankets yields an interesting result. Note from Table 5.3.1 that Blanket #1 still has much better thermal coupling (higher value of b) than Blanket #2. The value of a for Blanket #1, however, is significantly higher than that of Blanket #2. This is because

in a LOCA, the liquid lithium of Blanket #1 drains away. Recall from Section 4.2.2.1 that liquid lithium produces essentially no decay heat, and thus its presence effectively represents a heat sink. Thus, when the lithium drains away, there is a significant loss of heat capacity, but no corresponding decrease in the total decay heat production. This drives up the value of a. On the other hand, the solid Li_2O breeder in Blanket #2 is present in both a LOFA and a LOCA, so the value of a for these two cases in Blanket #2 remains essentially unchanged. The result is that at lower wall loads (< 8 MW/m^2), the better thermal coupling of Blanket #1 over Blanket #2 yield a lower maximum temperature in Blanket #1. At wall loads above 8 MW/m^2, however, the maximum temperature reached in the base case LOCA in Blanket #1 is higher than that of Blanket #2, due to the higher value of a in Blanket #1. The conclusion is that while liquid lithium is an excellent heat sink and heat conduction medium in the event of a LOFA, the fact that it may drain in a LOCA leaves the blanket at a potential thermal safety disadvantage. Designs that prevent the complete drainage of lithium, such as TITAN (see Section 5.2.4), will alleviate this problem and greatly enhance the safety margin of the blanket.

5.4.2 Impact of Shield/Coil Geometry (Tokamak vs. Reversed-Field-Pinch)

The basic material compositions of Blankets #1 and #3 are very similar. That is, they are both self-cooled liquid lithium blankets with VCrTi structure (see Figures 2.1.2 and 2.3.1). They both contain reflector/manifold regions which consist mostly of steel (MT-9). The difference is in the fact that the RFP Blanket #3 has copper coils, and does not require the large magnet shield that is seen at the back of Blanket #1. The impact that this geometric difference has on the temperature response to LOFA/LOCA is examined in this section.

Note from Table 5.3.1 that the value of a, in both the LOFA and LOCA cases, for Blanket #3 is less than half that of Blanket #1. This is due to the fact that Blanket #3 *lacks* the magnet shield found in Blanket #1. The shield in Blanket #1

consists of 90% Fe1422, which produces a very high decay heat density. Note from Figure 4.2.1 that the shield produces almost half of the decay heat in Blanket #1 at shutdown, and more than half after one hour. This is the reason that the value of a is higner for Blanket #1 than for Blanket #3. Replacing the Fe1422 shield in Blanket #1 with an MT-9 shield reduces the value of a by 30%, to about 45 in the LOFA case. Blanket #3 has only the copper coils behind the blanket, which produce very little decay heat but provide a significant amount of heat capacity, resulting in the small value of a for this blanket. The indication is that Blanket #3 is actually less sensitive to wall load variations, and can be operated at a higher wall load, than Blanket #1. Using a low activation material for the shield in Blanket #1 would result in the same advantage for the tokamak blanket.

The value of b in Table 5.3.1 is significantly lower for Blanket #3 than for Blanket #1. There are two reasons for this. First, the conductivity through Blanket #3 is slightly lower than that of blanket #1, due mainly to the higher concentration of steel in the manifold region (see Figures 2.1.2 and 2.3.1). Figure 5.4.4 gives the temperature vs. radial distance profile for the two blankets under base case LOFA conditions, at the time at which the maximum first wall temperature is reached in each blanket. Note that the slopes are very similar for the first 32 cm, where both blankets consist of similar fractions of lithium and VCrTi. Beyond that, Blanket #3 consists of a manifold region which contains 80% steel, 10% VCrTi, and 10% lithium, as opposed to 60% steel, 10% VCrTi, and 30% lithium in the manifold region of Blanket #1. Because of the relative conductivities of these three materials [5.4], the conductivity in this region is slightly lower in Blanket #3 than in Blanket #1, causing a larger temperature gradient and a lower value of b in Blanket #3. The second reason has to do with the initial temperature distribution. In Blanket #1, the initial temperature distribution is given in Figure C.2.1 (Appendix C), and has a slight gradient from the first wall to the back of the blanket. Thus, immediately after accident initiation, the temperature of the first wall drops as this gradient flattens out. This contributes to a higher value of b. On the other hand, Blanket

Figure 5.4.4 Effect of Blanket Materials on Spatial Temperature Distribution Following LOPA, Blanket #1 (A2C1PL) vs. Blanket #3 (E4C1PL)

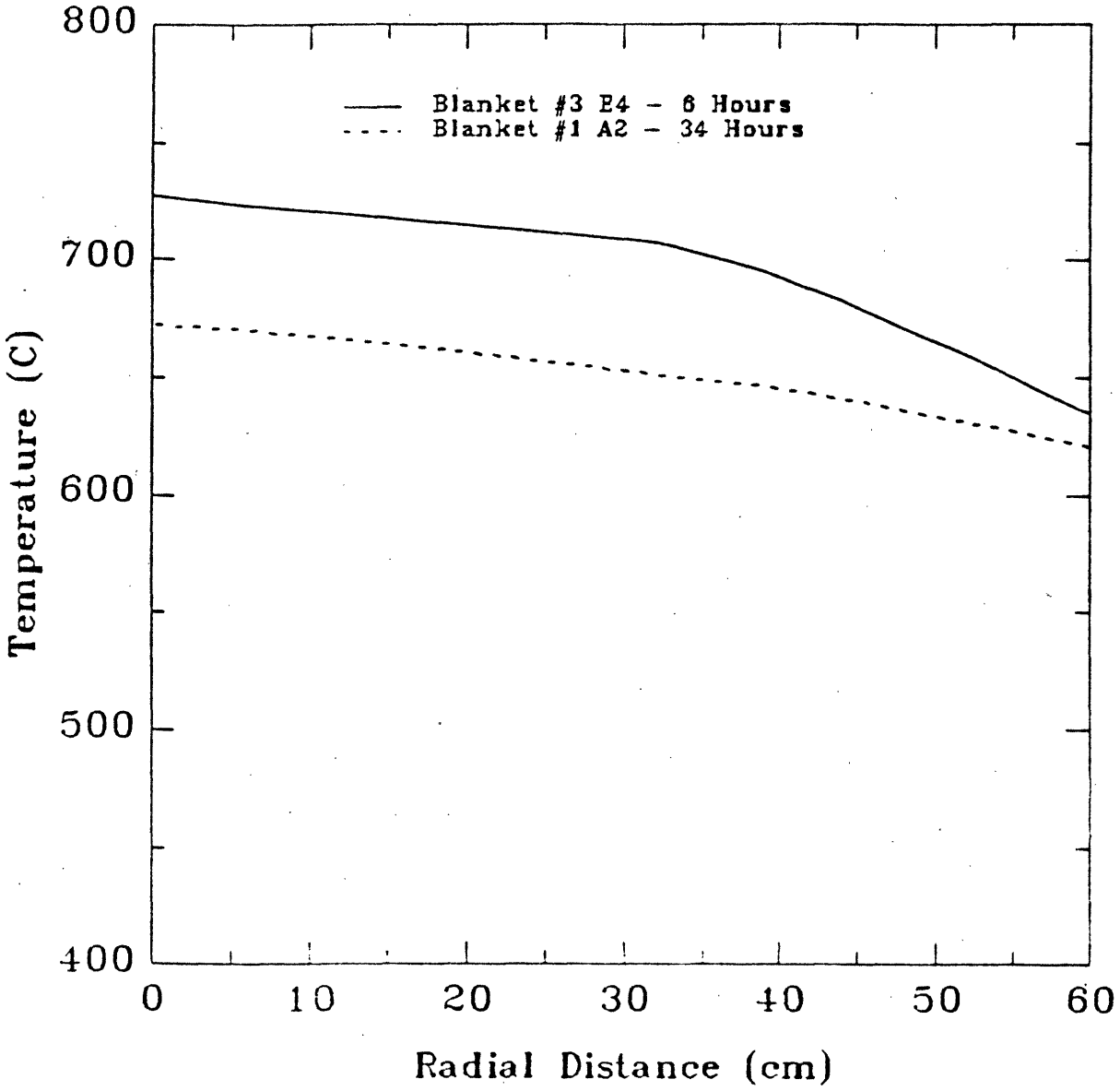

#3 has an initial temperature distribution which is assumed to be flat, i.e., the initial temperature is constant across the blanket [5.15]. This initial distribution is shown in Figure C.2.2 (Appendix C). Thus, after accident initiation, there is no initial temperature drop in the first wall. This leads to a lower value of b. The base case LOFA was analyzed for Blanket #3 with an initial temperature distribution similar to that of Blanket #1. The resulting value of b was -140.3, which shows that most of the difference between the value of b for Blanket #1 and that of blanket #3 is due to the intitial temperature distribution. The thermal coupling between the first wall and heat sink of the two blankets is actually very similar.

5.4.3 Availability of Heat Sink

In the base case scenarios presented in Section 5.2.1, it is assumed that heat will radiate from the back of the shield (or coil in Blanket #3) to some constant temperature heat sink. The fact that this heat sink is removing heat from the system is what causes the temperature to reach a maximum and then decrease. As was stated, in all of the cases, the first wall temperature is decreasing after 48 hours. For instance, in the tokamak blankets, the magnet coil is behind the shield. It is assumed that this coil does not lose cooling, and thus remains at a constant temperature (see Section 5.2.1.2). The shield, therefore, radiates heat to the coil, but the coil remains at a constant temperature, regardless of how much heat it absorbs from the shield. In this way, the coil represents a constant temperature heat sink. It is possible, however, that there will be no "constant temperature"heat sink. That is, it is possible that the coil will also lose cooling, and thus will experience a temperature rise. This would reduce the effectiveness of the coil as a heat sink. In the worst case, the coil temperature would be the same as the shield temperature, and thus no heat would be transferred from the shield to the coil. In essence, this would mean that the shield is insulated, that is, there is no heat sink. The sensitivity to the heat sink availability of some of the blankets is examined in this section.

The thermal coupling of the first wall to the heat sink is represented numerically by the parameter b in equation (5.12) and Table 5.3.1. Having no heat sink essentially means that b will be zero. Blankets with high values of b will be most affected by the lack of a heat sink, since the maximum temperatures in these blankets are kept low by the good thermal coupling. Blankets with low values of b, which are not well coupled to the heat sink anyway, should not be as sensitive to availability of the heat sink.

The undercooling cases of interest in this analyis are Case 1 (base case LOFA) and Case 4. Note in Table 5.2.2 that the parameters for Case 1 and Case 4 are the same except for the heat sink availability. Case 1 assumes the presence of a constant temperature heat sink. Case 4 assumes there is no heat sink, that is, that the back of the shield is insulated. Figures 5.4.5a and 5.4.5b give a graphic illustration of the impact of heat sink availability, by comparing the temperature response of Case 1 with that of Case 4. Each of these figures is a temperature vs. wall load plot. Figure 5.4.5a is for Blanket #1, and Figure 5.4.5b is for Blanket #2.

In Case 1, the temperature reaches a maximum and then decreases, as more and more heat is radiated to the heat sink. Call the time at which this maximum is reached t_{max} (hours). Recall from the discussion in Section 5.4.1.4 that t_{max} is about 34 hours in Blanket #1, and t_{max} is about 1.5 hours in Blanket #2. In contrast, there is no heat sink in Case 4, so all of the heat produced will remain in the blanket/shield system. This means the temperature will continue to rise indefinitely. For this reason, plotting the maximum temperature in Case 4 is not meaningful. No maximum is ever really reached. Instead, what is plotted for Case 4 is the first wall temperature at t_{max}. Again, t_{max} is the time at which the maximum temperature is reached *in Case 1.*

Figure 5.4.5a is for the first wall of Blanket #1. It compares the Case 1 temperature at 34 hours with the Case 4 temperature at 34 hours. Figure 5.4.5b is for the first wall of Blanket #2. It compares the Case 1 temperature at 1.5 hours with

Figure 5.4.5a Effect of Heat Sink on First Wall Temperature 34 Hours After LOPA in Blanket #1 - A2C1PL vs. A2C4PL

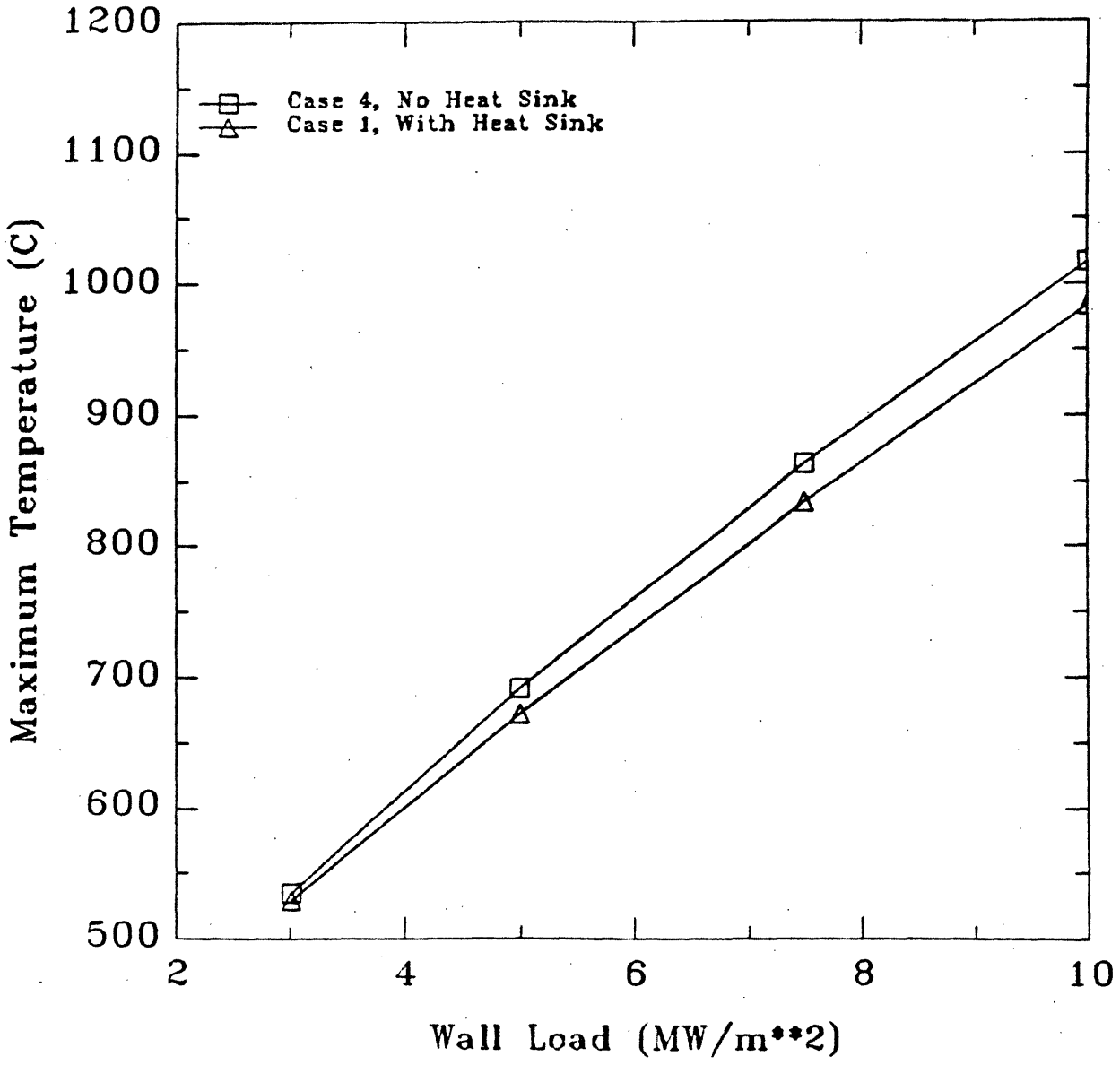

Figure 5.4.5b Effect of Heat Sink on First Wall Temperature 1.5 Hours After LOPA in Blanket #2 – D4C1DC vs. D4C4DC

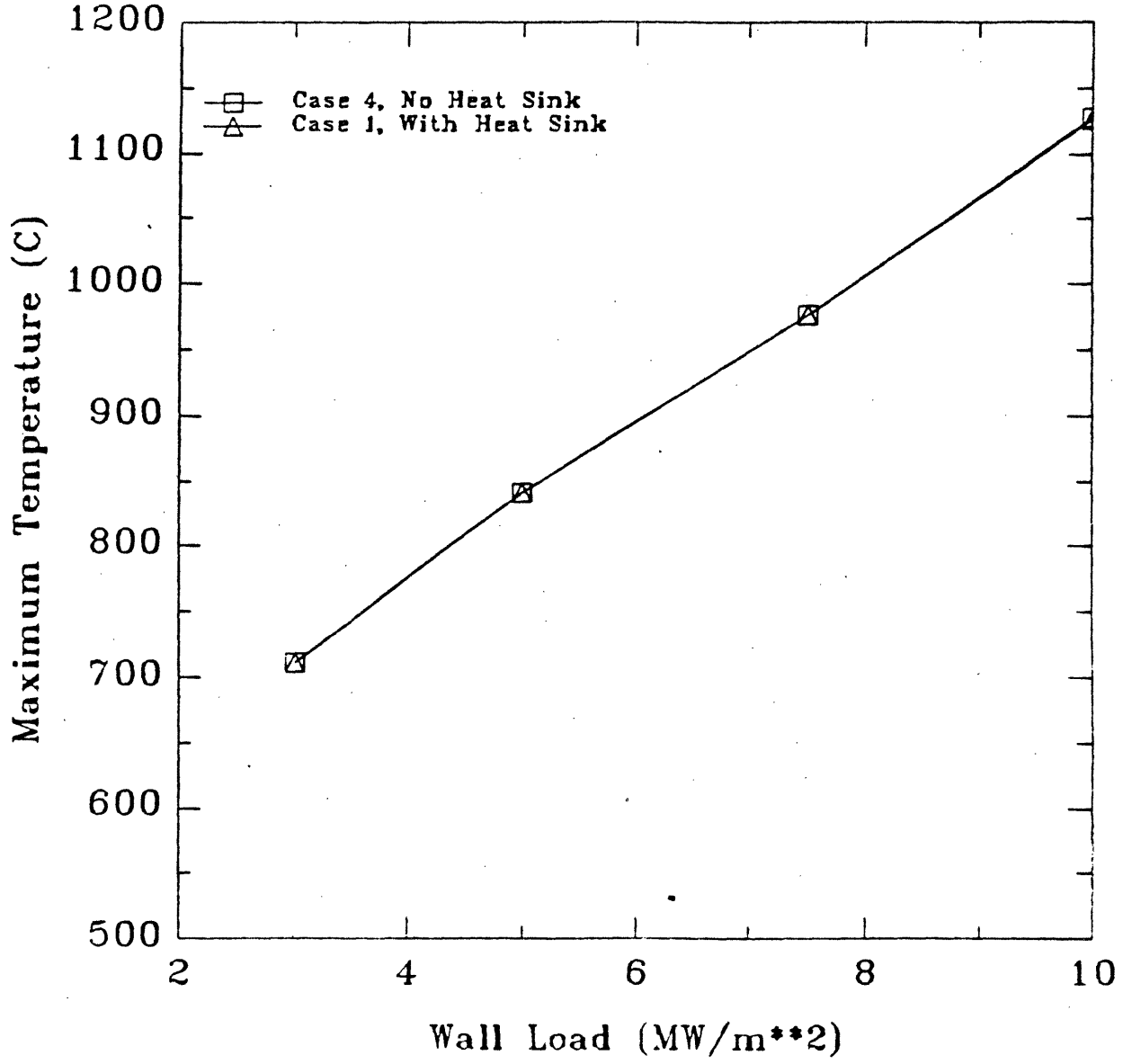

the Case 4 temperature at 1.5 hours. In Case 1, these are the maximum temperatures, that is, the Case 1 temperatures shown in Figures 5.4.5a and 5.4.5b are the same as those shown in Figure 5.3.1 for Blankets #1 and #2 respectively.

Note that for Blanket #1 (Figure 5.4.5a), there is a small but significant difference in the temperatures reached when the heat sink is available as opposed to when it is unavailable. This is as expected, given the high value of b for the Blanket #1 LOFA in Table 5.3.1. For Blanket #2, the temperatures for the two cases are exactly the same. This indicates that the presence (or absence) of a heat sink has no effect on the maximum temperatures reached in Blanket #2, which is also the indication given by the low value of b in Table 5.3.1 for the Blanket #2 LOFA.

Regarding the maximum temperature reached in the first wall in the first 24 hours, the availability of a heat sink will have a small effect on those blankets which are well coupled to the heat sink (high value of b), and no effect on those blankets which are not well coupled to the heat sink. Regarding the overall temperature vs. time behavior of the first wall (and the rest of the blanket), however, heat sink availability is of major concern. Whereas in all the cases presented in the previous sections show the first wall temperature decreasing after 48 hours, it is clear that with no heat sink, the temperature will continue to rise. Figure 5.4.6 shows the temperature vs. time behavior of the first wall of Blanket #1 to the Case 1 LOFA and the Case 4 LOFA. The behavior shown in Figure 5.4.6 is expected, and does not really provide any additional insight into the temperature response behavior. It merely should be stated that the presence of a heat sink is important for long times after accident initiation.

5.4.4 Wall Radiative Emissivity

Compared to conduction, heat transfer via radiation is inefficient, except at high temperatures. For this reason, the limiting pathway for heat to go from the first wall/blanket to the heat sink are the radiation gaps between the blanket and

Figure 5.4.6 Effect of Heat Sink on First Wall Temperature History Following LOPA in Blanket #1 – (A2C1PL) vs. (A2C4PL)

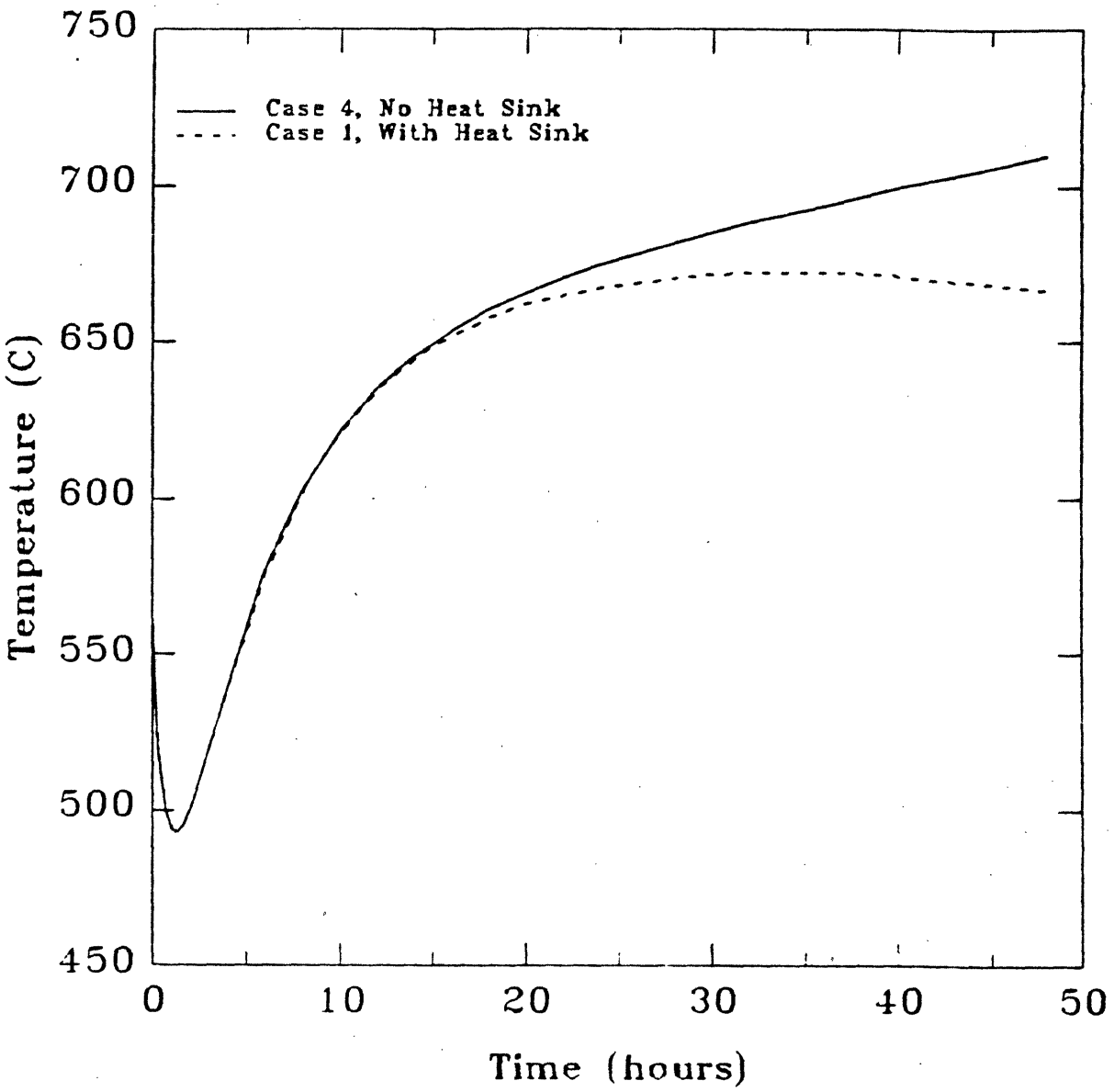

the shield and between the shield and the heat sink. This makes the value of radiative emissivity ϵ on the walls at the back of the blanket, the front and back of the shield, and the front of the heat sink, very important. This parameter represents a significant uncertainty in the temperature response of the first wall, and thus it is important to determine the sensitivity of the first wall temperature response to its value.

In all of the cases presented in the previous sections, the emissivity of the surfaces at the back of the blanket, the front of the shield, the back of the shield, and the front of the heat sink is 0.5 (see Section 5.2.1; note exception of Section 5.4.3). The values of emissivity of all of these surfaces, as well as of the surfaces in the interior of the blanket, were varied in a parametric study to determine the effect on the temperature response.

As in Section 5.4.3, it is expected that the blankets most affected will be those with high values of b, since these rely most on good coupling between the first wall and heat sink to keep the maximum temperatures down. Decreasing the emissivity across the gaps will inhibit the thermal coupling and cause a decrease in the value of b, and hence an increase in the maximum temperature.

Figures 5.4.7a and 5.4.7b show the temperature vs. wall load for Blankets #1 and #2 for the base case LOFA (Case 1) and the Case 3 LOFA, which is the same as the Case 1 LOFA except the emissivity across the vacuum gaps is 0.10 (see Table 5.2.2). As for Figures 5.4.5a and 5.4.5b (see Section 5.4.3), the temperature given for Case 3 is the temperature at the time that the maximum is reached in Case 1, t_{max}. In almost all the instances considered, the Case 3 temperature is still rising after 48 hours, due to the reduced thermal coupling to the heat sink. Thus it is more appropriate to consider the temperature at t_{max} than the actual Case 3 maximum temperature.

The results, as expected, are similar to those given in Section 5.4.3. Blanket #2 temperatures are essentially identical in the two cases, indicating that the maximum

Figure 5.4.7a Effect of Blanket/Shield Thermal Coupling on First Wall Temperature 34 Hours After LOPA in Blanket #1 - A2C1PL vs. A2C3PL

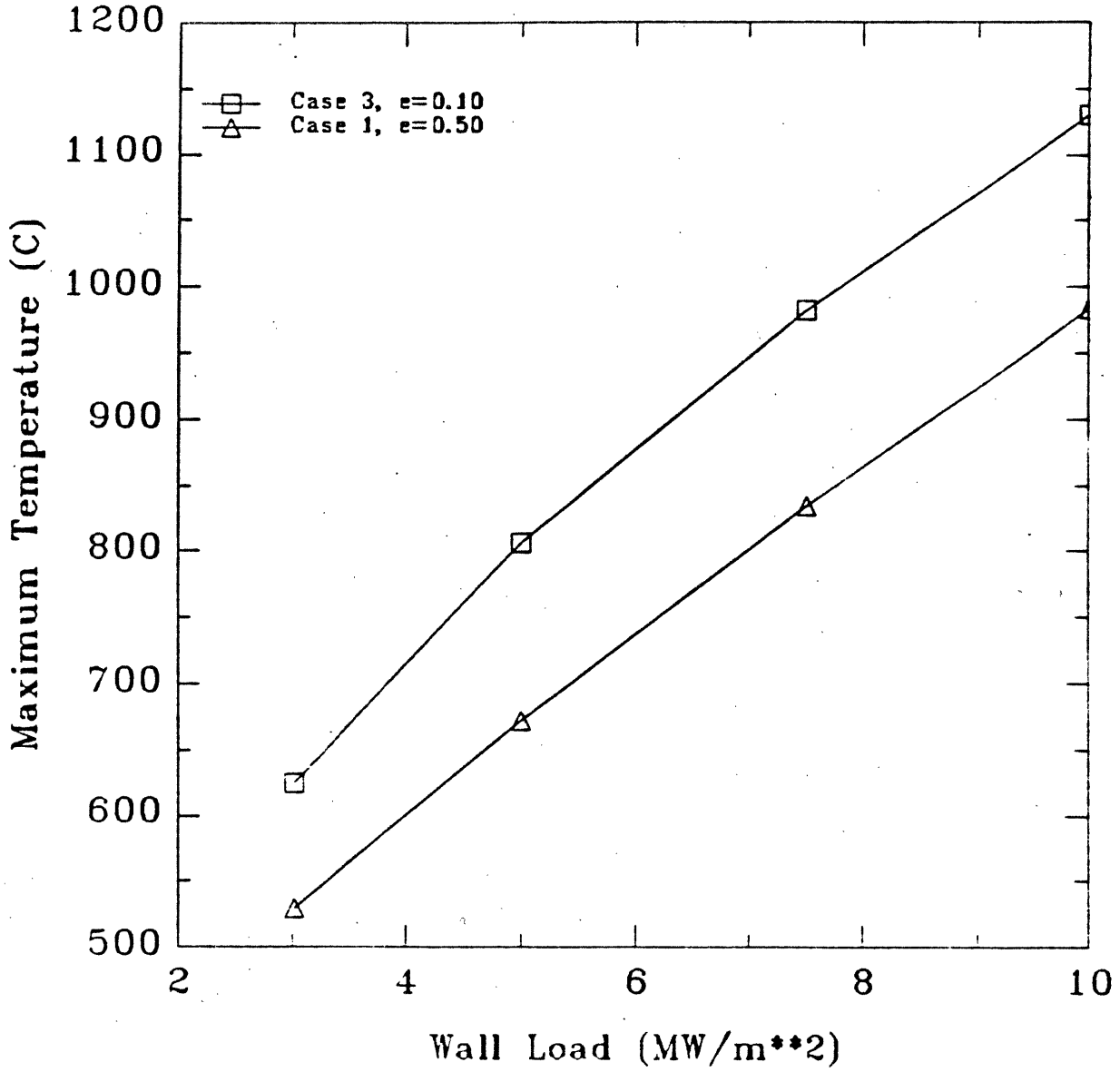

Figure 5.4.7b Effect of Blanket/Shield Thermal Coupling on First Wall Temperature 1.5 Hours After LOFA in Blanket #2 – D4C1DC vs. D4C3DC

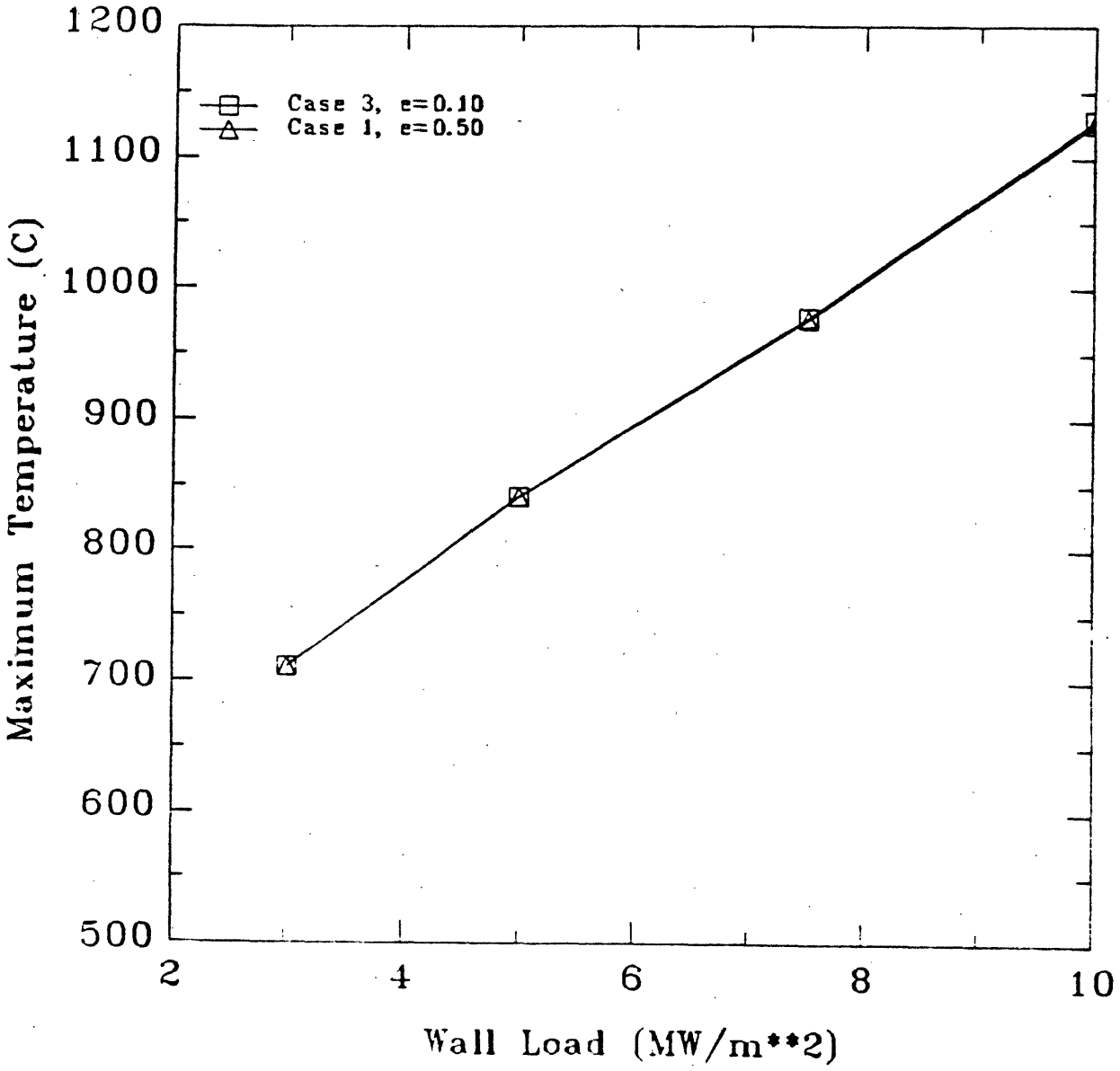

temperature in this blanket does not depend on thermal coupling to the heat sink. In Blanket #1, there is a large difference in the temperatures reached, in fact, much larger than in Figure 5.4.5a. This indicates that the maximum temperature reached in the first wall of Blanket #1 is more sensitive to the coupling of the first wall to the shield than the first wall to the heat sink. That is, the "dumping"of heat from the blanket to the shield is more important in keeping the first wall/blanket temperatures down than the dumping of heat from the shield to the heat sink. Thus, while it was determined in Section 5.4.3 that the heat sink availability was not especially important in terms of the maximum first wall temperature reached within the first 48 hours, it is clear that coupling to the shield is very important. This poses an interesting design problem.

The shield is operated at a low temperature, and the heat deposited in it is essentially wasted, that is, is not recovered in useful form [5.4]. For this reason, effort is made to reduce the fraction of the total heat which is deposited in the shield during operation [5.4,5.25]. There are two ways in which this can be achieved for a given blanket. The first way is to increase the blanket thickness, which decreases the number of neutrons that leak through to the shield [5.25]. The second way is to reduce the thermal coupling between the blanket and the shield, such that heat deposited in the blanket is not transferred to the shield and subsequently lost. That is, during operation, blanket performance is enhanced if the blanket is thermally insulated from the shield. This is the primary purpose of the vacuum gap between the blanket and the shield - to reduce the amount of heat that is lost to the shield during operation. On this basis, it would be desirable to keep the radiative emissivities of the structural walls on either side of this gap as low as possible. Doing this, however, will have adverse effects on the safety margin of the blanket, as is indicated in Figure 5.4.7a.

The problem is to find a trade-off between the degree of blanket insulation required for acceptable normal operating performance (i.e., power output), and the level of thermal coupling between the blanket and the shield required for thermal

safety. The trade-off evolves because any mechanism which further insulates the blanket from the shield, while improving the operational performance of the blanket, will represent a sacrifice in safety. Conversely, any mechanism which improves the thermal coupling between the blanket and the shield will yield a safety benefit, but will also mean an economic penalty (i.e., lower power output, more waste heat).

The ideal solution would be to keep the blanket insulated from the shield during operation, but design a mechanism which would improve the heat transfer between the blanket and the shield in the event of an accident. An example of this type of solution would be to maintain the vacuum gap during operation, but allow the reactor cover gas into this vacuum gap in the event of an accident. This would greatly enhance the heat transfer between the blanket and the shield, and thus reduce the maximum temperature reached in the first wall after the accident. Precisely how to accomplish this is uncertain, but it may be possible to design a fail-safe valve which would open either at accident initiation (sudden plasma shut-off) or when the temperature at the back of the blanket reaches a specified limit. There are also some problems associated with this approach. Most importantly, if the cover gas contains any oxygen, allowing it to come in contact with the hot blanket structure would cause oxidation. This is especially a problem with vanadium (see Section 3.2.2). In blankets that use liquid lithium, oxygen-carrying gases would also increase the likelihood of a lithium-oxygen fire. This approach requires strict control of the content of the reactor cover gas, and it may not be practical. It is perhaps more reasonable to ensure that the structural surfaces on either side of this gap have higher radiative emissivities. While this would increase the heat loss to the shield during operation, it has the benefit of enhanced thermal safety for undercooling events.

The radiative emissivity of in-blanket structural surfaces is much more constrained than that of the outside walls. Making the surface rough, or putting an oxide layer on it, will increase the emissivity [5.26]. However, either of these mechanisms will weaken the corrosion resistance of the structure [5.4]. In terms of

corrosion resistance, it is best to have a shiny, smooth, impurity-free surface. This will generally result in a low emissivity. This is the basis for choosing an emissivity of 0.10 as the base case value for in-blanket surfaces (see Section 5.2.1).

Given these constraints, it is not likely that the in-blanket surfaces can be machined for high emissivity the way the outside walls can. However, it is possible that as a result of corrosion, these surfaces can become rougher and penetrated with corrosive (coolant impurity) elements [5.4]. This in turn can increase the emissivity of the surface. Furthermore, Sparrow and Cess [5.26] report that after repeated heating and cooling, the emissivity of stainless steel will increase. The result is that, while at the beginning-of-life the emissivity of in-blanket surfaces will likely be low due to the desirability of smooth, shiny surfaces, the emissivity can experience a substantial increase during operation, due to corrosion and thermal cycling.

To examine the effect of varying the emissivity of in-blanket structures, the Case 6 LOCA (see Table 5.2.2) was run for Blankets #1 and #2. The Case 6 LOCA is the same as the Case 2 (base case) LOCA except the emissivity of in-blanket structures is 0.50 (instead of 0.10). Figure 5.4.8a shows the maximum temperature reached in the first wall of Blanket #1, as a function of wall load, for these two cases. Note that there is a significant difference (up to 200 °C). This is due solely to the enhanced thermal coupling of the first wall to the heat sink as a result of the increased emissivity. The value of b for the Case 6 LOCA for blanket #1 is 134.1, which is substantially higher than the base case LOCA value of 30.0. Also, the value of a is slightly lower for Case 6. While the ratio of decay heat to heat capacity is the same for the two cases, there is a slight non-linear effect (see Section 5.3) which favors the case with the higher b value.

The Blanket #2 results are shown in Figure 5.4.8b. Note that there is a very large difference in maximum temperature reached, especially at low wall loads. The value of b for the Case 6 LOCA in Blanket #2 is 175.6, which is even higher than

Figure 5.4.8a Effect of Emissivity of in-Blanket Structures on Maximum First Wall Temperature After LOCA in Blanket #1 - A2C2DC vs. A2C6DC

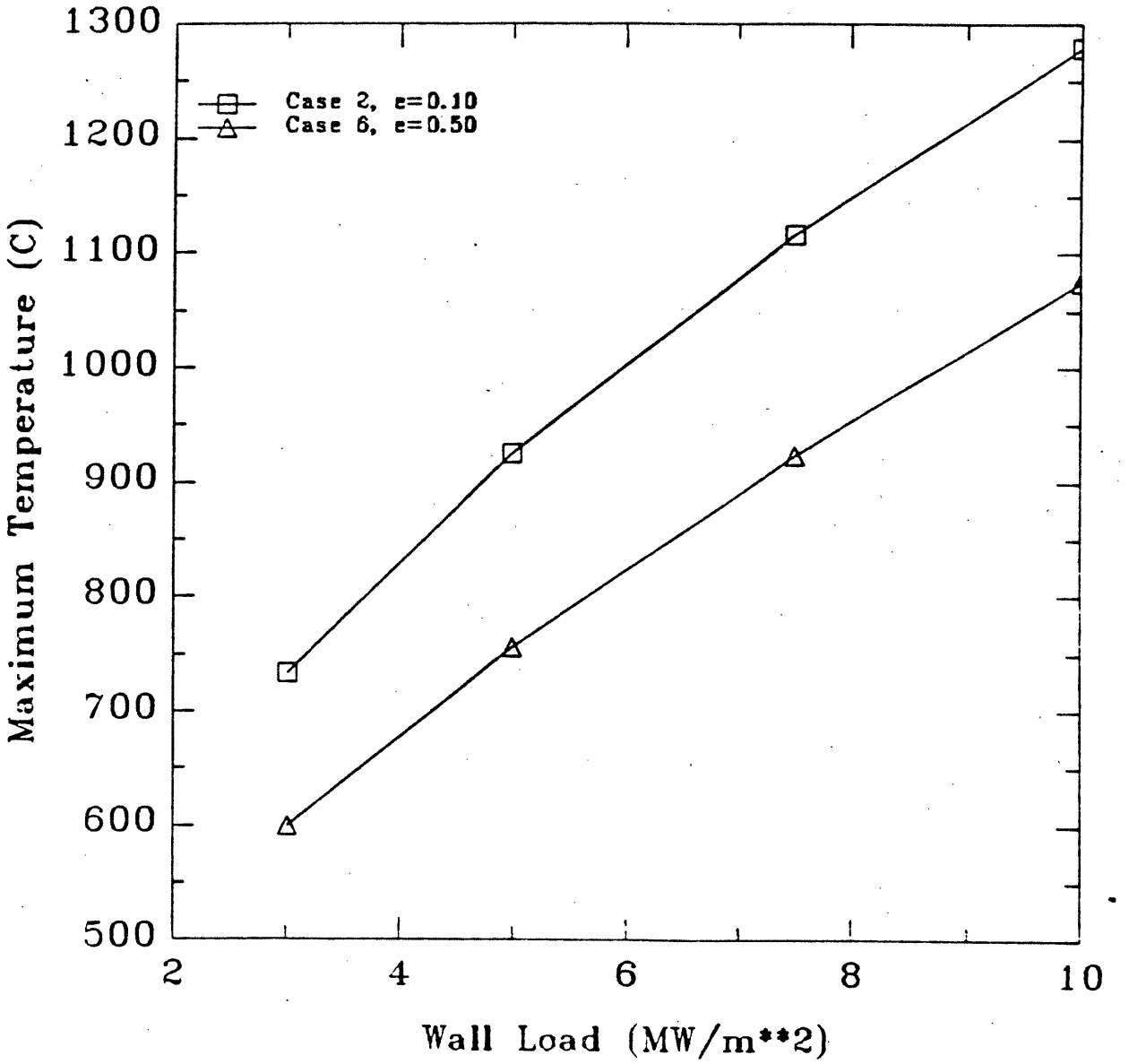

Figure 5.4.8b Effect of Emissivity of in-Blanket Structures on Maximum First Wall Temperature After LOCA in Blanket #2 - D4C2PL vs. D4C6PL

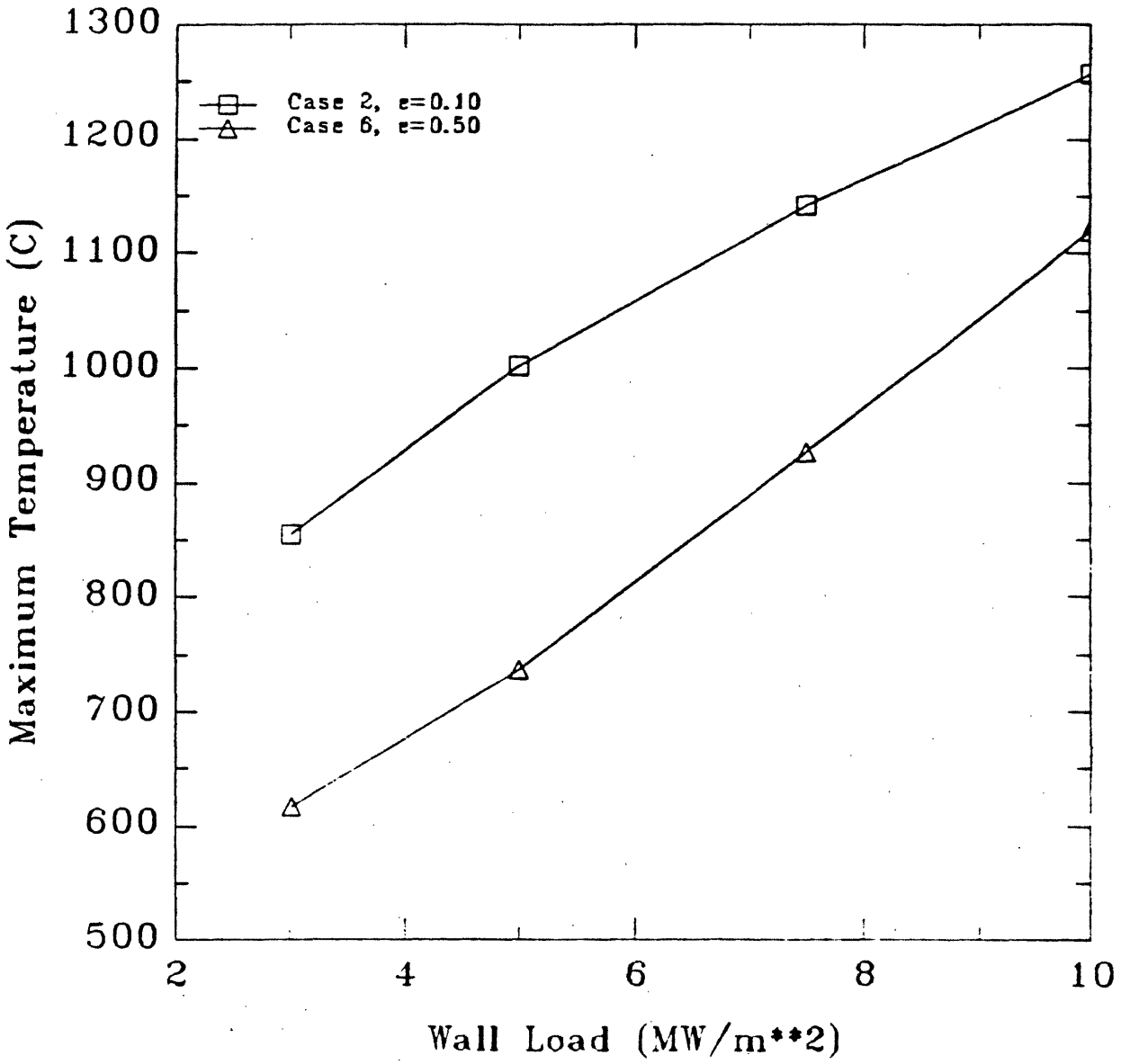

the Blanket #1 value. This is because with the increased emissivity, radiation heat transfer becomes more efficient than conduction, especially at high temperatures.

The conclusion is that the maximum temperature reached in the first wall is sensitive to the radiative emissivity of the in-blanket structures, especially during a LOCA, when the lack of coolant implies that radiation is the only available heat transfer path. It is likely that these emissivities will be low, due to the constraints on the structural surface characteristics and coolant purity as a result of corrosion. However, given its potential impact, further investigation into the emissivity of these surfaces, particularly after operation, is warranted.

5.4.5 Continued Plasma Burn

At accident initiation, i.e., pump failure or pipe rupture, it is not likely that the plasma will immediately stop burning. In fact, the plasma will continue to burn until some outside event causes it to cease. This could be an excessively high first wall temperature, which would cause ablation of the first wall, resulting in a high influx of impurities into the plasma, thus quenching it. Or, the plasma could be shut off by some operator (or automatic) action, such as magnet shut-off, or turning off the pellet injector (plasma fueling) or auxiliary heating. Calculations were done to determine the time-to-failure of the first wall in the event the plasma continues to burn after cooling is lost. These calculations are presented in Chapter 7. For the purposes of the analyses presented in this chapter and in Chapter 6, however, a detailed analysis of the plasma burn rate vs. time behavior after undercooling accident initiation was considered beyond the scope of this work. Thus, the simplified plasma shutdown time was taken as shown in Figure 5.1.2. Additional discussion regarding the assumption of continued plasma burn vs. immediate plasma shut-off is given in Section 5.2.1. The uncertainty surrounding these assumptions warrant that the impact of continued plasma burn on the temperature response be examined.

As far as the maximum first wall temperature is concerned, it is expected

that blankets in which the first wall is thermally well coupled to the rest of the blanket will not show a large difference between the continued-plasma-burn (PL) and decay-heat-only (DC) cases. Blankets wih thermally insulated first walls, such as Blanket #2, will show a larger difference. This is because well coupled first walls will not sustain a temperature gradient; that is, as the first wall temperature rises due primarily to the plasma heat flux, the heat will be immediately transported to the rest of the blanket, thus minimizing the plasma-induced peak. First walls which are more insulated will become very hot before they begin to cool off due to conduction or radiation.

The plasma-continuation (PL) and decay-heat-only (DC) cases were run for both the base case LOFA and LOCA for Blankets #1 and #2. The results verify the expected behavior. The smallest difference between the PL maximum temperature and the DC maximum temperature occurs in the Blanket #1 LOFA, where the thermal coupling is the best (note the value of b in Table 5.3.1), whereas the largest difference occurs in the Blanket #2 LOCA. It should be noted that even in the Blanket #2 LOCA, the difference in the maximum temperature reached is less than 25 °C. This indicates that in terms of maximum temperature, plasma continuation in the mode shown in Figure 5.1.2 has a very small effect. This behavior contributes the equivalent of three full-power seconds of plasma burn. Plasma continuation for longer times would have a larger effect, but given the uncertainty in the plasma shutdown mode, and its relatively minor effect, no further analysis regarding this issue was conducted.

In both the plasma-continuation and decay-heat-only scenarios, the temperature response of the first wall is very similar for times after the first 30 minutes, with only a small difference in the maximum temperature reached. In terms of the temperature response of the first wall for short times after accident initiation, however, when operator (or automatic) mitigation schemes would be minimal, the continued plasma burn can have a significant impact. The plasma-induced peaks are reached within five seconds, whereas the decay-heat induced peaks are not reached for a

number of hours. The analysis presented in Chapter 7 focuses on the short term impact of continued plasma burn on the first wall structural integrity.

In terms of the structural damage that results from the overall, 48 hour first wall temperature response, the difference between the PL and DC cases is extremely small. In the Blanket #1 base case LOFA, at 10 MW/m^2, the PL case reaches a thermal creep rupture fraction of 4.0e-03, vs. 3.2e-03 for the DC case. At lower wall loads, the rupture fractions accumulated after 48 hours are very similar in the PL and DC cases as well. Similar results are found in the Blanket #1 base case LOCA. In Blanket #2, due to the reduced thermal coupling, the differences are more significant. In the base case LOFA, assuming the plasma continues to burn leads to thermal creep rupture in the first wall in 10 seconds, whereas the rupture time in the DC case is about 30 minutes. In the base case LOCA, acute structural failure is assumed to occur at wall loads of 5 MW/m^2 and above (caused by exceeding 900 °C temperature limit; see Chapter 3) for both the PL and DC cases. The difference is in the time it takes to exceed the 900 °C limit. In the DC case, it takes 40 minutes at a wall load of 5 MW/m^2, and 15 minutes at a wall load of 10 MW/m^2. In the PL case, it takes 20 minutes at 5 MW/m^2. At wall loads above this, the 900 °C limit is exceeded in the first five seconds, due to the plasma induced temperature rise. Again, Chapter 7 provides additional discussion on this issue as it relates to the time available to mitigate the accident. In any case, it is recommended that some effort be made to characterize the behavior of plasma burn following an accident.

The overall conclusion is that the temperature response, and the resulting structural damage, is not very sensitive to whether the plasma continues to burn for a few seconds, or it turns off immediately at accident initiation. The effect is larger for blankets which have thermally-insulated first walls, such as Blanket #2.

5.5 Inboard vs. Outboard

In Section 4.5, the decay heat level of the outboard side of Blanket #1 was compared with that of the inboard side. The results show that while the higher neutron fluxes on the outboard side lead to higher decay heat densities in regions near the first wall, the increased thickness of the outboard shield result in a lower *average* decay heat density on the outboard side. This lower average should translate into a lower temperature rise.

Figure 5.5.1 shows the maximum temperature reached in the first wall after the base case LOFA (Case 1) for the inboard and outboard sides of Blanket #1. The results presented here assume immediate plasma shut-off, so plasma burn effects will not affect the results of this comparison. It is interesting to note that the maximum temperatures reached on the outboard side are higher than on the inboard side, contrary to the results presented in Section 4.5. The reason for this is the higher decay heat densities in the first wall and blanket regions on the outboard side. This is partially offset by the presence of the very large outboard shield, which has a low average decay heat density. As is presented in Section 4.5, the decay heat density in the first wall and blanket of the outboard side is 15% - 20% higher than on the inboard side. Note from Figure 5.5.1 that the actual maximum temperature rise is only about 4% higher on the outboard side, so it is seen that the larger outboard shield does partially offset the higher decay heat density in the first wall. It is expected that if the thermal coupling to the shield was improved, the impact of the large outboard shield would increase, and the maximum temperatures reached on the outboard side would be lower than those on the inboard side.

The effect of the overall lower average decay heat density on the outboard side can be seen more clearly by comparing the results of the Case 4 LOFA. The Case 4 LOFA is the same as the base case LOFA, except there is no available heat sink. In the base case LOFA, the temperature at the back of the inboard shield is higher than at the back of the outboard shield. Thus, more heat is radiated to the

Figure 5.5.1 Maximum First Wall Temperature Following LOFA vs. Wall Load for Inboard and Outboard Versions of Blanket #1, With Heat Sink Available – A2C1DC

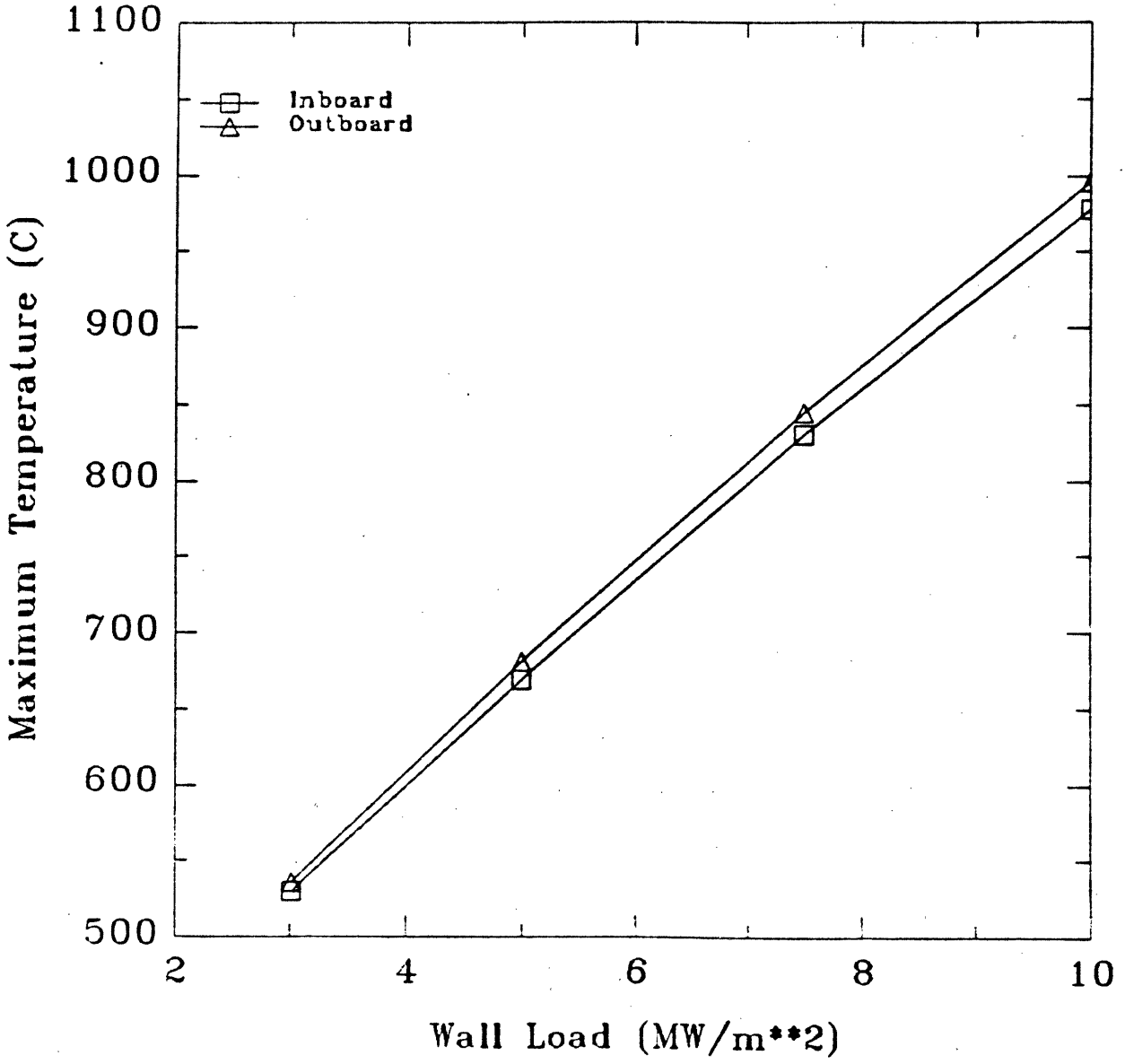

Figure 5.5.2 Maximum First Wall Temperature Following LOFA vs. Wall Load for Inboard and Outboard Versions of Blanket #1 With No Heat Sink Available (Insulated Shield) – A2C4DC

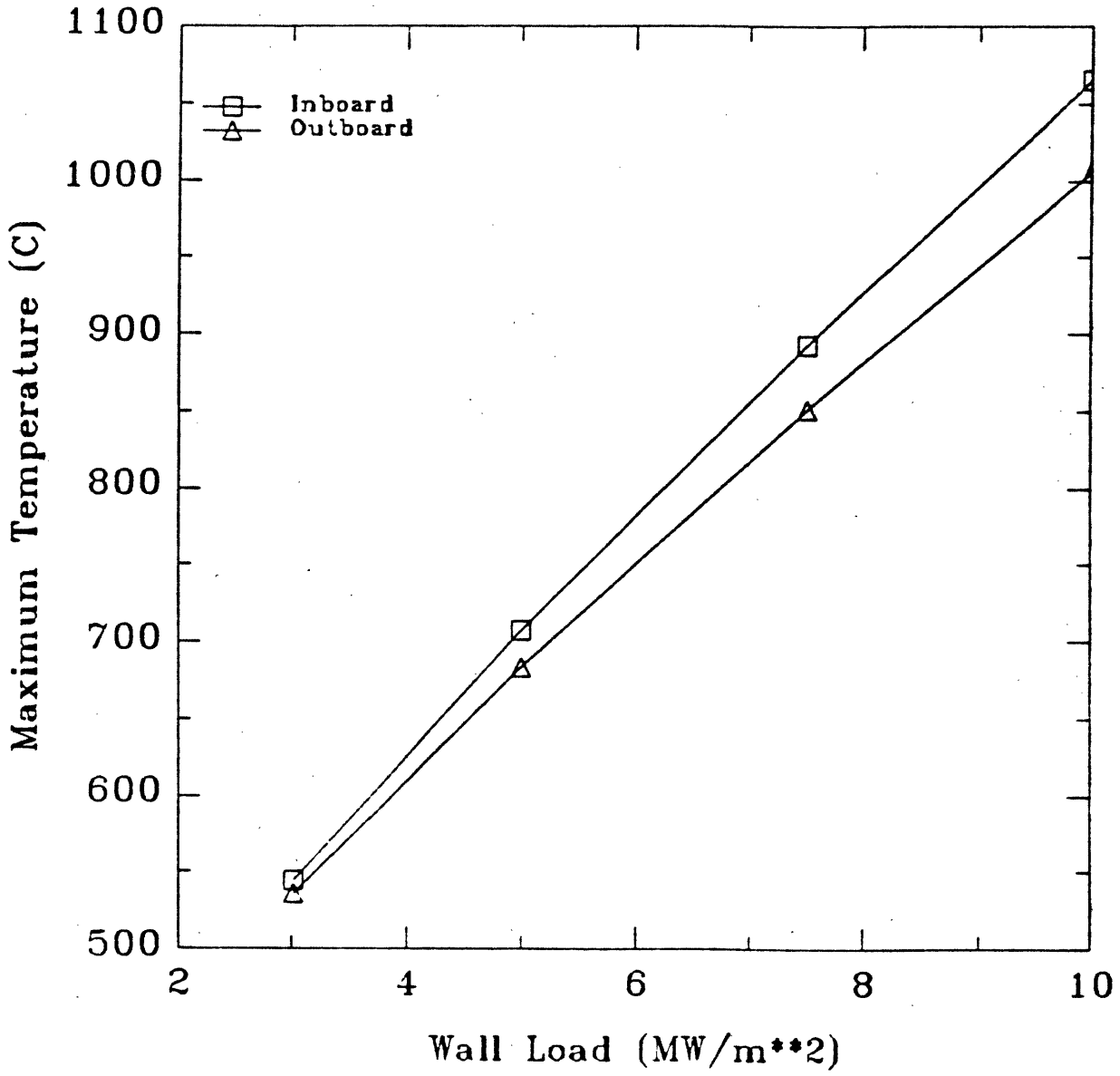

heat sink on the inboard side, which contributes partially to the lower maximum temperatures on the inboard side seen in Figure 5.5.1. If the heat sink is removed, and the blanket/shield system is isolated, then the temperature rise will depend exclusively on the ratio of total decay heat to total heat capacity. This ratio is lower on the outboard side. Figure 5.5.2 shows the temperature at 48 hours vs. wall load behavior of the inboard and outboard first walls following the Case 4 LOFA. In both instances, the temperatures are still rising at 48 hours, due to the insulated boundary condition. Note that here, the inboard temperatures are about 15% higher than the outboard temperatures.

In summary, the higher decay heat density in the front regions of the outboard blanket, due to higher neutron fluxes, will result in higher maximum temperatures in the base case scenarios. The additional heat capacity on the outboard side provided by the larger shield will reduce this effect somewhat. If the systems are insulated, then the additional heat capacity (i.e., lower average decay heat) on the outboard side will result in a lower temperature rise.

5.6 Cylindrical vs. Slab Geometry

The heat transfer model used in THIOD, as described in Section 5.1, uses slab geometry. It is assumed that a slab representation of the actual blanket geometry should introduce negligible error in the calculations. To verify this assumption, the code was modified to use cylindrical geometry. Details of this modification are included in Appendix D. The results of the cylindrical analysis are compared to the slab model in this section.

There are two ways to view the toroidal geometry of the tokamak (or RFP). The first is from an overhead view, such as that shown in Figure B.2.1, where the torus is assumed to be a vertical annular cylinder, and the θ direction is the toroidal direction. It is seen that with this view, the slab approximation overestimates the blanket volume on the inboard side and underestimates the blanket volume on the

outboard side. The decay heat source is calculated as a *density*, i.e., W/cm^3, thus adding or subtracting volume will not necessarily change the ratio of decay heat density to volumetric heat capacity. However, the decay heat source is highest at the first wall and lowest at the back. This means that the slab approach will underpredict the decay heat to heat capacity ratio on the inboard side and overpredict the ratio on the outboard side. Thus, it is expected that the temperatures predicted with the slab approximation will be lower than the cylindrical approach on the inboard side, and higher than the cylindrical approach on the outboard side.

The second way to view the torus is from the centerline of the plasma, where the θ direction is the poloidal direction. In this view, it is clear that the slab will always underestimate the blanket volume at the back of the blanket, and thus overestimate the temperature rise. On the inboard side, the toroidal and poloidal views are opposing, and the net result will depend on the aspect ratio and blanket thickness. On the outboard side, the two views are parallel, and thus the cylindrical approach will result in a lower temperature than the slab approach.

The RFP Blanket #3 was chosen as the example to do the cylindrical vs. slab analysis. The reason for this is that in the RFP, unlike the tokamak, the inboard and outboard blankets are the same. Thus, the toroidal and poloidal cylindrical variations could be compared without having to do separate analyses for the inboard and outboard sides. The effect of using cylindrical geometry with the toroidal view is discussed first, followed by the results of the poloidal cylindrical analysis. Finally, the two effects are combined to get an indication of the overall effect of using a slab approximation for the actual toroidal geometry. For the purposes of this discussion, it is convenient to define the ratio of decay heat to heat capacity as β, where

$$\beta = \frac{q'''_{\text{decay}}(r)}{\rho c_p(r)} \tag{5.21}$$

where $q'''_{\text{decay}}(r)$ is merely the decay heat density $\dot{q}'''_{\text{decay}}(r,t)$ integrated over time.

Figure 5.6.1 shows the maximum temperature vs. wall load in the first wall of Blanket #3 for the base case LOCA (Case 2) using slab geometry, the inboard and outboard sides of the toroidal cylinder, and the poloidal cylinder. The results exhibit the expected behavior. The inboard toroidal cylinder has the least volume at the back of the blanket, where β is the smallest. Thus, the volume-averaged value of β in this case is larger than the slab case, and hence the temperature rise is higher. The outboard toroidal cylinder has *more* volume at the back, where β is the lowest, and thus the volume-averaged value of β for this case is lower than the slab, and the temperature rise is lower.

In both the inboard and outboard toroidal cases, the magnitude of the difference between the slab and cylindrical temperature rise depends on the ratio of blanket thickness to first wall radius. This essentially represents the degree of curvature of the cylindrical annulus that defines the blanket in the toroidal cylindrical geometry. Note on the inboard side of Blanket #3, the ratio of blanket thickness to first wall major radius is

$$C_i = \frac{X}{R-a} \tag{5.22}$$

where

C_i represents the degree of curvature of the inboard blanket,

X is the blanket thickness,

R is the major radius, and

a is the minor radius.

On the outboard side, this ratio would be

$$C_o = \frac{X}{R+a} \tag{5.23}$$

Figure 5.6.1 Effect of Model Geometry on Maximum First Wall Temperature Following LOCA for Blanket #3 – E4C2DC

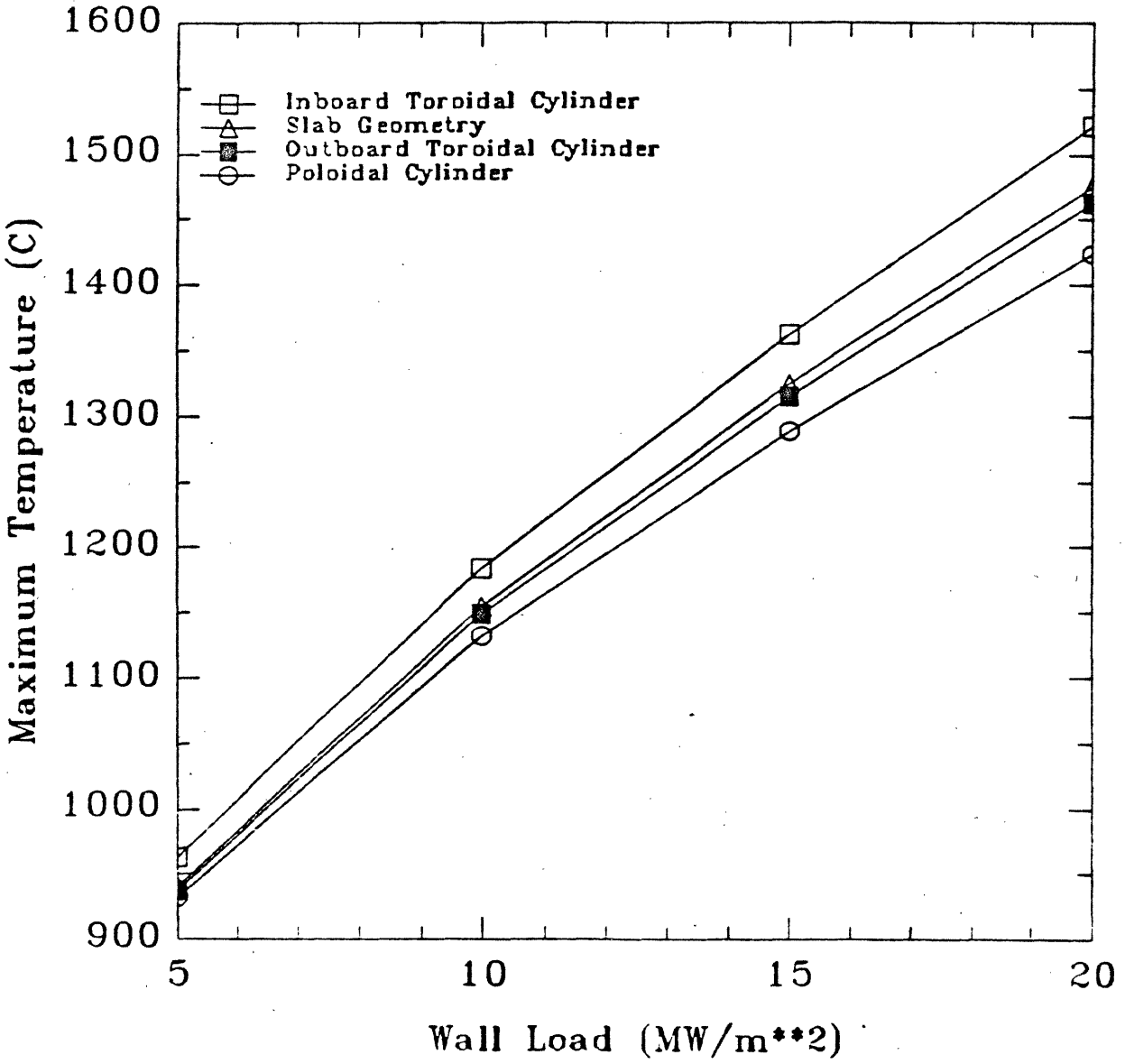

where

C_o represents the degree of curvature of the outboard blanket.

For the RFP Blanket #3, the values of X, R, and a are 0.805 m, 4.225 m, and 0.65 m respectively, where X includes the magnet coils. Thus, the values of C_i and C_o are

$C_i = 0.225,$

$C_o = 0.165.$

It is expected, then, that the difference between the slab and toroidal cylinder results will be greater for the inboard side than the outboard side. This is clearly the case in Figure 5.6.1. Note that in the STARFIRE tokamak geometry used for Blanket #1, $C_i = 0.26$ and $C_o = 0.25$, so the effect in the tokamak will be slightly more pronounced than in the RFP.

For the poloidal cylinder, the difference between the cylindrical and slab results will depend on the ratio of the blanket thickness to the first wall minor radius plus the blanket thickness, i.e.,

$$C_p = \frac{X}{a + X} \tag{5.24}$$

The value of C_p is 0.55, which is higher than C_i, indicating that the difference between the toroidal inboard cylinder and the slab is smaller than the difference between the poloidal cylinder and the slab. This again is the case in Figure 5.6.1, although the two are very similar.

To determine the effect of the actual toroidal geometry, the two cylindrical approaches must be combined. On the inboard side, as was mentioned, the two are opposite, that is, the toroidal cylinder yields a higher temperature rise, whereas the poloidal cylinder yields a lower temperature rise than the slab. To get an idea of

how the two effects will combine, the ratio of the temperature rise for each case can be multiplied. That is, the temperature rise in the slab, toroidal inboard cylinder, and poloidal cylinder cases at 15 MW/m^2 are defined as

ΔT_{slab} = Maximum temperature rise in slab case.

$\Delta T_{\text{inb.tor.}}$ = Maximum temperature rise in toroidal inboard cylinder case.

$\Delta T_{\text{pol.}}$ = Maximum temperature rise in poloidal cylinder case.

Then the ratios are defined as

$$R_{\text{it}} = \frac{\Delta T_{\text{inb.tor.}}}{\Delta T_{\text{slab}}} \tag{5.25}$$

$$R_{\text{pl}} = \frac{\Delta T_{\text{pol.}}}{\Delta T_{\text{slab}}} \tag{5.26}$$

To get the net effect of the two cylinders, the two ratios are multiplied to get the net ratio,

$$R_{\text{net}} = R_{\text{it}} \times R_{\text{pl}} \tag{5.27}$$

The same can be done for the outboard side, with R_{it} being replace by R_{ot}.

By inserting the values of the ΔT's into equations (5.25) and (5.26), the net ratios can be found. The values are

$R_{\text{it}} = 1.052$,

$R_{\text{ot}} = 0.986$, and

$R_{\text{pl}} = 0.949$.

Thus, on the inboard side,

$$R_{net,inb} = 0.998,$$

and it is seen that the two effects just about exactly cancel. Thus, given the geometry of the RFP Blanket #3, on the inboard side the slab approximation introduces negligible error in the temperature response calculation. On the outboard side, where the two cylindrical effects both give a lower temperature rise than the slab case,

$$R_{net,out} = 0.936.$$

Here it is seen that there is a significant (although small) error introduced by using a slab geometry. Recall from Section 5.2.1 that for the RFP Blanket #3, the outboard blanket was analyzed. This means that the temperature responses given for Blanket #3 in the previous sections are conservative by about 6% due to geometry effects. This difference, while significant, is not sufficient to change any of the conclusions regarding this blanket given in the previous sections.

The overall conclusion is that the error introduced by representing toroidal blankets with slab geometry depends on the ratio of the blanket thickness to the major and minor radii. On the inboard side, toroidal and poloidal effects cancel, and the slab approximation is adequate. On the outboard side, toroidal and poloidal effects combine, and the slab approximation will overestimate the temperature rise slightly. The error introduced is on the conservative side and is not so large as to be of major concern.

5.7 Summary

Transients involving loss-of-system-cooling are the most commonly considered mechanisms that result in elevated temperatures. Loss-of-cooling transients are generally divided into two groups, namely, Loss-of-Flow Accidents (LOFA) and Loss-of-Coolant Accidents (LOCA). The temperature response to these accidents, using a model that considers heat conduction and radiation only, was analyzed in

this chapter. The temperature histories calculated were analyzed with the temperature limit models developed in Chapter 3 to determine the potential for structural failure. The temperature histories of different blankets were compared to determine design features which lead to enhanced thermal safety. Also, some operational parameters were varied to determine the post-accident temperature sensitivity to these parameters, as well as develop operational guidelines which will help insure thermal safety.

The development of the model used to calculate the temperature response, a computer code called THIOD, is described in Section 5.1.1 and Appendix D. The assumptions used to define the accident scenarios are described in Section 5.1.3.

5.7.1 Temperature Response to Base Case Accidents

In Section 5.2.1, the parameters that correspond to the "base case" LOFA and LOCA are discussed. This is followed by an analysis of the temperature response to these base case transients of four of the six blankets presented in Chapter 2. The six blankets chosen encompass the range of design variations considered in this work.

The Li/Li/VCrTi tokamak Blanket #1 is found to be inherently safe from structural damage at the nominal neutron wall load of 5 MW/m^2 for both the base case LOFA and LOCA, as long as no oxygen is allowed to leak into the system. In the event of oxygen in-leakage, the temperatures reached in the LOCA are sufficient to cause rapid oxidation of the vanadium structure, resulting in gross first wall failure. In any case, critical radio-isotope release is not expected on the basis of response to decay heat. Note that this result does not consider the possibility of a lithium fire.

At the nominal neutron wall load of 5 MW/m^2, the Li_2O/He/MT-9 tokamak Blanket #2 will likely suffer thermal creep rupture in the base case LOFA, due primarily to the high pressure stress in the first wall assumed in this case. The base case LOCA will result in acute structural failure of the first wall. In both instances,

the failure will occur in about 30 minutes. The MT-9 structure does not suffer from the oxidation problems that VCrTi does, and neither of these accidents will release significant radioactivity.

The Li/Li/VCrTi Reversed-Field-Pinch (RFP) Blanket #3 operates at a much higher wall load (15 MW/m^2) than the tokamak blankets. This high wall load is directly responsible for a large temperature rise in the event of loss-of-cooling. In the base case LOFA, no structural damage is likely to occur at this nominal wall load, but the safety margin is very small. It should be pointed out that in the event of a LOFA which is caused by flow blockage, in which the pressure induced first wall stress could remain high ($\sim$ 100 MPa), thermal creep rupture is likely to occur at about the 20 hour mark (see Table 5.2.3). The base case LOCA is likely to cause acute structural failure in about an hour. If oxygen does get into the system, vanadium oxidation, coupled with the extremely high temperatures, could lead to the mobilization of a significant fraction of the radioactive inventory. For this reason, it is highly recommended that in the design of high wall load, high power density machines, safety issues receive considerable attention.

Due to the nature of the D-D fuel cycle, the D-D tokamak Blanket #6 operates at a much lower neutron wall load (1.17 MW/m^2) than the D-T blankets. This gives the D-D blanket a significant advantage in terms of thermal safety. The temperatures reached in both the base case LOFA and LOCA are very manageable in terms of thermal safety. However, the base case LOFA will likely cause thermal creep rupture in Blanket #6, due primarily to the high pressure stress in the first wall, which stems from the continued presence of the high pressure coolant. The base case LOCA will not lead to structural failure, indicating that it would be beneficial to depressurize the coolant in the event of a LOFA.

5.7.2 Impact of Wall Load Variations

For all of the blankets, the thermal analysis was carried out over a range of

neutron wall loads, to determine the sensitivity of the post-accident temperature to the operational wall load. The results indicate that the maximum temperature reached after an accident is linearly dependent on the wall load (Γ_n), as is shown in Figures 5.3.1 and 5.3.2. To examine this effect, it is convenient to define the *temperature rise*, ΔT, as

$$\Delta T = T_{max} - T_o \tag{5.11}$$

where T_o is the initial temperature of the first wall.

The linear dependence of T_{max} on Γ_n allows us to express ΔT as

$$\Delta T = a\Gamma_n - b \tag{5.12}$$

where a and b are constants. The values of a and b for all of the blankets, in both the LOFA and LOCA scenarios, are given in Table 5.3.1. The temperature rise ΔT is related to the total heat produced in the blanket (Q_{tot}), the heat storage capacity of the blanket (C_{tot}), and the total heat that is transferred to the heat sink (Q_{HS}), where Q_{tot}, C_{tot}, and Q_{HS} are defined mathematically in equations (5.13) to (5.15). Furthermore, the total heat produced in the blanket is a linear function of the neutron wall load, as is shown in equation (5.17). The relation between ΔT and the parameters given in equations (5.13) to (5.15) and (5.17) is

$$\Delta T = \frac{q_t}{C_{tot}}\Gamma_n - \frac{Q_{HS}}{C_{tot}} \tag{5.18}$$

which is seen to have the same form as equation (5.12). By comparing equations (5.12) and (5.18), it is seen that

$$a = \frac{q_t}{C_{tot}} \tag{5.19}$$

$$b = \frac{Q_{HS}}{C_{tot}} \tag{5.20}$$

Equations (5.19) and (5.20) provide an important physical insight into the components of the temperature rise ΔT. Referring to equations (5.12), (5.19), and (5.20), the parameter a is the ratio of the time-integrated decay heat density to the heat storage capacity of a particular blanket. This is primarily a material property, although it is affected by other factors, such as the neutron spectrum. The parameter b essentially represents the thermal coupling between the first wall and the heat sink, and is more a function of the geometric design of a particular blanket, although it also is a material property. Blankets with good radial conduction paths and high radiative emissivities will have high values of b. In terms of minimizing the temperature rise, it is clearly desirable to have a low value of a and a high value of b. This represents a useful design tool from the standpoint of thermal safety. Candidate blanket materials can be compared by comparing their a values, whereas different geometric configurations can be compared by comparing their b values.

The maximum temperature vs. wall load analysis is also useful in defining maximum allowable wall loads. By using the temperature histories in conjunction with the material limits models presented in Chapter 3, the minimum wall loads required to cause structural failure and radioactive release can be calculated. Since these wall loads are the minimum required to cause failure, they are also the maximum allowed to avoid failure. The wall loads required to cause thermal creep rupture, acute structural failure, and radio-isotope release for some of the blankets are given in Table 5.3.2. Operation at or above the wall loads shown in Table 5.3.2 will result in the specified failure in the particular accident scenario, i.e., LOFA or LOCA. Examination of Table 5.3.2 allows the following general conclusions regarding the safety performance of the four blankets considered under the LOFA/LOCA conditions.

Excluding the possibility of oxygen in-leakage, Blanket #1 meets the criteria

for inherent safety at its nominal neutron wall load (5 MW/m^2). Blanket #2 will likely suffer structural failure at its nominal wall load (also 5 MW/m^2), but poses no threat to the public from radio-isotope release. At the nominal wall load of 15 MW/m^2, Blanket #3 will almost certainly suffer structural failure, and has the potential to release a significant fraction of its radioactive inventory. This is due solely to the high operational wall load of this blanket. Finally, the D-D Blanket #6 could possibly suffer structural failure, but also could be considered passively safe, at its nominal wall load of 1.17 MW/m^2. Whether it fails depends on whether the coolant can be depressurized in the event of a LOFA. Depressurizing the coolant would not greatly affect the temperature response, but would greatly reduce the first wall stress. In any case, this blanket also poses no threat in terms of radio-isotope release.

5.7.3 Impact of General Variations

Other than the wall load, a number of other parameters were varied to determine their effect on the temperature response, and the different blankets were compared in attempt to define design guidelines that improve thermal safety. These variations included materials selection, geometric configuration, availability of a heat sink, the radiative emissivity of structural surfaces, and the impact of continued plasma burn. A summary of the obtained results follows.

5.7.3.1 Materials Impact

A number of comparisons between different materials were made. This included comparisons between structural materials, breeder materials, and the effect of a neutron multiplier.

The decay heat behavior of the structural steels MT-9 and Fe1422 was analyzed and compared in Section 4.2.1.4. Note that MT-9 is a version of HT-9 which

has been modified for low activation [5.21], and is used throughout this study. In this analysis, it was calculated that Fe1422 produces as much as an order of magnitude more decay heat than the modified MT-9. This additional decay heat has a substantial impact on the temperature response, such that blankets that use Fe1422 as the manifold structural material are subject much higher temperatures in the event of a LOFA/LOCA than those which use MT-9. For this reason, the use of Fe1422 in any of the blanket regions is not recommended. While MT-9 is more expensive than Fe1422, the improvement in thermal safety that MT-9 provides will easily offset the cost. This is true for other low activation steels as well, such as those proposed by Gelles et. al. [5.28].

Due to the production of radioactive isotopes of lead, the breeder material $Li_{17}Pb_{83}$ produces substantially more decay heat than liquid lithium †. Furthermore, liquid lithium has a higher volumetric heat capacity and a higher thermal conductivity than LiPb, making it a better heat sink and heat transfer medium. Thus, the temperature rise after a LOFA in liquid lithium blankets will generally be lower than in LiPb blankets. On the other hand, if the accident (i.e., LOCA) causes the breeder (or breeder/coolant) material to drain, then the LiPb blanket will experience a lower temperature rise than the lithium blanket. This is because LiPb absorbs more neutrons, especially low energy neutrons, than lithium, leaving less neutrons available to produce activation products in the structural material. That is, the decay heat level in the structural material is lower in the LiPb blanket. The same effect can be realized by enriching the lithium in ^{6}Li.

In Section 4.2.3, it is found that the inclusion of the neutron multiplier beryllium in the Li_2O/He/MT-9 blanket results in a 15% - 25% increase in the decay heat density. This has a small but significant impact on the temperatures reached after a LOFA/LOCA, with the beryllium blanket reaching higher temperatures.

† This assumes that the tritium produced by both materials is constantly being removed, such that the tritium contribution to the decay heat is negligible.

The impact increases with the operational neutron wall load. The recommendation is that the negative impact on thermal safety should be taken into account when considering the use of a neutron multiplier to improve blanket performance.

5.7.3.2 Impact of Shield/Coil Geometry

The tokamak Blanket #1 and the RFP Blanket #3 consist of the same materials. The difference between the two lies in the fact that Blanket #1 includes a large shield to protect the superconducting magnets behind it, whereas Blanket #3 is backed directly by copper magnet coils. The decay heat to heat capacity ratio is higher in the shield material of Blanket #1 than it is in the copper coils of Blanket #3. This means that the temperature rise in Blanket #1 is more sensitive to the wall load (i.e., Blanket #1 has a higher value of a in equation (5.12)), such that the copper-magnet Blanket #3 can be safely operated at higher wall loads than the superconducting-magnet Blanket #1. Replacing the steel in the Blanket #1 shield with a low activation material would result in the same advantage for the superconducting tokamak.

5.7.3.3 Availability of Heat Sink

The presence of a constant temperature heat sink was assumed in all of the analyses presented in Sections 5.2 and 5.3. If there is no such heat sink, the actual temperatures reached in the first 24 hours of a LOFA/LOCA will be at most only slightly higher than those presented in those sections. The difference is larger in blankets which are thermally well coupled to the heat sink than in those which are not. At longer times there is a much more significant difference, since insulated systems (i.e., those with no heat sink) will continue to experience a temperature rise, whereas the temperature in systems with a heat sink will reach a maximum, then begin to decrease.

5.7.3.4 Wall Radiative Emissivity

The maximum temperature reached in the first wall after a LOFA/LOCA can be highly sensitive to the radiative emissivity of the blanket structural surfaces, particularly in a LOCA. The degree of sensitivity depends on how well the first wall is thermally coupled to the heat sink and/or shield. Increasing the emissivities on either side of the vacuum gap between the blanket and the shield will improve the thermal coupling between the blanket and the shield, which in turn will significantly reduce the maximum first wall temperature by increasing the amount of heat that is dumped into the shield. This creates a conflict between the safety and operational interests of fusion reactor design.

During operation, it is desirable to keep the amount of heat that is deposited in the shield to a minimum. This is because the shield is operated at a low temperature, and thus the heat deposited in it is not recovered in a useful form. Therefore, in the interests of operational performance, it is beneficial to keep the blanket thermally insulated from the shield, so as to reduce the amount of heat that flows from the blanket to the shield. However, for the reasons outlined above, from a safety standpoint it is better to have good thermal coupling between the blanket and the shield. The ideal solution would be to keep the blanket and shield thermally insulated from each other during operation, but design a mechanism which would improve the thermal coupling in the event of an accident. An example of this type of solution would be to maintain the vacuum gap during operation, but allow the reactor cover gas into this vacuum gap in the event of an accident. This would greatly enhance the heat transfer between the blanket and the shield, and thus reduce the maximum temperature reached in the first wall after the accident. This particular solution introduces some problems, such as the possibility of oxidation of the hot structural surfaces if there is any oxygen in the cover gas. If no such "ideal"solution can be found, then it is recommended that a proper trade-off between the operational and safety interests be found. The structural surfaces on either side of the vacuum gap can then be machined to obtain the radiative emissivities that yield

the desired level of thermal coupling.

This design flexibility does not exist for structural surfaces within the blanket itself. To maintain good corrosion resistance, these surfaces must be shiny and smooth. Unfortunately, shiny, smooth surfaces have low radiative emissivities. During operation, however, corrosion and thermal cycling can cause an increase in the emissivity of these surfaces, resulting in improved thermal coupling between the first wall and the shield. The impact is potentially significant, and thus the issue deserves further attention.

5.7.3.5 Continued Plasma Burn

There is no guarantee that the plasma will shut-off at the moment coolant or coolant flow is lost. It is more likely that the plasma will continue to burn for a few seconds. If the continued plasma burn behavior is similar to that shown in Figure 5.1.3, that is, if the plasma only burns for the equivalent of a few full power seconds, then it was found that the impact on the overall temperature rise is quite small. It does result in an initial temperature spike in the first five seconds, and in some cases this initial temperature peak can cause structural damage. For the most part, however, the results of the thermal analysis presented in this chapter are not sensitive to whether continued plasma burn was included or not. It should be reiterated that this conclusion applies only to a short plasma burn, such as that shown in Figure 5.1.3.

5.7.4 Inboard vs. Outboard

In Section 4.5, the decay heat level of the inboard and outboard versions of Blanket #1 were compared. It is seen that the at the front of the blanket, the decay heat density is higher on the outboard side, but at the back of the shield, it is higher on the inboard side. Overall, the inboard side has a higher average

decay heat density. In terms of the temperature response to a LOFA/LOCA, the higher decay heat density at the front of the outboard blanket leads to a higher temperature rise. The effect is reduced somewhat by the additional heat storage capacity on the outboard side, contained primarily in the large outboard shield. If the two systems are thermally insulated, the lower average decay heat density on the outboard side will lead to a lower temperature rise.

5.7.5 Cylindrical vs. Slab Geometry

The model used to calculate the temperature in these analyses uses one-dimensional slab geometry as an approximation to the toroidal geometry that actually exists. The validity of this approximation was verified by comparing the slab model results with results obtained using cylindrical geometry. It was found that on the inboard side, toroidal and poloidal effects cancel each other, and slab geometry turns out to be a good approximation to the real-life geometry. On the outboard side, the toroidal and poloidal effects combine, with the result being that the slab approximation overpredicts the temperature rise. The difference between the slab and cylindrical results scales as the ratio of the blanket thickness to the major and minor radii. In all the cases of interest, the difference between the models is small, and the error introduced by using slab geometry is acceptable.

[5.1] N.E. Todreas and M.S. Kazimi, Nuclear Reactor Thermal Analysis, Hemisphere, to be published 1988.

[5.2] Report of the Senior Committee on Environmental, Safety and Economic Aspects of Magnetic Fusion Energy, Final Report, U.S. DOE, to be issued as a Livermore National Laboratory report, 1987.

[5.3] S.J. Piet, M.S. Kazimi, L.M. Lidsky, Potential Consequences of Tokamak Fusion Reactor Accidents: The Materials Impact, Massachusetts Institute of Technology Plasma Fusion Center, PFC/RR-82-19, June 1982.

[5.4] D.L. Smith et al., Blanket Comparison and Selection Study (BCSS) - Final Report, Argonne National Laboratory, ANL-84-1, September 1984.

[5.5] J.H. Lienhard, A Heat Transfer Textbook, Prentice-Hall, Inc., Englewood Cliffs, N.J., 1981.

[5.6] H.C. Hottel and A.F. Sarofim, Radiative Heat Transfer, McGraw Hill, New York, 1967.

[5.7] V.V. Gerasimov, editor, Corrosion of Reactor Materials: A Collection of Articles, AEC-TR-5219, 1960.

[5.8] R.L. Miller, et. al., Advanced Tokamak Reactors Based on the Spherical Torus (ATR/ST), Los Alamos National Laboratory, LA-10740-MS, June 1986.

[5.9] B. Malinovic, Natural Convection Characteristics of Liquid Metal Cooled Fusion Reactors, S.M. Thesis, Nuclear Engineering Department, Massachusetts Institute of Technology, 1986.

[5.10] J.E. Massidda, Power Flattening in D-T Tokamak Fusion Reactor Blankets, S.M. Thesis, Department of Nuclear Engineering, Massachusetts Institute of Technology, 1985.

[5.11] J.H. Huang and M.E. Sawan, Three-Dimensional Neutronics Analysis for the MARS Blanket, Trans. Amer. Nucl. Soc., 46, pp. 229-231, 1984.

[5.12] R.C. Weast, Editor-in-Chief, CRC Handbook of Chemistry and Physics, 65th Edition, CRC Press, Inc., 1984.

[5.13] C.P. Yu, Relationship of Material Properties in the Design of a Fusion Reactor First Wall, Doctoral Dissertation, Nuclear Engineering Department, Massachusetts Institute of Technology, 1981.

[5.14] O.A. Adegbulugbe, Structural Design Limits for Fusion First Walls, Doctoral Dissertation, Nuclear Engineering Department, Massachusetts Institute of Technology, 1981.

[5.15] F. Najamabadi, N.M. Ghoniem, R.W. Conn, et al., The TITAN Reversed-Field Pinch Fusion Reactor Study, Scoping Phase Report, UCLA-PPG-1100, January, 1987.

[5.16] E.T. Cheng, Radioactivation Characteristics for Deuterium- Tritium Fusion Reactors, Nuclear Technology/Fusion 4, 1983.

[5.17] F.M. Mann, Transmutation of Alloys in MFE Facilities as Calculated by REAC (A Computer Code System for Activation and Transmutation), Hanford Engineering Development Laboratory, HEDL-TME-81-37, August 1982.

[5.18] S.J. Brereton and M.S. Kazimi, Safety and Economic Comparison of Fusion Fuel Cycles, PFC/RR-87-7, Massachusetts Institute of Technology, Plasma Fusion Center, August 1987.

[5.19] S. Glasstone and A. Sesonske, Nuclear Reactor Engineering, 3rd Edition, p. 376, Van Nostrand Reinhold Company, New York, 1981.

[5.20] J.P. Holdren and S. Fetter, Contribution of Activation Products to Fusion Accident Risk: Part II. Effects of Alternative Materials and Designs, Nuclear Technology/Fusion 4, pp. 599-617, November 1983.

[5.21] S. Fetter, Radioligical Hazards of Magnetic Fusion Reactors, Lawrence Livermore National Laboratory, LLNL MS#61485F, 1985.

[5.22] D.K. Sze, A.M. Hassanein, S.J. Piet, C.P.C. Wong, W.D. Bjorndahl, An Assessment of Problems Associated With Tritium Containment, Fusion Technology, Vol. 8, pp. 1985-1997, September 1985.

[5.23] W.M. Stacy, Jr., FUSION : An Introduction to the Physics and Technology of Magnetic Confinement Fusion, John Wiley & Sons, 1984.

[5.24] Ed Cheng, GA Technologies, Inc., personal communication, April, 1987.

[5.25] Y. Gohar, Design Analyses of Self-Cooled Liquid Metal Blankets, Argonne National Laboratory, ANL/FPP/TM-208, December 1986.

[5.26] E.M. Sparrow and R.D. Cess, Radiation Heat Transfer, Brooks/Cole Publishing Co., Belmont, CA, 1966.

[5.27] C.C. Baker et al., STARFIRE - A Commercial Tokamak Fusion Power Plant Study, Argonne National Laboratory, ANL/FPP-80-1, September 1980.

[5.28] D.S. Gelles, N.M. Ghoniem, and R.W. Powell, Low Activation Ferritic Alloys Patent Description, UCLA/ENG-87-9, March 1987.

[5.29] R. Siegel and J.R. Howell, Thermal Radiative Heat Transfer, Scientific and Technical Information Division, Office of Technology Utilization, National Aeronautic and Space Administration, 1969.

[5.30] B.G. Logan, A Rationale for Fusion Economics Based on Inherent Safety, Lawrence Livermore National Laboratory, UCRL-91761, November 1984.

[5.31] U.R. Evans, An Introduction to Metallic Corrosion, 3rd Edition, Edward Arnold Publishing Co., Metals Park, OH, 1982.

[5.32] J.G. Crocker and D.F. Holland, Safety and Environmental Issues of Fusion Reactors, Proceedings of the IEEE, Vol. 69, No. 8, August 1981.

[5.33] R.A. Krakowski, Parametric Results Using Generomak Model with Emphasis on Power Density Versus Inherent-Safety Tradeoffs, Memorandum to ESECOM, March 1986.

[5.34] A.C. Smith, et. al., The Moving-Ring Field-Reversed Mirror Reactor, Annual Report 1979-1980, Pacific Gas & Electric Company, August 1981.

[5.35] G.A. Carlson, et. al., Field-Reversed Pilot Reactor, Electric Power Research Institute, AP-1544, Reactor Project 922, September, 1980.

[5.36] R.J. LeClaire and J.E. Meyer, The Impact of Thermal Fatigue and Other Design Limits on Pulsed Commercial Tokamak Reactor Design, Journal of Fusion Energy, Vol. 4, No. 5, pp. 353-364, 1985.

6. Impact of Natural Convection Cooling

The temperature response analysis presented in Chapter 5 accounted for conductive and radiative heat transfer only. This was based on the assumption that in a Loss-of-Flow Accident (LOFA), the coolant stops flowing immediately (i.e., at time=0), and in a Loss-of-Coolant Accident (LOCA), the coolant "disappears"at time=0. For a LOCA, this meant ignoring time-to-drain effects, which, as was stated, can be significant in reducing the temperature rise in the first few minutes, but would probably have a minimal impact on the long-term temperature rise. In the LOFA, however, as the coolant system remains intact there is a possibility that flow would continue at some reduced flow rate, due to buoyancy effects. Assuming that the secondary coolant cycle continued to operate and remove heat from the primary coolant, the continued primary coolant flow could remove a substantial amount of heat from the first wall/blanket, and dramatically impact the temperature response in the LOFA.

The phenomenon of coolant flow, despite the lack of a pump or any other externally added pressure head, is known as natural convection. Briefly, a pressure head is established due to buoyancy effects, which arise because the coolant, as it passes through the blanket, is being heated. The heated fluid thermally expands and thus becomes less dense than the cooler fluid. The hotter, lighter fluid will rise, and thus there will be some flow of the fluid in the loop. Figure 6.0.1 gives a schematic of a fusion reactor flow loop.

Figure 6.0.1 Schematic of Typical Fusion Reactor Primary Flow Loop

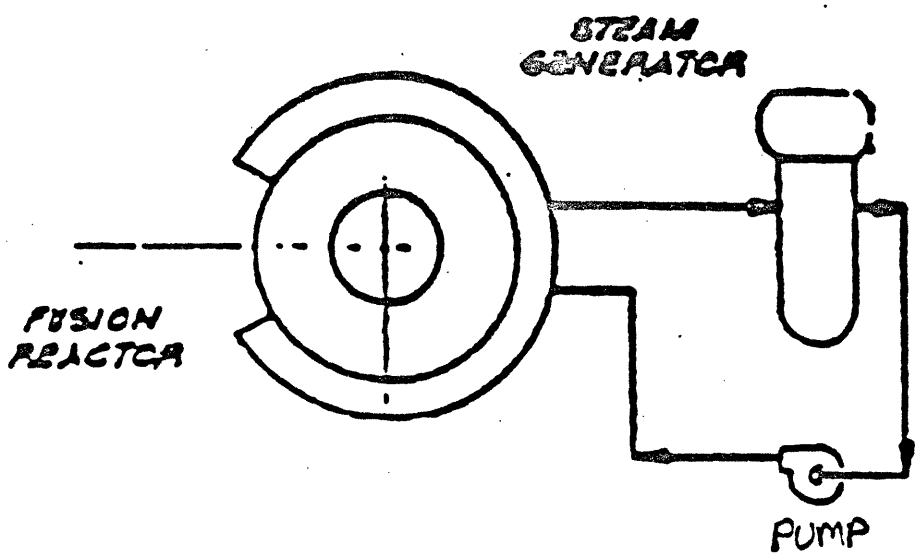

Quantifying the potential for natural convection cooling of fusion reactors has been addressed only in a few previous works. In this chapter, a model for predicting the flow rate and heat transfer characteristics of the coolant under natural convection conditions is presented. This is followed by presentation of the results of the model, as applied to the blankets under consideration in this study.

6.1 Model for Natural Convection Analysis

The model for the natural convection analysis is essentially divided into two parts. The first part is primarily based on the work of Malinovic [6.1, 6.2] and others [6.3]. It involves calculating the flow rate of the coolant under natural convection. In the second part, using flow rate calculated in the first part, the heat transfer characteristics of the flowing coolant are determined. These characteristics are incorporated into the THIOD heat transfer model as additional terms to equation (5.8).

The flow rate of the coolant under transient conditions is found by equating the available pressure head with the total pressure drop around the loop, including the inertial terms. The pressure rise is due to buoyancy, while the pressure drop is due to friction, MHD effects, and inertial effects. The equation to be solved, then, is

$$\Delta P_B = \Delta P_{fric} + \Delta P_{MHD} + \Delta P_T \tag{6.1}$$

The pressure gain, as stated, is due to buoyancy effects, and is found by

$$\Delta P_B = \rho \beta g L \Delta T(t) \tag{6.2}$$

where

ρ is the coolant density (kg/m^3),

$\beta = \frac{-1}{\rho}\frac{\partial \rho}{\partial T}$ is the thermal expansion coefficient of the coolant (K^{-1}),

g is the acceleration due to gravity (9.8 m/s^2),

L is the thermal elevation difference (m), which is the difference in height between the point where the heat is removed (in the heat exchanger) and the heat is added (in the blanket), and

$\Delta T(t)$ is the temperature rise of the coolant as it passes through the blanket.

This pressure gain term is balanced by the pressure drop terms. In all cases, there is a friction pressure drop, which is characterized as

$$\Delta P_f = \int_{x_1}^{x_2} \frac{fG^2}{2D_e\rho} dl \tag{6.3}$$

where x_1 and x_2 are start and end point of the flow channel, f is the Darcy friction factor, G is the mass flux (kg/m^{2}s), and D_e is the hydraulic diameter of the channel. In the case of laminar flow, which turns out to be the case of interest, f in a circular tube is equal to $\frac{64}{Re}$, where Re is the Reynold's number. Thus, the friction pressure drop becomes

$$\Delta P_f = \int_{x_1}^{x_2} 32\frac{\mu}{\rho}\frac{\dot{m}_i}{AD_e^2} dl \tag{6.4}$$

Using the results of Malinovic [6.1, 6.2], who examined natural convection in the BCSS tokamak blanket geometry, equation (6.4) can be reduced to

$$\Delta P_f = K_{fric}\dot{m} \tag{6.5}$$

where K_{fric} is an effective parameter that represents the geometry of the flow loop and the properties of the coolant, i.e., μ and ρ.

$$K_{fric} = \sum_j 32 \frac{\mu}{\rho} \frac{l_j}{A_j D_{ej}^2} \tag{6.6}$$

where the j subscript refers to the flow channel. The sudden expansion (or contraction) of the fluid as it passes from one flow channel to another will also cause a pressure loss. This is treated in a manner similar to the friction pressure drop, resulting in an equation of the form of equation (6.5). In this analysis, the constant K_{fric} represents both the friction and expansion/contraction pressure drop coefficients. Additional discussion on treatment of the friction pressure drop is given in Appendix E.

In the liquid metal cooled blankets, there is also a pressure drop due to MHD effects. These arise from the fact that the liquid metal, which is a conductor, is flowing transverse to a magnetic field. There are two contributing terms to the MHD pressure drop, the first being due to wall conductivity effects and the second due to three dimensional effects such as sudden contractions and expansions, and bends in flow direction with respect to the magnetic field. According to Malinovic [6.1, 6.2], in the BCSS tokamak geometry, the 3D effects are negligible compared to the wall conductivity effects, and thus are not treated here. The MHD pressure drop term thus becomes

$$\Delta P_{\text{MHD}} = \sigma \frac{\dot{m}}{\rho A} \overline{B}^2 \frac{\delta l_p}{\alpha} \tag{6.7}$$

where

σ is the conductivity of the coolant channel wall $(\Omega - m)^{-1}$,

A is the (average) coolant channel area (m^2),

$\overline{B}$ is the average magnetic field strength (T),

δ is the average coolant channel wall thickness (m),

l_p is the total coolant channel length for flow perpendicular to the magnetic field (m), and

a is the average coolant channel radius or half-width (m).

During transients, there is also the mass temporal acceleration in the loop. This arises from the fact that at the instant the pump stops, the coolant is still flowing at the forced convection rate. The coolant's own inertia, then, will cause it to continue flowing. Eventually, it will reach the new steady-state, natural convection flow rate. Expressed as a pressure drop, it is

$$\Delta P_T = \sum_{N=1}^{J} \frac{l_N}{A_N} \frac{d\dot{m}_N}{dt} \tag{6.8}$$

where,

l_N is the length of flow section N,

A_N is the cross sectional area of flow section N, and

$\dot{m}_N$ is the mass flow rate in flow section N.

Note that since $\frac{d\dot{m}}{dt}$ is negative during a LOFA, the inertia term will actually turn out to be a pressure *rise*, contributing positively to the flow rate until the new steady state is reached. Using knowledge of loop geometry and size, equation (6.8) can be written as,

$$\Delta P_T = I \frac{d\dot{m}}{dt} \tag{6.9}$$

$$I = \sum_{N=1}^{J} \frac{l_N}{A_N} \frac{d\dot{m}_N}{dt}$$

Substituting equations (6.2), (6.5), (6.8) and (6.9) into equation (6.1) gives an equation for $\dot{m}$, namely

$$\rho \beta g L \Delta T(t) = K_{fric} \dot{m} + \sigma \frac{\dot{m}}{\rho A} \overline{B}^2 \frac{\delta l_p}{a} + I \frac{d\dot{m}}{dt} \tag{6.10}$$

To solve equation (6.10) in finite difference form, the time derivative term is approximated as

$$\frac{d\dot{m}}{dt} = \frac{\dot{m}^n - \dot{m}^{n-1}}{\Delta t} \tag{6.11}$$

where the superscript n refers to the time step. The $\dot{m}$'s in equation (6.11) are approximated as the linear average between $\dot{m}^{n-1}$ and $\dot{m}^n$. Thus, the equation for $\dot{m}^n$ is:

$$\dot{m}^n = \left[\frac{\sigma\overline{B}^2\delta l_p}{2\rho A\alpha} + \frac{K_{fric}}{2} + \frac{I}{\Delta t}\right]^{-1}\left[\rho\beta g L\Delta T - \left(\frac{\sigma\overline{B}^2\delta l_p}{2\rho A\alpha} + \frac{K_{fric}}{2} - \frac{I}{\Delta t}\right)\dot{m}^{n-1}\right] \tag{6.12}$$

All of the parameters on the right hand side of equation (6.12) are known except ΔT. This ΔT is the temperature rise of the coolant as it passes through the blanket, i.e.,

$$\Delta T = T_{out} - T_{in} \tag{6.13}$$

where

T_{in} is the coolant temperature at the inlet to the blanket, and

T_{out} is the coolant temperature at the outlet of the blanket.

It is assumed that the mechanism for removing heat from the coolant remains operational during the transient. That is, the secondary flow loop, which removes the heat from the primary blanket coolant, continues to operate at the same base temperature as during normal operation. This means that T_{in}, which is also the temperature of the coolant after it exits the heat exchanger, can be assumed constant at all times. The value of T_{in} will be that for normal operation.

The evaluation of T_{out}, on the other hand, is somewhat more complicated. In the blankets of interest, there are a number of different flow channels, connected

in series. For instance, for Blanket #1, the flow geometry in the blanket is shown in Figure 2.1.3. The coolant enters the blanket in the manifold region, then flows into the poloidal blanket channels (shown in Figure 2.1.3), and finally into the toroidal first wall channels. Thus, the flow loop through the blanket consists of three channels connected in series. While the mass flow rate $\dot{m}$ must remain constant around the flow loop, the flow velocity V $(\dot{m}/\rho A)$ and Reynold's number (Re) will depend on the area of the flow channel geometry. It is the flow velocity and Reynold's number that determine the heat transfer characteristics of the coolant, and thus each channel must be treated separately.

Note that each of the flow channels described above correspond to one region of the blanket. The manifold channel corresponds to the manifold region, i.e., Region 5 in Figure 2.1.2. The poloidal blanket channel corresponds to the blanket region (Region 4) in Figure 2.1.2, and the toroidal first wall channel to Region 2 of Figure 2.1.2. Thus, T_{out} for each channel is the maximum T_i in the appropriate region. Furthermore, since the coolant flows from the manifold to the poloidal blanket to the toroidal first wall, the outlet temperature T_{out} of one channel is the inlet temperature T_{in} of the next channel. Thus, T_{in} for the manifold is the blanket inlet temperature, which is a constant, T_o. T_{in} for the poloidal blanket channel is T_{out} for the manifold, and T_{in} for the toroidal first wall is T_{out} for the poloidal blanket. Finally, T_{out} for the toroidal first wall is the total blanket T_{out}, and is the temperature used in equation (6.13) to get ΔT, which is used in equation (6.12) to solve for $\dot{m}$. T_{in} and T_{out} for each channel (or region) are important when the convective effects are added to the heat transfer equation (5.8) in THIOD, as will be seen.

Once $\dot{m}$ has been calculated from equation (6.12) for time step n, the heat transfer characteristics of the flowing coolant can be found. Convective heat transfer from a solid wall to a flowing coolant is described by the equation

$$\dot{q}''_{\text{convection}} = h(T_s - T_l) \tag{6.14}$$

where

h is the *heat transfer coefficient*, W/m^2 K,

T_s is the temperature of the solid wall, and

T_l is the temperature of the flowing coolant.

In order, then, to determine the heat that is tranferred from the blanket structure to the flowing coolant (and subsequently removed from the blanket), it is necessary to obtain a value for the heat transfer coefficient h. There exists a number of empirical relations which have been developed for this purpose. These relations are based on several non-dimensional parameters that represent the coolant properties and the flow characteristics. The coolant flow in channel j is characterized by the Reynold's number Re, where

$$Re_j = \frac{\rho V_j D_{e_j}}{\mu} \tag{6.15}$$

where

V_j is the coolant velocity (m/s) in channel j,

D_{e_j} is the hydraulic diameter of channel j, and

μ is the viscosity of the coolant (kg/m· s).

The coolant properties are characterized by the Prandlt number Pr, where

$$Pr = \frac{c_p \mu}{k} \tag{6.16}$$

where

c_p is the coolant specific heat (J/kg· K), and

k is the coolant thermal conductivity (W/m· K).

It is convenient to combine the Reynold's and Prandtl numbers to form the Peclet number, where

$$Pe_j = R\epsilon_j Pr \tag{6.17}$$

Finally, the heat tranfer characteristics of the fluid in channel j are characterized by the Nusselt number Nu, where

$$Nu_j = \frac{h_j D_{e_j}}{k} \tag{6.18}$$

where h_j is the heat transfer coefficient for channel j.

To calculate h_j, a relation between Nu and the known parameters included in Pe is needed. For natural convection problems involving liquid metals, the recommended equation (6.9) is

$$Nu = 5.0 + (\overline{\psi} Pe)^{0.8} \tag{6.19}$$

where $\overline{\psi}$ is the average value of the parameter ψ, which is a function of the Prandtl and Reynolds numbers as well as the position in the flow channel. The value of $\overline{\psi}$ is found empirically by the relation

$$\overline{\psi} = 1 - \frac{1.82}{Pr(\epsilon_m/\nu)^{1.4}_{max}} \tag{6.20}$$

where

ϵ_m is the momentum diffusivity of the fluid, and

ν is the kinematic viscosity of the fluid ($\frac{\mu}{\rho}$).

Any values of $\overline{\psi}$ that are below zero are taken to be zero. The value $(\epsilon_m/\nu)_{max}$ is found graphically from the Reynold's number. On a log-log scale, the plot is almost linear, and thus a mathematical correlation can be found. This turns out to be

$$(\epsilon_m/\nu)_{max} = (2.90 \times 10^{-2})(Re^{0.769}) \tag{6.21}$$

Another effect of the flowing coolant, which applies only in turbulent flow, is the *eddy conductivity* of the fluid. The eddy conductivity represents an increase in the thermal conductivity of the flowing fluid due to cross-flow, which transfers heat across the channel. In general the flow could be turbulent, so this term cannot be neglected. The term k_e can be represented as

$$k_e = \rho c_p \epsilon_h \tag{6.22}$$

where ϵ_h is the *eddy diffusivity* of the fluid. This k_e is then added to the thermal conductivity of the stagnant fluid to obtain the total thermal conductivity of the flowing fluid, which is used when calculating the heat flow across coolant channels. For liquid metals, ϵ_h is not the same as the momemtum diffusivity ϵ_m; instead, it is represented as

$$\epsilon_h = \overline{\psi}\epsilon_m \tag{6.23}$$

The ϵ_m used here is the same as the $(\epsilon_m)_{max}$ found above.

The method of solution proceeds as follows. For each flow channel j, from the previous known value of ΔT_j and the other parameters, the $\dot{m}^n$ is found from equation (6.12). Then, using equations (6.15), (6.16), and (6.17), the Peclet number, Pe_j, is found. Next, using equations (6.21) and (6.20), the value of $\overline{\psi}$ is calculated.

This is then input into equation (6.19) to determine Nu_j, from which the value of h_j is derived. Finally, from equations (6.23) and (6.22), the value of k_{e_j} is found.

All of this analysis, from equations (6.1) through (6.23), is done in subroutine CONVECT. The purpose of CONVECT is to return the value of $\dot{m}$ and the values of h_j and k_{e_j} for each flow channel j to the main code THIOD. These parameters are used in a modified version of the heat transfer equation (5.8) to calculate the T_i^n.

The heat transfer analysis presented in Chapter 5. which ignored convection, was done using equation (5.8), which was derived from equation (5.1). When convection is included, equation (5.1) becomes

$$\rho(\mathbf{r})c_p(\mathbf{r},T)\left(\frac{\partial T(\mathbf{r},t)}{\partial t}\right)+\mathbf{v}\cdot\nabla(\rho c_p\Delta T)=\dot{q}'''_{decay}+\nabla\cdot\dot{q}''(\mathbf{r},t) \tag{6.24}$$

In one dimensional slab geometry, with x being the direction of heat flow and z being the direction of fluid flow (i.e., $\mathbf{v}=v_z$), this equation becomes

$$\rho(x)c_p(x,T)\frac{\partial T(x,t)}{\partial t}+\rho c_p v_z\frac{\partial \Delta T(z,t)}{\partial z}=\dot{q}'''_{decay}+\nabla\cdot\dot{q}''(x,t) \tag{6.25}$$

This equation is now integrated over the length element Δx_i, resulting in

$$\Delta x_i(\rho c_p)_i\frac{dT_i(t)}{dt}+\Delta x_i\frac{\dot{m}_i c_p}{A}\frac{\partial \Delta T(z,t)}{\partial z}=\int_{\Delta x_i}\dot{q}'''_{decay}(x,t)dx+\dot{q}''_{i-1,i}-\dot{q}''_{i,i+1} \tag{6.26}$$

where the following substitution has been made:

$$v_{z_i}=\frac{\dot{m}_i}{\rho A} \tag{6.27}$$

where A is the area of the flow channel in which mesh point i is located. Note that if point i is in a solid structure, where no flow is taking place, then $\dot{m}_i$ will be zero, and the second term on the left hand side of equation (6.26) will drop out. The heat flux terms $\dot{q}''_{i-1,i}$ and $\dot{q}''_{i,i+1}$ represent the heat flux from mesh zone $i-1$ to i and i to $i+1$ respectively. In the general case, in which convection and conduction can both be taking place, these are

$$\dot{q}''_{i-1,i} = \frac{\Delta k_{i-1}\left(\frac{T_{i-1}-T_i}{x_i-x_{i-1}}\right)A_{cond} + h_{i-1,i}\left(T_{i-1}-T_i\right)A_{conv}}{\left(A_{cond}+A_{conv}\right)}$$

$$\dot{q}''_{i,i+1} = \frac{\Delta k_i\left(\frac{T_i-T_{i+1}}{x_{i+1}-x_i}\right)A_{cond} - h_{i,i+1}\left(T_i-T_{i+1}\right)A_{conv}}{\left(A_{cond}-A_{conv}\right)} \tag{6.28}$$

where

A_{cond} is the area of the conduction heat flow path,

A_{conv} is the area of the convection heat flow path, and

Δk_i terms are defined in equation (5.7).

The convective heat transfer coefficients $h_{i-1,i}$ and $h_{i,i+1}$ are as defined above in equation (6.14) and calculated by subroutine CONVECT.

As the coolant flows through the channel in the z direction, it is being heated. If it is assumed that this heating is uniform along the flow channel, then

$$\Delta T(z,t) = \frac{\Delta T(l,t)z}{l} \tag{6.29}$$

where l is the length of the flow channel. Furthermore, it is assumed that $T_i(t)$ is at $z = l$; then

$$\left[\frac{\partial \Delta T(z,t)}{\partial z}\right]_{z=l} = \frac{(T_i(t) - T_{in,i})}{l} \tag{6.30}$$

where $T_{in,i}$ is the inlet temperature for the channel. If equations (6.28), (6.29), and (6.30) are substituted into equation (6.26), the result is

$$\Delta x_i(\rho c_p)_i \frac{dT_i(t)}{dt} + \Delta x_i \frac{\dot{m}_i c_p}{A}\left(\frac{T_i(t) - T_{in,i}}{l}\right) = \int_{\Delta x_i} \dot{q}'''_{decay}(x,t)dx \tag{6.31}$$

$$+ \Delta k_{i-1}\left(\frac{T_{i-1} - T_i}{x_i - x_{i-1}}\right) + h_{i-1,i}(T_{i-1} - T_i)$$

$$- \Delta k_i\left(\frac{T_i - T_{i+1}}{x_{i+1} - x_i}\right) + h_{i,i+1}(T_i - T_{i+1})$$

The time derivative is approximated as

$$\frac{dT_i}{dt} = \frac{T_i^n - T_i^{n-1}}{\Delta t} \tag{6.32}$$

and substituted into equation (6.31). This is now arranged into the form of equation (D.7),

$$-A_i T_{i+1} + B_i T_i - C_i T_{i-1} = D_i \tag{D.7}$$

to get the implicit equation for T_i^n with convection included. Upon performing this manipulation, it is found that the parameters A_i, B_i, C_i, and D_i for equation (D.7) are

$$A_i = \frac{\Delta t}{\rho c_{p_i}}\left(\frac{\Delta k_i}{x_{i+1} - x_i} + h_{i-1,i}\right)$$

$$B_i = 1 + \frac{\Delta t}{\rho c_{p_i}} \left(\frac{\Delta x_i \dot{m}_i c_p}{Al} + \frac{\Delta k_{i-1}}{x_i - x_{i-1}} + h_{i-1,i} + \frac{\Delta k_i}{x_{i+1} - x_i} + h_{i,i+1} \right)$$

$$C_i = \frac{\Delta t}{\rho c_{p_i}} \left(\frac{\Delta k_{i-1}}{x_i - x_{i-1}} + h_{i,i+1} \right)$$

$$D_i = T_i^{n-1} + \frac{\dot{m}_i c_p T_{in,i} \Delta t}{Al(\rho c_p)_i} + \frac{1}{\Delta x_i (\rho c_p)_i} \int_{\Delta t} \int_{\Delta x_i} \dot{q}'''_{decay}(x,t) dx dt + (\dot{q}''_{rad}) \Delta t \quad (6.33)$$

Equation (D.7), with the values of A_i, B_i, C_i, and D_i given in equations (6.33), is solved in the convection option of THIOD. The results of this analysis are presented in the following sections.

6.2 Results of Natural Convection Analysis

In the blankets considered in this study, there are three different coolant materials. Blankets #1 and #3 use liquid lithium, and Blanket #4 uses liquid lithium-lead. These are the liquid metal cooled blankets. Blankets #2, #5, and #6 all use helium coolant.

In the liquid metal cooled blankets, the bulk of the pressure drop is due to MHD effects. Since the MHD pressure drop scales as $\overline{B}^2$, reducing the magnetic field (turning off the magnets) has a profound effect on the pressure drop, and thus the flow rate ($\dot{m}$), which in turn has a major impact on the natural convection contribution to the cooling of the blanket. In the helium cooled blankets, there is no MHD pressure drop, thus $\dot{m}$ is solved for with equation (6.12), except the $\overline{B}^2$ terms are neglected. Thus, the pressure drop is due only to friction, and very little can be done to reduce it. The result, presented in the following section, is that natural convection in the helium-cooled blankets has a negligible impact on the

overall blanket temperature response, and thus is not treated in any detail. In the liquid metal cooled blankets, it is found that if the magnetic field can be reduced in a relatively short amount of time, the flow rate is sufficient to limit the LOFA temperature increases to values much lower than what was presented in Chapter 5.

To examine the effects of the magnetic field behavior and the magnitude of the friction pressure drop, a number of convection cases were run. These cases are summarized in Table 6.2.1. All of the convection cases correspond to the the Case 1 base case LOFA (designation C1) from Chapter 5. The parameters varied in the convection analysis are the magnetic field strength and the constants used to calculate the friction pressure drop. The cases in the convection analysis are designated cases M1 through M6. Remember that all of the convection cases are C1 LOFA's. The friction pressure drop calculation is discussed in detail in Appendix E.

The first convection case has the nominal parameters for both magnetic field and friction pressure drop. The nominal magnetic field strength is 7.5 Tesla in the tokamaks and 4.75 Tesla in the RFP. This is held constant in Case M1. In the second convection case (Case M2), the magnetic field is turned off. This is done by diverting the current through a resistor, such that the field strength decays exponentially. A reasonable decay rate is two orders of magnitude in 30 minutes [6.5]. The friction constants remain at their nominal values in Case M2. Convection Case M3 refers only to the RFP Blanket #3. Since the RFP has resistive copper coils, it is conceivable that the magnetic field can be completely shut off in a very short time. In case M3, the magnetic field strength is assumed to go to zero at accident initiation. The friction constants again remain at their nominal values. The remaining cases are used to examine the impact of the friction pressure drop on the natural convection analysis. Since the friction pressure drop terms are calculated heuristically, they are subject to substantial uncertainty. In Case M4, the magnetic field remains constant at its nominal (operational) value, while the friction constants are reduced by an order of magnitude. This case is used primarily to examine the

Table 6.2.1 Summary of Different Convection Cases Analyzed.

case #	Magnetic Field Behavior	Turbulent Fric. Const.	Laminar Fric. Const.
M1	constant, nominal	nominal	nominal
M2	10^{-2} Decay in 30 min	nominal	nominal
M3	immediate shut-off	nominal	nominal
M4	constant, nominal	0.1x nominal	0.1x nominal
M5	10^{-2} Decay in 30 min	0.1x nominal	0.1x nominal
M6	10^{-2} Decay in 30 min	10x nominal	10x nominal

helium cooled Blanket #2, where there is no MHD pressure drop. In Case M5, the magnetic field is reduced as in Case M2, that is, it decays by two orders of magnitude every 30 minutes. The friction constants in Case M5 are reduced by an order of magnitude from their nominal values. In Case M6, the magnetic field again decays by two orders of magnitude every 30 minutes, but the friction constants are increased by an order of magnitude from their nominal values. The remaining designation, i.e., for blanket (A2, D4, E4, etc.) and for plasma continuation (PL) vs. decay heat only (DC), is the same as described in Chapter 5.

6.2.1 Natural Convection in Helium Cooled Blankets

As was stated, the flow rate during natural convection in the helium cooled blankets is obtained from equation (6.12) without the MHD terms. To get a zeroth-order feel for the effect natural convection will have on the temperature response, it is sufficient to solve for the steady-state temperature rise of the coolant as it pases through the blanket. The steady state flow rate is found from equation (6.10), ignoring the MHD and temporal acceleration terms. The flow rate is thus

$$\dot{m} = \frac{\rho \beta g L \Delta T(t)}{K_{fric}} \tag{6.34}$$

Following the method of Malinovic [6.1, 6.2], to zeroth order, the coolant temperature rise ΔT can be found by

$$\dot{m} c_p \Delta T = \dot{q} \tag{6.35}$$

where $\dot{q}$ is the total decay heat (W) of the blanket. Combining equations (6.34) and (6.35) results in

$$\Delta T = \left[\left(\frac{\dot{q}}{c_p} \right) \left(\frac{K_{fric}}{\rho \beta g L} \right) \right]^{0.5} \tag{6.36}$$

From Chapter 4, for the helium-cooled Blanket #2, this decay heat level is on the order of 1.0 MW per unit axial height. If it is assumed that the torus has an axial height of about 2 × the minor radius (2.14 m), then $\dot{q}$ becomes about 4 MW. The values of the coolant properties are discussed in Appendix E. The value of L is assumed to be about 10 meters [6.1, 6.2], but could be as high as 20 m. The optimistic value of 20 m will be used here.

To get the value of K_{fric}, the design parameters for Blanket #2, as given in the BCSS (p. 8-18, Table 8.4-1) are used. From this table, the reactor thermal power is about 5400 MW. Assuming that 25% of this is deposited on the inboard side (from results presented in Section 4.5), this means that 1350 MW are removed by the coolant in the inboard blanket. Using a value for c_p for helium of 5200 J/kg-°K, and a ΔT of 235 K (from BCSS Table 8.4-1), the inboard $\dot{m}$, as found from equation (6.35), is about 1100 kg/s. From Table 8.10-24 (p. 8-130), the total pressure drop in the inboard blanket is 0.095 MPa, and the pressure drop for the inlet and outlet piping, as well as the steam generator, is 0.067 MPa. The effective pressure drop, for the fraction of the coolant that passes through the inboard blanket (as opposed to the outboard blanket), is 0.162 MPa. Thus, K_{fric} for the inboard blanket, as defined in equation (6.5), is 147 (where ΔP is expressed in Pa and $\dot{m}$ in kg/s).

Note that during operation, the helium flow is turbulent, and thus equation (6.5) does not apply. During natural convection, however, once the steady state flow rate is reached, the flow will likely be laminar. Thus, defining K_{fric} in equation (6.5) is difficult, but for these purposes, the calculated value of 147 will be used for illustration. The treatment of the friction constant K_{fric} is discussed in detail in Appendix E. Briefly, a turbulent correlation is used, in which the pressure drop is proportional to the square of the flow rate ($\dot{m}^2$). The proportionality constant K_{fric} is a function of the Reynold's number. During laminar flow, K_{fric} scales as

Re^{-1}, thus the pressure drop is linearly dependent on the flow rate.

Continuing with the calculation of equation (6.36), inserting the values of the parameters on the right hand side, it is found that $\Delta T = 450$ °C. Given the inlet temperature of 275 °C, it is seen that the helium will exit the blanket at 725 °C, which is in the temperature range of the first wall of Blanket #2 for the Case 1 LOFA (no natural convection) discussed in Chapter 5. This implies that including natural convection in the LOFA calculation will not greatly impact the temperature response. This result potentially is sensitive to the K_{fric} parameter, however, and thus the impact of natural convection in the helium cooled Blanket #2 was investigated.

The model discussed in Section 6.1, with some modifications as discussed in Appendix E, was used to calculate the temperature response of Blanket #2 to the base case LOFA. Two cases were run. These are Cases M1 and M4 in Table 6.2.1.

The temperature response of the first wall, for the nominal neutron wall load of 5 MW/m^2, for these two cases, are given in Figure 6.2.1a. Figure 6.2.1a also gives the temperature response of the base case (no convection) LOFA discussed in Chapter 5, for both plasma continuation (PL) and decay heat only (DC). Recall that the base case LOFA for the helium cooled blankets assumes immediate plasma shut-off (DC), since it was assumed that the effect of the coolant coast-down time would negate the effect of the continued plasma burn. The convection cases (M1 and M4) assume continued plasma burn, since the coolant coast down effects are automatically included in the convection analysis. The maximum temperature reached in the first wall as a function of neutron wall load for these four cases is given in Figure 6.2.1b.

Note in Figure 6.2.1 that the first wall temperature response for the nominal K_{fric} natural convection Case M1 is very similar to Case C1DC, which is the LOFA without convection but assuming decay heat only. Thus, it appears that the assumption that the convection effects of coolant coast down would negate the

Figure 6.2.1a First Wall Temperature History After LOFA for Blanket #2
With and Without Natural Convection

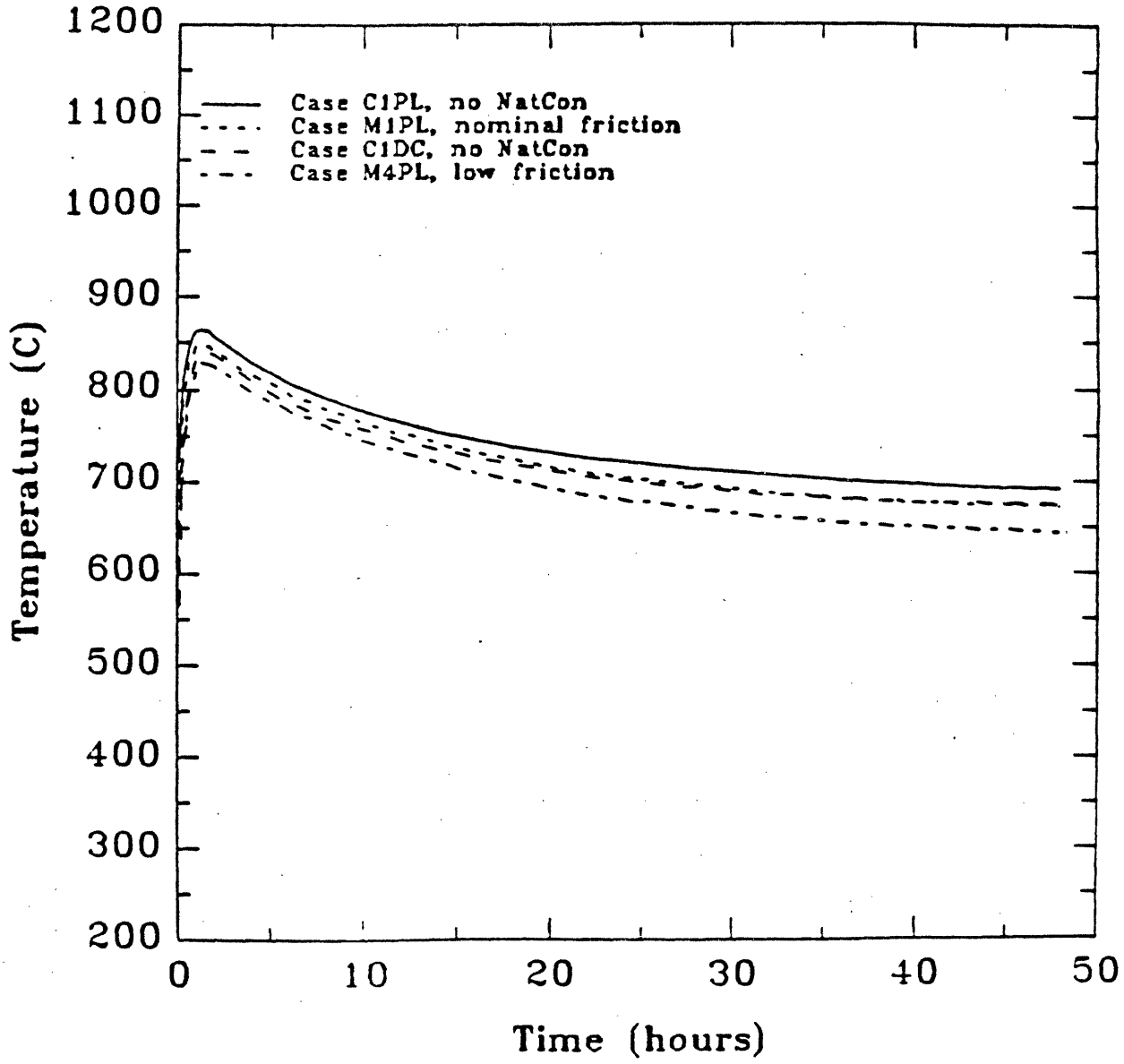

Figure 6.2.1b Maximum First Wall Temperature vs. Wall Load for Blanket #2 With and Without Natural Convection

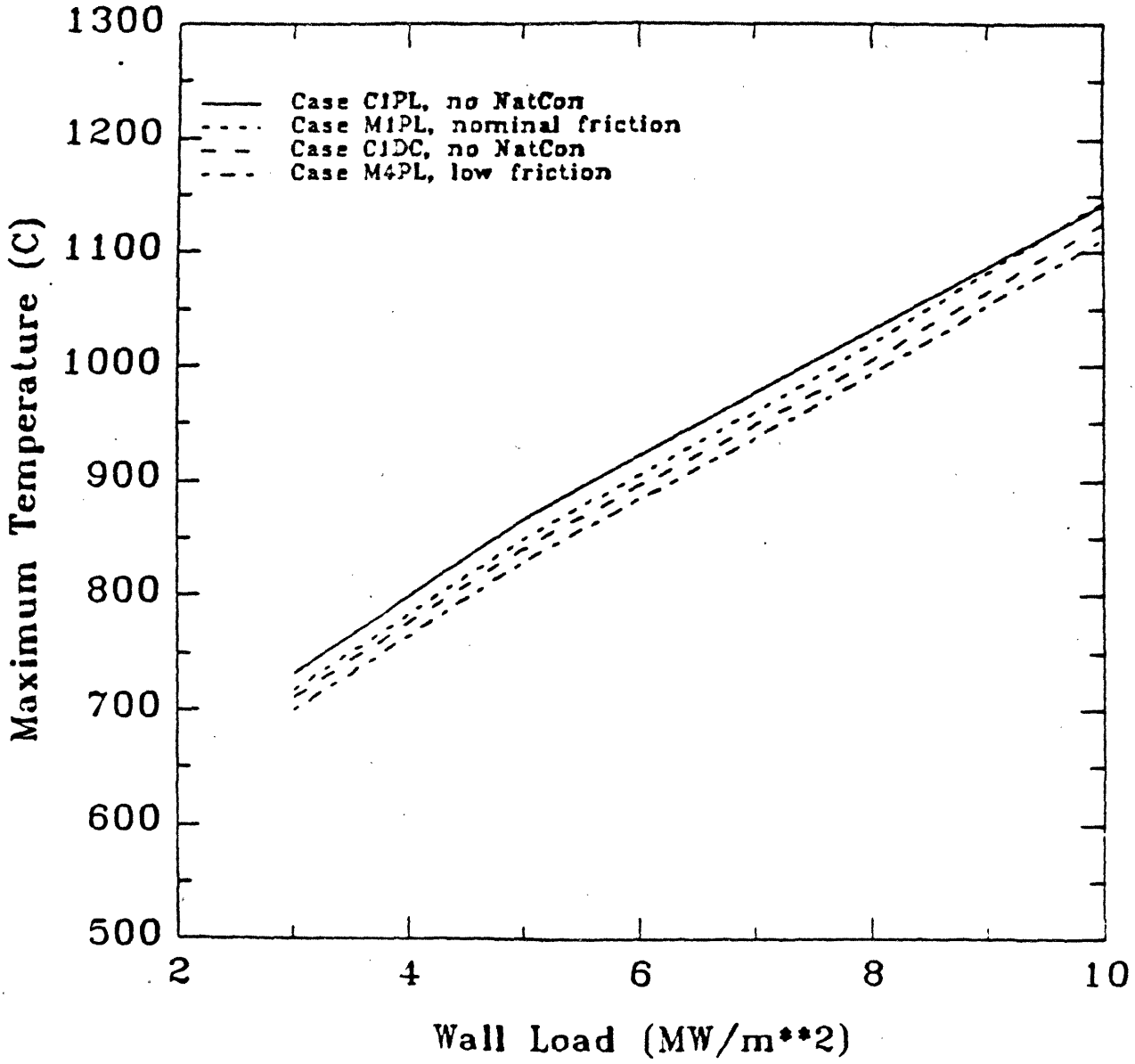

continued plasma burn effects is a valid one. Using the low value of K_{fric}, Case M4, has a small but noticeable impact on the temperature response. However, from Figure 6.2.1b, it is seen that there is no more than a 25 - 30 °C difference between this case (M4), which is an optimistic convection case, and the base case LOFA C1DC, which assumes no convection, at any wall load. This verifies the "back of the envelope"calculation at the beginning of this section, which indicated that the impact of natural convection in the helium cooled blankets would be minimal. For this reason, natural convection in the helium cooled blankets was not investigated further. The conclusion is that in helium cooled systems, due mostly to a low coolant density, natural convection after pump failure can not be expected to mitigate the consequences discussed in Chapter 5.

6.2.2 Natural Convection in Li/Li/V Tokamak Blanket #1

The potential for convective cooling in liquid metal cooled systems is much better than in helium cooled systems. Equation (6.36) was derived to give a general idea of the convection potential by defining the maximum coolant temperature rise ΔT. Note that ΔT is inversely proportional to the coolant properties ρ, β, and c_p as

$$\Delta T \propto \left(\frac{1}{\beta \rho c_p}\right)^{1/2} \tag{6.37}$$

The product $\beta \rho c_p$ is 28 times higher for liquid lithium than for helium, which indicates that the ΔT will be five times lower in the lithium cooled system than in the helium cooled system. This means that ΔT for the lithium system will be about 80 °C. It must be remembered, however, that the liquid metal cooled systems are subject to an MHD pressure drop which, at moderate to high values of the magnetic field strength B, will dominate the total pressure drop term. For this reason, if the magnetic field stays on, it is likely that natural convection in liquid lithium cooled

systems will have no more impact than it does in helium cooled systems. Including the MHD pressure drop, the steady state equation that defines ΔT becomes

$$\rho\beta g L\Delta T = \sigma\frac{\dot{m}}{\rho A}\overline{B}^2\frac{\delta l_p}{\alpha} + K_{fric}^{lam}\dot{m}^2 \tag{6.38}$$

As stated, the friction pressure drop term can be neglected. Using the relation [6.34] to substitute for $\dot{m}$, and solving for ΔT, yields

$$\Delta T = \left[\frac{\sigma\overline{B}^2\delta l_p q}{\rho^2\beta c_p A\alpha g L}\right]^{1/2} \tag{6.39}$$

Using the values given in Appendix E, $\overline{B}$=7.5 Tesla, the liquid lithium ΔT is about 600 °C. The value of q used is the same as that used for the helium ΔT, but is reduced to correspond to one flow channel, since the geometry parameters are for one flow channel only. So it is seen that under these circumstances, including MHD will have a very minor impact on the temperature rise. If the magnetic field can be turned off, however, or at least reduced in strength, the back-of-the-envelope analysis presented above, for friction pressure drop only, indicates that natural convection can have a major impact on the temperature response in liquid metal cooled systems.

The base model for the liquid metal natural convection analysis is presented in Section 6.1. The friction pressure drop term is discussed in Appendix E. This term is only important when the magnetic field is turned off. This model was applied to Blanket #1. The details of the coolant properties and flow loop geometry are presented in Appendix E. The results of this analysis follow. Please refer to Table 6.2.1 for designation of cases.

The temperature response to the base case LOFA, with the magnetic field remaining constant at its operational value (Case M1), is given in Figures 6.2.2a and 6.2.2b, along with the response calculated without convection (Case C1). As

Figure 6.2.2a First Wall Temperature History After LOFA for Blanket #1 With and Without Natural Convection. In convection Case M1, magnetic field remains constant at operational value.

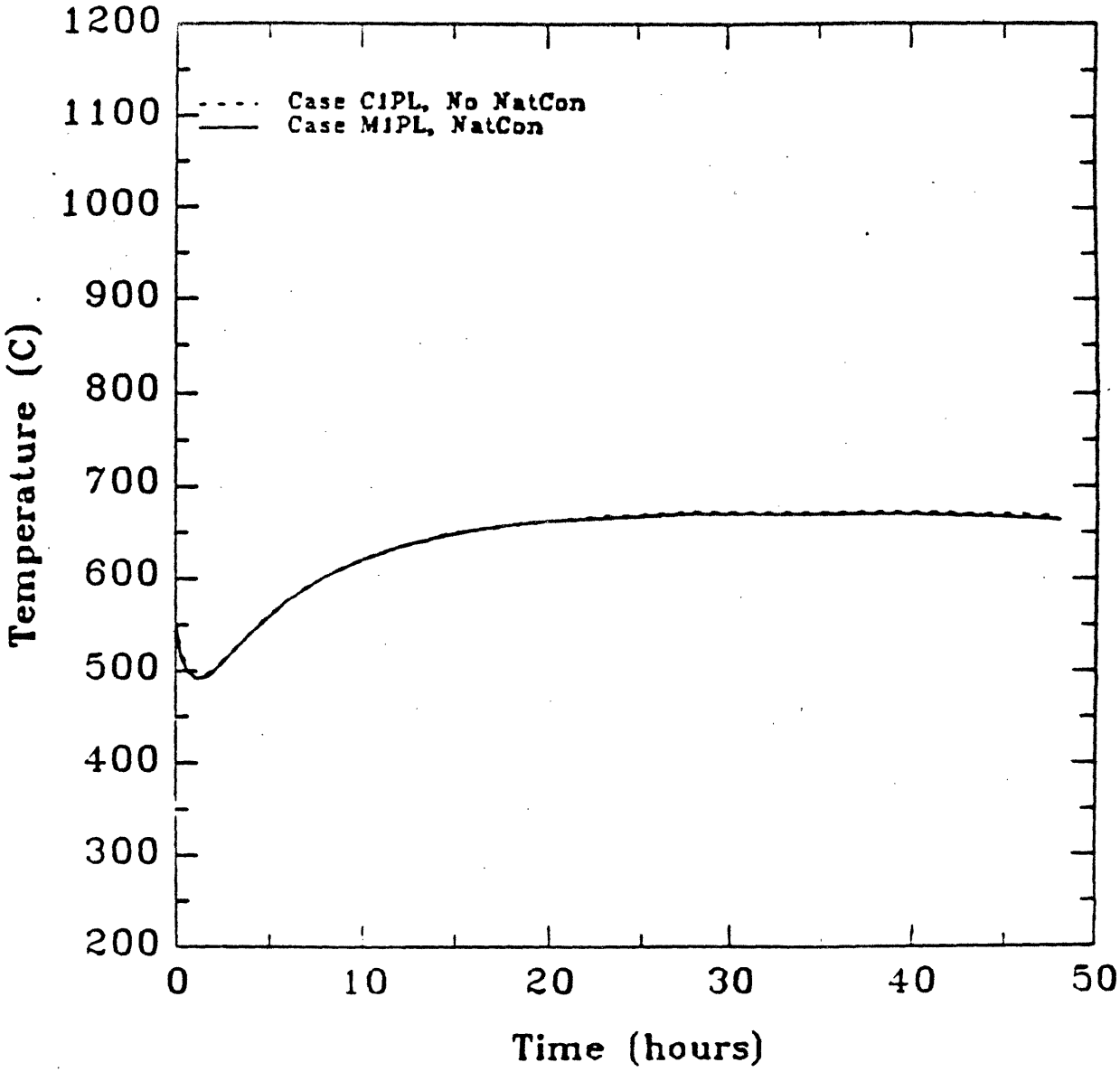

Figure 6.2.2b Maximum First Wall Temperature vs. Wall Load for Blanket #1 With and Without Natural Convection. In convection Case M1, magnetic field remains constant at operational value.

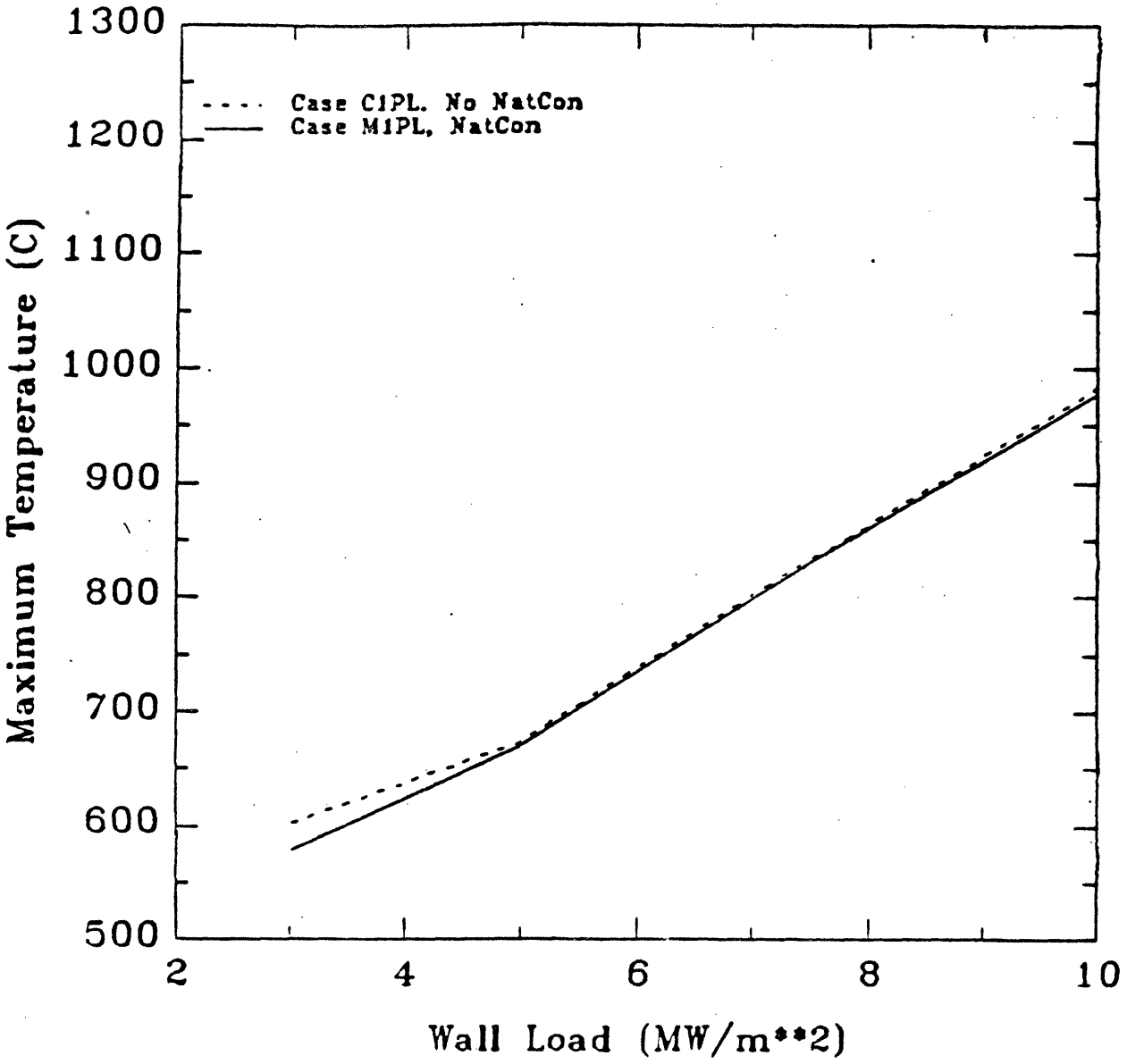

can be seen, the difference is negligible, which indicates that the flow rate of the lithium coolant is so small that it essentially carries no heat out of the blanket. This is the expected result and supports the conclusions of earlier works that under a magnetic field, the high MHD pressure drop eliminates the potential for natural convection cooling in liquid lithium systems.

In superconducting magnet systems, unlike normal resistive magnets, the magnet cannot be simply "turned off" by turning off the current. However, it is possible to reduce the magnetic field by diverting the current through a resistor, which would cause the magnetic field strength to decay exponentially. Under these conditions, a reasonable decay rate would be a two order of magnitude decay in 30 minutes [6.5]. This means that 30 minutes after accident initiation, the magnetic field strength would be 10^{-2} of its operational value, and after one hour, it would be 10^{-4} times its operational value. The decay would continue at this rate for the duration of the transient, however, after the first hour, the 10^4 reduction in the field would be enough to make the MHD pressure drop term negligible compared to the friction pressure drop term.

This magnetic field behavior, with the nominal friction pressure drop constants is designated Case M2 (see Table 6.2.1). The temperature response of Blanket #1 to the Case M2 LOFA is given in Figures 6.2.3a and 6.2.3b, again with the response to the no-convection LOFA Case C1. The differences here are very large. Note in Figure 6.2.3a that the temperature decreases almost immediately to well below the operating temperature. There is a plasma-induced temperature rise, leading to a maximum temperature, in the first five seconds (which is not clear in Figure 6.2.3a). All of the maximum temperatures for Case M2 plotted in Figure 6.2.3b are plasma-induced, occurring within five seconds. Immediately after this peak is reached, the continued coolant flow cools the blanket rapidly, reaching a quasi-steady state of about 350 °C, which is 50 °C above the coolant inlet temperature. This is in contrast to the results presented in Chapter 5, in which there was often a plasma-induced peak, then a decrease in temperature, followed by a second temperature

Figure 6.2.3a First Wall Temperature History After LOFA for Blanket #
With and Without Natural Convection. In convection Case M2
magnetic field decays two orders of magnitude in 30 minute

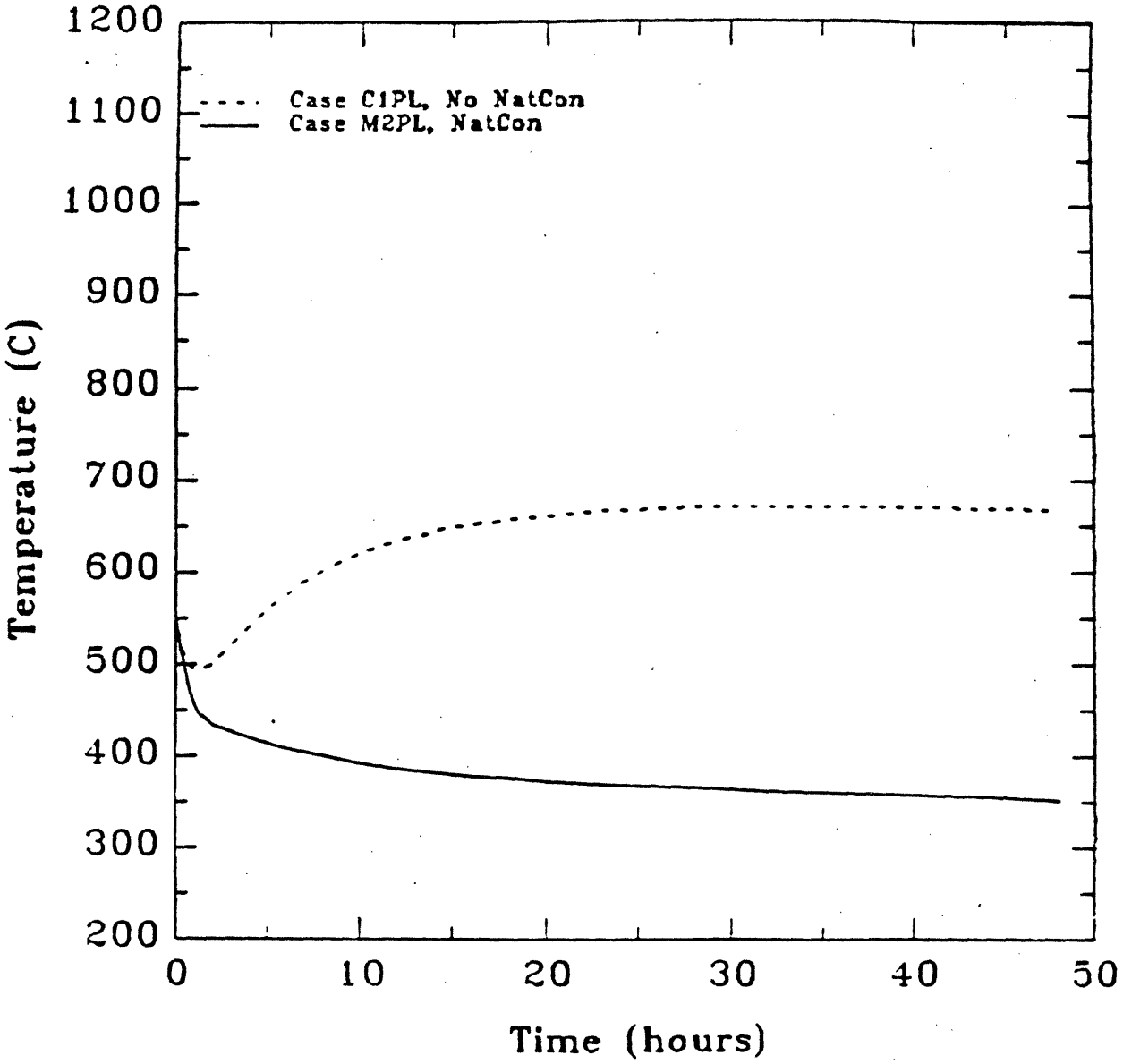

Figure 6.2.3b Maximum First Wall Temperature vs. Wall Load for Blanket #1 With and Without Natural Convection. In convection case M2, magnetic field decays two orders of magnitude in 30 minutes. All peak temperatures for Case M2 are plasma induced

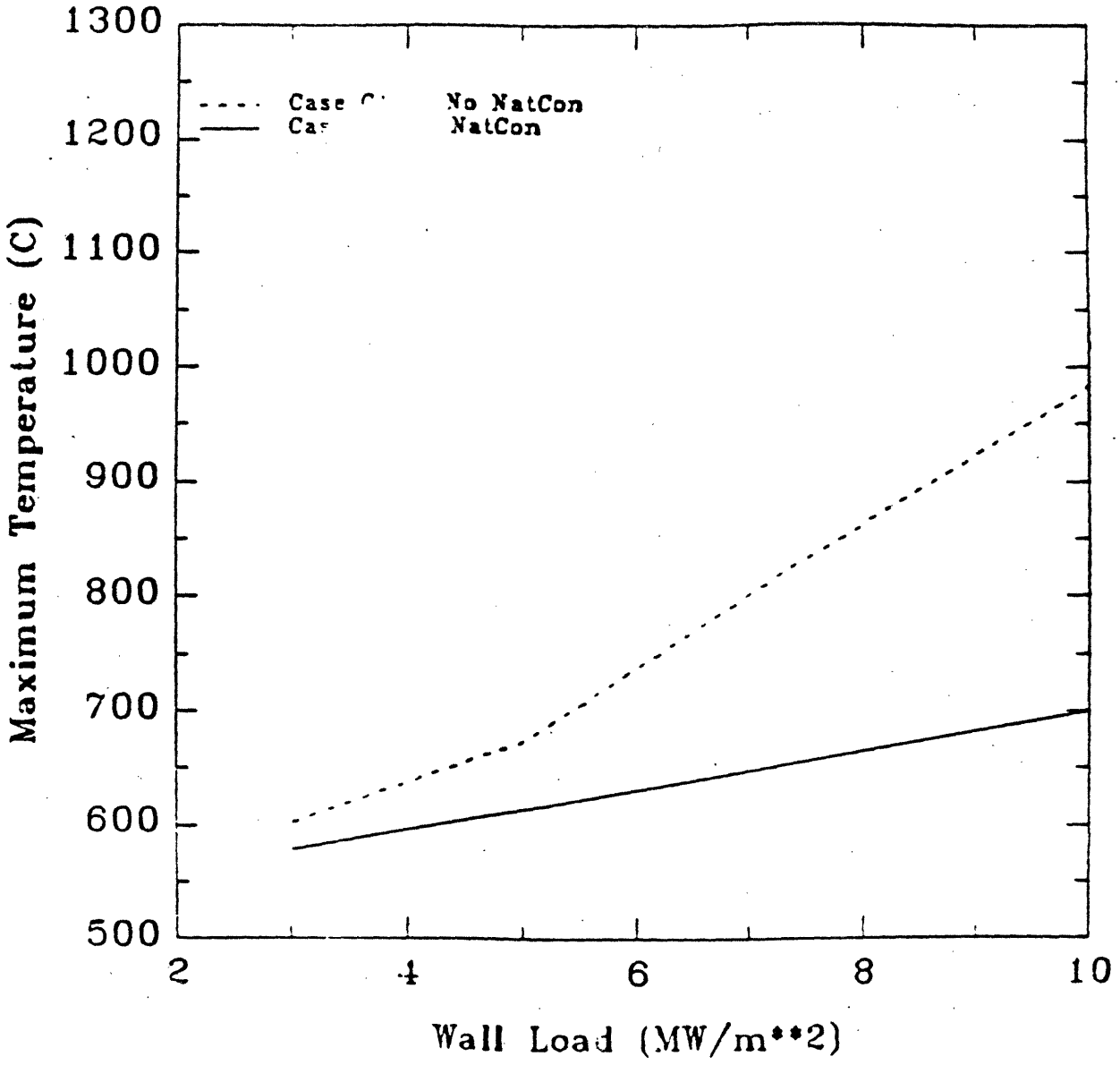

peak, which was the result of decay heating. In these convection cases, there is no second temperature peak. Following the plasma-induced peak, the temperature declines steadily to its quasi-steady state value, and thus there is no decay heat-induced temperature peak.

Although the result is obvious, it is useful to compare the coolant flow rates for convection Cases M1 and M2. In both cases, the flow becomes laminar almost immediately. Thus, according to the forced convection model (see Appendix E), the Nusselt numbers, and therefore the heat transfer coefficients h, will be the same in either case. This means that any difference in the temperature response between the two cases is due strictly to the coolant flow rate $\dot{m}$. As is clear from Figures 6.2.2a and 6.2.3a, there is a large difference in the temperature responses in the two cases. The coolant flow rates ($\dot{m}$, kg/s) for both cases plotted in Figure 6.2.4. In both cases, the flow rate drops very rapidly from its initial value of 1639 kg/s to below 0.1 kg/s, before rising to its steady state† value. The initial drop is so rapid that it cannot be seen in Figure 6.2.4. Note that the steady-state flow rate for Case M2 is almost three orders of magnitude higher than that for Case M1. During the steady state condition, the M2 pressure drop is due only to friction, while the M1 pressure drop is due to MHD and friction. Thus, the MHD pressure drop with the operational magnetic field is three orders of magnitude larger than the friction pressure drop with the nominal friction constants K_{fric}^{lam} and K_{fric}^{turb}.

It can be concluded from these results that as long as the magnetic field remains on, the exact value of the friction constants is not important. However, when the

---

† The "steady-state"condition referred to in the convection analysis is not a true steady state, because the decay heat source, $\dot{q}'''_{\text{decay}}$, is constantly decaying with time. This means that the coolant temperature rise ΔT will also decrease with time, and so will the flow rate $\dot{m}$. At long times (> 24 hours), however, the time rate-of-change of all of these parameters is small, and thus the condition resembles a true steady state.

Figure 6.2.4 Natural Convection Flow Rate vs. Time in one module of Blanket #1 with constant magnetic field (Case M1) and decaying magnetic field (Case M2).

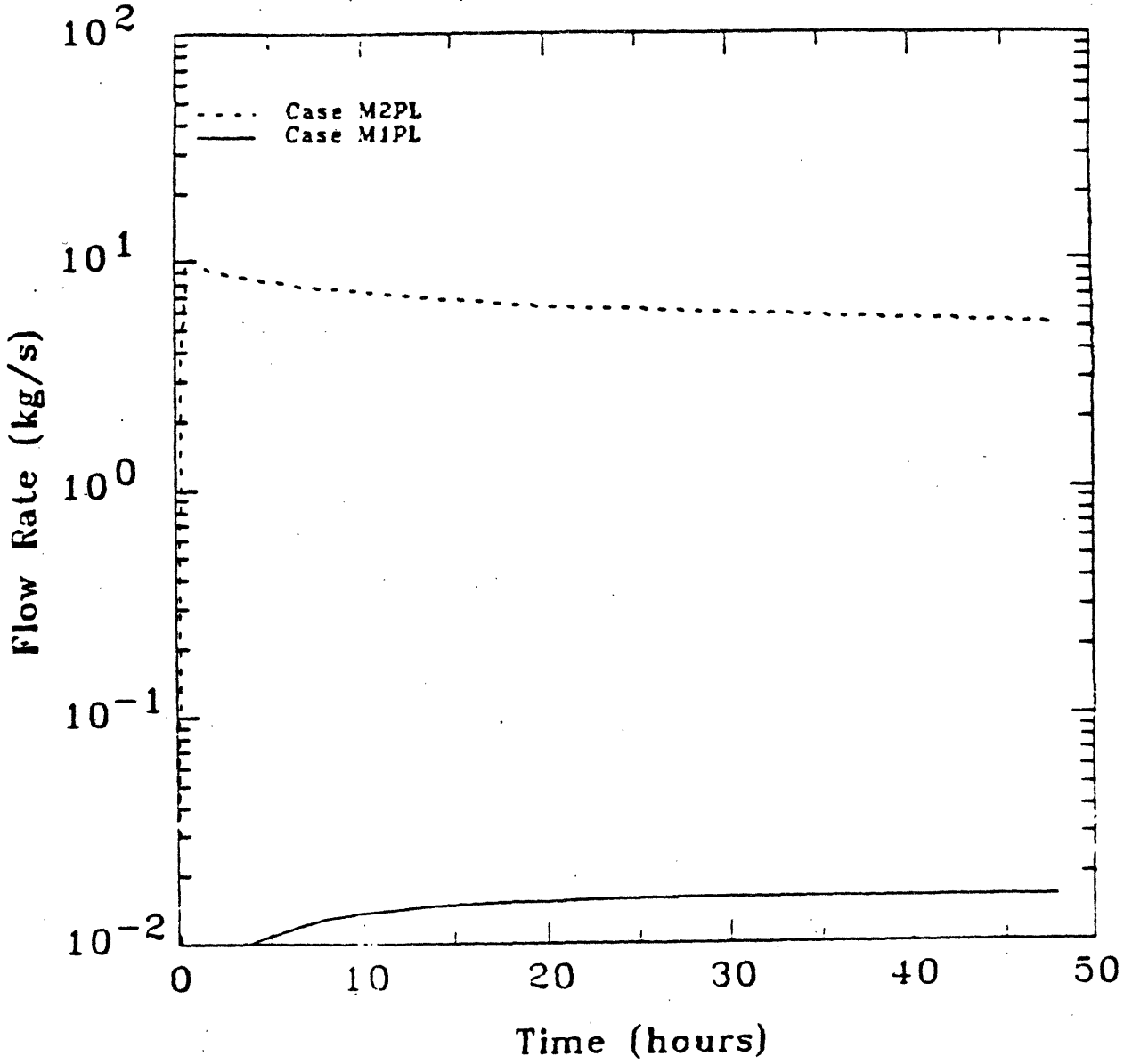

magnetic field is turned off (i.e., reduced by at least two orders of magnitude in a time that is short compared to the length of the transient), the values of the friction constants become very important. The heuristic nature of the calculation of these constants (see Appendix E) is subject to considerable of uncertainty, and thus an order of magnitude variation in their values is not inconceivable. Furthermore, the indication from the results presented in Figure 6.2.4 and discussed above is that an order of magnitude increase in K_{fric} would cause a significant *decrease* in the flow rate, which could greatly impact the Case M2 temperature response presented in Figure 6.2.3a. For this reason, the friction constants were varied by an order of magnitude in either direction from their nominal values, with the same magnetic field decay behavior (i.e., two orders of magnitude decay every 30 minutes). The case with the reduced friction constants is Case M5, and the case with the increased friction constants is M6 (see Table 6.2.1).

Figure 6.2.5a presents the temperature vs. time behavior of the first wall of Blanket #1 in Cases M1, M5, and M6. The flow rate vs. time behavior for these three cases is given in Figure 6.2.5b. Note that the case with the highest flow rate is the case with the lowest temperature rise, as expected. It should be pointed out that the maximum temperatures reached in all of these cases are essentially the same. This is because the maximum temperatures are plasma-induced and are reached within five seconds. In this short time, the magnetic field has not yet decayed significantly, and thus the friction pressure drop term is still not important. As far as the steady state temperature goes, however, the factor of 10 increase in the friction constants (Case M6) leads to an 80 °C increase in the coolant temperature rise, which is a factor of about 2.4 greater than the nominal case (M2). Meanwhile, a factor of 10 decrease in the friction constants (Case M5) leads to a 30 °C decrease in the coolant temperature rise, which is a decrease of a factor of 2.3 from that of Case M2. It is interesting to note that the steady state flow rate in Case M5 is 2.6 times greater than Case M2, while that of Case M6 is 2.9 times less than Case M2. These ratios correspond almost exactly with the ratios of the coolant temperature

Figure 6.2.5a First Wall Temperature History After LOFA for Blanket #1
With low friction pressure drop (Case M5), nominal friction pressure drop (Case M2), and high friction pressure drop (Case M6). All cases with decaying magnetic field.

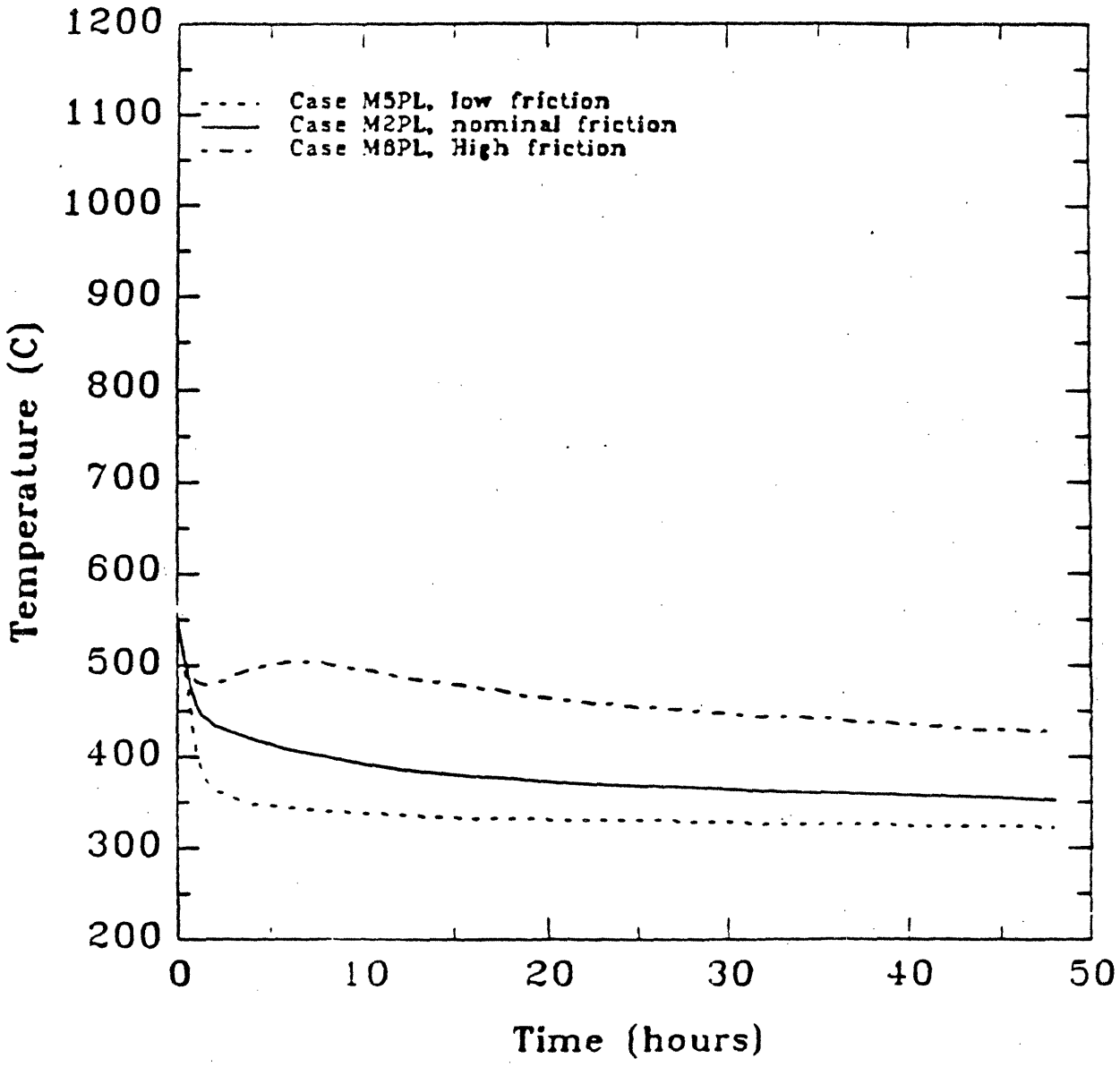

Figure 6.2.5b Natural Convection Flow Rate vs. Time in one module of Blanket With low friction pressure drop (Case M5), nominal friction pressure drop (Case M2), and high friction pressure drop Case (M6). All cases with decaying magnetic field.

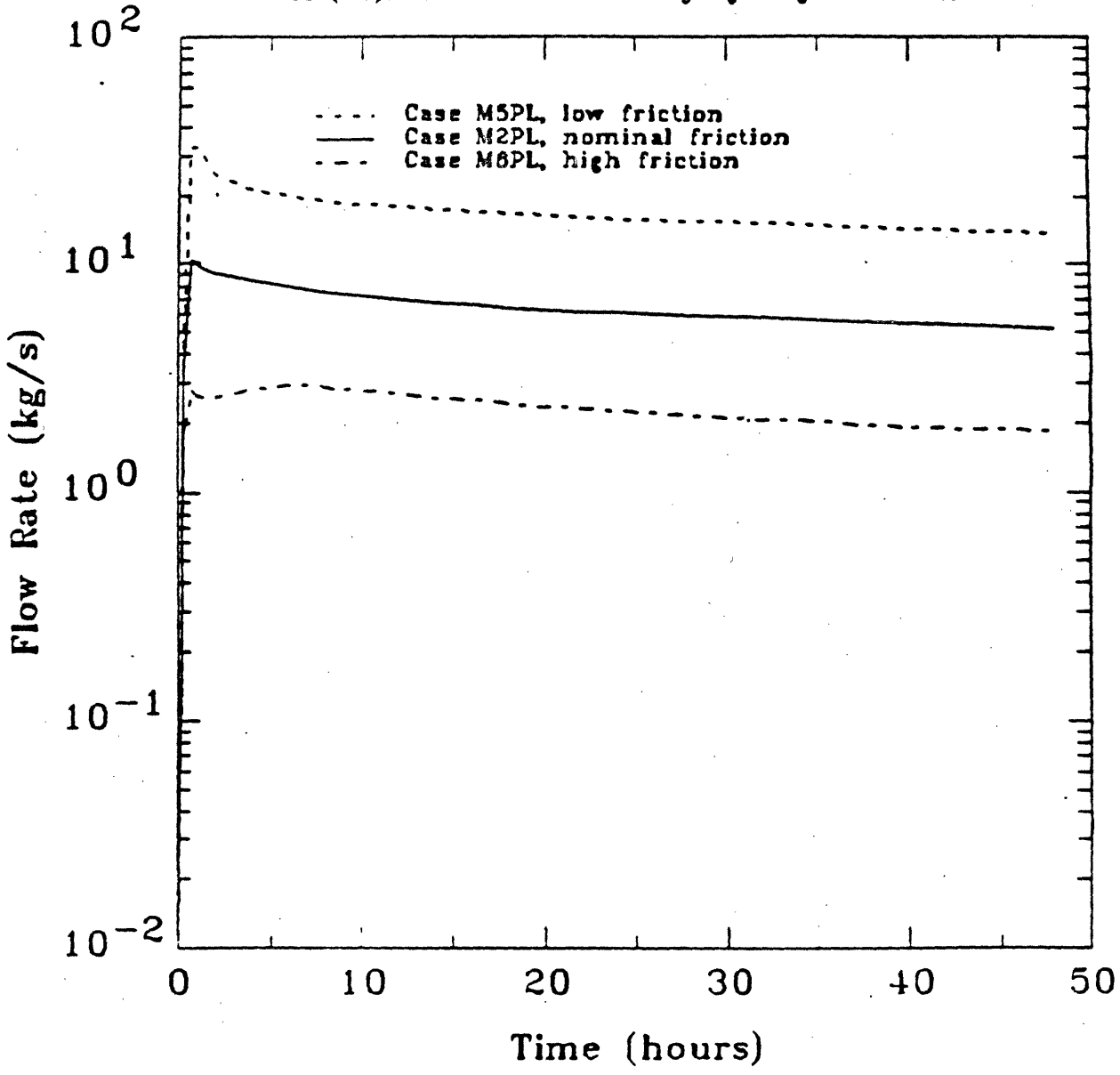

rise ΔT, supporting the contention that the impact of natural convection cooling relies primarily on the flow rate, and not the heat transfer coefficients h (which are the same in all three cases).

It is clear from these results that if the magnetic field can be turned off in a reasonable amount of time, liquid lithium natural convection has the potential to keep the blanket temperature well below the limits. If. however, the magnetic field can not be turned off, natural convection will be completely suppressed, and the conclusions regarding the temperature rise and potential for damage given in Chapter 5 will apply. It is therefore highly recommended that the superconducting magnets be designed with an allowance for a fairly rapid shut-down. Ideally, this mechanism would be directly coupled to other accident indicators, such as pump speed or coolant flow rate, for more rapid and reliable response. Such a mechanism would not necessarily be considered inherent safety, since it does rely on an external electrical or mechanical subsystem which has the potential for failure. However, it seems reasonable that such a system could be fail-safe, and would certainly represent a large improvement in the overall thermal safety of the reactor. One advantage of this would be that a pump-failure LOFA would require only pump replacement or repair, since no structural damage would occur. Thus, the reactor could be re-started soon after the accident.

6.2.3 Natural Convection in LiPb/LiPb/VCrTi Tokamak Blanket #4

The only difference between Blankets #1 and #4 that is of significance is in the coolant material. The material choice can have a significant impact. Note in equation (6.39) that the steady state temperature rise scales as $(\rho^2 \beta c_p)^{-1/2}$. This factor is 46 times larger for LiPb than for lithium [6.1, 6.2], which indicates that the temperature rise will be almost seven times lower in the LiPb system. This will not be the case, however, since, at the operational magnetic field strength, the ΔT for lithium is bounded by the temperature reached when no convection is assumed,

which is less than the ΔT calculated with equation (6.39). Even considering this, the conclusion that ΔT will be lower for LiPb is still valid. Note that this corresponds to the MHD case, in which the magnetic field stays on. In the case where the magnetic field is turned off, and the pressure drop is due only to friction, the steady state ΔT scales as $(\rho\beta c_p)^{-1/2}$. This factor is only 2.5 times greater for LiPb than for Li, so the temperature rise should only be about 1.6 times lower.

Figures 6.2.6a and 6.2.6b compare the temperature response to the convection Case M1 with that of the non-convection Case C1 LOFA's for Blanket #4. Note that, unlike for the lithium case (Blanket #1), there is a significant difference between Case M1 and C1, even with the magnetic field on. Note that the coolant inlet temperature for LiPb is 250 °C, which is 50 °C less than for lithium. This issue is discussed in Appendix E. Briefly, since the initial blanket temperature of Blanket #4 is 50 °C less than that of Blanket #1, the coolant inlet temperature was also decreased by 50 °C in order to keep the same operational coolant temperature rise, as well as eliminate the possibility that a different set of initial conditions could lead to different results. Note also that lithium lead is assumed to flow upward in the blanket, unlike the downward flow assumed in the BCSS design.

The indication from Figure 6.2.6 is that allowing for convection in the LiPb blanket reduces the maximum and steady-state temperatures to safe levels, even at high wall loads. This being the case, it appears that in LiPb blankets, it may not be necessary to shut off the magnets in the event of pump failure. This represents a substantial advantage over the liquid lithium blanket, for which it is recommended that the superconducting magnets be designed such that they can be shut off fairly quickly.

Figures 6.2.7a and 6.2.7b show the temperature response to the M2 convection LOFA, in which the magnets are shut off (two order of magnitude decay in 30 minutes), compared to the C1 no-convection LOFA. The behavior seen here is very similar to the lithium case (Figure 6.2.3). In fact, the coolant temperature rise in

Figure 6.2.6a First Wall Temperature History After LOFA for Blanket #4 With and Without Natural Convection. In convection Case M1, magnetic field remains constant at operational value.

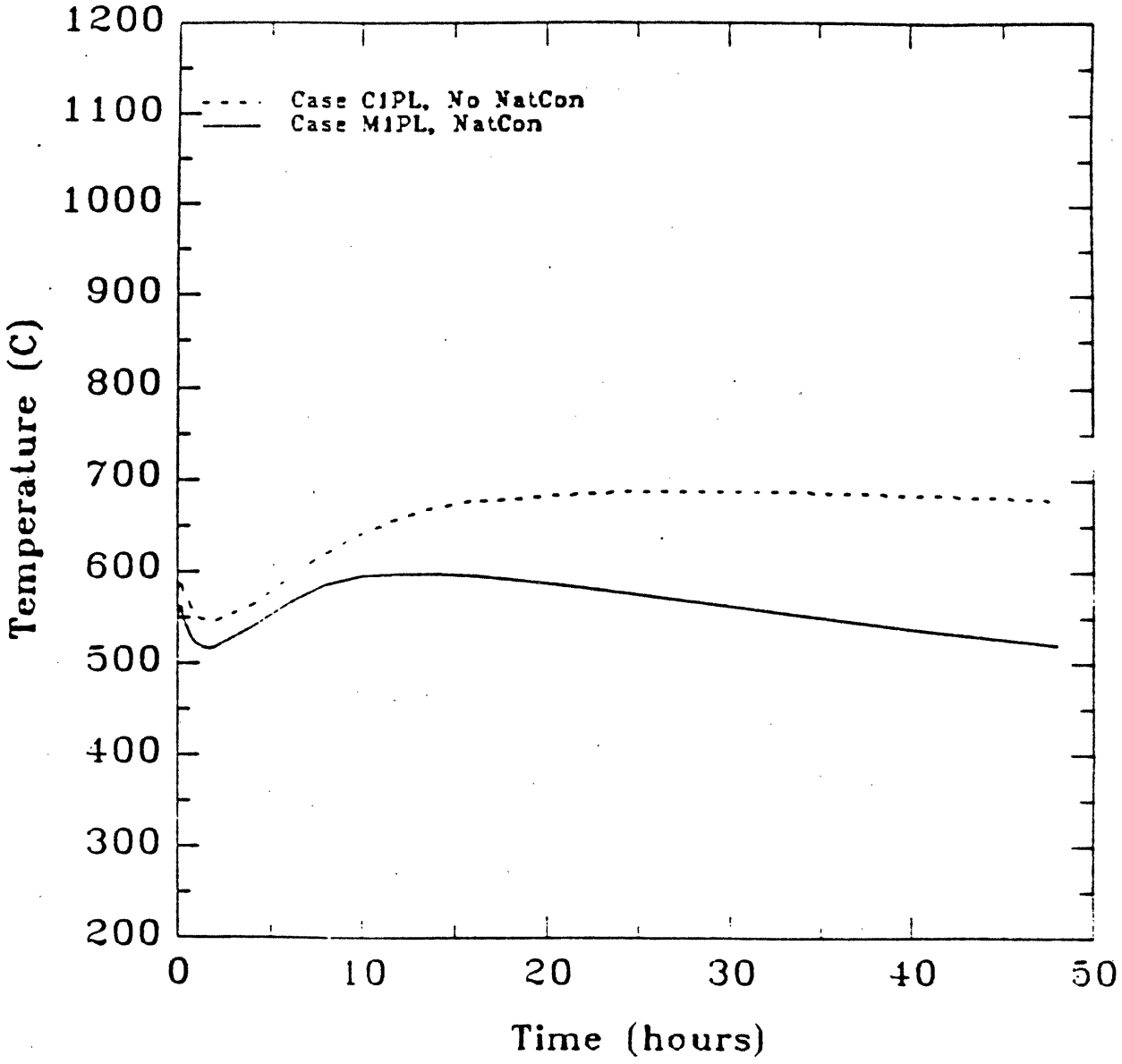

Figure 6.2.6b Maximum First Wall Temperature vs. Wall Load for Blanket #4 With and Without Natural Convection. In convection Case M1, magnetic field remains constant at operational value.

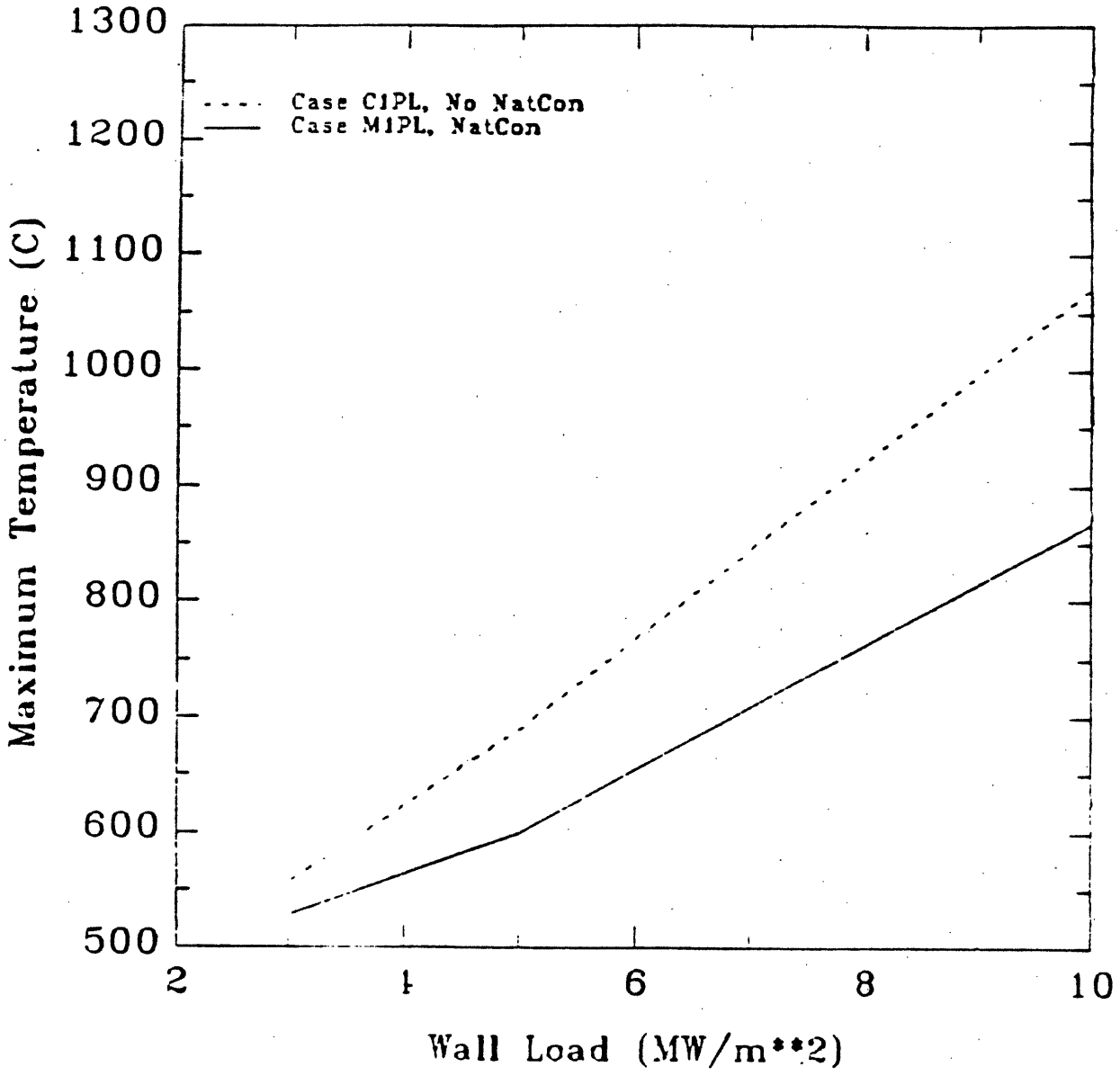

Figure 6.2.7a First Wall Temperature History After LOFA for Blanket #4 With and Without Natural Convection. In convection Case M2, magnetic field decays two orders of magnitude in 30 minutes

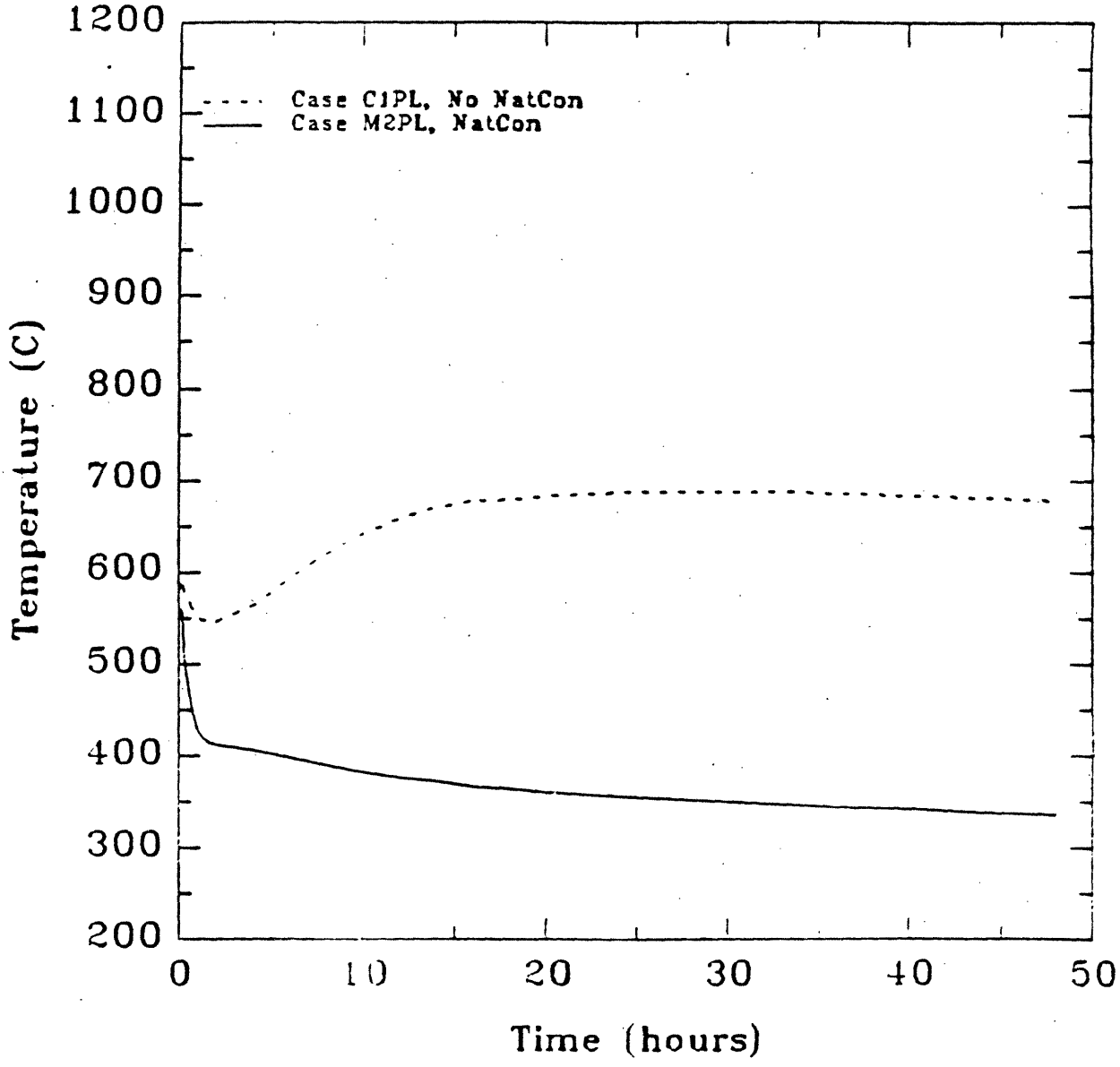

Figure 6.2.7b Maximum First Wall Temperature vs. Wall Load for Blanket #4 With and Without Natural Convection. In convection Case M2, magnetic field decays two orders of magnitude in 30 minutes. All peak temperatures for Case M2 are plasma induced

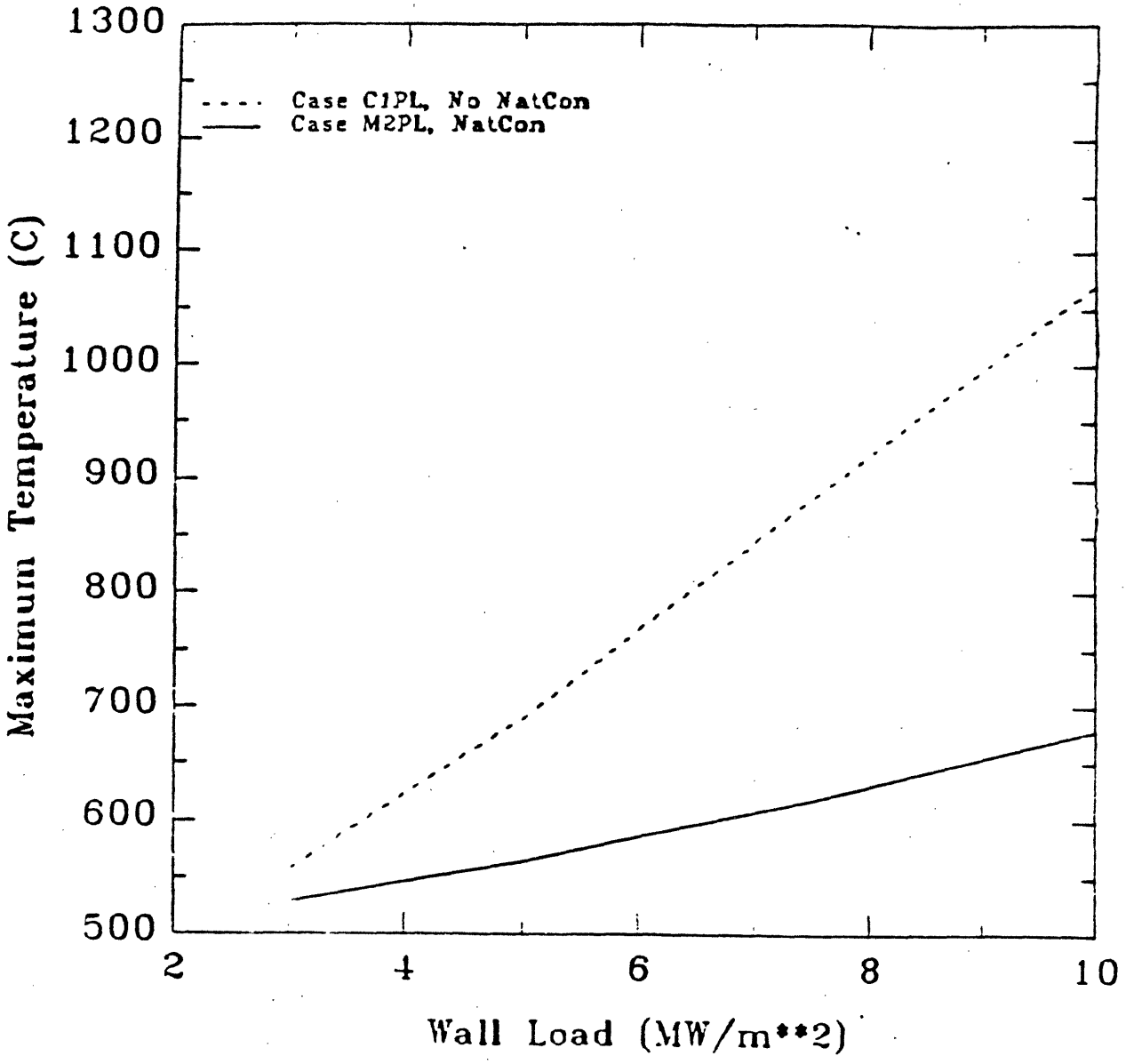

the LiPb case appears to be slightly higher than for lithium. With the magnetic field essentially shut off, there is no MHD pressure drop. This means the coolant temperature rise ΔT is not dependent on the coolant property $\rho^2 \beta c_p$, as it is in the MHD case. In the friction-only case, the steady state coolant ΔT is found by equating the buoyancy pressure head with the friction pressure drop. The flow rates in this case are found to be turbulent in the first wall channel, and so the friction pressure drop is found with equations (E.1) and (E.7). Equating this friction pressure drop with the buoyancy pressure head yields

$$\Delta T = \left[\frac{C_f^{turb} \mu^{0.25}}{\rho \beta c_p^{1.75}} \right]^{\frac{1}{2.75}} \tag{6.40}$$

Substituting the appropriate values for the liquid lithium cooled Blanket #1 and the $Li_{17}Pb_{83}$ cooled Blanket #4 (see Appendix E) shows that the temperature rise in the $Li_{17}Pb_{83}$ system is about 20% higher than in the lithium system.

6.2.4 Natural Convection in Li/Li/V RFP Blanket #3

The Reverse-Field-Pinch Blanket #3 has essentially the same material composition as, and thus is expected to display natural characteristics similar to, Blanket #1. However, the RFP has resistive copper magnets, which, unlike the superconducting magnets of the tokamaks, can be completely shut off in a very short time by shutting off the current that drives them. This process requires rapidly dumping a large amount of electrical energy which, at least in theory, can be done. Whether this contributes any benefit in terms of thermal safety by aiding natural convection beyond the exponential decay of the field strength that was assumed for the tokamak blankets is a relevant issue.

First, it should be noted that the RFP operates at a lower magnetic field than the STARFIRE reference value [6.8] for the tokamaks used in this analysis. This is discussed in Appendix E. This lower magnetic field will result in better convective

Figure 6.2.8a First Wall Temperature History After LOFA for Blanket #3 With and Without Natural Convection. In convection Case M1, magnetic field remains constant at operational value.

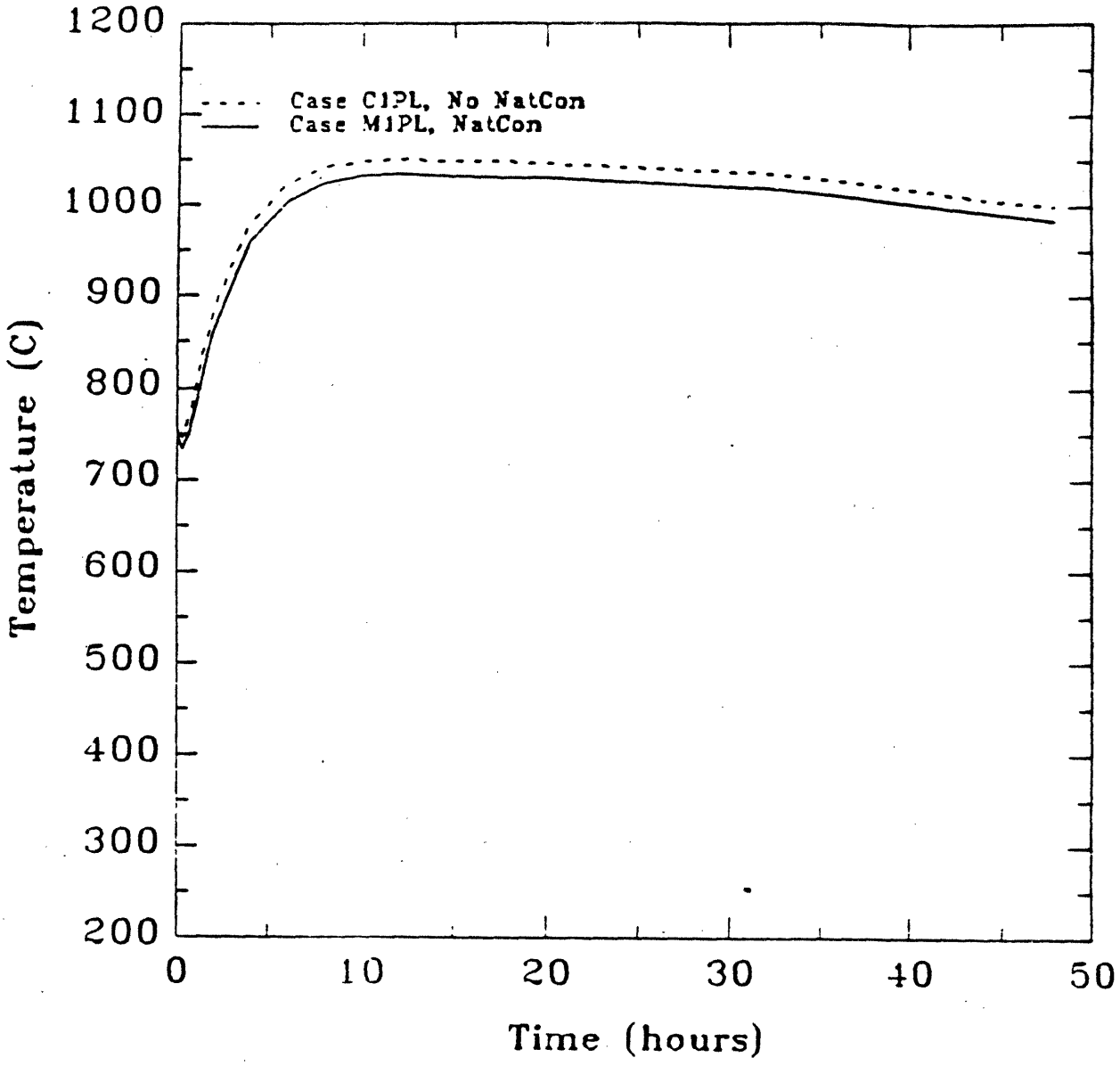

Figure 6.2.8b Maximum First Wall Temperature vs. Wall Load for Blanket #3 With and Without Natural Convection. In convection Case M1, magnetic field remains constant at operational value.

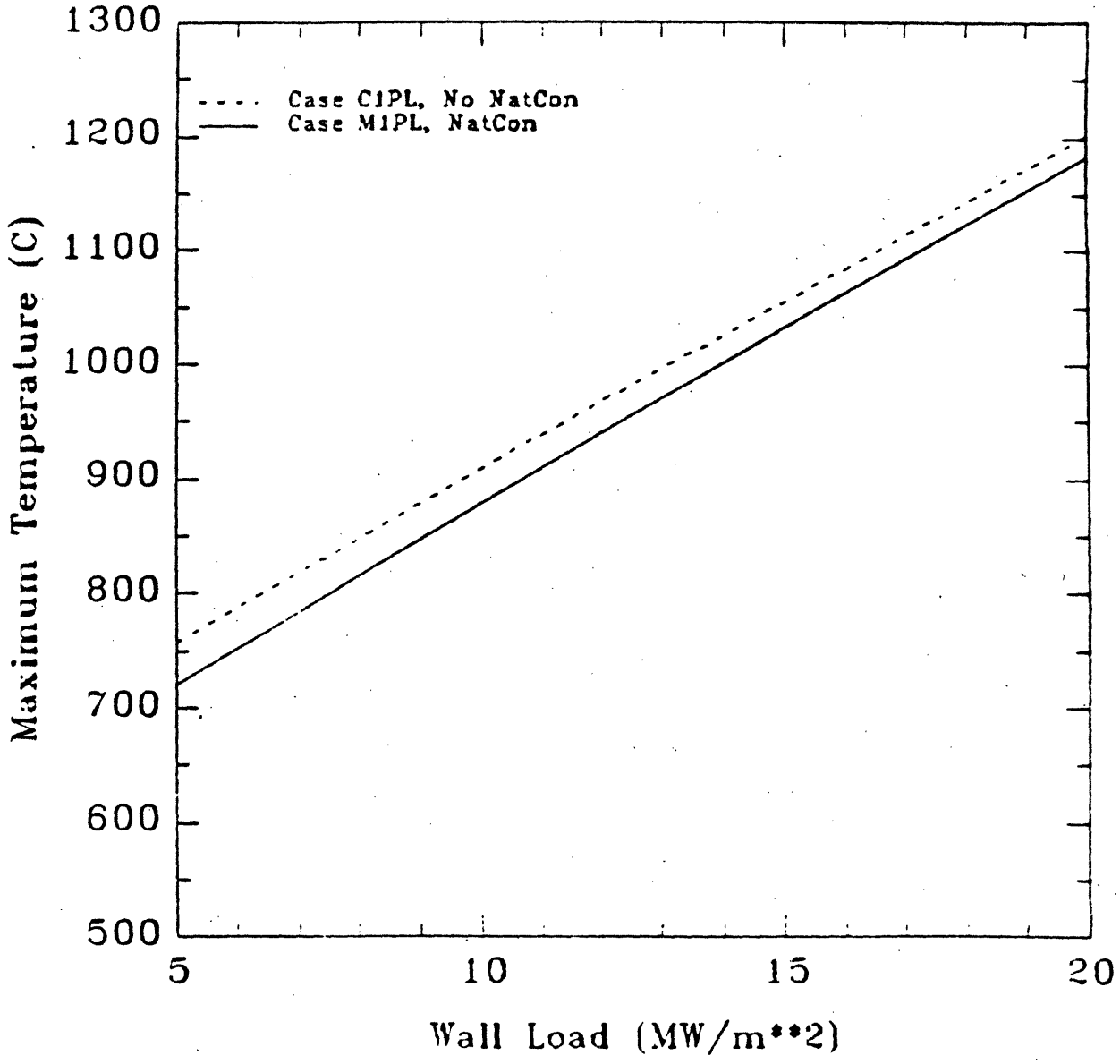

heat removal than the tokamaks in the case where the magnets stay on (Case M1). Furthermore, the resistive copper magnets of the RFP can be more quickly turned off, which is another advantage for the RFP. These factors must both be considered when comparing the results of the convection analysis for the tokamak blanket (Blanket #1) and the RFP blanket (Blanket #3).

Figures 6.2.8a and 6.2.8b give the temperature response in the first wall of Blanket #3 to the convection Case M1 and the no-convection Case C1 LOFA's at the nominal 15 MW/m^2 wall load. Unlike Blanket #1, there is a small but noticeable difference in the temperature response between the no-convection and convection cases when the magnetic field remains at its operational value. This is due primarily to the lower magnetic field in the RFP. The difference is still very small, however, indicating that operation at a lower B-field will not sufficiently enhance natural convection cooling in lithium cooled blankets.

The ability to shut off the copper magnets essentially immediately could have a significant impact. The temperature responses of Blanket #3 to convection Cases M1, M2, and M3 (see Table 6.2.1) are plotted in Figures 6.2.9a and 6.2.9b. In Case M2, turning off the magnetic field means the field strength decays by two orders of magnitude every 30 minutes. In Case M3, the magnetic field is completely shut off, such that B=0.0, at time=0. Note from Figure 6.2.9a that this immediate shut-off causes the plasma induced peak temperature, which is reached in about three seconds, to decrease rapidly to well below the operational temperature. This rise-to-peak (three seconds) and then decrease is so rapid that it is not distinguishable in Figure 6.2.9a, where it appears as if the temperature starts at about 300 °C. The peak temperatures are given in Figure 6.2.9b. The difference between Cases M2 and M3 is small, but increases with wall load. At the nominal wall load of 15 MW/m^2, the difference in the peak temperatures between Cases M2 and M3 is about 50 °C. This difference is potentially significant, however, at the relatively low values of peak temperature being reached ($\sim$ 850 - 900 °C), will not likely make a difference in overall thermal safety. Note from Figure 6.2.9a that the steady state

Figure 6.2.9a First Wall Temperature History After LOFA for Blanket #3
With constant magnetic field (Case M1), decaying magnetic field (Case M2), and zero magnetic field (Case M3).

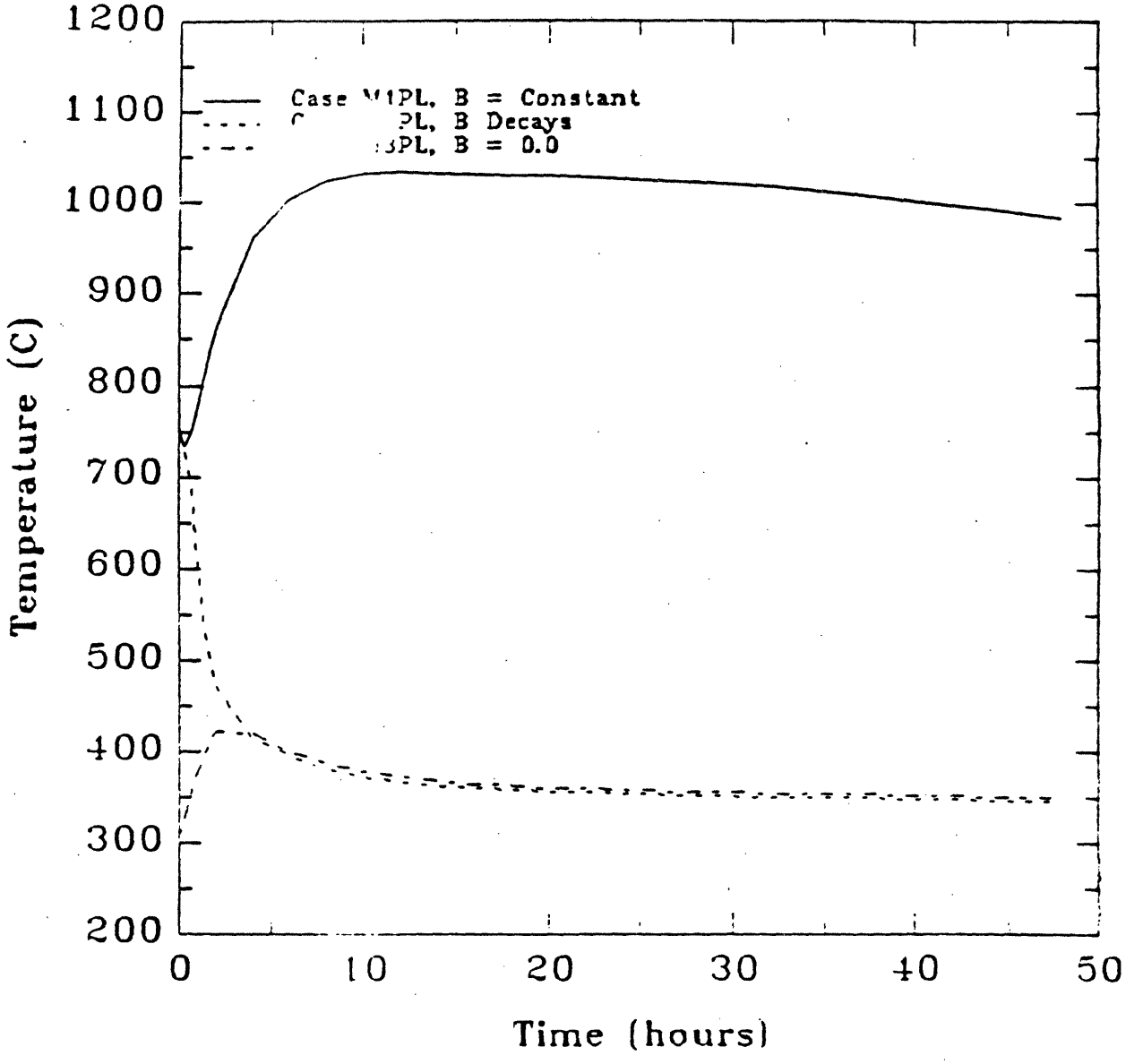

Figure 6.2.9b Maximum First Wall Temperature vs. Wall Load for Blanket #3 With constant magnetic field (Case M1), decaying magnetic field (Case M2), and zero magnetic field (Case M3). All peak temperatures for Cases M2 and M3 are plasma induced.

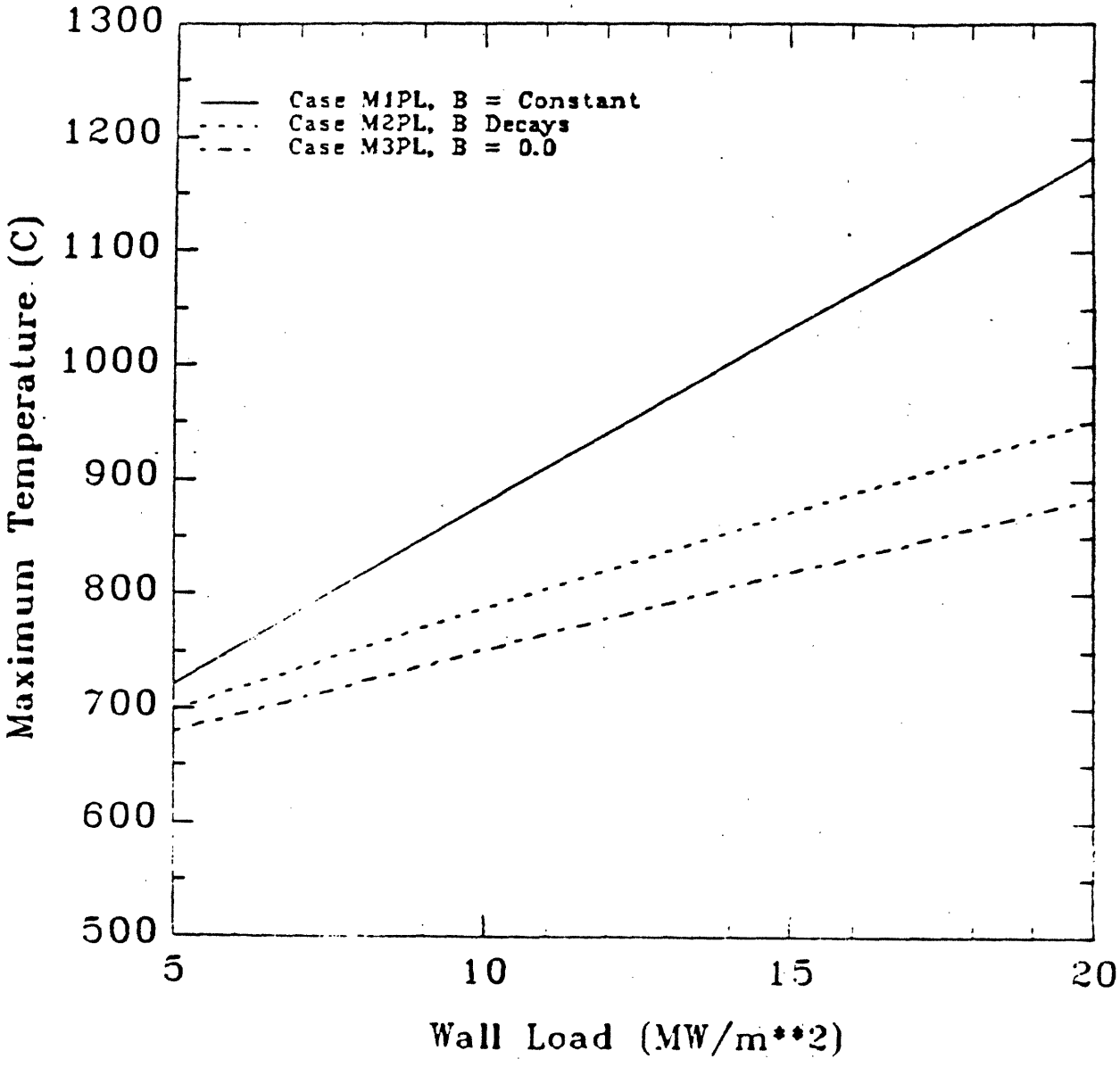

temperatures in Cases M2 and M3 are virtually identical. This is as expected, since at long times (> 2 hours), the magnetic field in Case M2 has decayed to essentially zero.

The response to Case M2, as well as the steady state response to Case M3, is very similar to the response to Case M2 in Blanket #1. This is because the impact of convection depends on the coolant material properties and the flow loop geometry. The overall mechanical configuration, and thus the flow loop geometry, is very similar for the tokamak and the RFP. The conclusion is that, in terms of natural convective cooling, the RFP does not represent an inherent advantage over the tokamak.

6.3 Conclusions for Natural Convection

The results clearly show that natural convection cooling can successfully mitigate the consequences of Loss-of-Flow Accidents in liquid metal cooled reactors. The properties of the coolant are very important in determining the impact. The low density of helium render it ineffectual as a natural convection medium, such that the temperature response of helium-cooled blankets is not affected by natural convection. The impact in liquid metal-cooled blankets can be very significant, but because of MHD effects, depends strongly on the magnitude of the magnetic field. Due to desirable coolant properties, liquid lithium-lead ($Li_{17}Pb_{83}$) can significantly reduce the temperature rise in the event of a LOFA, even if the magnetic field remains at the operational value. This is not true of liquid lithium. The impact of natural convection in liquid lithium-cooled systems depends on the exact magnitude of the magnetic field, however, at the fields that are currently considered for use in fusion power reactors, i.e., $\sim$ 5 - 10 Tesla and above, natural convection in lithium is almost completely suppressed.

Turning off the magnets, or substantially reducing the field strength in a relatively short time, greatly improves the impact that natural convection will have on

the temperature response. Plasma-induced peak temperatures, which are reached in the first few seconds of the transient, will be reduced only slightly. At longer times, however, the temperatures can be reduced to safe levels such that there is no danger of structural damage. For this reason, it is important to design superconducting magnets such that they can be shut off or experience a two order of magnitude field reduction in relatively short times, i.e., < 1 hour. This is especially true in lithium-cooled systems. The ability to shut off copper magnets in extremely short times causes a reduction in the (plasma-induced) peak temperature, although the longer term (steady-state) temperature response will be similar. Copper magnets offer an advantage in that they can always be shut off fairly rapidly, whereas the shutdown time of superconducting magnets is somewhat uncertain, and could be rather long.

In the event that the magnets can be shut-off, the natural convection impact further depends on the hydrodynamic (i.e., friction and form loss) pressure drop of the flow loop. It is desirable to reduce this pressure drop as much as possible. However, this parameter is far less important than the magnetic field behavior. When the magnetic field is turned off, an order of magnitude decrease in the friction constants (usually referred to as f and K_f) will result in only about a factor of 2 or 3 decrease in the steady state coolant temperature rise. In these instances, this temperature rise is usually low enough such that a factor of three is not important. Such changes in the friction constants result in an even smaller difference in the (plasma-induced) peak first wall temperature.

[6.1] B. Malinovic, Natural Convection Characteristics of Liquid Metal Cooled Fusion Reactors, S.M. Thesis, Nuclear Engineering Department, Massachusetts Institute of Technology, 1986.

[6.2] B. Malinovic and M. Kazimi, Passive Decay Heat Removal in Liquid-Metal Cooled Reactors, Fusion Technology 10, (3), pp. 1205-1210, November 1986.

[6.3] W. E. Kastenberg, On Design Criteria for After and Decay Heat Removal in Fusion and Fusion-Fission Power Plants, Nuclear Engineering and Design/Fusion 1 pp. 51-60 (1984).

[6.4] S. Glasstone and A. Sesonske, Nuclear Reactor Engineering, 3rd Edition, p. 376, Van Nostrand Reinhold Company, New York, 1981.

[6.5] Joel H. Schultz, MIT Plasma Fusion Center, Personal Communication, June 1986.

[6.6] Clement Wong, GA Technologies, Inc., Personal Communication, March 1987.

[6.7] P.J. Gierszewski, B. Mikic, and N.E. Todreas, Natural Circulation in Fusion Reactor Blankets, ASME Journal of Heat Transfer V. 80-HT-69, pp. 1-7, July, 1980.

[6.8] R.L. Miller, et. al., Advanced Tokamak Reactors Based on the Spherical Torus (ATR/ST), Los Alamos National Laboratory, LA-10740-MS, June 1986.

[6.9] O.E. Dwyer, Liquid Metal Heat Transfer, in "Sodium-NaK Engineering Handbook,"Vol. 2, O.J. Foust, Ed., Gordon and Breach, 1976.

[6.10] F. Najamabadi, N.M. Ghoniem, R.W. Conn, et al., The TITAN Reversed-Field Pinch Fusion Reactor Study, Scoping Phase Report, UCLA-PPG-1100, January, 1987.

[6.11] N.E. Todreas and M.S. Kazimi, Nuclear Reactor Thermal Analysis, Hemisphere, to be published 1988.

[6.12] R.A. Gross, Survey of Reactor Aspects of Compact Fusion Concepts, Nuclear Technology/Fusion, Vol. 4, September 1983.

[6.13] R.L. Hagenson and R.A. Krakowski, Compact Reversed-Field Pinch Reactors (CRFPR): Sensitivity Study and Design-Point Determination, Los Alamos National Laboratory, LA-9389-MS, July 1982.

[6.14] Walker, J. S., Liquid-Metal MHD Flow in a Duct Whose Cross-Section Changes from a Rectangle to a Trapezoid, with Applications in Fusion Blanket Designs, Argonne National Laboratory, ANL/FPP-TM-206-01, 1986.

[6.15] D.L. Smith et al., Blanket Comparison and Selection Study (BCSS) - Final Report, Argonne National Laboratory, ANL/FPP-84-1, September 1984.

[6.16] Frank M. White, Fluid Mechanics, McGraw-Hill Book Company, New York, 1979.

7. Plasma Overpower/Continuation Transients

In addition to the undercooling transients discussed in Chapters 5 and 6, a mismatch between the power and cooling can arise from an increase in the power level. The problem stems from the fact that the power could increase by some incremental amount, and perhaps continue to increase due to a positive feedback mechanism, while the cooling rate (i.e., coolant velocity) remains at the nominal level. This mismatch will result in a rise in the first wall temperature until the plasma shuts off, or until a new (higher) steady state temperature value is reached, depending on the behavior of the plasma power increase.

In either case, unlike the Loss-of-Flow and Loss-of-Coolant transients discussed previously, the primary stress in the first wall will remain at the operational level, while the thermal stress becomes higher as the temperature gradient in the first wall increases (due to the higher plasma heat flux). The combination of increased temperature and high stress can result in either acute structural failure or thermal creep rupture of the first wall.

Note that the overpower phenomenon is similar to the LOFA or LOCA cases in which the plasma continues to burn. Recall from Chapters 5 and 6 that the post-accident time behavior of the plasma power was given by an assumption. The effect of the continued plasma burn (versus immediate plasma shut-off) was discussed briefly in Section 5.4.5. In this previous discussion, no mechanism was described which would cause the plasma to shut off, or to follow the behavior given in Figure

5.1.3. It is possible that the plasma would continue to burn, until gross structural failure or evaporation of coating material caused a mass influx of impurities into the plasma.

Clearly, the problem at hand is that the plasma-induced temperature excursions could lead to failure of the first wall if the plasma continues to burn without some kind of "automatic shut-off mechanism". One such mechanism, as proposed by Grant Logan [7.1], is that of a "fuse plug". This consists of a small section of the first wall, or a plug, that is made of a material other than the rest of the first wall. Behind this plug would be a small canister of high pressure helium. The idea would be that in the event of a plasma-induced temperature excursion, this plug would fail at some time before the bulk of the first wall fails. When the plug fails, the helium behind it would escape into the plasma chamber, thus diluting (and extinguishing) the plasma.

The purpose of this chapter is to analyze this plasma shut-off mechanism, and the issues that must be considered when designing the plug. The issues that first come to mind are to identify the failure mechanism (i.e., melting, acute structural failure, thermal creep rupture) of importance, and the time scale involved, that is, the time-to-failure. The model for this analysis is discussed in Section 7.1. Section 7.2 presents the results of the analysis as applied to a vanadium alloy (V-15Cr-5Ti) first wall and an HT-9 first wall, since these are the first wall materials of the blankets considered in this study. The HT-9 used in this study is actually a low activation version, which is referred to as MT-9. The only difference between MT-9 and HT-9 are the activation characteristics. The thermal and mechanical properties of the two steels are the same. This chapter does not deal with structural activation, and so the designation HT-9 is maintained. This is because the material properties used in this chapter were taken from the reference data on HT-9 [7.2,7.3,7.7]. In Section 7.3, the results of Section 7.2 are used to identify the material properties that are required of the fuse plug material.

The model to determine the overpower (or plasma-induced) temperature response of the first wall is based on the code THIOD. Only the first wall is considered. The heat source consists of both the plasma heat flux on the front face of the first wall, as well as the operational power density in the first wall from neutron interactions. This volumetric heat source tends to be small compared to the surface heat flux, but the effect is included for completeness. For the boundary condition in the overpower cases, it is assumed that the coolant temperature at the back face of the first wall remains constant, as does the heat transfer coefficient h between the first wall and the flowing coolant. To analyze the LOFA or LOCA cases with continued plasma burn, the value of h is varied to reflect the fact that the coolant is not flowing or is no longer present.

The first wall is not represented as a single mesh point, as it is in the analyses presented in Chapters 5 and 6. Instead, a much more detailed spatial mesh is used, in order to determine the extent of damage that the first wall experiences during the transient. It is also necessary to obtain an accurate temperature gradient across the first wall in order to assess the thermal stresses in the wall. The first walls analyzed are those of Blankets #1 and #2. In both cases, the End-of-Life (EOL) wall thickness is used (3.0 mm for VCrTi Blanket #1, 1.5 mm for HT-9 Blanket #2). The sensitivity of the results to the thickness of the first wall is determined through a parametric study. The initial temperature distribution across the first wall was found by setting the temperature of the coolant behind the first wall. For the VCrTi case, the coolant temperature (T_{coolant}) is 751 K, and for the HT-9 case, it is 728 K. This, along with the heat transfer coefficient h from the wall to the coolant, determines the temperature at the back of the wall, since during operation, all the heat both entering the wall and being produced in it must be transferred to the coolant. The operational gradient was found by inputting T_{coolant} and h into the code and running it for the nominal plasma power level. This yields as a result the operational (steady-state) temperature distribution in the first wall, from which

the operational temperature gradient ΔT is found. For the VCrTi wall, ΔT is 107 K, and for the HT-9 wall, ΔT is 53 K.

The rest of the model used to determine the temperature response to the overpower transients is the same as that presented in Chapter 5 and Appendix D. Unlike the results presented previously, however, the structural damage analysis here is carried out simultaneously with the temperature response analysis. This requires simultaneous calculation of the stress level in the first wall. The total stress in the first wall is due to the coolant pressure and the thermal gradient.

7.1.1 Determination of First Wall Stress

To determine the stress level in the first wall, it is assumed that the first wall is a long cylinder, with flowing coolant in the inner annulus. There are two components of the stress in the first wall. The first is due to the pressure of the coolant. This stress is treated with a simple thin-shell model, such that the pressure stress is constant across the thickness of the first wall and is given by

$$\sigma_p = \frac{pR}{\delta} \tag{7.1}$$

where

p is the coolant pressure (MPa),

R is the radius of the first wall cylinder (m), and

δ is the effective thickness of the first wall (m).

Note that in the thin-shell model, it is assumed that $\frac{R}{\delta} \gg 1$. The coolant pressure p and the cylinder radius R remain constant. The effective first wall thickness δ, however, changes with time, as is discussed is Section 7.1.2.

The second stress component is the thermal stress, which arises from the temperature gradient across the first wall. During operation, there exists a steady state temperature gradient which leads to a thermal stress. Mechanical strain during operation works to relieve this stress, such that it is assumed that at EOL, the thermal stress across the first wall is zero. Thus, the operational temperature distribution is the "zero point"for the thermal stress in the first wall. During the overpower transient, the temperature gradient increases, and during the plasma-continuation LOFA and LOCA cases, the temperature gradient decreases. In either case, the change in the gradient causes a thermal stress. The thermal strain at mesh point i, ϵ_i, is found by

$$\epsilon_i = \alpha(T_i - T_{io}) \tag{7.2}$$

where

α is the thermal expansion coefficient of the first wall material (K^{-1}), and

T_{io} is the initial temperature at mesh point i.

The thermal stress at any mesh point i is related to the difference between the thermal strain ϵ_i at point i and the average thermal stress ϵ_{ave} across the first wall as

$$\sigma_t^i = \frac{E}{1-\nu}(\epsilon_{ave} - \epsilon_i) \tag{7.3}$$

where

E is Young's Modulus for the first wall material (MPa), and

ν is Poisson's ratio.

The total stress at mesh point i is then the sum of the pressure stress and the

thermal stress at point i, such that

$$\sigma_i = \sigma_p + \sigma_t^i \tag{7.4}$$

7.1.2 Determination of First Wall Damage

Once the temperature vs. time history is known, as well as the stress in the first wall, the level of structural damage can be determined. As is discussed in Chapter 3, there are two damage mechanisms: acute structural failure, which occurs when the applied stress exceeds the ultimate tensile strength (UTS) of the material, and thermal creep rupture, which occurs when the applied stress (at elevated temperatures) causes excessive creep.

Both the UTS and creep resistance are temperature dependent material properties. Thus, due to the temperature gradient, the degree of structural damage will vary across the thickness of the first wall. The question is whether the first wall as a whole has failed, and the time it takes for that failure to occur. Both the acute failure and thermal creep rupture analyses are carried out simultaneously with the temperature response calculation. The processes described in the next two sections are carried out during each time step, until failure by either mechanism has occurred, or until four hours have passed. It is assumed that four hours is sufficient time to intervene and halt the overpower transient by external means.

7.1.2.1 Acute Structural Failure

As was stated, the ultimate tensile strength of the first wall material is a temperature dependent property. The assumption given in Chapter 3 is that above a certain temperature, the UTS is essentially zero, such that structures which reach this temperature are assumed to have suffered acute structural failure. This as-

sumption is necessitated by the lack of high temperature strength data for VCrTi and HT-9. For the analyses presented in Chapters 5 and 6, using this assumption is sufficient for defining a maximum allowable temperature in the first wall. In this chapter, the goal is to calculate the failure time, given the calculated stress and temperature distributions within the first wall. This requires knowledge of the UTS as a function of temperature, in order to determine whether the UTS has been exceeded. The relations used for this analysis are given below. These relations are gross extrapolations of limited data bases, and are used primarily to illustrate the methodology, as well as make zeroth-order guesses of the failure time. They should not be construed as accurate representations of the high temperature strength characteristics of VCrTi and HT-9, and for this reason were not included in the discussion of material limits given in Chapter 3.

To obtain a relation correlating the UTS to the temperature, the mechanical property data presented in the BCSS [7.2] was approximated as a linear function of temperature. Then, the UTS for the "slab"of material represented by mesh point i can be found with the temperature T_i, using

$$U_i = a_{\mathrm{UTS}} T_i + b_{\mathrm{UTS}} \tag{7.5}$$

where

U_i is the ultimate tensile strength of the "slab"in mesh zone i (MPa), and

a_{UTS} and b_{UTS} are coefficients derived from the data in reference [7.2]. These values are,

for VCrTi:

a_{UTS} = -1.133

b_{UTS} = 1719

for HT-9:

a_{UTS} = -0.900

b_{UTS} = 1241

Using U_i and σ_i, it can be determined if the material in mesh zone i has "failed". If σ_i exceeds U_i, then it is assumed that this slab has failed. This does not necessarily mean the first wall has failed, however, since there may still be some portion of the first wall which has not failed. When mesh zone i fails, it is assumed that that part of the first wall is no longer capable of supporting any of the load on the first wall. Thus, the effective thickness of the first wall, δ, is reduced by the thickness of mesh zone i, i.e., Δx_i. Mathematically, if $\sigma_i > U_i$, then

$$\delta = \delta - \Delta x_i \tag{7.6}$$

If, because of this reduction, δ becomes zero (or less), then the first wall is considered to have suffered acute structural failure. This is because a δ of zero or less means that every mesh zone comprising the first wall has failed, thus, the entire first wall has failed. The time at which δ reached zero is then the failure time. If δ is still above zero, then the first wall is considered to have not yet failed. However, note from equation (7.2) that the pressure stress in the wall is inversely proportional to δ. Given the reduction in δ (equation (7.6)), this means that the pressure stress in the part of the wall that has not yet failed will increase. This is because, essentially, if some part of the wall is assumed to be no longer capable of supporting a load, then the load must be supported by an effectively thinner wall, resulting in higher stresses.

7.1.2.2 Thermal Creep Rupture

Like the UTS, thermal creep resistance is highly temperature dependent. Treat-

ment of the temperature dependence of the creep process using Larson-Miller theory is described in detail in Chapter 3 and Appendix A. To obtain the Larson-Miller Parameter for mesh zone i given the stress σ_i, the following correlations are used:

For VCrTi:

$$P_i = -48.86\sigma_i + 7.266(10^4) \tag{7.7}$$

For HT-9:

$$P_i = -6.879(10^3)log_{10}(\sigma_i) + 4.183(10^4) \tag{7.8}$$

Note that the correlation for VCrTi is the same as that given in Appendix A, while that for HT-9 is different. The difference in the HT-9 correlation reflects the difference in creep behavior at the lower temperature and higher stress regimes experienced in the overpower transient analysis. This correlation comes from the data presented in reference [7.3].

Once the Larson-Miller parameter P_i is known, the rupture fraction for mesh zone i, f_r^i is calculated in the same manner as is described in Chapter 3 and Appendix A. When f_r^i exceeds one, then it is assumed that the material in zone i has failed, and, just as in the acute failure analysis, the effective first wall thickness δ is reduced by Δx_i. Again, if δ reaches zero, then the first wall is considered to have failed due to thermal creep rupture.

It should be noted that, since the front of the first wall is the hottest, it is generally expected that both acute structural damage and thermal creep rupture will begin at the front and "propagate"toward the back face. Thus, there will be some overlap of the region that has failed due to structural failure and that which has failed due to thermal creep rupture. In this instance, the effective first wall thickness δ is not reduced by the thickness of *both* regions, but only by the larger

thickness. That is, the total thickness that has suffered acute structural failure is labeled δ_{acute}, and the thickness that has suffered thermal creep rupture is δ_{creep}. Then, the effective first wall thickness δ is reduced only by the maximum of δ_{acute} and δ_{creep}, not the sum of the two.

7.2 Results of Overpower Transient Analysis

The model described in the previous section was applied to the structural materials VCrTi and HT-9, using a number of different plasma power vs. time scenarios, as well as the LOFA and LOCA cases with continued plasma burn. The results obtained essentially consist of the time to failure and the failure mechanism. In some instances, no failure occurred within the four hour maximum. The results presented in this section are not intended to give an accurate indication of the actual time to failure in the event of plasma overpower transients. Instead, they are to be considered as a zeroth-order "guess"at the failure time, and used for comparative purposes between the structural materials, and to give an indication of the desirable properties of potential fuse plug materials.

7.2.1 Increased Plasma Heat Flux

A number of different plasma power excursions were considered for the cases in which the plasma power (surface heat flux) is above the nominal level, while the cooling remains active. The results of any other behavior can be inferred from the results obtained here. The plasma power is represented by the surface heat flux Γ_h. Mathematically, the heat flux time behavior is represented as

$$\Gamma_h = \Gamma_h^{nom}(1 + ct^p) \tag{7.9}$$

where

Γ_h is the surface heat flux (MW/m^2),

Γ_h^{nom} is the nominal surface heat flux (MW/m^2),

t is the time (seconds), and

c and p are inputted constants.

The values of c and p were varied. The two cases examined most thoroughly are the step increase case and the linear increase case. In the step increase case, the exponent p is zero, and in the linear increase case, p=1. Note that when p=0, the plasma power increases by a factor of c+1 and then remains at that level. When p=1, the power increases by an increment of Γ_h^{nom} every $1/c$ seconds.

Tables 7.2.1a and 7.2.1b give the results of the overpower analysis for VCrTi and HT-9 respectively. The tables give the values of c and p, then show the maximum first wall temperature rise (ΔT_{max}), the average first wall temperature rise at the time that the maximum is reached (ΔT_{ave}), the failure time (t_{fail}), and the fraction of the first wall that has failed due to acute failure and thermal creep rupture. A value of 1.0 in either of these columns indicates failure by the specified mechanism.

Analysis of the results presented in Table 7.2.1 is useful for obtaining a feel for what takes place in the overpower transient. In the cases where p=0.0, that is, when the power increases incrementally and then remains constant at the elevated level, the temperature distribution rapidly reaches a new steady state based on the new power level. Recall that the power level is increased by a factor of c+1. In these cases, the temperature difference between the wall and the coolant increases by the same factor, to account for the fact that c+1 times as much heat is being transferred to the coolant. As was stated in Section 7.1, it is assumed that over the relatively short time frame of the overpower transient, the coolant temperature T_{coolant} remains constant. The temperature difference between the wall and the coolant is relatively small, only a few degrees, thus the temperature at the back face of the wall changes only very slightly. The temperature gradient ΔT, which

Table 7.2.1a Results of Overpower Analysis for VCrTi. First wall thickness = 3.0 mm.

c	p	ΔT_{max} (°C)	ΔT_{ave} (°C)	t_{fail} (hours)	Acute Failure Fraction*	Thermal Creep Fraction*
1.0	0.0	104.2	53.6	> 4	0.0	0.0
4.0	0.0	391.3	201.4	> 4	0.0	0.03
5.0	0.0	480.1	247.2	> 4	0.07	0.17
6.0	0.0	566.0	291.6	> 4	0.17	0.23
7.0	0.0	649.3	334.7	> 4	0.23	0.43
7.25	0.0	669.8	345.3	> 4	0.23	0.50
7.50	0.0	690.1	355.8	> 4	0.33	0.63
7.75	0.0	710.2	366.2	2.38	0.90	1.0*
8.0	0.0	730.2	376.5	1.23	0.93	1.0*
8.1	0.0	738.2	380.7	9.54e-01	0.93	1.0*
8.2	0.0	746.1	384.8	7.43e-01	0.93	1.0*
8.25	0.0	750.1	386.8	6.50e-01	1.0*	0.97
8.50	0.0	769.8	397.0	3.46e-01	0.83	1.0*
8.75	0.0	789.5	407.2	1.78e-01	0.87	1.0*
9.0	0.0	808.9	417.3	8.61e-02	0.93	1.0*
9.1	0.0	814.7	420.3	6.65e-04	0.93	1.0*
9.2	0.0	815.9	420.8	4.97e-04	0.93	1.0*
9.25	0.0	816.5	421.1	4.59e-04	0.93	1.0*
9.50	0.0	819.5	422.5	3.61e-04	0.93	1.0*
9.75	0.0	822.6	424.0	3.11e-04	0.93	1.0*
10.0	0.0	825.6	425.4	2.77e-04	0.93	1.0*
11.0	0.0	837.6	431.0	2.03e-04	0.93	1.0*
12.0	0.0	849.6	436.7	1.65e-04	0.93	1.0*
13.0	0.0	861.8	442.4	1.40e-04	0.93	1.0*
14.0	0.0	874.2	448.3	1.22e-04	0.93	1.0*
0.10	1.0	816.3	421.1	2.54e-02	0.93	1.0*
0.25	1.0	815.6	420.7	1.02e-02	0.93	1.0*
0.50	1.0	816.8	421.3	5.15e-03	0.93	1.0*
0.75	1.0	818.0	421.9	3.47e-03	0.93	1.0*
0.10	2.0	846.5	436.4	2.80e-03	0.97	1.0*
0.50	2.0	852.3	438.9	1.31e-03	1.0*	0.83

* A value of 1.0 indicates failure by this mechanism.

Table 2.1b Results of Overpower Analysis for HT-9. First wall thickness = 1.5 mm.

c	p	ΔT_{max} (°C)	ΔT_{ave} (°C)	t_{fail} (hours)	Acute Failure Fraction*	Thermal Creep Fraction*
1.0	0.0	55.1	29.1	> 4	0.0	0.0
2.0	0.0	109.8	57.9	> 4	0.0	0.0
3.0	0.0	164.1	86.6	> 4	0.0	0.0
4.0	0.0	218.0	115.0	> 4	0.0	0.07
4.5	0.0	244.7	129.1	> 4	0.0	0.13
5.0	0.0	271.4	143.2	> 4	0.0	0.33
5.5	0.0	298.0	157.3	2.53	1.0*	0.73
6.0	0.0	324.5	171.3	1.57	1.0*	0.73
6.5	0.0	350.8	185.2	1.03	1.0*	0.73
7.0	0.0	377.1	199.1	6.82e-01	1.0*	0.73
7.5	0.0	403.3	212.9	4.10e-01	1.0*	0.73
8.0	0.0	429.4	226.7	2.18e-01	1.0*	0.73
8.5	0.0	455.4	240.5	1.50e-01	1.0*	0.80
9.0	0.0	481.3	254.2	8.89e-02	1.0*	0.80
9.1	0.0	486.5	256.9	6.39e-02	1.0*	0.80
9.2	0.0	489.0	258.2	3.37e-04	1.0*	0.0
9.3	0.0	488.2	257.7	2.56e-04	1.0*	0.0
9.4	0.0	487.4	257.2	2.20e-04	1.0*	0.0
9.5	0.0	486.5	256.7	1.97e-04	1.0*	0.0
10.0	0.0	484.4	255.2	1.43e-04	1.0*	0.0
10.5	0.0	484.9	255.1	1.18e-04	1.0*	0.0
11.0	0.0	485.4	255.1	1.02e-04	1.0*	0.0
12.0	0.0	486.5	255.0	8.03e-05	1.0*	0.0
13.0	0.0	487.1	202.4	6.64e-05	1.0*	0.0
14.0	0.0	488.1	254.5	5.66e-01	1.0*	0.0

* A value of 1.0 indicates failure by this mechanism.

essentially is linearly dependent on the heat flux, also increases by a factor of $c+1$. What is really being measured by this analysis, then, is the ability of the first wall to handle higher power levels, i.e., higher wall loads.

The results in Table 7.2.1 can also be used to define a "maximum allowable"overpower transient. That is, if, for a given overpower transient, the time behavior of the plasma power and the duration of the transient are known, an equivalent factor can be found and used to check if failure is likely to occur. This is done by defining the *plasma power multiplication factor*, $m(t)$, as the instantaneous increase in the plasma power, such that

$$\Gamma_h(t) = m(t)\Gamma_h^{nom} \tag{7.10}$$

Note that for the behavior described by equation (7.9),

$$m(t) = 1 + ct^p \tag{7.11}$$

For the cases where p=0, it is clear the $m(t)$ will simply equal $c+1$, which is constant. Figure 7.2.1 plots the the time-to-failure t_{fail} vs. the surface heat flux (MW/m^2) on the first wall. Note that the nominal heat flux for the tokamaks is 1 MW/m^2, thus the value of the heat flux in Figure 7.2.1 is equivalent to $c+1$ as given in Table 7.2.1. The idea is that for any power multiplication factor, the time-to-failure can be read from Figure 7.2.1. This is useful in the following way. If the time behavior of a specific overpower transient is known, then the instantaneous power multiplication factor $m(t)$ can be found at any time, and t_{fail} for that $m(t)$ can be found from Figure 7.2.1. Now, if it is known that the power remains at the specified power level for a certain length of time, say Δt^n, then the "damage fraction"that will occur is found by dividing Δt^n by t_{fail}^n. That is,

Figure 7.2.1 Failure Time vs. Heat Flux for VCrTi and HT-9 First Walls

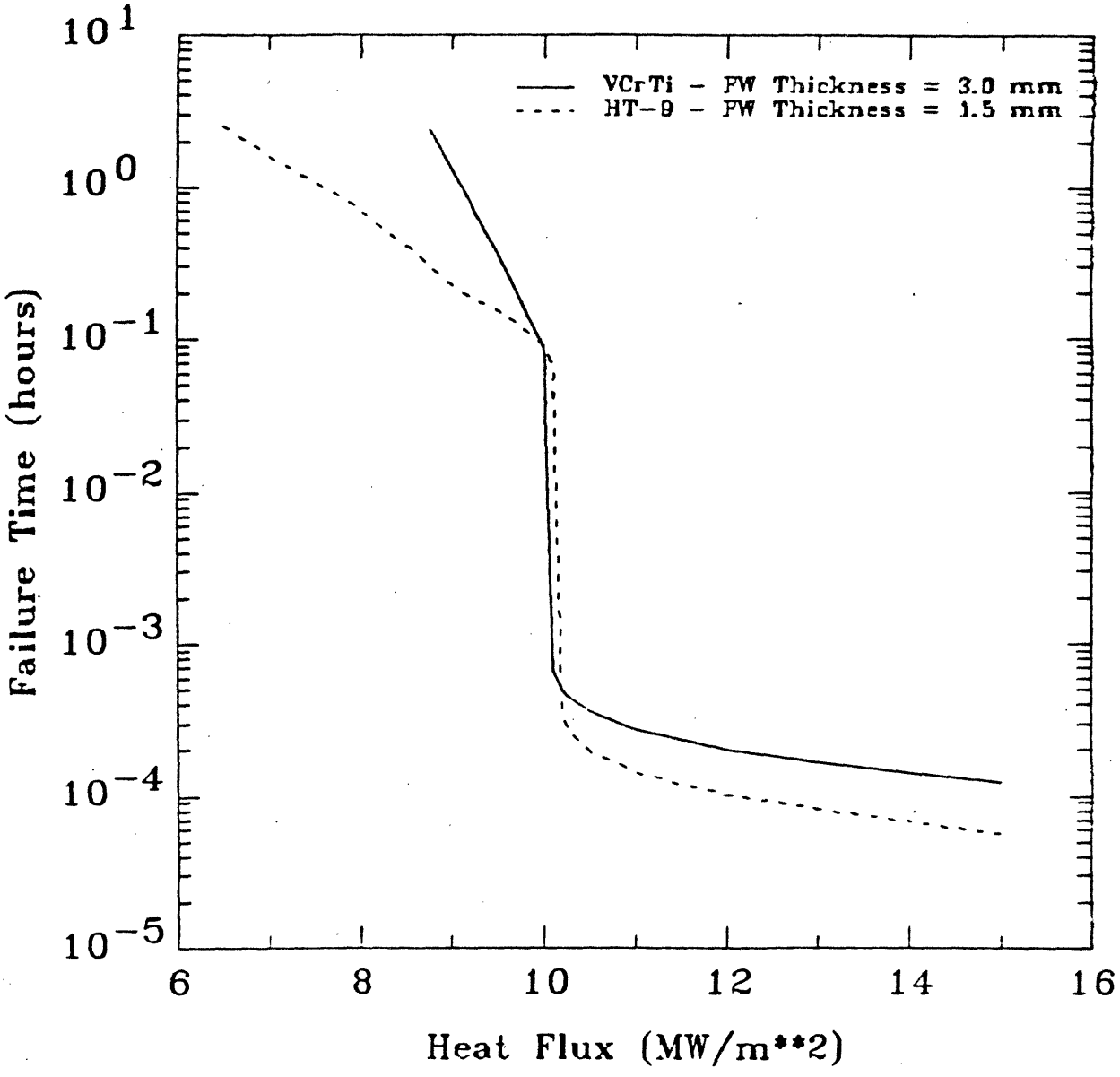

$$f^n_{damage} = \frac{\Delta t^n}{t^n_{fail}} \tag{7.12}$$

where the n superscript refers to the time step. By approximating the actual time behavior of $m(t)$ by a series of "steps", that is, by discrete increments of time Δt^n over which the power level is constant, then the damage fraction can be summed up over time as

$$f_d = \sum_n f^n_{damage} \tag{7.13}$$

When f_d exceeds one, it can be assumed that the first wall has failed, and the actual time-to-failure will be

$$t_{fail} = \sum_n^N \Delta t^n \tag{7.14}$$

where N is the number of the time step in which f_d exceeded one.

It is clear from Figure 7.2.1 that the failure time decreases dramatically over a narrow range of heat flux. This heat flux, which is about 10 MW/m^2 for the VCrTi and HT-9 cases, can be loosely referred to as a "threshold"heat flux for the specific first wall. This means that overpower transients which generate heat fluxes above the threshold will cause first wall failure almost immediately. Overpower transients which do not generate heat fluxes above the threshold may not cause first wall failure, depending on the duration of the transient. In these cases, failure can be predicted by the "damage fraction"model described above.

The threshold heat flux idea is supported by examining the results in Table 7.2.1 for the cases when p=1 and p=2. For VCrTi, the threshold heat flux is about 10 MW/m^2, and the nominal (operating) heat flux is 1 MW/m^2. This means that the threshold power multiplication factor is about 10. The power multiplication factor

$m(t)$ is given by equation (7.11). The indication is that failure will occur when $m(t)$ equals 10, or when $ct^p = 9$. Note that when p=1 and c=0.1, this occurs when t=90 seconds (note that the times given in Table 7.2.1 are in hours), which is very close to the failure time given in Table 7.2.1 for this case. Other combinations of p and c yield the same result; the first wall fails just about the time that the heat flux reaches the threshold.

Note that although the threshold heat flux is the same for VCrTi and HT-9, there are differences in the behavior of these materials. VCrTi shows a much longer failure time than HT-9 at heat fluxes below the threshold, and a slightly longer failure time (about a factor of two) above the threshold. Note from Table 7.2.1 that for VCrTi, the power must be increased by a factor of 4 before significant damage occurs in the first four hours, and failure does not occur in the first four hours unless the power level is increased by at least a factor of 8.5. While the HT-9 wall also remains damage-free up to a four-fold increase in power, a factor of 6.5 increase causes acute failure in two and a half hours. It is possible that part of this difference is due to the difference in thickness of the two first walls. The VCrTi wall is twice as thick as the HT-9 wall. This greater thickness reduces the pressure stress in the wall, however, increasing the thickness of the HT-9 wall would result in higher thermal stresses, thus it is not clear that any benefit would be realized by using a thicker HT-9 wall.

To examine this, the HT-9 wall thickness was varied, and the analysis repeated. The results of this parametric study are shown in Figure 7.2.2, which shows the time-to-failure (t_{fail}) vs. heat flux for HT-9 walls of various thicknesses. Note that the threshold heat flux *decreases* as the wall thickness *increases*. This is due solely to the fact that a thicker wall yields a larger temperature gradient than a thinner wall. This larger gradient has two effects. First, it generates a higher temperature at the front of the wall, since the temperature at the back of the wall is about the same in all the cases. Second, it causes greater thermal stresses. These two effects cause the wall to fail more rapidly. At any rate, it is clear from these results that

Figure 7.2.2 Failure Time vs. Heat Flux for HT-9, Varying First Wall Thickness

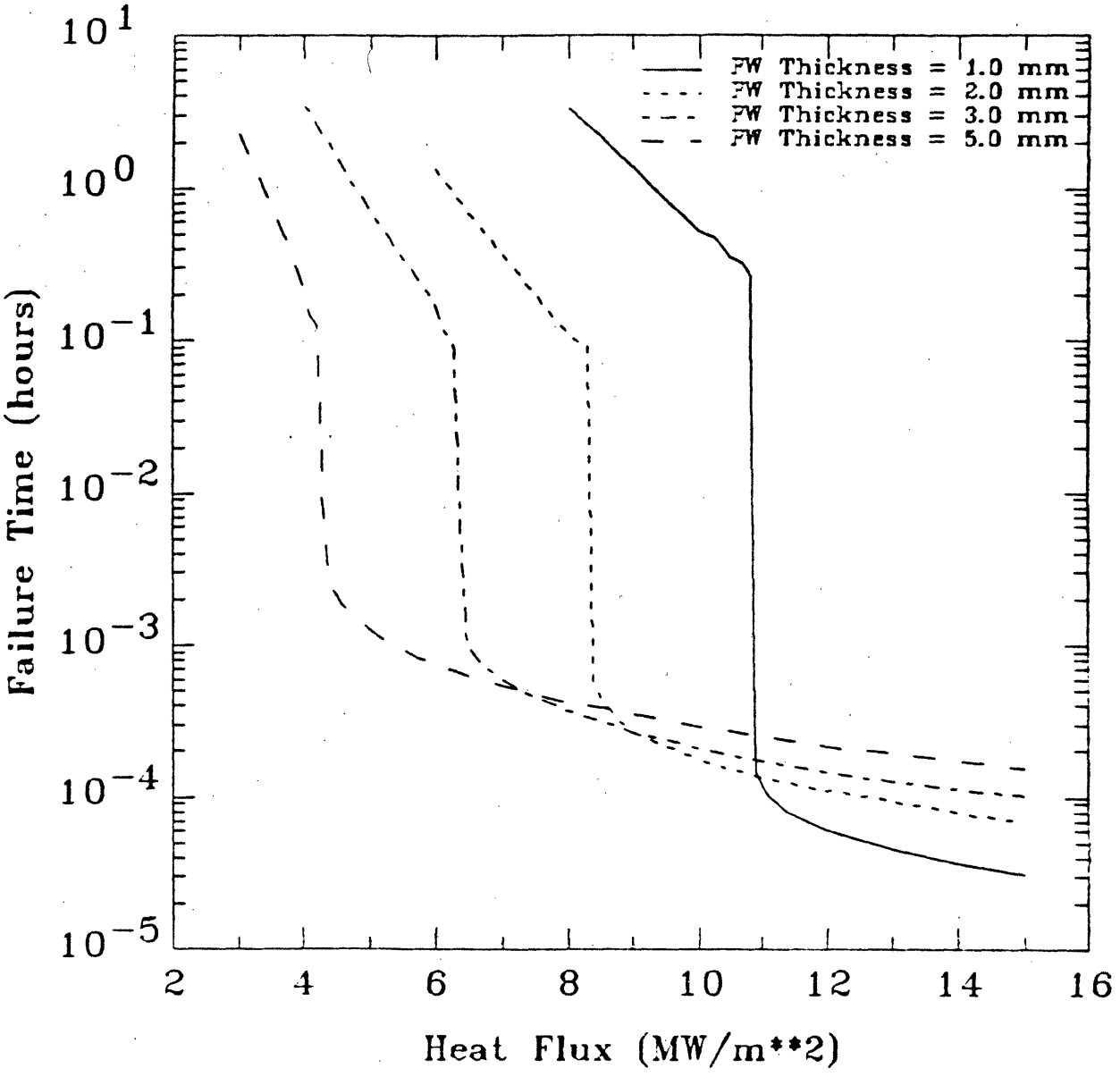

VCrTi is the better choice for first wall material, due to superior high-temperature mechanical properties.

7.2.2 LOFA/LOCA With Plasma Continuation

The LOFA/LOCA analyses presented in Chapters 5 and 6 included a discussion on the continued plasma burn (PL) vs. the immediate plasma shut-off (DC) cases. The continued plasma burn behavior that was assumed for these analyses is discussed in Sections 5.1.3.1, 5.4.5, and 6.2. This behavior, shown in Figure 5.1.3, is purely an assumption. No mechanism was offered which would cause the shutdown of the plasma. It is possible that in the event of a LOFA/LOCA, the plasma would continue to burn until gross structural failure of the first wall occurred. The time frame for this failure would clearly be short compared to the decay heat induced failure times discussed in Chapter 5. With the plasma power (surface heat flux) remaining at its nominal level, the reduction of the coolant flow rate in the LOFA case, and the removal of the coolant in the LOCA case, coupled with the decrease in the effective heat transfer coefficient from the first wall to the coolant (or across the vacated coolant channel), will cause the first wall temperature to rise sharply.

To obtain an estimate of the failure time in the continued plasma burn case, the overpower transient model is used with the plasma power (surface heat flux) held constant at the nominal level (1 MW/m^2 for the tokamaks). The convective heat transfer coefficient from the first wall to the first wall coolant channel is calculated with the method described in Section 6.1 and Appendix E, as is the flow rate of the coolant in the LOFA case. It is assumed that the structural wall behind the first wall coolant channel remains at a constant temperature. While this is an optimistic assumption, it should be valid for short failure times, and should only have a significant impact on the results in cases where the failure time is long. To offset this assumption, another case is run in which it is assumed that there is no heat tranfer from the coolant channel to the back structural wall; that is, that the

system consisting of the first wall slab and adjacent coolant channel is thermally insulated. These two assumptions form the bounding cases for what is actually taking place, and thus a range of failure times can be found.

Another assumption involves the coolant pressure. There is some discussion regarding this issue in Section 3.2.1. The bounding cases in this instance would be to assume that the coolant remains at the operational pressure (conservative case), and to assume that the coolant depressurizes to one atmosphere or less (optimistic case). Further, the assumption is made that the heat tranfer properties of the coolant are not affected by the coolant pressure.

Considering the above discussion, the plasma continuation analysis involves four cases. The cases are designated in Table 7.2.2. The time-to-failure for VCrTi and HT-9 for each of these four cases is shown in Table 7.2.3, with the case designation shown in parentheses. Since these four cases are essentially the bounding cases, the actual time-to-failure should lie within the limits defined by the values in Table 7.2.3.

The results for VCrTi indicate that the damage mechanism is far more dependent on the temperature than on the stress. The difference in the temperatures reached in the insulated and uninsulated cases is over 200 °C. This has a marked effect on the failure time, as is seen in Table 7.2.3. On the other hand, decreasing the stress by a factor of 30 (from 3 MPa nominal to 1 atm) only increases the failure time by 33% in the insulated case. The primary conclusion to be drawn from this is that any design mechanism aimed at protecting the first wall from plasma induced failure should concentrate on keeping the temperature down, and not be so concerned with the stress level. The fuse plug concept could be very applicable here. The secondary conclusion is that it appears that a VCrTi wall subject to a heat flux of 1 MW/m^2 should survive for at least 30 seconds after losing forced convection cooling, and perhaps much longer if a heat transfer pathway from the first wall is maintained.

Table 7.2.2 Plasma Overpower/Continuation Case Designation.

Case #	Heat Transfer FW to Coolant	Heat Transfer - Coolant to Constant Temp Back Wall	Coolant Pressure
1	Forced Convection	Not Applicable	Nominal
2	Natural Convection	Natural Convection	Nominal
3	Natural Convection	Natural Convection	1 atm
4	Natural Convection	Insulated	Nominal
5	Natural Convection	Insulated	1 atm

Table 7.2.3 Plasma Continuation Failure Times.

Material	Thermal Boundary	Coolant Pressure: Nominal		1 atm	
		Time (s)	Case #	Time (s)	Case #
VCrTi	Insulated	27.2	(4)	36.0	(5)
	Uninsulated	>1.44e+05	(2)	>1.44e+05	(3)
		Time (s)	Case #	Time (s)	Case #
HT-9	Insulated	4.01	(4)	6.63	(5)
	Uninsulated	7.76	(2)	195.	(3)

The results for HT-9 are similar. It is seen more clearly from these results that decreasing the stress has a greater impact on the failure time at lower temperatures, i.e., in the uninsulated case. Again, however, it is clear that a large decrease in the stress (factor of 50) only has a relatively small impact on the failure time ($\sim$ 65% increase) at the high temperatures reached in the insulated case. This verifies the importance of reducing temperature, as opposed to stress, as an attempt to protect the first wall. The secondary conclusion here is that an HT-9 wall subject to 1 MW/m^2 heat flux could fail in as few as five seconds - and at any rate will not last more than a few minutes - after forced convection cooling is lost.

The results of the plasma continuation analysis point out the need to establish an automatic plasma shut-off mechanism to avoid plasma induced failure after LOFA/LOCA. Operator or other external means of intervention cannot be counted on to terminate the plasma in the short time required to prevent first wall damage, especially for designs which use superconducting magnets, where a rapid decrease of the confining magnetic field will be difficult to achieve. The fuse plug concept introduced by Logan [7.1] and discussed earlier should be considered for this purpose. This problem is primarily one of materials selection.

7.3 Fuse Plug Material Selection

A detailed investigation of specific materials which exhibit the desired behavior is considered beyond the scope of this work. In any case, such a search would be severely hindered by the lack of very high temperature strength property data. The strength properties of VCrTi and HT-9 used for the analyses presented in this chapter are themselves gross extrapolations of limited data bases. Further guesses at the high temperature behavior of other materials is unlikely to yield useful results without unacceptable uncertainty. However, some criteria can be extracted from the results presented above.

The behavior seen for HT-9 and VCrTi in Figure 7.2.1 has an interesting impli-

cation on the selection of the fuse plug material. The idea of the "threshold" heat flux is actually well suited to the fuse plug concept. Ideally, the fuse plug material will have a threshold heat flux which is well below that of the first wall material, but significantly above the operational heat flux. In this case, the plug will withstand the operating conditions without premature or inadvertent failure. During an overpower transient, the plug will fail when the heat flux reaches its threshold, thus releasing the pressurized helium behind it and terminating the transient before the remainder of the first wall suffers significant damage.

This means that the fuse plug material should have similar strength properties to the first wall material in the operating temperature range, but should show a steeper fall off of ultimate tensile strength (UTS) as the temperature increases above the operating level. This could be in the form of a steady decrease of the UTS, or a sudden fall-off at some elevated temperature. In this instance, the fall-off should occur at a temperature that is significantly above the operating range but substantially below the temperatures reached in the first wall at the threshold heat flux.

The results of the plasma continuation analysis do imply an interesting possibility in terms of specific material combinations. This would be to use HT-9 as the fuse plug material in a VCrTi first wall. Its consideration of being used for the first wall material itself indicates that HT-9 can withstand the operating conditions sufficiently. It is clear from Table 7.2.3 that the HT-9 will fail well before the VCrTi in the event of a LOFA/LOCA. These are the desired properties of the plug material. In terms of the overpower transient, however, Figure 7.2.1 indicates that the two materials have similar threshold heat fluxes.

References for Chapter 7

[7.1] B.G. Logan, A Rationale for Fusion Economics Based on Inherent Safety, Lawrence Livermore National Laboratory, UCRL-91761, November 1984.

[7.2] D.L. Smith et al., Blanket Comparison and Selection Study (BCSS) - Final Report, Argonne National Laboratory, ANL/FPP-84-1, September 1984.

[7.3] J.E. Chafey and J.B. Wattier, Estimation of Allowable Design Stress Values for 12Cr-1Mo-0.3V Steel, General Atomic Project 4230, GA-A14610, February 1978.

[7.4] H.Th. Klippel, The Thermal Response of the First Wall of a Fusion Reactor Blanket to Plasma Disruptions, ECN-137, September 1983.

[7.5] H.Th. Klippel, Thermal Analysis of Bare and Coated SS316 First Wall Under Plasma Disruption Conditions, ECN Petten, June 1985.

[7.6] R.J. Onega, W.R. Becraft, C.A. Kulkielka, The Thermal Consequences to the First Wall of a Deuterium-Tritium-Fueled Tokamak due to a Major Plasma Disruption, Nuclear Science and Engineering 75, pp. 243-257, 1980.

[7.7] Metals Handbook: Ninth Edition, Volumes I and II, American Society of Metals, Metals Park, Ohio, 1978.

[7.8] S.J. Piet, M.S. Kazimi, L.M. Lidsky, Potential Consequences of Tokamak Fusion Reactor Accidents: The Materials Impact, Massachusetts Institute of Technology Plasma Fusion Center, PFC/RR-82-19, June 1982.

8. Summary and Conclusions

Although fusion reactor design is still at a relatively early stage, it is important that safety concerns be included in the design process. Fusion energy appears to offer significant safety and environmental advantages over alternative sources of energy. The potential for fusion reactors to be inherently safe from damage, even under severe accident conditions, will have a significant impact on whether a commercial fusion reactor is ever built.

This report investigates some of the thermal aspects of fusion reactor safety; in particular, the thermal and structural response of fusion blankets to power/cooling mismatches. There are essentially two types of power/cooling mismatches, both of which will result in elevated temperatures in the first wall and blanket. The first type involves loss-of-cooling, and is referred to as an undercooling transient. The second type involves an increase in the power level with no corresponding increase in the cooling rate, and is referred to as an overpower transient. The purpose of this study is to develop a methodology and establish guidelines to determine whether blankets can be designed that will passively cool themselves without risk of critical radiation exposure to the public, and without damage to the reactor, in the event of a power/cooling mismatch, and to identify elements of blanket design which enhance thermal safety. Design elements which hinder thermal safety are also identified, and suggestions for alternative approaches are given. The impact of some operational parameters is also examined, with the goal of developing operational

guidelines to insure passive safety with respect to loss-of-cooling transients. It must be stressed that this study considered only loss-of-cooling transients, and the results and conclusions presented herein cannot necessarily be generalized to include other classes of accidents.

8.1 Summary of Reference Blanket Selection

The analyses described in this work were carried out on some or all of six reference blankets, which were chosen from a variety of sources. The underlying assumptions behind the important design parameters of each blanket, such as operational neutron wall load and surface heat flux, operating temperature range, and blanket lifetime, were verified through a brief literature survey. Some of these parameters, such as wall load and blanket lifetime, are perhaps somewhat optimistic but do not appear unreasonable when compared to earlier designs. The tritium breeding ratios and blanket multiplication factors were checked to ascertain that they are in the acceptable range. The general features of the six blankets are displayed in Table 2.0.1.

All of the blankets chosen were taken from up-to-date sources, and represent the current approaches to fusion blanket design. Blanket #1 was chosen as a representative self-cooled, liquid-metal tokamak blanket. It consists of liquid lithium breeder/coolant, with vanadium alloy V-15Cr-5Ti structure. This particular design was ranked by the BCSS [8.1] as very promising. Blanket #2 was chosen as a representative gas-cooled, solid breeder tokamak blanket. The breeder material is Li_2O, the coolant is helium, and the structure is a version of HT-9 which has been modified for reduced activation [8.2]. This version of HT-9 is called MT-9 in this report. This blanket was also ranked by BCSS as very promising. Blanket #3 is part of a Reversed-Field-Pinch (RFP) reactor, and was chosen to contrast with Blanket #1. It has the same material composition as Blanket #1, but since the RFP uses copper magnets, it does not have a large magnet shield behind the blanket. Blanket #3

is also designed for a very high neutron wall load. Both of these differences have an interesting impact on thermal safety, and thus comparisons between Blankets #1 and #3 are useful. Blanket #4 was also chosen to contrast with Blanket #1. Blanket #4 is the same as Blanket #1 except that it uses lithium-lead $Li_{17}Pb_{83}$ as the breeder/coolant material. Thus, comparing Blankets #1 and #4 essentially amounts to comparing the thermal safety characteristics of liquid lithium with those of lithium-lead. Blanket #5 was chosen to contrast with Blanket #2, also to examine a materials impact. Blankets #2 and #5 are identical except that Blanket #5 has beryllium in the breeder region, to improve the neutronic performance. Here, the idea is to determine the thermal safety impact of including a neutron multiplier. Finally, Blanket #6 is part of a D-D reactor, and consists of helium-cooled solid steel structure, that is, there is no breeder material. Blanket #6 was chosen to examine some of the thermal safety characteristics of the D-D fuel cycle.

8.2 Summary of Material Limits

Material limits affect the thermal design of a fusion reactor in a variety of ways. In terms of normal operation, the lifetime of the blanket system is limited by the ability of the first wall material to withstand the neutron fluence, cyclic heat load, and erosion rate. In an off-normal condition such as a LOFA or LOCA, the elevated temperatures experienced by the structural components can lead to damage and/or the release of radioactive isotopes. Thus it is important to attempt to quantify the various limits that affect the thermal design, as well as the consequences of exceeding these limits.

Determining the operating lifetime of the first wall based on the atomic displacement limit (measured in displacements-per-atom, dpa) is somewhat uncertain due to the uncertainty in the dependence of the dpa rate on the neutron energy. This issue is important, particularly when comparing alternate fuel cycles, in which the neutron spectra are different from the D-T spectrum. There exist two conflict-

ing viewpoints, one which suggests that the dpa rate is linearly dependent on the product of neutron fluence and neutron energy [8.3], and one which suggests that the dpa rate depends only on neutron fluence [8.4]. The actual situation probably lies somewhere in between.

In the event of a transient which leads to elevated temperatures, the material limits of interest involve the dependence on temperature of the Ultimate Tensile Strength (UTS), creep resistance, and oxidation characteristics of the structural materials. Elevated temperatures in structural materials can cause melting, acute structural failure, thermal creep induced failure, and oxidation or volatization, all of which could lead to the release of radioactive isotopes.

The high temperature data base for the candidate structural materials VCrTi and HT-9 is quite limited, requiring extrapolation of the lower temperature data. The UTS of the VCrTi alloy suffers a dramatic decrease above 1200 °C [8.5]. For this reason, it is assumed that VCrTi components which go above 1200 °C will suffer acute structural failure. Extrapolation of the HT-9 data [8.1,8.6,87.,8.8] indicates that the UTS will be very close to zero at 900 °C, and thus it assumed that HT-9 components which go to temperatures above this will also suffer acute structural failure. Whether structural damage actually occurs will depend on the stress in the component. It is possible that the stress will be very low, and thus damage will not occur. However, at these temperatures, VCrTi and HT-9 experience changes in their micro-structure, due to re-crystallization. This will cause an unrecoverable loss of ductility, and thus regardless of whether structural damage occurs, the affected components will not be re-usable. The acute structural failure mechanism encompasses this scenario.

The data base for thermal creep is also very limited. Larson-Miller theory is used to extrapolate the available data to the high temperature, low stress regime of interest in a LOFA/LOCA. Description of this model is given in Chapter 3 and Appendix A.

The VCrTi alloy oxidizes readily above 650 °C [8.9 - 8.12], forming the liquid V_2O_5. This could result in severe structural damage. However, the ESECOM study [8.13] indicates that the temperature would have to exceed 1500 °C for at least 10 hours to mobilize sufficient radioactivity to result in a short-term 200 rem whole body dose (the first seven day dose and 50% of days eight through 30) at the site boundary, assuming no containment, and the most pessimistic weather and plume dispersion conditions. This 200 rem limit is somewhat more stringent than the NRC two hour dose limit of 25 rem. MT-9 does not experience the same oxidation problem as VCrTi, but the overall conclusions regarding radio-isotope mobilization for the MT-9 elements are similar for those of VCrTi [8.13,8.17].

8.3 Summary of Decay Heat Analysis

The first step in calculating the temperature response to the various transients is to determine the heat source present within the system. In the undercooling transient analysis, it is assumed that a fairly rapid plasma shutdown can always be achieved in the event of an accident [8.13,8.14]. Thus, the heat source is these transients is from the decay of the radionuclides which have been created in the blanket as the result of neutron interactions.

In both D-T and D-D fusion reactors, the neutrons produced in the plasma enter the first wall/blanket regions, where they interact with the various elements that comprise the blanket. Some of these interactions transform stable isotopes into radioactive isotopes. These radioactive isotopes then decay, and in the process deposit the decay energy in the form of heat. The heat thus produced is referred to as decay heat.

The decay heat is calculated by first determining the operational neutron fluxes in the blanket. This is done using the one-dimensional neutronics code ONEDANT, developed at Los Alamos National Laboratory [8.18]. The fluxes are then used as an input to the activation/transmutation code REAC, which was developed at

Hanford Engineering and Development Laboratory [8.19]. REAC calculates the specific activity of the radioactive isotopes produced in the blanket for a given irradiation time at given locations in the blanket. From the information, the decay heat density as a function of position and time after shutdown is calculated.

Due to the mechanism of decay heat production, the amount of decay heat produced is a highly material dependent property. In all of the blankets, it is the structural material which produces the vast majority of decay heat. The vanadium alloy V-15Cr-5Ti yields a relatively low level of decay heat density at shutdown. Furthermore, most of this heat is produced by the short-lived isotope ^{52}V, and thus the total decay heat level of VCrTi decays quickly, by as much as an order of magnitude or more in one hour. This makes VCrTi an excellent choice of structural material from the decay heat standpoint.

The modified version of the ferritic alloy HT-9, called MT-9, also produces a fairly low level of decay heat at shutdown. Most of this heat comes from the longer lived manganese isotopes ^{54}Mn and ^{56}Mn, and thus the decay heat level of MT-9 will decay more slowly than that of VCrTi, e.g., it will take about 24 hours to decay by an order of magnitude. Beyond one day, however, the total decay heat level of the MT-9 is also very low, making it another good choice of structural material from the decay heat standpoint.

The structural steel Fe1422 has a high (14%) manganese content, which yields a very high decay heat level at shutdown, due primarily to the manganese isotopes mentioned above. Furthermore, due to the relatively long life of these isotopes, this level decays quite slowly. It takes as long as three months for the decay heat level of Fe1422 to decay by an order of magnitude. For this reason, use of Fe1422 in the blanket is not recommended. In areas where the magnitude of the neutron flux is low and the spectrum is mostly thermal (i.e., the flux is highly attenuated), such as in the magnet shield of a superconducting tokamak, use of Fe1422 may be acceptable.

In the breeder materials, the decay heat level is not as important a factor, since these materials yield lower decay heat levels than the structural materials. In particular, assuming that tritium is removed at the same rate that it is produced, both liquid lithium and the solid ceramic Li_2O produce essentially no decay heat, and thus from the standpoint of decay heat, both are excellent choices for breeder material. Conversely, the eutectic $Li_{17}Pb_{83}$ yields two isotopes of lead, ^{203}Pb and ^{209}Pb, which contribute significant amounts of decay heat. The level of decay heat produced by $Li_{17}Pb_{83}$ is still lower than that of the structural materials, however, and thus, while LiPb is the least attractive of the three breeder materials considered, it should not present a particular problem in terms of decay heat.

Utilization of a neutron multiplier to improve the tritium breeding ratio in fusion blankets has been widely considered. The most attractive candidate neutron multiplier is beryllium. Beryllium increases the magnitude of the overall neutron flux, but especially of the lower energy flux.The altered flux spectrum can have a significant impact on the decay heat level. The increased slow flux in systems which use beryllium results in a decay heat level that is about 25% higher in the first hour, and about 15% higher after one day. This effect is material dependent, but these values, which are specifically for the Li_2O/He/MT-9 system, should be representative.

One simplifying assumption used in the calculation of the decay heat level in a fusion reactor is that γ-rays emitted by decaying isotopes deposit their energy at the location they are produced. In reality, these γ's will transport through the blanket and deposit their energy in a smeared fashion across the blanket. Including this effect in the calculation results in a decay heat density profile that is smoother, i.e., has a lower peak-to-average ratio, than when local deposition is assumed. This means that including the γ-transport effect will lower the calculated decay heat in regions where it is highest, and raise it in regions where it is lowest. The total decay heat will be the same in either case, however, and thus the impact on the temperature response to undercooling transients is minimal.

The different neutron spectrum and different neutron-to-thermal power ratio experienced in D-D vs. D-T reactors has an impact on the decay heat level produced. In a D-D reactor, the neutron spectrum is softer, and a lower fraction of the total fusion energy comes from neutrons. This will result in a lower decay heat fraction, that is, a lower ratio of the decay heat density to the operational power density. However, many D-D blankets are designed to maximize the blanket multiplication factor by using mostly steel. This high concentration of structural material results in a higher decay heat level. These opposing effects will cancel to a certain degree, and the final result will depend on the specific D-D design. It is recommended that the added design flexibility in the D-D reactor be used to minimize the activation level in the blanket, by constructing at least part of the blanket with a low activation material. If this is done, the D-D fuel cycle offers an excellent safety advantage in terms of decay heat.

8.4 Summary of Undercooling Transient Analysis

Transients involving loss-of-system-cooling are the most commonly considered mechanisms that result in elevated temperatures. Loss-of-cooling transients are generally divided into two groups, namely, Loss-of-Flow Accidents (LOFA) and Loss-of-Coolant Accidents (LOCA).

The temperature response to undercooling transients was analyzed with a model developed during this study. The model consists of a one-dimensional finite difference heat transfer code called THIOD (Transient Heating In One Dimension). The input to THIOD consists primarily of the geometry and material composition of the blanket, and the heat source. THIOD then outputs the temperature distribution of the entire blanket as a function of time. The model is described in detail in Chapter 5 and Appendices C and D.

The Li/Li/VCrTi tokamak Blanket #1 can be considered inherently safe from structural damage at the nominal neutron wall load of 5 MW/m^2 for both the base

case LOFA and LOCA, as long as no oxygen is allowed to leak into the system. In the event of oxygen in-leakage, the temperatures reached in the LOCA are sufficient to cause rapid oxidation of the vanadium structure, resulting in gross first wall failure. In any case, the radio-isotope mobilization in both events would be significantly smaller than that associated with life-threatening levels around the plant.

The Li_2O/He/MT-9 tokamak Blanket #2 has a first wall which consists of a slab of MT-9, backed by a region of pure helium. Should the heat removal capacity of the coolant be lost, i.e., in a LOFA or LOCA, the only mechanism for the removal of heat from the first wall is via thermal radiation to the rest of the blanket structure. For the purposes of corrosion resistance, it is desirable for this first wall structure to have a smooth, shiny surface, which means that the radiative emissivity of this surface will be low [8.20]. Thus, the first wall will be almost thermally insulated until it gets very hot. The high temperatures reached in this blanket will likely cause thermal creep rupture in the Case 1 LOFA, due primarily to the high pressure stress in the first wall assumed in this case. De-pressurizing the coolant would decrease the stress level in the first wall, which would alleviate the thermal creep problem. The Case 2 LOCA will result in acute structural failure of the first wall. In both the LOFA and LOCA, the failure will occur in about 30 minutes. The high first wall temperatures and resulting failure in this blanket are due to the design of the first wall. It is recommended that the first wall be designed with permanent radial conduction paths to avoid this problem. The MT-9 structure does not suffer from the oxidation problems that VCrTi does, and neither of these accidents will release significant radioactivity.

The Li/Li/VCrTi Reversed-Field-Pinch (RFP) Blanket #3 operates at a very high wall load (15 MW/m^2), and thus experiences a large temperature rise in both LOFA and LOCA. In the base case LOFA, no structural damage is likely to occur at this nominal wall load, but the safety margin is very small. The base case LOCA is likely to cause acute structural failure in about an hour. If oxygen does get into the system, vanadium oxidation, coupled with the extremely high temperatures,

could lead to the mobilization of a significant fraction of the radioactive inventory. For this reason, it is highly recommended that in the design of high wall load, high power density machines, safety issues receive considerable attention.

Due to the nature of the D-D fuel cycle, the D-D tokamak Blanket #6 operates at a much lower neutron wall load (1.17 MW/m^2) than the D-T blankets. This gives the D-D blanket a significant advantage in terms of thermal safety. The temperatures reached in both the base case LOFA and LOCA are lower than in the D-T cases. However, the base case LOFA will likely cause thermal creep rupture in Blanket #6, due primarily to the high pressure stress in the first wall, which stems from the continued presence of the high pressure coolant. The base case LOCA will not lead to structural failure, indicating that it would be beneficial to depressurize the coolant in the event of a LOFA.

In all the blankets, the maximum temperature reached after an accident is linearly dependent on the operational neutron wall load (Γ_n), as is shown in Figures 5.3.1 and 5.3.2. Mathematically, this can be expressed as

$$\Delta T = a\Gamma_n - b \tag{5.12}$$

where a and b are constants. The values of a and b for all of the blankets, in both the LOFA and LOCA scenarios, are given in Table 5.3.1. The temperature rise ΔT is related to the total decay heat produced in the blanket (Q_{tot}), the heat storage capacity of the blanket (C_{tot}), and the total heat that is transferred to the heat sink (Q_{HS}), where Q_{tot}, C_{tot}, and Q_{HS} are defined mathematically in equations (5.13), (5.14), and (5.15). It was shown in Chapter 5 that

$$a = \frac{q_t}{C_{tot}} \tag{5.19}$$

$$b = \frac{Q_{HS}}{C_{tot}} \tag{5.20}$$

where q_t is the total decay heat produced in two days per unit neutron wall load, that is, the total decay heat divided by the wall load.

The parameter a is the ratio of the time-integrated decay heat density to the heat storage capacity of a particular blanket. This is primarily a material property, although it is affected by other factors, such as the neutron spectrum. The parameter b essentially represents the thermal coupling between the first wall and the heat sink, and is more a function of the geometric design of a particular blanket, although it also is a material property. Blankets with good radial conduction paths and high radiative emissivities will have high values of b. In terms of minimizing the temperature rise, it is clearly desirable to have a low value of a and a high value of b. This represents a useful design tool from the standpoint of thermal safety. Candidate blanket materials can be compared by comparing their a values, whereas different geometric configurations can be compared by comparing their b values.

The wall loads required to cause thermal creep rupture, acute structural failure, and radio-isotope release for some of the blankets are given in Table 5.3.2. Operation at or above the wall loads shown in Table 5.3.2 will result in the specified failure in the particular accident scenario, i.e., LOFA or LOCA. Dividing the wall load at which failure will occur by the nominal wall load gives a thermal safety factor. Table 8.4.1 gives the nominal wall load and the thermal safety factor for the three failure modes for each blanket.

The substantial increase in decay heat production in Fe1422 over that in MT-9 has a significant impact on the temperature response, such that blankets that use Fe1422 as the manifold structural material are subject to much higher temperatures in the event of a LOFA/LOCA than those which use MT-9. For this reason, the use of Fe1422 in any of the blanket regions is not recommended.

The increase in the decay heat production in systems which use a neutron multiplier has a small but significant impact on the temperatures reached after a LOFA/LOCA, with the multiplier blanket reaching higher temperatures. The impact increases with the operational neutron wall load. The recommendation is

Table 8.4.1 Thermal Safety Factors for Structural Failure and Radioactive Release for Each Blanket.

Blanket #	Nominal Wall Load	LOFA/ LOCA	Thermal Creep Rupture	Acute Structural Failure	Radioactive Release*
1	5.0 MW/m^2	LOFA	>2	>2	$\gg$2
		LOCA	~1.6	1.76	>2
2	5.0 MW/m^2	LOFA	~0.6	1.22	>2
		LOCA	~1.2	0.72	>2
3	15 MW/m^2	LOFA	~1.13	1.33	>1.33
		LOCA	~0.47	0.73	~1.33
6	1.17 MW/m^2	LOFA	~0.85	1.54	>2
		LOCA	>2	1.54	>2

* Excluding effects of possible lithium fire (Blankets #1 and #3 only).

that the negative impact on thermal safety should be taken into account when considering the use of a neutron multiplier to improve blanket performance.

The maximum temperature reached in the first wall after a LOFA/LOCA can be highly sensitive to the radiative emissivity of the blanket structural surfaces, particularly in a LOCA. The degree of sensitivity depends on how well the first wall is thermally coupled to the heat sink and/or shield. Increasing the emissivities on either side of the vacuum gap between the blanket and the shield will improve the thermal coupling between the blanket and the shield, which in turn will significantly reduce the maximum first wall temperature by increasing the amount of heat that is dumped into the shield. This creates a conflict between the safety and operational interests of fusion reactor design.

During operation, it is desirable to keep the amount of heat that is deposited in the shield to a minimum. This is because the shield is operated at a low temperature, and thus the heat deposited in it is not recovered in a useful form. Therefore, in the interests of operational performance, it is beneficial to keep the blanket thermally insulated from the shield, so as to reduce the amount of heat that flows from the blanket to the shield. However, for the reasons outlined above, from a safety standpoint it is better to have good thermal coupling between the blanket and the shield. The ideal solution would be to keep the blanket and shield thermally insulated from each other during operation, but design a mechanism which would improve the thermal coupling in the event of an accident. An example of this type of solution would be to maintain the vacuum gap during operation, but allow the reactor cover gas into this vacuum gap in the event of an accident. This would greatly enhance the heat transfer between the blanket and the shield, and thus reduce the maximum temperature reached in the first wall after the accident. This particular solution introduces some problems, such as the possibility of oxidation of the hot structural surfaces if there is any oxygen in the cover gas. If no such "ideal" solution can be found, then it is recommended that a proper trade-off between the operational and safety interests be found. The structural surfaces on either side of the

vacuum gap can then be machined to obtain the radiative emissivities that yield the desired level of thermal coupling.

The difference between the results obtained using slab vs. cylindrical geometry to model the toroidal geometry of the tokamak blankets scales as the ratio of the blanket thickness to the major and minor radii of the tokamak. In all the cases of interest, the difference between the models is small, and the error introduced by using slab geometry is acceptable. In the RFP Blanket #3, this error was found to be about 6% on the outboard side, and less than 1% on the inboard side.

8.5 Summary of Natural Convection Analysis

In a Loss-of-Flow Accident (LOFA) that is caused by pump failure, it is possible that the coolant will continue to flow even after the pump fails. The phenomenon of coolant flow, despite the lack of a pump or any other externally added pressure head, is known as natural convection. Briefly, a pressure head is added to the coolant due to buoyancy effects, which arise because the coolant, as it passes through the blanket, is being heated. The heated fluid thermally expands and thus becomes less dense than the cooler fluid. The hotter, lighter fluid will rise, and thus there will be some flow rate of the fluid in the flow loop. Assuming that the secondary coolant cycle continues to operate and remove heat from the primary coolant, the continued primary coolant flow will remove heat from the first wall/blanket system, and thus limit the LOFA temperature rise.

Natural convection effects are included in the calculation of the LOFA temperature response by adding the subroutine CONVECT to the heat transfer code THIOD. Inputs to CONVECT include the time behavior of the magnetic field, the coolant properties, and the geometry of the flow loop. Given these inputs, CONVECT calculates the natural convection flow rate of the coolant, and the heat tranfer coefficients h and k_e for the coolant channels within the blanket. The model for CONVECT is described in Chapter 6 and Appendix E.

The convection analysis carried out in this work adequately demonstrates that natural convection cooling can successfully mitigate the consequences of a Loss-of-Flow Accident. The properties of the coolant are very important in determining the impact. The low density of helium render it ineffectual as a natural convection medium, such that the LOFA temperature response of helium-cooled blankets is not affected by natural convection. The impact in liquid metal-cooled blankets can be very significant, but because of MHD effects, depends strongly on the magnitude of the magnetic field. Due to desirable coolant properties, liquid lithium-lead ($Li_{17}Pb_{83}$) can significantly reduce the temperature rise in the event of a LOFA, even if the magnetic field remains at the operational value. This is not true of liquid lithium. Natural convection in lithium is almost completely suppressed as long as the magnetic field remains present.

Turning off the magnets, or substantially reducing the field strength in a relatively short time, greatly improves the impact that natural convection will have on the temperature response. Plasma-induced peak temperatures, which are reached in the first few seconds of the transient, will be reduced only slightly. At longer times, however, the temperatures can be reduced to safe levels such that there is no danger of structural damage. For this reason, it is important to design superconducting magnets such that they can be shut off or experience a two order of magnitude field reduction in relatively short times, i.e., < 1 hour. This is especially true in lithium-cooled systems. The ability to shut off copper (resistive) magnets in extremely short times causes a reduction in the (plasma-induced) peak temperature, although the longer term (steady-state) temperature response will be similar to the case in which the superconducting magnet field strength is reduced by two orders of magnitude every 30 minutes. Copper magnets offer an advantage in that they can always be shut off fairly rapidly, whereas the shutdown time of superconducting magnets is somewhat uncertain, and could be rather long.

8.6 Summary of Plasma Overpower/Continuation Analysis

Besides the decay heat induced undercooling transients, temperature excursions can be caused by increases in the plasma power, or if the plasma continues to burn after cooling is lost. These plasma-induced temperature excursions could lead to failure of the first wall if the plasma continues to burn without some kind of "automatic shut-off mechanism".

The results show that in an overpower transient, the failure time of the first wall decreases dramatically over a narrow range of heat flux, as is demonstrated in Figure 7.2.1. The heat flux at which this decrease in the failure time occurs can be referred to as a threshold heat flux. Overpower transients which generate heat fluxes above the threshold will result in first wall failure almost immediately. The results also show that increasing the thickness of the first wall *decreases* the threshold heat flux, by increasing the thermal stress in the first wall. In the event that the plasma continues burning after cooling is lost, the results indicate that the failure time is not especially sensitive to the first wall stress, but is more sensitive to the temperatures reached in the wall. The first wall temperature reached is strongly affected by the nature of the thermal boundary at the back of the first wall.

All of the overpower/continuation results indicate that these transients can cause first wall failure in a matter of seconds. Thus it is important to design a mechanism which will shut off the plasma in either of these circumstances. The fuse plug concept introduced by Logan [8.15] is perhaps applicable. It appears that HT-9 would be an appropriate fuse plug material for a VCrTi first wall.

8.7 Recommendations for Future Work

Throughout the course of this work, attempts to quantify the consequences of the temperature transients calculated were plagued by a serious lack of materials property data in the temperature range of interest. This lack of high temperature

strength data for the fusion alloys necessitated assumptions and extrapolations, the validity of which could not be confirmed. Furthermore, the first wall structural damage analysis carried out in this work did not include a detailed determination of the post-accident stress levels in the first wall. Both of these issues were the cause of some controversy surrounding the results presented herein and concurrently presented in the ESECOM report [8.13], which seem somewhat more conservative than the results presented in the TITAN report [8.16]. It is recommended that, to facilitate future safety analyses, a substantial investigation be made to characterize the strength properties of the fusion alloys at high temperatures, i.e., above 1000 °C. This should include both the temperature dependence of the ultimate tensile strength, and the creep resistance. It is equally important to characterize the post-accident first wall stress. This involves a number of items, including accurately determining the coolant pressure in a Loss-of-Flow Accident, and determining the magnitude and effect of the secondary stress that is caused by thermal creep during operation.

In terms of the thermal analysis, it is not especially recommended that more sophisticated analytical tools be used (e.g., multi-dimensional heat transfer codes) until more detailed reference blanket designs are available. In the immediate future, new work should concentrate on addressing some of the issues raised in this work. For instance, how best to keep the blanket insulated from the shield during normal operation, but to provide good thermal coupling between the blanket and the shield after shutdown. This raises an interesting blanket design problem. If this is impossible, then effort should focus on the trade-off between operational and safety performance that this issue represents, with the goal being to determine the optimum level of thermal coupling between the blanket and the shield.

The undercooling transient analysis shows that a LOFA in the helium cooled Blankets #2 and #6 would lead to thermal creep rupture of the first wall. This is in large part due to the stress in the first wall, since it was assumed in the helium cooled LOFA that the coolant pressure remains at its operational value. Lowering

the stress would greatly reduce the creep rate, such that creep induced failure would likely not occur in a LOFA. For this reason, it would be advantageous in a LOFA to depressurize the coolant. Exactly how this would be accomplished is not clear, and is worth investigating. The level to which the stress must be reduced to avoid failure should also be determined.

Another point worth examining is the first wall design of the helium cooled Blanket #2. The high temperatures reached in this blanket are primarily due to the design of the first wall, which has no radial conduction paths connecting it to the rest of the blanket. The effect of radial conduction paths could be examined with a one-dimensional model, simply by replacing some of the helium directly behind the first wall with a conducting material.

It was mentioned in Section 5.2.4 that it could be possible to design liquid metal cooled blankets such that a complete coolant drain from the entire blanket module would be an incredible event. This approach was used in the TITAN study to improve the safety of that blanket. Given the potential safety advantage such a design would represent, this issue deserves further attention.

Due to its low operational neutron wall load, the D-D fuel cycle has excellent potential for passive safety. The thermal safety margin for the D-D Blanket #6, however, is small (see Table 8.4.1). This is because Blanket #6 consists of solid steel, to optimize blanket energy multiplication. The solid steel blanket produces a high level of decay heat, and thus is a poor design from a thermal safety standpoint. The thermal safety margin of this blanket could be greatly improved by using low activation material in the blanket region. An examination into the trade-off between economics and safety of using low activation materials in D-D blankets would yield some interesting results regarding the potential advantages of the D-D fuel cycle. Such an analysis would give a clearer indication of the potential safety benefits of D-D fusion over D-T fusion.

Perhaps the most useful design tool developed in this work relates to the linear

dependence of the transient temperature rise to the operational neutron wall load. The definition of the parameters a and b in equation (5.12), given by equations (5.19) and (5.20), allows for the comparison of the safety performance of different materials and different blanket designs without the need for detailed thermal analyses. Efforts designed to improve thermal safety can concentrate on decreasing a or increasing b. Some effort should be made to determine which material combinations yield the lowest (and highest) values of a, and which blanket geometries yield the highest (and lowest) values of b. The values of a and b for new blanket designs can then be compared to these "best"values to determine where (and how much) improvement can be made.

The convection analysis carried out in this work adequately demonstrates that natural convection, in liquid metal cooled reactors at least, can sufficiently mitigate the consequences of a LOFA. Some effort should be made to refine and expand the somewhat simplistic analysis that was performed. In particular, the MHD pressure drop should be analyzed in more detail, with effort aimed at identifying methods of reducing this pressure drop. Some investigation should also be made to examine the post-accident behavior of the magnetic field, and methods for shutting off superconducting magnets.

Finally, the plasma overpower/continuation analysis reveals that first wall failure can occur rapidly in either of these transients. Considerable effort should be made to identify an automatic plasma shut-off mechanism, such as Logan's fuse plug. In performing this analysis, some effort should be concentrated on quantifying the thermal boundary condition at the back of the first wall, since the results are highly sensitive to this. The overpower/continuation analysis also requires fairly detailed knowledge of the high temperature strength properties of the relevant materials.

[8.1] D.L. Smith et al., Blanket Comparison and Selection Study (BCSS) - Final Report, Argonne National Laboratory, ANL/FPP-84-1, September 1984.

[8.2] S. Fetter, Radioligical Hazards of Magnetic Fusion Reactors, Lawrence Livermore National Laboratory, LLNL MS#61485F, 1985.

[8.3] D.R. Olander, Fundamental Aspects of Nuclear Reactor Fuel Elements, Technical Information Center, U.S. Department of Energy, TID-26711-PI, 1976.

[8.4] S.J. Brereton, Safety and Economic Comparison of Fusion Fuel Cycles, PFC/RR-87-7, Massachusetts Institute of Technology Plasma Fusion Center, August 1987.

[8.5] D.K. Sze, Argonne National Laboratory, Personal Commumication, July 1985.

[8.6] J.E. Chafey and J.B. Wattier, Estimation of Allowable Design Stress Values for 12Cr-1Mo-0.3V Steel, General Atomic Project 4230, GA-A14610, February 1978.

[8.7] R.J. Amodeo and N.M. Ghoniem, Development of Design Equations for Ferritic Alloys in Fusion Reactors, Nuclear Engineering and Design/Fusion, 2, p. 97, 1985.

[8.8] R.E. Gold and R. Bajaj, Mechanical Property Evaluation of Path C Vanadium Scoping Alloys, Alloy Development for Irradiation Performance - Semiannual Progress Report DOE/ER-0045/10, pp. 122-141, October 1983.

[8.9] R.M. Neilson, Volatility of V15Cr5Ti Fusion Reactor Alloy, Idaho National Engineering Laboratory, EGG-M-25985, December 1986.

[8.10] R.C. Weast, Editor-in-Chief, CRC Handbook of Chemistry and Physics, 65th Edition, CRC Press, Inc., 1984.

[8.11] Y.S. Touloukian, editor, Thermophysical Properties of High – Temperature Solid Materials, Thermophysical Properties Research Center, Purdue University, Volume 4-I, p. 524.

[8.12] Audiere, Madi, and Grenet, Electrical and Thermal Properties of V_2O_5, J. Mater. Sci., 17 [10], pp. 2973-2978, 1982.

[8.13] Report of the Senior Committee on Environmental, Safety and Economic Aspects of Magnetic Fusion Energy, Final Report, U.S. DOE, to be issued as a Livermore Laboratory report, 1987.

[8.14] C.C. Baker et al., STARFIRE - A Commercial Tokamak Fusion Power Plant Study, Argonne National Laboratory, ANL/FPP-80-1, September 1980.

[8.15] B.G. Logan, A Rationale for Fusion Economics Based on Inherent Safety, Lawrence Livermore National Laboratory, UCRL-91761, November 1984.

[8.16] F. Najamabadi, N.M. Ghoniem, R.W. Conn, et al., The TITAN Reversed-Field Pinch Fusion Reactor Study, Scoping Phase Report, UCLA-PPG-1100, January, 1987.

[8.17] S.J. Piet, et. al., Oxidation/Volatilization Rates in Air for Candidate Fusion Reactor Blanket Materials, PCA and HT-9, J. Nucl. Mater. 141 – 143, pp. 24-28, November/December 1986.

[8.18] R.D. O'Dell et al., User's Manual for ONEDANT: A Code Package for ONE-Dimensional, Diffusion-Accelerated, Neutral- Particle Transport, Los Alamos National Laboratory, LA-9184-M, February 1982.

[8.19] F.M. Mann, Transmutation of Alloys in MFE Facilities as Calculated by REAC (A Computer Code System for Activation and Transmutation), Hanford Engineering Development Laboratory, HEDL-TME-81-37, August 1982.

[8.20] E.M. Sparrow and R.D. Cess, Radiation Heat Transfer, Brooks/Cole Publishing Co., Belmont, CA, 1966.

A. Details of Material Limits Calculations

There are essentially two models to calculate the thermal creep response of the first wall presented in Chapter 3. The first is used when the stress is known and constant in time, the second when the stress is a thermal stress only, and will change in time as it is relaxed by thermal creep. In both models, the idea is to calculate the time-to-rupture t_r at a given temperature and stress level. For a given known stress, if t_r is known at a certain temperature, then it can be found at any other temperature using the Larson-Miller Parameter. This analysis is discussed in Chapter 3.

For cases where the stress is known and remains constant throughout the transient (e.g. due to constant coolant pressure), the Larson-Miller Parameter is used to calculate t_r given the temperature history calculated by THIOD. This is sufficient to determine whether and when thermal creep rupture will occur.

A.1 VCrTi Thermal Creep Calculations

The limited data base for the thermal creep behavior of the VCrTi alloy requires extrapolation of the existing data. Larson-Miller theory represents an extrapolation of sorts, but additional extrapolation is required to obtain both the value of the

constant C in the Larson-Miller equation (3.8), and the dependence of P on stress.

The available data on VCrTi thermal creep behavior is from Bajaj and Gold [A.1], and is shown in Table A.1.1. Some of the specimens which were tested had oxygen impurities implanted in order to examine the impact that these impurities would have on the thermal creep behavior. However, as is discussed Section 3.3, it is very important in VCrTi systems to have an oxygen-free environment, due to the oxidation problem of this alloy. Thus, for the purposes of this work, only the data reported in reference [A.1] for specimens without added oxygen were used. These data are marked with an asterisk in Table A.1.1. As it turns out, data exist for three such tests (actually, there are four, but in one of them the specimen never failed, thus no time-to-rupture could be determined).

Others [A.2] have suggested a linear dependence of the Larson-Miller parameter on stress. Assuming this to be the case allows the expression

$$P = a\sigma + b \tag{A.1}$$

where a and b are constants, and σ is the stress in MPa. Combining this with equation (3.8) yields, with T in ^oK,

$$T(C + \ln t_r) = a\sigma + b \tag{A.2}$$

Note that the $\log_{10}$ in equation (3.8) has been replaced by the natural log (ln) here. This will effect the value of C, but not the overall results of the analysis. The three unknowns in equation (A.2) are C, a, and b. The oxygen-free data given in Table A.1.1 consists of three sets of (T, t_r, σ). Inserting these three data points into equation (A.2) allows the simultaneous solution of the three unknowns.

Solving for a, b, and C results in

Table A.1.1 Creep Rupture Data for V-15Cr-5Ti (from Reference [A.1]).

Sample	Additional Oxygen Content (wppm)	Temperature (°C)	Stress (MPa)	Rupture Time (hours)
VCT-15	0	650	414	1055†
VCT-82-5B	600	700	414	17.7
VCT-17*	0	750	368	115
VCT-18*	0	750	345	327
VCT-82-1B	600	750	345	791.9
VCT-82-2B	1200	750	345	780.0
VCT-16*	0	800	276	629.0
VCT-82-3B	600	800	276	547.8
VCT-82-4B	1200	800	276	1543.3

† No failure occurred during test. Cumulative Strain at termination of test was 0.5%.

* No additional oxygen added. These data were used to determine constants a, b, and C as discussed in Section A.1.

a = -48.86

b = 7.266e+04

C = 48.7

Thus, at any stress, the Larson-Miller parameter P can be found using equation (A.1) and the values of a and b. Then, at any temperature, the rupture time t_r can be found from P, using the value of C. This is how the creep rupture analysis was carried out for all the blankets with VCrTi first walls (Blankets #1, #3, and #4).

A.2 HT-9 Thermal Creep Analysis

The available data base for HT-9 allows for a more involved calculation in cases where there is essentially no primary pressure stress, but there is a secondary thermal stress, as in the case of a LOCA. During normal operation, pressure and thermal stresses will exist in the first wall. It is expected that relaxation will occur during operation such that the thermal stress will be alleviated by straining. The magnitude of the strain would be, at the most, that required to bring the thermal stress to zero. This strain would be equal to

$$\epsilon = \frac{(1-\nu)}{\mathrm{E}}\,\sigma \tag{A.3}$$

where

ϵ = strain

ν = poisson's ratio

E = Young's modulus (MPa)

σ = stress (MPa)

When the loss of coolant accident takes place, there will be no thermal stress in the first wall because the operational temperature gradient will still be present and the first wall will have strained to accommodate this. However, given the relatively poor effectiveness of radiation heat transfer at the back face of the first wall (see Section 5.4.4), and the relatively high thermal conductivity of the HT-9, immediately after accident initiation, the temperature gradient in the first wall will become very close to zero. Thus, a secondary, strain-induced stress will be imposed on the first wall, which will be equal in magnitude but opposite in sign to the initial operational thermal stress. This stress, along with the elevated temperatures due to the LOCA, will cause thermal creep. This creep will work to relax the stress, but the elevated temperature could lead to a rupture strain that is less than the strain required to relieve the stress. This would cause thermal creep rupture.

The analysis to determine whether the first wall will rupture is broken into two parts. In the first part, a stress vs. time history for the first wall is calculated from the temperature vs. time data calculated by THIOD, and a creep rate correlation from Amodeo and Ghoneim [A.3]. This correlation is

$$\dot{\epsilon} = \frac{B}{k\,T}(\sigma - \sigma_0)^3 \exp\left(\frac{-Q^*}{k\,T}\right) \qquad (A.4)$$

where

$B = 7.385 \times 10^{-3}$

$Q^* = 1.23$ eV

$k = 8.6207 \times 10^{-5}$ $(\frac{eV}{K})$

$\sigma_0 = aT + C$ (ksi)

$a = -0.2185$ $(\frac{ksi}{K})$

$c = 198.1783$ (ksi)

The stress history is calculated as follows. Given the initial value of stress and temperature, the strain rate at time=0 is found from equation (A.4). This strain rate is multiplied by a small time increment Δt to obtain the amount of strain that occurred during that time. The new strain, at time step n, where time $t = n\Delta t$, is

$$\epsilon^n = \epsilon^{n-1} - \dot{\epsilon}^{n-1} \cdot \Delta t \tag{A.5}$$

where ϵ^{n-1} is the thermal strain from the previous time step. Now, the new stress can be found from equation (A.3) using this new value of strain. Then, the new strain rate is calculated with equation (A.4) using the new value of stress and the temperature at time $n\Delta t$, as previously calculated by THIOD. This is continued until a stress vs. time history, $\sigma(t)$, has been calculated for the length of the transient.

Having this stress history, along the with the temperature history, means that (σ, T) are known at all times during the transient. Using the HT-9 thermal creep data reported by Chafey and Wattier [A.4], a correlation that relates the time-to-rupture t_r, at a fixed temperature of 1200 °F (649 °C), to the stress was constructed. This correlation is

$$\log_{10}\sigma = 1.657 - 0.199 \log_{10} t_r \tag{A.6}$$

where

σ = applied stress (ksi)

t_r = time to thermal creep rupture (h)

Using the known value of stress at time t $(= n\Delta t)$, the time-to-rupture t_r for 1200 °F can be found. Inserting this into equation (3.8) (along with the 1200 °F temperature) yields a value of the Larson-Miller parameter P for the specified stress.

Then, the known value of the temperature at time t is inserted into equation (3.8), and, now knowing the value of P, the rupture time t_r can be found for the stress-temperature combination that exists at time t. The fraction of this rupture time that is consumed will be $\frac{\Delta t}{t_r}$, which is the rupture fraction f_r defined in Chapter 3, equation (3.9). The rupture fraction is summed up in the same way as is described in Section 3.2. The results of these calculations are given in Chapter 5.

References for Appendix A

[A.1] R.E. Gold and R. Bajaj, Mechanical Property Evaluation of Path C Vanadium Scoping Alloys, Alloy Development for Irradiation Performance - Semiannual Progress Report DOE/ER-0045/10, pp. 122-141, October 1983.

[A.2] R.A. Krakowski, Creep Rupture Conditions for Case 4 Loss-of-Flow Accident in Reference to Mujid Kazimi Memo of May 11, 1987, Memorandum to ESECOM, May 28, 1987.

[A.3] R.J. Amodeo and N.M. Ghoniem, Development of Design Equations for Ferritic Alloys in Fusion Reactors, Nuclear Engineering and Design/Fusion, 2, p. 97, 1985.

[A.4] J.E. Chafey and J.B. Wattier, Estimation of Allowable Design Stress Values for 12Cr-1Mo-0.3V Steel, General Atomic Project 4230, GA-A14610, February 1978.

B. Calculational Details of Chapter 4

B.1 Converting REAC Output to Heat Source Input

In Section 4.1, the procedure for obtaining the heat source input $\dot{q}'''_{decay}(x,t)$ is outlined, leading to equation (4.2):

$$\dot{q}'''_{decay}(x,t) = \sum_i a_i e^{-\lambda_i t} e^{-\mu_i x} \tag{4.2}$$

The values a_i and μ_i are obtained from the REAC output in the following manner.

Step 1:

Find the concentration (atom/barn-cm) of all the elements in the region to be considered. Run REAC, inputting all of the elements present. REAC assumes that the concentration of these parent elements is 0.08 atom/barn-cm, so the actual concentrations must be normalized to this value.

Step 2:

From the REAC output file ACTOUT, get the activation (Ci/cm^3) for each of the radio-isotopes produced from a given parent element at a specific location within the region being considered. Say, for instance, there is a steel structure,

with an iron concentration of 7.152e-02 atom/barn-cm (the value for pure HT-9). This concentration must be normalized to the 0.08 atom/barn-cm value assumed by REAC, thus obtaining a "concentration factor"of 0.894. It is assumed that the activation of any isotope scales linearly with the concentration of the parent element [B.1]. Thus, the activation of each isotope resulting from Fe, say Mn^{56}, as given by REAC, is multiplied by the concentration factor, 0.894. This gives the *actual* activation of Mn^{56}, as the result of Fe, at the specified location.

Step 3:

Repeat step 2 for Mn^{56} which comes from other elements. In this example, the HT-9 also contains Mn, which will also produce Mn^{56}. The concentration factor for Mn is 6.93e-03. Thus, the activation of Mn^{56} which results from parent element Mn, as given by REAC, must be multiplied by 6.93e-03. This is then added to the activation of Mn^{56} which came from Fe. This must be repeated for any and all parent elements which produce Mn^{56}. The sum is then the total true activation (Ci/cm^3) of Mn^{56} at that location.

Step 4:

Convert Ci/cm^3 to W/cm^3. This is done by multiplying the activation (Ci/cm^3) by 3.7e+10 (decays/sec)/Ci, thus obtaining the activation of Mn^{56} in decays/sec-cm^3. This is then multiplied by the decay energy (i.e., average energy per decay) of Mn^{56}, in Joules. This then results in the decay heat density, in W/cm^3, produced by Mn^{56} at shutdown at the specified location.

Step 5:

Repeat steps 2 - 4 for another location in the same region. If the region is very thin, then one point in the middle will suffice, and step 5 can be skipped. For thicker regions, it is reasonable to use two points (locations), one at the front and one at the back of the region. This will then give the decay heat density (W/cm^3) of the given isotope (Mn^{56} in this example) at the front and the back of the region. It is

assumed that the decay heat density of any given isotope will fall off exponentially from the front to the back of a homogenous region, since this is the behavior of the neutron flux [B.1,B.2]. Thus the decay heat density goes as $e^{-\mu_i x}$. Now say the HT-9 region is 20 cm (0.20 m) thick. To find μ_i, the ratio of the decay heat levels at the back and the front must first be found. So in this instance,

$$e^{-(\mu_i)(0.2m)} = \frac{\dot{q}_i'''(back)}{\dot{q}_i'''(front)} \qquad \text{(B.1.1)}$$

Now μ_i can be found by taking the natural log of the ratio on the right hand side of equation (B.1.1) and dividing by -0.20. This gives μ_i in m^{-1}.

Step 6:

Now that μ_i is known, the next step is to find a_i. The a_i are all normalized to the front of the first wall. The decay heat density from the given isotope at shutdown, for any location x in the region, can then be represented as

$$\dot{q}_i'''(x) = a_i e^{-\mu_i x} \qquad \text{(B.1.2)}$$

The a_i can be found by using the decay heat level at the front of the region in question. Say the front of the HT-9 region is 30 cm (0.30 m) from the front of the first wall. Then the value of a_i can be found by substituting the $\dot{q}_i'''$ at the front of the region in the left hand side of equation (B.1.2), and 0.30 for x in the right hand side, and dividing by $e^{(-\mu_i)(0.30)}$.

Since all radioactive isotopes decay with a characteristic decay constant λ_i, the decay heat density produced by a given isotope will decay as $e^{-\lambda_i t}$. So the decay heat density from a particular isotope i, as a function of time t and position x *within a given region* can be expressed as

$$\dot{q}_i'''(x,t) = a_i e^{-\mu_i x} e^{-\lambda_i t} \qquad \text{(B.1.3)}$$

It must be stressed that the a_i and μ_i are only valid for the given region. A different region, with a different material composition, thickness, and distance from the first wall, will have different values of a_i and μ_i, even for the same isotope.

Finally, the total decay heat for the region is found by summing equation (B.1.3) over all the isotopes present in the region, resulting in equation (4.2). Since there can be hundreds of isotopes present, only those which contribute significantly to the overall decay heat should be considered, and the rest can be safely neglected.

B.2 Calculation of Decay Heat Fraction

The decay heat fraction represents the decay heat level in the blanket normalized to the operating heat output of the blanket. It is useful in comparing the decay heat levels of different blankets or systems, such as D-T vs. D-D fuel cycles. The decay heat fraction f_d is defined simply as

$$f_d = \frac{\text{total decay heat}}{\text{total operating heat}} \qquad \text{(B.2.1)}$$

The decay heat analysis was carried out in one dimension, using cylindrical geometry. The torus is represented as a vertical cylinder, consisting of concentric rings. Figure B.2.1 shows the vertical cylinder as viewed from the top. The innermost ring is the inboard shield/blanket; just outside of this is the plasma; and outside the plasma is the outboard blanket/shield. The magnets, which would occupy the space inside the inboard shield (inboard leg) and outside the outboard shield (outboard leg) were not considered in this study.

To find the total decay heat, the decay heat density (W/m^3) must be integrated over the total volume. Given the geometrical representation described above, the

Figure B.2.1 Tokamak Cylindrical Geometry as viewed from above (Toroidal View
R = Major Radius, a = Minor Radius

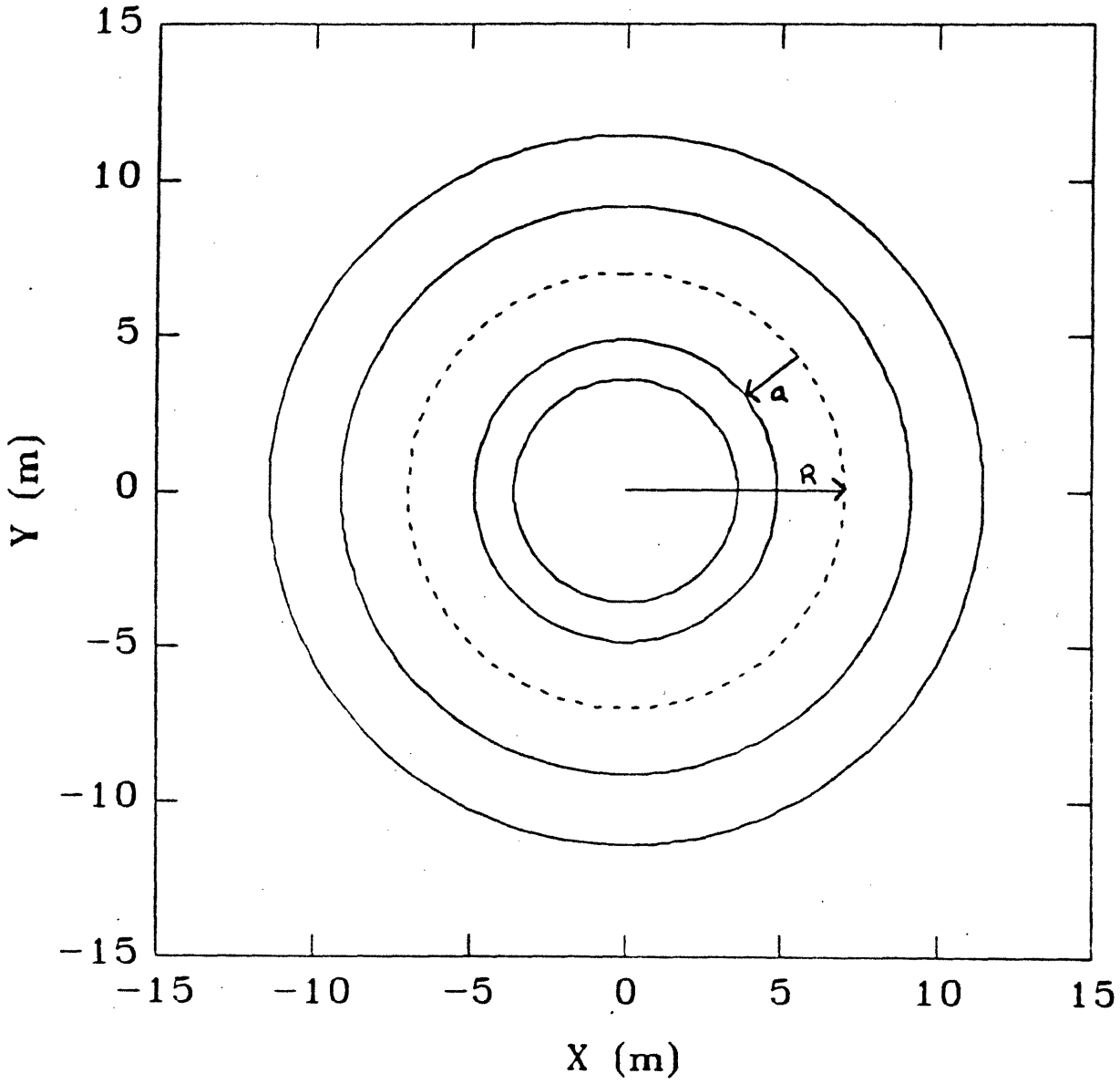

decay heat density is actually integrated over the *area* of a horizontal slab of the vertical cylinder. This gives the total decay heat per unit axial length, i.e., (W/m). The decay heat per unit axial length, $\dot{q}'_{decay}$, is found by

$$\dot{q}'_{decay}(t) = \int d\theta \int r dr \dot{q}'''_{decay}(r,t) \qquad \text{(B.2.2)}$$

Assuming that there is no θ dependence, the $\int d\theta$ merely becomes a factor of 2π. The integration over r is carried out by first realizing that $\dot{q}'''_{decay}(x,t)$ depends exponentially on x, i.e., goes as $e^{-\mu x}$ (see Appendix B.1). Next, the following relation is used to substitute r for x:

Inboard Side: r = R - a - x

Outboard Side: r = R + a + x

where R is the major radius and a is the minor radius of the torus (see Figure B.2.1). The integration is then fairly straightforward.

The total operating heat is found in a simpler, more heuristic manner. The total amount of heat entering the blanket (inboard or outboard) is simply the wall load (MW/m^2) times the first wall area (m^2). Given the geometry shown in Figure B.2.1, what is used is the first wall area *per unit axial length*,

Inboard

$$A_{fw} = 2\pi(R-a) \qquad \text{(B.2.3)}$$

Outboard

$$A_{fw} = 2\pi(R+a) \qquad \text{(B.2.4)}$$

where A_{fw} will have the units m^2/m. Some of the energy entering the blanket is in the form of neutrons, and some is in the form of heat radiated from the plasma. The energy carried by neutrons will be increased by the blanket energy

multiplication factor. Thus, the total operating energy per unit axial length of the blanket, $\dot{q}'_{op}$ will be

$$\dot{q}'_{op} = [(L_n M_b) + L_h] A_{fw} \tag{B.2.5}$$

where

L_n = neutron wall load,

M_b = blanket multiplication factor,

and

L_h = heat flux radiated to the first wall from the plasma.

The mathematical representation of the decay heat fraction, as is given in equation (B.2.1), is thus

$$f_d(t) = \frac{\dot{q}'_{decay}(t)}{\dot{q}'_{op}} \tag{B.2.6}$$

Note that $\dot{q}'_{op}$ remains constant with time.

The value $f_d(t)$ is what is plotted in Figures 4.2.1, 4.2.2, 4.2.6, and 4.4.1.

References for Appendix B

[B.1] E.T. Cheng, Radioactivation Characteristics for Deuterium- Tritium Fusion Reactors, Nuclear Technology/Fusion 4, 1983.

[B.2] J.E. Massidda, Power Flattening in D-T Tokamak Fusion Reactor Blankets, Master's Thesis, Department of Nuclear Engineering, Massachusetts Institute of Technology, 1985.

C. Inputs to THIOD

There are essentially four areas of input for the code THIOD. First there is the configuration of the blanket, that is, the thickness and composition of each region. For all of the blankets, this information is given in Chapter 2, as displayed in Figures 2.1.2 through 2.6.1. Note that the blanket geometry is represented as a one-dimensional slab, except for the analyis presented in Section 5.5 (see also Appendix D), where one-dimensional cylindrical geometry is used. The second area of input involves the heat source, which consists of the plasma power (surface heat flux and volumetric neutron heating) and the decay heat density. Assumptions regarding the plasma power are given in Sections 5.1.3.1, 5.2.1.4, and 5.4.5. Further discussion regarding the effect of plasma burn is given in Chapter 7. The decay heat density is discussed in Chapter 4 and Appendix B. Third, there are the thermal properties of the materials being used, such as thermal conductivity, density, and heat capacity. Finally, there is the initial temperature distribution. Discussion of these last two areas of input is given here.

C.1 Material Thermal Properties

The thermal properties of interest are the thermal conductivity k, the density ρ, and the heat capacity c_p. In the convection analysis presented in Chapter 6, additional properties of the coolant material are required. These parameters are

discussed in Appendix E. A variety of references were used to get this information for all of the materials considered in this work.

C.1.1 Thermal Conductivity

For most materials, thermal conductivity is a fairly strong function of temperature [C.1 - C.7]. Thus, representing the conductivity as a constant could lead to unacceptable errors. In many cases, the temperature dependence can be somewhat complicated. However, for the purposes of simplicity, the thermal conductivity is represented as a linear function of temperature. Thus, the conductivity of a material at temperature T is represented

$$k(T) = U_k T + V_k \tag{C.1}$$

The values of U_k and V_k for all the materials used are shown in Tables C.1.1a, C.1.1b, and C.1.1c. Also shown is the reference designation for the source of the information. Table C.1.1a is for the structural materials, Table C.1.1b is for the breeder/coolant materials, and Table C.1.1c is for the magnet and shield materials.

Note that for some materials, the conductivity is constant, that is, the value of U_k is zero. In these instances, information on the temperature dependence of the conductivity in the temperature range of interest was not available. Also note that the MgO conductivity is assumed constant above 450 °C. Again, no information on the actual conductivity vs. temperature was available at these temperatures. At lower temperatures, the data was fit with the values of U_k and V_k shown. Extrapolation to higher temperatures with these values of U_k and V_k, however, would result in a negative conductivity. Thus, for lack of better information, it was assumed that the conductivity levels out above 450 °C. The same approach was taken for B_4C, where it was assumed that the conductivity levels out above 100 °C.

Table C.1.1a Thermal Conductivity Parameters U_k and V_k, Volumetric Heat Capacity Parameters $U_{\rho c_p}$ and $V_{\rho c_p}$ and their references for the structural materials.

Material	U_k	V_k	Reference	$U_{\rho c_p}$	$V_{\rho c_p}$	Reference
VCrTi	1.350e-02	1.761e+01	[C.1]	1.220e+03	2.412e+06	[C.1]
HT-9*	4.000e-03	2.410e+01	[C.1]	4.920e+03	1.989e+06	[C.1]
Fe1422	see					

* The HT-9 used in this study is a version which has been modified for low ac: n [C.8]. The material properties, however, were assumed to be those given for HT-9 in the BCSS [C.1].

Table C.1.1b Thermal Conductivity Parameters U_k and V_k, Volumetric Heat Capacity Parameters $U_{\rho c_p}$ and $V_{\rho c_p}$ and their references for the breeder/coolant materials.

Material	U_k	V_k	Reference	$U_{\rho c_p}$	$V_{\rho c_p}$	Reference
He	2.390e-04	8.310e-02	[C.7]	-6.046e-01	8.190e+02	[C.2]
Lithium	1.905e-02	3.493e+01	[C.1]	-3.444e+01	1.987e+06	[C.1]
$Li_{17}Pb_{83}$	0.000e+00	1.700e+01	[C.6]	-4.954e+02	1.680e+06	[C.1]
Li_2O	-2.667e-03	4.600e+00	[C.1]	0.000e+00	2.934e+06	[C.1]
Be	-5.727e-02	1.284e+02	[C.5]	1.070e+03	3.231e+06	[C.5]
H_2O	1.320e-04	5.688e-01	[C.2]	-1.494e+03	4.611e+06	[C.2]

Table C.1.1c Thermal Conductivity Parameters U_k and V_k, Volumetric Heat Capacity Parameters $U_{\rho c_{p'}}$ and $V_{\rho c_{p'}}$ and their references for the magnet/shield materials.

Material	U_k	V_k	Reference	$U_{\rho c_{p'}}$	$V_{\rho c_{p'}}$	Reference
SS304	1.800e-02	8.406e-00	[C.3]	7.074e+02	3.474e+06	[C.3]
MgO	-7.478e-02†	5.924e+01	[C.4]	3.997e+02	3.621e+06	[C.4]
Cu	-4.333e-02	4.074e+02	[C.2]	8.626e+02	3.210e+06	[C.5]
B_4C	-5.733e-02‡	4.019e+01	[C.4]	3.009e+03	1.053e+06	[C.4]

† Above 450 °C, assume conductivity levels out at 5.2 W/m-K (value at 450 °C).

‡ Above 100 °C, assume conductivity levels out at 18.8 W/m-k (value at 100 °C).

For all the materials, the linear behavior chosen was that which most closely matches the actual data in the temperature range of interest. This range is from 500 °C to 1000 °C for the materials in the blanket, since this encompasses most of the temperature histories given in Chapters 5, 6, and 7. For the materials in the shield/coil region, such as MgO, B_4C, SS304, and Cu, the range is from 20 °C to 500 °C, since this is the temperature range found in these regions in most of the cases presented in Chapters 5 and 6.

The thermal conductivity within each region of the blanket is found by weighting the conductivity of each conduction path (i.e., material) by its area. That is, for region j, the conductivity k_j is found by

$$k_j = \sum_m k_m f_A^m \tag{C.2}$$

where

k_m is the thermal conductivity of material m, and

f_A^m is the fraction of the area, in the yz plane, that material m encompasses. This area fraction is assumed to be the same as the volumetric fraction of material m in region j.

Due to the assumption for f_A^m, it is clear that k_j really represents a volumetric average of all the materials within region j. This method for determining k_j is valid, because in all the blanket considered, the conduction paths are homogeneous in the radial direction (direction of heat flow). That is, conduction paths consisting of different materials are arranged in parrallel, such that weighting the conductivity of each conduction path by its area will give the proper total conductivity for the region.

C.1.2 Volumetric Heat Capacity

The volumetric heat capacity, in units of J/m^3K, is the product of the density ρ (kg/m^3) and the specific heat capacity c_p (J/kg-K). Both of these parameters are functions of temperature, although for the solid structural materials, the density only varies slightly in the temperature range of interest. Note in Section 5.1, in the description of the model basis of THIOD (i.e., equations (5.1) through (5.10)), that the parameters ρ and c_p always appear as a product, that is, ρc_p. For this reason, and for simplicity, the input parameter to THIOD is the product of ρ and c_p, which yields the volumetric heat capacity.

As for the thermal conductivity, the parameter ρc_p is assumed to be a linear function of temperature. This is found by taking the product of ρ and c_p at various temperatures within the range of interest and making a best-fit line. The equation for ρc_p of a particular material at temperature T is thus of the same form as equation (C.1), that is,

$$\rho c_p(T) = U_{\rho c_p} T + V_{\rho c_p} \tag{C.3}$$

The values of $U_{\rho c_p}$ and $V_{\rho c_p}$ for all the materials are given in Tables C.1.1a, C.1.1b, and C.1.1c, along with the references.

C.2 Initial Temperature Distribution

The spatial temperature distribution at accident initiation can impact the temperature response of the blanket (see Section 5.4.2). However, including this variation could bias the comparison between blankets in favor of that with the favorable initial temperature distribution. Thus, except for the RFP Blanket #3, all the blankets were assumed to have the same initial temperature distribution. This distribution was taken from that given in the BCSS for Blanket #1 [C.1], and is shown

in Figure C.2.1. This is based on the operational temperature distribution, which was determined in the BCSS by thermal-hydraulics calculations. There is a slight gradient from the first wall to the back of the blanket, which is the result of the decreasing operational power density.

Not all of the blankets are the same thickness. For those blankets which are thinner than Blanket #1 (Blankets #2 and #5), the initial temperature distribution is the same as the front of Blanket #1, that is, the distribution shown if Figure C.2.1, but cut off at the appropriate blanket thickness. For Blanket #6, which has a greater thickness than Blanket #1, the gradient is continued to the back of the blanket.

The initial distribution in the shield was chosen more arbitrarily. The shield is operated at low temperature [C.1] and the heat deposited in it is wasted. The indication is that the shield will operate at room temperature. Clearly, in terms of the temperature response of the blanket, a low shield temperature will result in a lower first wall temperature. Thus, assuming a higher initial shield temperature is conservative. On this basis, for all of the blankets except the RFP Blanket #3, the initial shield distribution was chosen to be 100 °C, constant across the thickness of the shield (see Figure C.2.1). The temperature of the heat sink was chosen to be the same as that of the shield, so that at time=0, there will be no heat transfer from the shield to the sink.

The RFP is a somewhat different case, since it operates at a very high power density and is a very thin blanket. The initial temperature distribution for this blanket was taken from reference [C.9], and is shown in Figure C.2.2. Note that the initial distribution is flat. This can have a slight impact on the post-accident temperature response, as is discussed in Section 5.4.2. The RFP Blanket #3 also does not contain a shield, but is backed by the copper PF and TF coils. These coils will be operated at a low temperature to minimize the resistance of the copper. The initial temperature of the coils is assume to be room temperature (20 °C). Again,

Figure C.2.1 Initial Temperature Distribution in Blanket #1

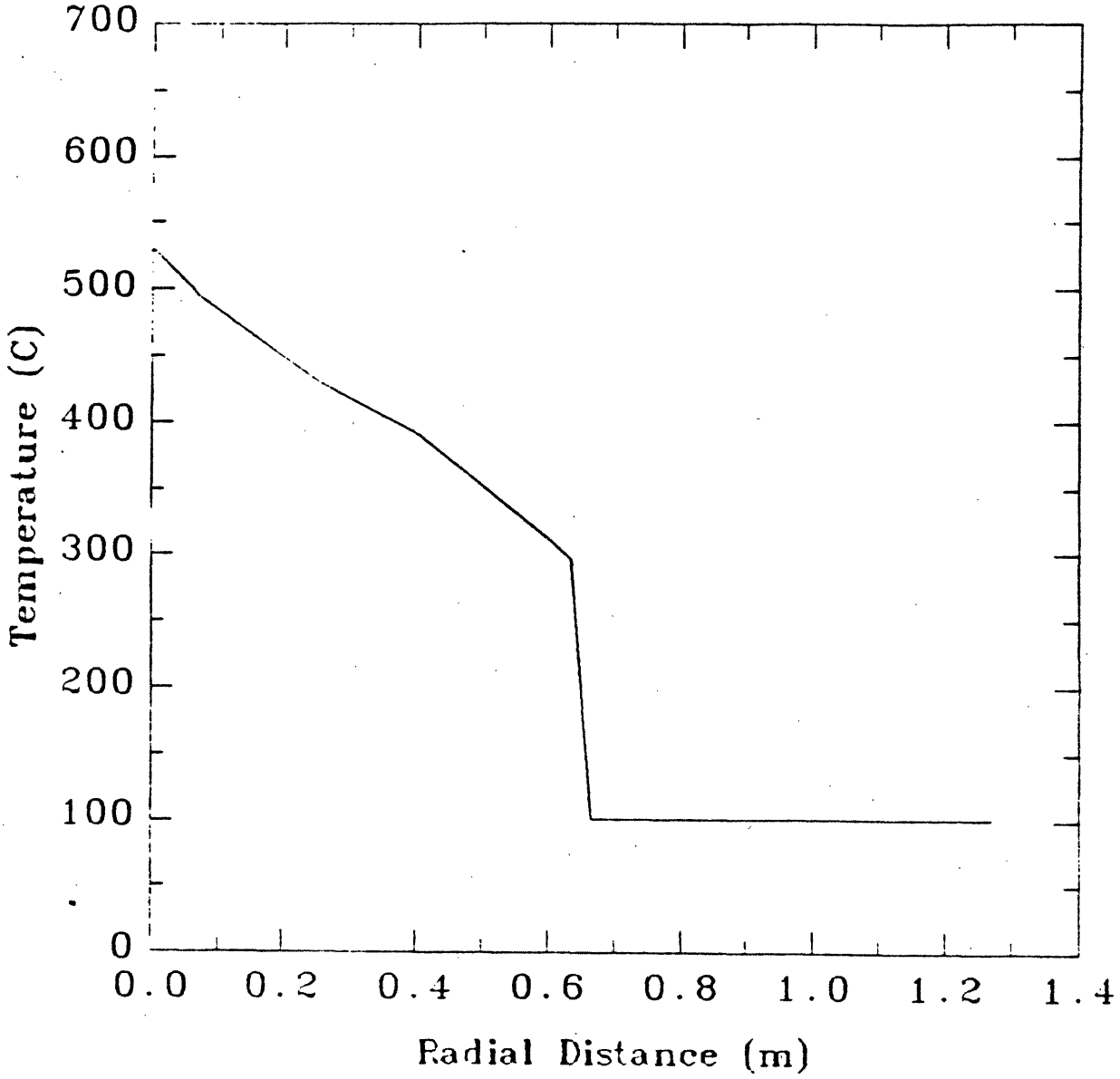

Figure C.2.2 Initial Temperature Distribution in Blanket #3

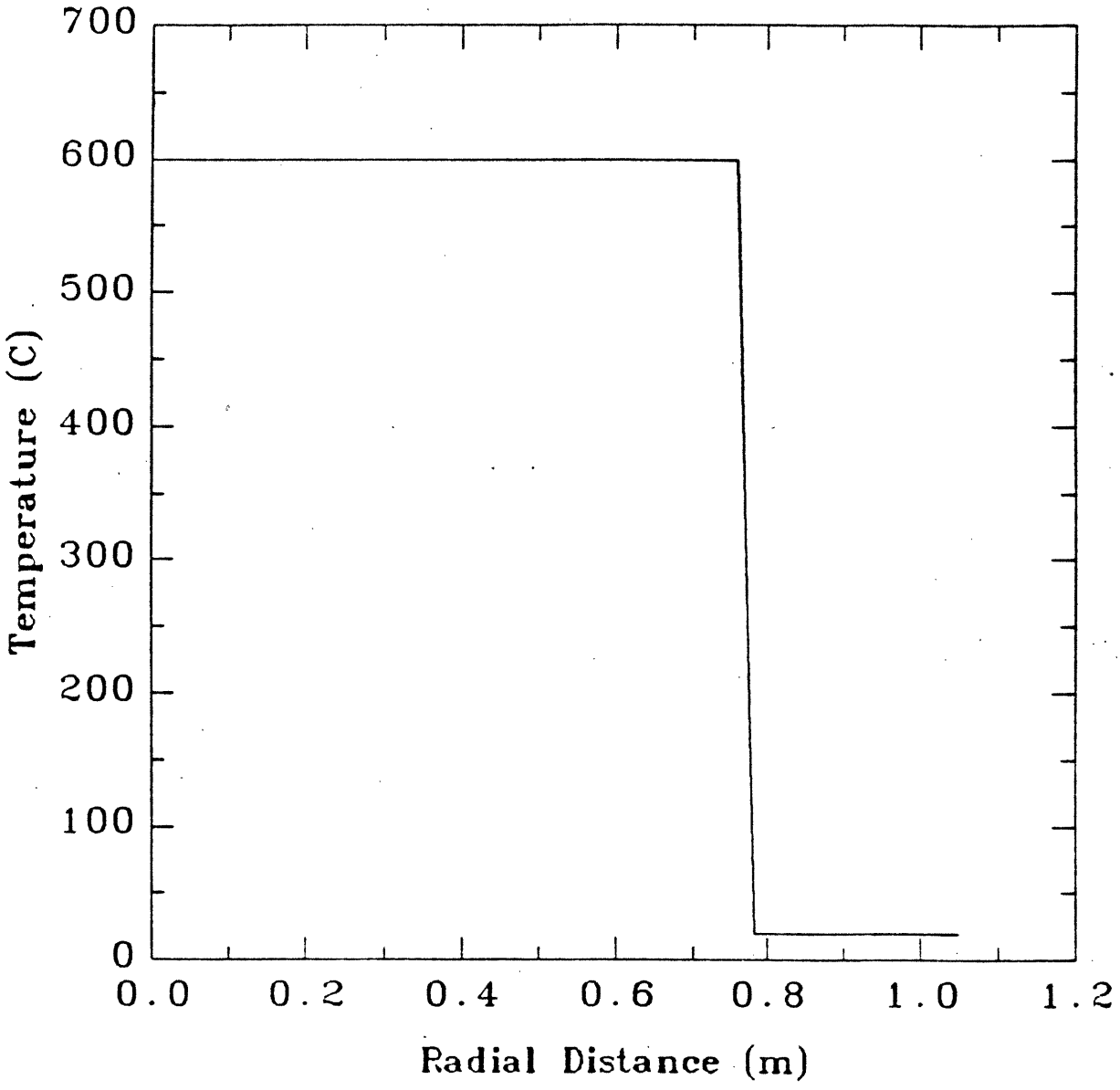

the heat sink is assumed to be the same temperature as the coil initial temperature, in this case 20 °C.

References for Appendix C

[C.1] D.L. Smith et al., Blanket Comparison and Selection Study (BCSS) - Final Report, Argonne National Laboratory, ANL-84-1, September 1984.

[C.2] J.H. Lienhard, A Heat Transfer Textbook, Prentice-Hall, Inc., Englewood Cliffs, N.J., 1981.

[C.3] Peckner and Bernstein, Handbook of Stainless Steels, McGraw Hill Book Company, 1977.

[C.4] R.C. Weast, Editor-in-Chief, CRC Handbook of Chemistry and Physics, 65th Edition, CRC Press, Inc., 1984.

[C.5] R.H. Perry, C.H. Chilton, Chemical Engineer's Handbook, 5th Edition, McGraw Hill Book Company, 1973.

[C.6] W.M. Stacy, Jr., FUSION : An Introduction to the Physics and Technology of Magnetic Confinement Fusion, John Wiley & Sons, 1984.

[C.7] G. Joos, Theoretical Physics, 2nd Edition, Hafner Publishing Company, New York, 1950.

[C.8] S. Fetter, Radioligical Hazards of Magnetic Fusion Reactors, Lawrence Livermore National Laboratory, LLNL MS#61485F, 1985.

[C.9] R.L. Miller, et. al., Advanced Tokamak Reactors Based on the Spherical Torus (ATR/ST), Los Alamos National Laboratory, LA-10740-MS, June 1986.

D. Numerical Solutions to Heat Transfer Equation

D.1 Explicit vs. Implicit Solutions

In Chapter 5, the heat transfer equation (5.9) is derived from the basic heat balance equation (5.1), with the assumption that no convection takes place. The result is

$$\frac{dT_i}{dt} = \left(\frac{1}{\Delta x_i \rho_i c_{p_i}(T)}\right)\left[\int_{\Delta x_i} \dot{q}'''_{decay}(x,t)dx + \Delta k_i \left(\frac{T_{i+1}-T_i}{x_{i+1}-x_i}\right)\right.$$

$$\left. -\Delta k_{i-1}\left(\frac{T_i - T_{i-1}}{x_i - x_{i-1}}\right) + \dot{q}''_{rad}(t)\Big|_{x=x_i-\frac{\Delta x_i}{2}}^{x=x_i+\frac{\Delta x_i}{2}}\right] \tag{5.9}$$

The first step in solving this equation numerically is to approximate the time derivative as $\frac{\Delta T_i}{\Delta t}$. This then yields

$$\frac{\Delta T_i^n}{\Delta t} = \left(\frac{1}{\Delta x_i \rho_i c_{p_i}(T)}\right)\left[\int_{\Delta x_i} \dot{q}'''_{decay}(x,t)dx + \Delta k_i \left(\frac{T_{i+1}-T_i}{x_{i+1}-x_i}\right)\right.$$

$$\left. -\Delta k_{i-1}\left(\frac{T_i - T_{i-1}}{x_i - x_{i-1}}\right) + \dot{q}''_{rad}(t)\Big|_{x=x_i-\frac{\Delta x_i}{2}}^{x=x_i+\frac{\Delta x_i}{2}}\right] \tag{D.1}$$

Note that the n superscript refers to the time step, such that

$$\Delta T_i^n = T_i^n - T_i^{n-1} \tag{D.2}$$

Given the discrete nature of Δt, each "time step"represents the addition of one time increment Δt to the time t. The various methods of solving equation (D.1) involve determining at which time step the values T_{i-1}, T_i, and T_{i+1} on the right hand side of equation (D.1) should be considered. In the purely explicit method, all the values on the RHS of equation (D.1) are from the previous time step. Thus, the explicit equation is

$$\frac{\Delta T_i^n}{\Delta t} = \left(\frac{1}{\Delta x_i \rho_i c_{p_i}(T)}\right)\left[\int_{\Delta x_i} \dot{q}'''_{decay}(x,t)dx + \Delta k_i \left(\frac{T_{i+1}^{n-1} - T_i^{n-1}}{x_{i+1} - x_i}\right)\right.$$

$$\left. - \Delta k_{i-1}\left(\frac{T_i^{n-1} - T_{i-1}^{n-1}}{x_i - x_{i-1}}\right) + \dot{q}''_{rad}(t)\Big|_{x=x_i-\frac{\Delta x_i}{2}}^{x=x_i+\frac{\Delta x_i}{2}}\right] \tag{D.3}$$

Note that at time step n, all the values on the RHS of equation (D.3) are known, since they were solved in the previous time step, i.e., $n-1$. Then to find T_i^n, the RHS is evaluated from all these known values and multiplied by Δt. T_i^n is then found with the definition given in equation (D.2). Care must be taken in choosing the size of the time step in this approach. Too large a time step will lead to a mathematical instability. A general rule for the maximum allowable time step in the explicit approach is

$$\Delta t_{max} = 0.2 \times \frac{\Delta x_i^2}{\alpha} \tag{D.4}$$

where

$$\alpha = \frac{k}{\rho c_p}$$

With this restriction on the time step, it is assured that the solution of equation (D.3) will be stable. There will be some inaccuracy due to the discretization of the time derivative. This error can be reduced by reducing the size of the time step Δt. A smaller Δt, however, will result in a longer computing time. Thus, a trade-off must be reached between adequate accuracy and acceptable computing time.

Other variations of the explicit method can be made. Namely, when calculating T_i^n is equation (D.3), the value of T_{i-1}^n is already known. Thus, T_{i-1}^n can be substituted for T_{i-1}^{n-1} in the right hand side of equation (D.3). Furthermore, T_i^n can be substituted for T_i^{n-1} in the right hand side of equation (D.3), and then the equation is solved for T_i^n. This results in

$$\begin{aligned} T_i^n \left[1 + \left(\frac{\Delta t}{\Delta x_i (\rho c_{p_i})} \right) + \frac{\Delta k_{i-1}}{x_i - x_{i-1}} + \frac{\Delta k_i}{x_{i+1} - x_i} \right] \\ = T_i^{n-1} + \frac{1}{\Delta x_i (\rho c_p)_i} \int_{\Delta t} \int_{\Delta x_i} \dot{q}'''_{decay}(x,t) dx dt \\ + \left(\frac{\Delta t}{\Delta x_i (\rho c_p) i} \right) \left[\left(\frac{\Delta k_{i-1}}{x_i - x_{i-1}} + \right) T_{i-1}^n + \left(\frac{\Delta k_i}{x_{i+1} - x_i} \right) T_{i+1}^{n-1} \right] \end{aligned} \quad \text{(D.5)}$$

The restriction on the time step given in equation (D.4) still applies in this case, since this is still essentially an explicit method. Equation (D.5) is what is used in the explicit version of the code THIOD.

In the fully implicit approach, T_{i-1}, T_i, and T_{i+1} on the right hand side of equation (D.3) are all evaluated at time step n. The resulting equation is the same as (D.5) except that the T_{i+1}^{n-1} is replaced by T_{i+1}^n. This introduces a difficulty, since, when evaluating T_i^n, the value of T_{i+1}^n is not known. There are a number of

ways in which this difficulty can be overcome. One method is to put the equation in matrix form, i.e.,

$$[A][T^n] = [B] \tag{D.6}$$

where

$[A]$ is a tri-diagonal, $i \times i$ matrix which couples T_{i-1}^n, T_i^n, and T_{i+1}^n,

$[T]$ is a $i \times 1$ vector containing the T_i^n, and

$[B]$ is a $i \times i$ matrix that represents the heat source and the T_i^{n-1}.

Solving equation (D.6) involves inverting the matrix $[A]$. Since the elements in $[A]$ and $[B]$ are temperature and time dependent, they are always changing. Thus, for each time step, $[A]$ must be inverted. This is a cumbersome process, even for a tri-diagonal matrix, especially when the number of mesh points (i) is large.

There exists another approach to the implicit solution which is much simpler. As outlined in references [D.1] and [D.2], the method proceeds as follows. First, equation (D.5) is reduced to the form

$$-A_i T_{i+1} + B_i T_i - C_i T_{i-1} = D_i \tag{D.7}$$

Then it is stated that there are parameters E_i and F_i such that

$$T_i = E_i T_{i+1} + F_i \tag{D.8}$$

Using the boundary conditions at either boundary, the values of E_0 and F_0, or E_I and F_I, where I is the number of mesh points, can be determined. For the undercooling and overpower transient temperature response calculations in this work, the

boundary condition is that the front face of the first wall is insulated. That is, there is no heat flux across the face of the first wall †. Mathematically, this boundary condition can be represented by saying

$$T_1 = T_0 \tag{D.9}$$

Then it is seen immediately that

$$E_0 = 1$$

$$F_0 = 0 \tag{D.10}$$

By substituting the T_i in equation (D.8) into equation (D.7), and then doing the same for T_{i-1} (by substituting $i-1$ for i in equation (D.8)), the recursive relations for E_i and F_i turn out to be

$$E_i = \frac{A_i}{B_i - C_i E_{i-1}}$$

$$F_i = \frac{D_i + C_i F_{i-1}}{B_i - C_i E_{i-1}} \tag{D.11}$$

Using equations (D.10) and (D.11) and the (known) values of A_i, B_i, C_i, and D_i, one can determine the values of E_i and F_i, for i=0 to I, where I is the number of mesh points, at time step n. Next, starting at $i = I$, and using equation (D.8), the

† In the plasma continuation cases, the plasma heat flux continues to radiate to the first wall for some period of time. This heat flux is treated as a heat *source* at the first mesh point, i.e. T_1, and not a boundary condition at x=0.

T_i^n can be found. This is possible since T_{I+1} is known by the boundary condition at the back of the shield.

This implicit method is not subject to the time step restriction in equation (D.4), and thus larger time steps can be used without the solution becoming unstable.

For the analysis in Chapter 5, in which convection is ignored, the parameters A_i, B_i, C_i, and D_i can be defined from equation (D.5) as

$$A_i = \frac{\Delta t}{\rho c_{p_i}} \left(\frac{\Delta k_i}{x_{i+1} - x_i} \right)$$

$$B_i = 1 + \frac{\Delta t}{\rho c_{p_i}} \left(\frac{\Delta k_{i-1}}{x_i - x_{i-1}} + \frac{\Delta k_i}{x_{i+1} - x_i} \right)$$

$$C_i = \frac{\Delta t}{\rho c_{p_i}} \left(\frac{\Delta k_{i-1}}{x_i - x_{i-1}} \right)$$

$$D_i = T_i^{n-1} + \frac{1}{\Delta x_i (\rho c_p)_i} \int_{\Delta t} \int_{\Delta x_i} \dot{q}'''_{decay}(x,t) dx dt + (\dot{q}''_{rad}) \Delta t \qquad \text{(D.12)}$$

where all the parameters are as defined in Chapter 5.

It is useful to compare the accuracy and computing time required for the explicit method (equation (D.5)) and the implicit method outlined in equations (D.7) - (D.12). The accuracy is checked internally by keeping track of three parameters: the total heat produced, Q_{tot}, the total increase in stored heat, S_{tot}, and the total amount of heat that is transferred to the heat sink $Q_{\rm HS}$. These parameters are defined as follows:

$$Q_{tot} = \int_0^{2\text{days}} dt \int_X dx \dot{q}'''_{decay}(x,t)$$

$$S_{tot} = \sum_i \Delta x_i \rho c_{p_i} \Delta T_i \tag{D.13}$$

$$Q_{\mathrm{HS}} = \sum_n \dot{q}''_{\text{heat sink}} \Delta t_n$$

Note that, in slab geometry, all three parameters have the units $\mathrm{J/m^2}$. Clearly, all of the heat produced must either contributes to the blanket temperature is transferred to the heat sink. Thus,

$$Q_{tot} = S_{tot} + Q_{\mathrm{HS}} \tag{D.14}$$

Because of the approximations used in the numerical methods, the left hand side of equation (D.14) may not exactly equal the right hand side. The error E can be defined as

$$E = \frac{Q_{tot} - S_{tot} - Q_{\mathrm{HS}}}{Q_{tot}} \tag{D.15}$$

Clearly, a more accurate calculation will result in a smaller value of E. The important parameters in comparing the two calculational methods are the value of E and the computing time required. All of the calculations were performed on one of the CRAY computers of the National Magnetic Fusion Energy Computing Center, located at Lawrence Livermore National Laboratory. The computing time is measured in minutes of CPU (Central Processing Unit) time required to complete the calculation.

The size of the time step is very important to both E and CPU. A larger Δt will result in a larger E but a lower CPU, and vice versa. For the purposes of accuracy, the magnitude of Δt depends on the rate of change of the temperature, i.e., $\frac{\Delta T}{\Delta t}$. When $\frac{\Delta T}{\Delta t}$ is large, that is, when the temperature is changing rapidly such

as at the beginning of the transient, then it is important to keep Δt small so there will not be a large fluctuation in the temperature during any one time step. Later in the transient, when the temperatures have leveled out and are changing slowly, Δt can be increased without significantly sacrificing accuracy. This leads to a set of criteria for determining the time step size, which are outlined in Table D.1.1. Keep in mind that for the explicit method, the time step is always subject to the restriction of equation (D.4).

Comparisons of the values of E and CPU for the two methods are given in Table D.1.2. The time step restrictions are those given in Table D.1.1 unless otherwise stated. The indication from the first two entries is that the implicit method yields more accurate results in far less computing time. Note that the parameters Q_{tot}, S_{tot}, and Q_{HS} are calculated to five significant digits, and thus errors of less than 0.01% are not especially meaningful. Both of the implicit cases listed in Table D.1.2 have errors below 0.01%, and thus it is not significant that the case with the looser time step restrictions appears to have a lower error parameter E. It is significant, however, that both of these implicit cases have error parameters well below those of the explicit calculations. Note that loosening the time step restriction in the explicit case results in a faster computing time, but a higher error parameter.

D.2 Modification for Cylindrical Geometry

The physical basis for the code is the same for slab and cylindrical geometry. Recall that in slab geometry, the $x = 0$ origin is at the front face of the first wall, and x increases as the distance into the blanket (away from the first wall) increases. In cylindrical geometry, the $r = 0$ origin is at the centerline of the torus, as shown in Figure B.2.1. If one were to start at $r = 0$ and move in the r direction, first there would be the inboard blanket, then the plasma chamber, then the outboard blanket. For the cylindrical case, in one dimension, equation (5.1) becomes

Table D.1.1 Restrictions on Time Step Size for Explicit and Implicit Methods.

Method	$(\Delta T_i^n)_{max}$ (°C)	$\left(\frac{\Delta T_i}{\Delta t}\right)_{max}$ $\left(\frac{^\circ C}{s}\right)$	Multiply Δt by
Explicit†	≥ 1.0		0.5
	< 1.0	≤ 0.05	3.0
	< 1.0	$> 0.05, \leq 0.10$	2.0
	< 1.0	> 0.10	1.0
Implicit‡	≥ 5.0		0.5
	< 5.0	≤ 0.50	3.0
	< 5.0	$> 0.50, \leq 2.0$	2.0
	< 5.0	> 2.0	1.0

† Maximum time step for explicit case is 10.0 seconds.

‡ Maximum time step for implicit case is 500.0 seconds.

Table D.1.2 Error Parameter E and CPU time used for Implicit and Explicit versions of THIOD, with various time-step restrictions.

Case	Method	E (%)	CPU (min)
A2C1PL	Explicit	6.43	10
	Implicit	-4.96e-04	< 1
	Implicit*	1.96e-03	5.5
	Explicit†	16.6	4.1

* Using restrictions for Explicit method given in Table D.1.1.

† Using restrictions for Implicit method given in Table D.1.1, still subject to restriction [D.4].

$$\rho(r)c_p(r,T)\left(\frac{\partial T(r,t)}{\partial t}\right) = \dot{q}'''_{decay} + \frac{1}{r}\frac{\partial}{\partial r}\left(rk(r,T)\frac{\partial T(r,t)}{\partial r}\right) \qquad \text{(D.16)}$$

This equation is then integrated over $rdrd\theta$, where θ is the toroidal angle. The one-dimensional approach implies that there is no θ dependence. Thus, the factor of 2π that would appear in all the terms is simply ignored. The result is

$$\frac{1}{2}\left(r_2^2 - r_1^2\right)\rho c_{p_i}(T)\left(\frac{dT_i}{dt}\right) = \int_{\Delta r_i} \dot{q}'''_{decay}(r,t)rdr + \int_{\Delta r_i}\frac{1}{r}\frac{\partial}{\partial r}rk_i(T)\frac{\partial T_i(t)}{\partial r}$$

$$-\dot{q}''_{rad}(t)|_{r=r+\frac{\Delta r}{2}} - \dot{q}''_{rad}(t)|_{r=r-\frac{\Delta r}{2}} \qquad \text{(D.17)}$$

where,

$r_2 = r_i + \frac{\Delta r_i}{2}$, and

$r_1 = r_i - \frac{\Delta r_i}{2}$

In the inboard toroidal cylinder, note that the x axis, which starts at the first wall and increases into the blanket, is in the opposite direction to the r axis, which starts at the center of the torus. For both inboard and outboard cases, the mesh spacing is such that i=1 is the first mesh point in the first wall, and i increases as x, the distance into the blanket from the first wall, increases. This means that in the inboard side, r_{i-1} has a larger value than r_i, since r decreases with increasing x. The remainder of the derivation of the cylindrical equations will be carried out for the outboard side, i.e., the outboard toroidal and the poloidal cylinders. Remember that for the inboard toroidal cylinder, there will be some differences due to the difference in the orientation of the axes.

Due to geometrical effects, the radiation heat flux is given by

$$\dot{q}''_{rad} = v_f \sigma \epsilon_{ij} \left(T_i^4 - T_j^4\right) \tag{D.18}$$

where v_f is the geometric view factor. For radiation to or from a cylinder of larger radius, the view factor v_f=1. For radiation to or from a cylinder of smaller radius, the view factor $v_f = \frac{r_s}{r_l}$ where r_s is the smaller radius and r_l is the larger radius. [D.3].

Once again, $\dot{q}'''_{decay}(r,t)$ is an exponential function of r, and can be integrated analytically. However, it must be redefined to the appropriate $r = 0$ origin, which is not the same as the $x = 0$ origin in the slab approach. Transforming from the $x = 0$ origin to the $r = 0$ origin is done by substituting for x. On the inboard side, the substitution is

$$r = R - a - x \tag{D.19}$$

where R and a are the major and minor radii, respectively. It might be helpful to refer to Figure B.2.1. Note that for the outboard toroidal cylinder, and the poloidal cylinder, the substitution is

$$r = R + a + x \tag{D.20}$$

Making these substitutions into the heat source equation (4.2) discussed in Chapter 4 and Appendix B allows for the calculation of the heat source in cylindrical geometry.

The conduction integral, which must be solved numerically, is also different for the inboard and outboard sides, because of the different substitutions given in equations (D.19) and (D.20). For the outboard side, the conduction integral thus becomes

$$\int_{\Delta r_i} \frac{1}{r}\frac{\partial}{\partial r} r k_i(T) \frac{\partial T_i(t)}{\partial t} = r_2 k(r_2) \frac{T_{i+1} - T_i}{r_{i+1} - r_i} - r_1 k(r_1) \frac{T_i - T_{i-1}}{r_i - r_{i-1}} \qquad \text{(D.21)}$$

Substituting this into equation (D.17) yields

$$\frac{1}{2}\left(r_2^2 - r_1^2\right) \rho c_{p_i}(T) \left(\frac{dT_i}{dt}\right) = \int_{\Delta r_i} \dot{q}'''_{decay}(r,t) r dr + r_2 k(r_2) \frac{T_{i+1} - T_i}{r_{i+1} - r_i}$$

$$- r_1 k(r_1) \frac{T_i - T_{i-1}}{r_i - r_{i-1}} - \dot{q}''_{rad}(t)|_{r=r+\frac{\Delta r}{2}} + \dot{q}''_{rad}(t)|_{r=r-\frac{\Delta r}{2}} \qquad \text{(D.22)}$$

This can be rearranged to the form of equation (D.7), with the parameters A_i, B_i, C_i, and D_i being

$$A_i = \frac{\Delta t}{\frac{1}{2}(r_2^2 - r_1^2)\rho c_{p_i}} \left(\frac{r_1 k(r_1)}{r_i - r_{i-1}}\right)$$

$$B_i = 1 + \frac{\Delta t}{\frac{1}{2}(r_2^2 - r_1^2)\rho c_{p_i}} \left(\frac{r_2 k(r_2)}{r_{i+1} - r_i} + \frac{r_1 k(r_1)}{r_i - r_{i-1}}\right)$$

$$C_i = \frac{\Delta t}{\frac{1}{2}(r_2^2 - r_1^2)\rho c_{p_i}} \left(\frac{r_2 k(r_2)}{r_{i+1} - r_i}\right)$$

$$D_i = T_i^{n-1} + \frac{1}{\frac{1}{2}(r_2^2 - r_1^2)\rho c_{p_i}} \int dt \int_{r_1}^{r_2} \dot{q}'''_{decay}(r,t) r dr$$

$$- \left(\frac{\Delta t}{\frac{1}{2}(r_2^2 - r_1^2)\rho c_{pi}}\right) \left(\dot{q}''_{rad}(t)|_{r=r+\frac{\Delta r}{2}} - \dot{q}''_{rad}(t)|_{r=r-\frac{\Delta r}{2}}\right) \qquad \text{(D.23)}$$

In this equation, the $k(r_1)$ and $k(r_1)$ are similar to the Δk_i found in equations (D.12) and defined in equation (5.7). In cylindrical geometry, the k between mesh zones i and $i+1$ is defined as

$$k(r_2) = \frac{\Delta r_i + \Delta r_{i+1}}{r_i + \frac{\Delta r_i}{2}} \left[\frac{\Delta r_i}{k_i \left(r_i + \frac{\Delta r_i}{4} \right)} + \frac{\Delta r_{i+1}}{k_{i+1} \left(r_{i+1} - \frac{\Delta r_{i+1}}{4} \right)} \right]^{-1} \tag{D.24}$$

Note that between mesh zones $i-1$ and i, the parameter is called $k(r_1)$ and is defined with equation (D.24) by replacing i with $i-1$ and replacing $i+1$ with i.

The cylindrical problem is thus solved implicitly, using the same model described by equations (D.7) through (D.11), and using the parameters A_i, B_i, C_i, and D_i defined in equation (D.23) instead of those defined in equation (D.12).

References for Appendix D

[D.1] R.D. Richtmeyer, K.W. Morton, Difference Methods for Initial Value Problems, Interscience Publishers, a Division of John Wiley & Sons, New York.

[D.2] B. Carnahan, H.A. Luther, J.O. Wilkes, Applied Numerical Methods, John Wiley & Sons, New York.

[D.3] J.H. Lienhard, A Heat Transfer Textbook, Prentice-Hall, Inc., Englewood Cliffs, N.J., 1981.

E. Details and Inputs for Natural Convection Calculations

The model for the natural convection analysis is presented in Chapter 6. Incorporating natural convection into the heat transfer code THIOD involves the introduction of a number of new parameters. Most of these involve inputs to the code. The additional input parameters required for the natural convection analysis are discussed in Section E.3.

In Chapter 6, it is explained that the coolant flow rate ($\dot{m}$) is found by equating the buoyancy pressure rise with the total pressure drop around the flow loop. The pressure drop has three components. The first is the MHD pressure drop. The development of the MHD pressure drop, equation (6.6), is discussed in detail in the references for Chapter 6. The second pressure drop term is the mass temporal acceleration. This is also discussed in reference [E.1]. The final pressure drop term is the friction pressure drop. As is mentioned briefly in Chapter 6, treatment of the friction pressure drop is somewhat complicated. This treatment is discussed in Section E.1.

Once the flow rate is known, the next step is to determine the heat transfer coefficients h. The accepted method for determining h is with empirical correlations that relate the Nusselt number Nu to the coolant properties (represented by the Prandtl number Pr) and the flow characteristics (represented by the Reynold's number Re), as well as other dimensionless parameters. There is a number of different correlations that can be used, depending on the nature of the problem.

The calculation of h, once $\dot{m}$ is known, is discussed in Section E.2.

E.1 Calculation of Friction Pressure Drop ΔP_f

E.1.1 Equation for ΔP_f

In the development of the convection model presented in Chapter 6, the friction pressure drop is given in equation (6.4) as

$$\Delta P_f = \int_{x_1}^{x_2} 32 \frac{\mu}{\rho} \frac{\dot{m}_i}{A D_e^2} dz \tag{6.4}$$

which is reduced to equation (6.5),

$$\Delta P_f = K_{fric} \dot{m} \tag{6.5}$$

As is stated, this assumes that the flow is laminar. As it turns out, once the steady state flow rate is reached, the flow will be laminar in both the helium cooled and liquid metal cooled cases, although at higher wall loads, some of the liquid metal cases, in which the magnetic field is turned off, experience steady state flows which are in the transition region between laminar and turbulent flow. Before steady state is reached, however, the flows are turbulent. This warrants accounting for the friction pressure drop in turbulent flow. In turbulent flow, the expression corresponding to equation (6.5) is [E.2, E.3, E.4],

$$\Delta P_f = K_{fric}^{turb} \dot{m}^2 \tag{E.1}$$

The parameter K_{fric}^{turb} depends on the Reynold's number, as well as the flow channel geometry. According to the Fanning equation [E.2,E.3], the turbulent friction pressure drop is

$$\Delta P_f = 4f\frac{L}{D}\frac{\rho u^2}{2} \tag{E.2}$$

where f is the *friction factor*, and u is the flow velocity (m/s). Using the relation $\dot{m} = \rho A u$, equation (E.2) becomes

$$\Delta P_f = 4f\frac{L}{D}\frac{1}{2\rho A^2}\dot{m}^2 \tag{E.3}$$

Then, combining equations (E.1) and (E.3), it is seen that

$$K_{fric}^{turb} = 2f\frac{L}{D}\frac{1}{\rho A^2} \tag{E.4}$$

The factor f can be found with the Blasius equation (E.2),

$$f = 0.079Re^{-0.25} \tag{E.5}$$

substituting equation (E.5) into equation (E.4) and defining

$$C_f^{turb} = 2(0.079)\frac{L}{D}\frac{1}{\rho A^2} \tag{E.6}$$

then the turbulent friction constant becomes

$$K_{fric}^{turb} = C_f^{turb} Re^{-0.25} \tag{E.7}$$

which isn't really constant, since Re will change as the flow rate $\dot{m}$ changes. This is the form of K_{fric}^{turb} in equation (E.1) used in THIOD to calculate the friction pressure drop in turbulent flow. Determination of the value of C_f^{turb}, which is a constant, is given in the following section.

To simplify the code, it is desirable to use equation (E.1) to calculate the friction pressure drop in all flows. Comparing equations (E.1) and (6.5), it is seen that this can be done if, in laminar flow, the laminar friction constant K_{fric}^{lam} is made inversely proportional to the flow rate. Then equation (E.1) will have the same $\dot{m}$ dependence as equation (6.5). In fact, this is a common method of treatment [E.2, E.3]. This is typically accomplished by defining the friction factor f inversely proportional to Re. Then, in laminar flow, the friction pressure drop can be represented as

$$\Delta P_f = \frac{C_f^{lam}}{Re}\dot{m}^2 \tag{E.8}$$

where C_f^{lam} is a constant that corresponds to C_f^{turb} defined in equation (E.6). Equation (E.8) is the same as equation (E.1), except K_{fric}^{turb} is replaced by K_{fric}^{lam}, which is defined as

$$K_{fric}^{lam} = \frac{C_f^{lam}}{Re} \tag{E.9}$$

In THIOD, the friction pressure drop is calculated with the equation

$$\Delta P_f = K_f \dot{m}^2 \tag{E.10}$$

If the maximum Reynold's number is in the turbulent regime, which is generally considered to be $Re > 2100$, then K_f in equation (E.10) is set equal to K_{fric}^{turb}, as defined in equation (E.7). If the maximum Reynold's number is in the laminar regime ($Re < 2100$), then K_f is set equal to K_{fric}^{lam}, as defined in equation (E.9). The maximum Reynold's number is the Reynold's number in the flow channel which has the highest Reynold's number of all the flow channels.

E.1.2 Determination of Constants C_f^{turb} and C_f^{lam}

The values of the parameters C_f^{turb} and C_f^{lam} for all of the blankets considered in the convection analysis are given in Table E.1.1. The constant C_f^{turb} is given in equation (E.6), and is a function of the coolant density and the flow loop geometry, as is the constant C_f^{lam}. Technically, both C_f^{turb} and C_f^{lam} will be different for each flow channel in the flow loop. Determining these constants, as an average around the flow loop, can be very tricky, and at any rate would require detailed knowledge of the flow loop geometry. Given the current state of fusion reactor design, much of this detail is lacking. For this reason, and for simplicity, the constants C_f^{turb} and C_f^{lam} are found in a more heuristic manner.

E.1.2.1 Helium Cooled Blanket #2

The total pressure drop for the flow loop of Blanket #2 is given in the BCSS [E.5] (Tab. 8.10-24) as 162 kPa. Technically, this includes both friction and form loss pressure drops, but these are treated together in the manner described above. Also given in the BCSS are the first wall Reynold's number, which is 13226. This is the maximum Reynold's number for the flow loop.

The value of the operational flow rate $\dot{m}$ for the inboard blanket is given in Chapter 6 as 1.1 x 10^3 kg/s. There are 12 toroidal modules that form the total torus. Thus, the $\dot{m}$ for each module is $\frac{1.1 \times 10^3}{12}$, which is 91.67 kg/s. Inserting this value of $\dot{m}$, and the value of ΔP given above, into equation (E.1) yields a value of K_{fric}^{turb} of 19.3. This is then inserted into equation (E.7) along with the value of Re given above to obtain C_f^{turb}. This value turns out to be 206.7.

The value of C_f^{lam} is found by equating the pressure drop found with the turbulent formulation (equation (E.7)) and that found with the laminar formulation (equation (E.9)) at the transition Reynold's number of 2100. That is, at the transition, the pressure drop calculated should be the same regardless of whether the

Table E.1.1 C_f^{turb} and C_f^{lam} for Blankets Analyzed in Convection Analysis

Blanket #	Turbulent Fric. Const. C_f^{turb}	Laminar Fric. Const. C_f^{lam}
1	3.485e+04	1.123e+02
2	6.412e+04	2.067e+02
3	1.814e+03	5.848e+00
4	8.058e+03	2.598e+01

flow is considered laminar or turbulent. Since the $\dot{m}$ will be the same, and the pressure drop is the same, then K_{fric}^{turb} will equal K_{fric}^{lam}. Thus, combining equations (E.7) and (E.9) and solving for C_f^{lam} results in

$$C_f^{lam} = Re \times C_f^{turb} Re^{-0.25} \tag{E.11}$$

with Re equal to 2100. This yields a value of C_f^{lam} of 6.41e+04.

E.1.2.2 Liquid-Metal Cooled Blankets #1 and #4

Blankets #1 and #4, which are BCSS Tokamak designs cooled by liquid lithium and lithium-lead respectively, were analyzed by Malinovic and Kazimi [E.1, E.6]. In his analysis, which considered primarily the steady-state natural convection temperature rise, Malinovic determined the value of K_{fric} as it is given in equation (6.5), which assumes laminar flow. The laminar flow assumption is valid for the steady-state natural convection flow, especially when the magnetic field stays on. This value of K_{fric} was transformed into an equivalent C_f^{lam}. This was done by starting with equation (E.8), and substituting $\frac{\rho u D}{\mu}$ for Re and $\rho A u$ for $\dot{m}$ on the right hand side, and $K_{fric}\dot{m}$ on the left hand side. This results in

$$K_{fric}\dot{m} = C_f^{lam} \frac{\mu A}{D} \dot{m} \tag{E.12}$$

Canceling $\dot{m}$ from both sides, it is seen that C_f^{lam} can be found from the value of K_{fric} that was used by Malinovic. This value of K_{fric}, for a single first wall channel on the inboard side, is 0.488. The flow channel diameter D and area A for the first wall (where the flow rate is highest) are 3.21e-02 m and 1.125e-03 m^2 respectively. Inserting these into equation (E.12) yields a value of C_f^{lam} of 3.485e+04 for liquid lithium and 8.058e+03 for Li-Pb. The value of C_f^{turb} for each of these blankets is then found with equation (E.11). These values are 1.123e+02 and 2.598e+01 for

liquid lithium and lithium-lead respectively.

E.1.2.3 Liquid Lithium Cooled RFP Blanket #3

The friction constants for the RFP Blanket #3 are calculated in similar fashion to those of Blanket #2. In the design description of the RFP [E.7], the information on the coolant loop includes the operational friction pressure drop and the flow rate, as well as the Reynold's number. Following the method outlined in Section E.1.2.1, the pressure drop is given by equation (E.10). The pressure drop, flow rate, and Reynold's number given in reference [E.7] are 0.3 MPa, 1.24e+05 kg/s total, which corresponds to 1.033e+04 kg/s in each of the 12 segments, and 4.35e+05. It is assumed that in the toroidal direction, the flow channels in the blanket and manifold region of the RFP are 30 cm (0.3 m). This is the same thickness as in the radial direction for the blanket channels. Using the major and minor radii, and blanket thickness, it is calculated that each of the 12 segments is 2.7 m thick in the toroidal direction. Thus, there are nine blanket (and manifold) channels in each of the 12 segments. The friction pressure drop will be the same in each of the 12 segments, since they are connected in parrallel. The flow rate in each channel is $\frac{1.033e+04}{9}$, which is 1.148e+03 kg/s. Using equation (E.10) to obtain K_{fric}^{turb} given these values of $\dot{m}$ and ΔP_f, and then equation (E.7) to extract C_f^{turb}, yields a value for C_f^{turb} of 5.848. Using equation (E.11), the value of C_f^{lam} is 1.814e+03.

E.2 Calculation of Heat Transfer Coefficient h from $\dot{m}$

As was stated, the first part of the natural convection analysis involves the calculation of the flow rate $\dot{m}$. The parameter $\dot{m}$ appears directly in the heat transfer equations (6.32), and is important, since the flow rate determines the rate at which heat is transported out of the blanket via convection. However, before this can be calculated, the amount of heat being tranferred from the solid structure to

the flowing coolant must be calculated. This heat flux is given in equation (6.13). As is stated in Chapter 6, determination of the value of h, the heat transfer coefficient, is required.

The value of h is generally determined through the use of empirical correlations which relate the heat transfer characteristics of the flowing fluid to the fluid properties and flow characteristics. There are a large number of these correlations, and each is applicable to a specific type of problem. For the problem being considered here, there are essentially two approaches. Each is outlined in this section, with the corresponding correlation for h given. The results of the natural convection analysis using the two approaches is given, and a comparison is made.

E.2.1 Forced Convection Approach

The blanket module itself is only one small part of the overall flow loop. It is in the blanket that the heat is added to the fluid. After exiting the blanket, the coolant flows to the steam generator (or intermediate heat exchanger), where the heat is removed. The vertical center of heat extraction is L meters above the vertical center of heat addition (the center of the blanket), where L is the "thermal elevation difference". Typically, L is about 10 meters [E.1, E.6].

The model for calculating the flow rate $\dot{m}$ in the flow loop considers that heat is added at one point and extracted at another point, L meters above the point of heat addition. Because of buoyancy effects, this creates a pressure head in the coolant, which is balanced by the friction and MHD pressure drops, resulting in a natural convection flow rate. In the forced convection approach, it is assumed that this flow rate is, as far as the blanket itself is concerned, externally applied, and not directly dependent on the details of how the heat is added to the coolant within the blanket. For this reason, the empirical correlations used are those appropriate to forced convection problems.

E.2.1.1 Helium Cooled Blanket #2

For coolants with Prandtl numbers Pr on the order of one, which encompasses most non-liquid-metal coolants, the forced convection correlations used to find h are fairly simple. In fully developed laminar flow, as it turns out, the Nusselt number Nu is merely a constant. In the case of a constant heat flux from the wall to the coolant, which is the assumption used in the development of the model given in Chapter 6, this constant is 4.364 [E.8]. Thus, for laminar flow in the helium cooled Blanket #2, the heat transfer coefficients are found using $Nu = 4.364$.

In the case of turbulent flow, which applies during the transient time before steady-state is reached, the situation is slightly more complicated. One of the more common correlations used in this case is the Dittus-Boelter equation, which states

$$Nu = 0.023 Pr^{0.4} Re^{0.8} \tag{E.13}$$

This is the correlation is used in the helium cooled blanket for turbulent flow.

E.2.1.2 Liquid Metal Cooled Blankets

Convective heat transfer to liquid metals is different than for other coolants, primarily because heat transfer across the coolant channel is dominated by molecular conductivity, as opposed to momentum transfer [E.2, E.8]. The forced convection approach for liquid metal cooled blankets is the approach given in Chapter 6 in the development of the natural convection model.

E.2.2 Natural Convection Approach

The alternate approach to the problem is to say that the flow rate in the blanket is not externally applied, but is directly dependent on the details of how heat is

added to the coolant in the blanket. This is the essence of most natural convection problems. It is based on the fact that the flow rate of the coolant depends on the heat flux into the coolant, which depends on the heat transfer coefficient h, which in turn depends on the flow rate of the coolant. The "circularity"of this problem means that calculating h separately from $\dot{m}$ is impossible. This leads to a different set of empirical correlations which relate Nu to the flow characteristics. The correlations are considerable more complicated than those given in the forced convection approach.

In the natural convection approach, there are a number of new dimensionless parameters. Most importantly, there is the Grashof number Gr, which essentially relates the buoyancy force to the viscous force. The Grashof number is given as

$$Gr_L = \frac{g\beta\Delta T L^3}{\nu^2} \tag{E.14}$$

where

ν is the dynamic viscosity, i.e., $\frac{\mu}{\rho}$,

ΔT is the difference between the wall temperature T_w and the bulk fluid temperature T_b, and

L is the vertical length of the (heated) surface.

Typically, the Grashof number actually appears as a product with the Prandtl number. This product is called the Rayleigh number, and is given by

$$Ra_L = Gr_L Pr = \frac{g\beta\Delta T L^3}{\alpha\nu} \tag{E.15}$$

Churchill and Chu have presented a fairly extensive experimental data base, and have correlated the data. This correlation is valid over a full range of Prandtl numbers (i.e., for liquid metal and non-liquid metal coolants) as well as for both

turbulent and laminar flows. It is given as [E.8]

$$\overline{Nu}_L = 0.68 + 0.67 Ra_L^{1/4} \left[1 + \left(\frac{0.492}{Pr} \right)^{9/16} \right]^{-4/9} \quad \text{(E.16)}$$

where $\overline{Nu}_L$ refers to the average Nusselt number along the length of the heated surface L. This is the correlation used in the natural convection approach for all coolants in both laminar and turbulent flow.

E.2.3 Comparison of Forced vs. Natural Convection Approach

In both the forced and natural convection approaches, the calculation of the flow rate $\dot{m}$ is the same. Slight variations in the actual flow rates calculated can occur, due to the fact that, because of the different values of h, each model may calculate a different ΔT. This difference is expected to be small, however. The bulk of any difference between the models is expected to be in the better thermal coupling of the first wall to the heat sink in the model that calculates the higher h values.

The differences were examined by analyzing Blanket #1, Cases M1 and M2 (see Table 6.2.1), with each model. In Case M1, where the magnetic field stays on at its operational value, the flow rate $\dot{m}$ is very small. The impact that natural convection has in this case on the temperature response is minimal. Thus, it is expected that the difference between the forced and natural convection approaches will also be minimal. In case M2, where the magnetic field is turned off such that it decays exponentially by two orders of magnitude every 30 minutes, the flow rate is significant, and the impact of natural convection on the temperature response is substantial. Here, it is expected that any difference between the forced and natural convection models could be important.

The difference between the models can be seen by doing a sample calculation of Nu using each correlation. Except for during the very early stages of the transient,

the flow is laminar in all of the cases. In the forced convection approach outlined in Section 6.1, it is seen that at low values of Re, the value of $\overline{\psi}$ goes to zero. The Nusselt number, therefore, is simply equal to the constant 5.0 (see equation (6.18)). In the natural convection approach outlined in Section E.2.2 above, the Nusselt number remains a complicated function of Ra_L and Pr, even at low Re flows. Inserting the data for liquid lithium, it is found that Pr equals 0.039, while Ra_L is about 2.8e+07. Note that this Rayleigh number is found for a first wall channel length L of 3.02 m, and a ΔT of 0.01 °C. This value of ΔT was taken from the results of the calculation (remember, this ΔT represents the difference between the wall temperature and the fluid temperature, NOT the coolant temperature rise in the blanket). Inserting these values of Pr and Ra_L into equation (E.16) yields a value of $\overline{Nu}_L$ of 23.5, which is almost five times greater than the value of Nu predicted by the forced convection approach. Thus, the heat transfer coefficients h will be almost five times higher in the natural convection model.

Figure E.2.1 gives the maximum temperature in the first wall vs. wall load for Cases M1 and M2 for each model. Note that, as expected, the difference for Case M1 is practically non-existent. The difference for Case M2 is noticeable but small, with the natural convection model having the lower temperatures. This is as expected, considering the higher values of h predicted by the natural convection model. These differences are very small, and any error introduced from using the forced convection model, which is much simpler, can be ignored. The reason for these small differences, given the much larger Nusselt number calculated above, can be explained by the fact that higher h's lead to smaller ΔT's $(T_w - T_b)$. Thus, the heat flux from the wall to the coolant will not change very much between models. The actual rate of convective heat removal can be loosely represented as the product of the heat flux from wall to coolant times the flow rate $(\dot{m})$, since the heat must flow from the wall to the coolant, then be carried out of the blanket by the flowing coolant. Since the flow rate is very close to the same in either model, the rates of convective heat removal will be very close also, and thus the overall temperature

Figure E.2.1 Maximum First Wall Temperature vs. Wall Load for Blanket #1 using forced convection and natural convection approaches to calculate the heat transfer coefficient h in convection Cases M1 and M2

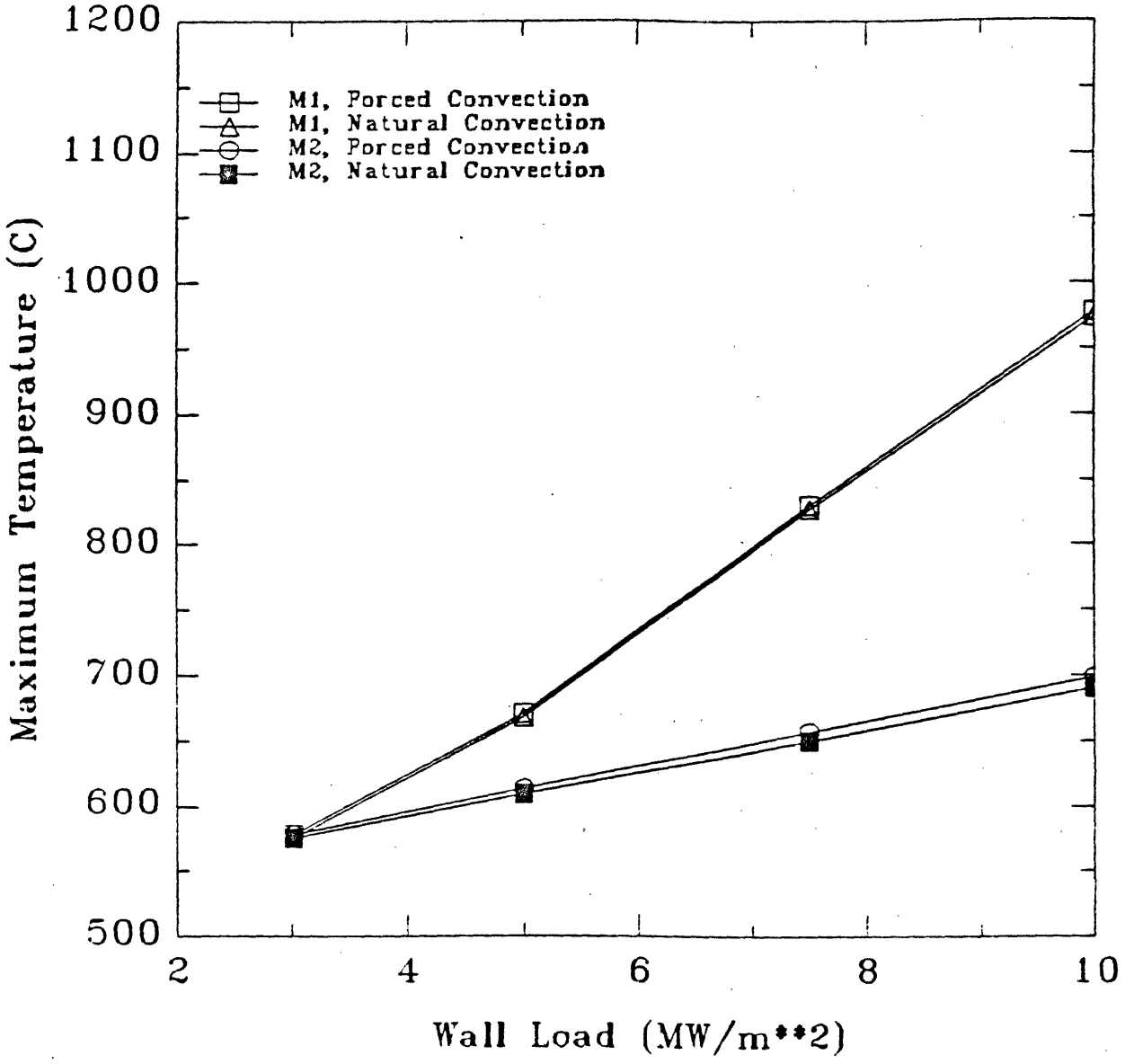

responses will be similar.

E.3 Inputs to Subroutine CONVECT

The model for the convection analysis presented in Chapter 6 and above in incorporated into the code THIOD primarily through the subroutine CONVECT. CONVECT calculates $\dot{m}$, then the h's for each channel, and returns these values to the main code. In order to perform these calculations, additional inputs are needed. The parameters that are needed are some properties of the coolant, and the geometry of the flow channels. The values used for the convection analysis for each of the blankets are discussed below.

E.3.1 Coolant Properties

In most convection analyses, the correlations dictate that coolant properties be evaluated at the mean of the wall temperature T_w and the coolant bulk temperature T_b. This can be important, since many of the coolant properties have a fairly strong dependence on temperature, especially for helium. Including a temperature dependence of the coolant properties, however, introduces a fair amount of complexity into the code. For the sake of simplicity, then, all coolant properties are constant with temperature, and the values used are those that correspond to the temperature which is expected to be in the range of interest.

Using constant coolant properties will introduce some error into the analysis. In particular, in the case of helium, the coolant expansion coefficient β is inversely proportional to temperature, while the density ρ is linearly dependent on temperature. Fortunately, these two parameters often appear in the equations as a product, thus canceling the temperature dependence. However, in the instances when either one or the other appears independently, assuming a constant value can introduce an error of as much as 20%, given the likely range of temperatures. It should be noted

that the natural convection analysis, especially in the case of the helium cooled blankets, is not meant to give accurate results on the temperature response, but is more meant to give an indication of the impact that natural convection can have on the temperature responses presented in Chapter 5. In the helium cases, this impact turns out to be small (as expected), thus a 20% error can be safely ignored.

In the liquid metal cooled cases, especially those in which the magnetic field is turned off, natural convection has a large impact on the temperature response. In these cases, it is much more important to use accurate coolant property data. Fortunately, the properties of lithium and lithium-lead are not as sensitive to temperature as those of helium. It is unlikely, then, that using constant values will introduce error of more than 10%. Given the other uncertainties and approximations that appear in the convection analysis (e.g., regarding the flow loop geometry, for which there is little detailed design information), this is not especially serious.

All of the properties relevant to the convection analysis, for each of the three coolants, are given in Table E.3.1, along with the temperatures at which they are given. Note that the values used are for temperatures which are intended to be in the middle of the range experienced by the coolant during the transient.

E.3.2 Flow Channel Geometry

The geometry of the flow loop for each of the blankets considered in the convection analysis (Blankets #1, #2, #3, and #4) was taken from the various references which describe the blankets. The bulk of the parameters were taken from the information given in Chapter 2. The parameters that need to be defined are, from equations (6.11) and (6.12),

T_{inlet}, the temperature of the coolant when it enters the blanket,

L, the thermal elevation difference (m),

Table E.3.1 Coolant Properties Relevant to Convection Analysis

Coolant	Temperature (°C)	ρ (kg/m^3)	β (1/°C)	μ (kg/m-s)	k (W/m-°C)	c_p (J/kg-°C)
Lithium	400	5.00e+02	1.94e-04	4.00e-04	4.96e+01	4.20e+03
Lithium-Lead $Li_{17}Pb_{83}$	400	9.35e+03	6.80e-04	1.73e-03	1.70e+01	1.60e+02
Helium	700	2.80e+00	1.00e-03	4.00e-05	3.22e-01	5.20e+03

A, the effective flow channel area (m^2),

t, the effective flow channel wall thickness (m),

l, the total flow channel length (m),

α, the "half-thickness"of the flow channel (m), and

l, the effective ratio of flow-channel-length to flow-channel-area, as defined in equations (6.7) and (6.8).

The values used for these parameters for each of the blankets are given in Table E.3.2. The T_{inlet} values for Blankets #1, #2, and #3 were taken from the references which describe the blankets. The T_{inlet} for Blanket #4 was taken as 50 °C less than that for Blanket #1, since the operating temperature of Blanket #4 is 50 °C less than Blanket #1 (see Chapter 2 and Appendix C). This means the temperature difference between the first and T_{inlet} during operation is the same for each blanket, thus the results will not be biased by the initial conditions. Each of the above g geometry parameters represents an effective average for the entire flow loop. This average value is used in equation (6.11) to calculate $\dot{m}$ for the entire flow loop.

Once the flow loop $\dot{m}$ is known, the flow rate (kg/s) and flow velocity (m/s) for each individual *flow channel* must be found. As was stated, in the blanket itself, the flow path of the coolant consists of a number of different flow channels connected in series. These channels, in general, have different dimensions, and thus will have different flow rates. It is the channel flow rate $\dot{m}_j$ and channel flow velocity v_j that are used in equations (6.14) - (6.17) to find the channel heat transfer coefficient h_j. Furthermore, it is the channel flow rate $\dot{m}_j$ that is used in equation (6.30) to calculate the nodal temperature T_i, where node i is in channel j. The channel flow rate $\dot{m}_j$ differs from the total loop flow rate $\dot{m}$ because a particular flow channel j may actually consist of a number of identical channels which are in parrallel. That is, the inlet manifold may consist of a single channel (or pipe). Once the flow enters the blanket, it splits into a number of identical, parrallel channels. Thus, if there

Table E.3.2 T_{inlet} and Flow Geometry Parameters for Each Blanket Analyzed in Convection Analysis

blanket #	T_{inlet} °C	L (m)	A (m^2)	t (m)	l (m)	α (m)	I (m^{-1})
1	300	10.0	0.24	0.002	25.0	0.30	7.643e+04
2	275	10.0	*	*	*	*	7.643e+04
3	300	10.0	0.54	0.005	25.0	0.22	7.643e+04
4	250	10.0	0.24	0.002	25.0	0.30	7.643e+04

* These parameters are relevant only to MHD pressure drop term, and thus are not relevant in the helium-cooled blanket #2.

are N of these parrallel channels, the flow rate in each of them, $\dot{m}_j$, will be $\frac{1}{N}$ times the total loop flow rate $\dot{m}$. This flow channel flow rate $\dot{m}_j$ is used in conjunction with the flow channel diameter D_{e_j} and area A_j to get the flow channel velocity v_j, Reynold's number Re_j, and heat transfer coefficient h_j.

This requires, for each flow channel, the following parameters:

F^j_{split}, the number of parrallel channels that compose flow channel j,

D_{e_j}, the hydraulic diameter of each individual channel, and

A_j, the flow area of each individual channel.

The values used for the flow channels in each blanket are given in Table E.3.3.

As was stated in Section 6.1, each flow channel corresponds to one region of the blanket. However, these regions consist of both flowing coolant and solid structure. Thus, heat transfer between adjacent regions will consist of both convection to the flowing coolant (represented with h_j) and conduction to the solid structure (represented with Δk_i). These heat transfer parameters must be multiplied by the appropriate material fractions to obtain the true effective values. To illustrate this point, consider the following example.

Assume node i is in the first region (first wall) of Blanket #1, as is displayed in Figure 2.1.2. Note from Figure 2.1.2 that this region consists of 100% VCrTi structure. Assume node $i+1$ is in region 2, which consists of 88.9% lithium coolant and 11.1% VCrTi structure (see Figure 2.1.2). Thus heat transfer from node i to node $i+1$ will consist of *convection* from the VCrTi of node i to the lithium of node $i+1$, and *conduction* from the VCrTi of node i to the VCrTi of node $i+1$. Recall that in the code THIOD, each region is homogenized according to material fraction. Thus, to properly represent the heat transfer from node i to node $i+1$, the heat transfer coefficient h_i (which represents convective heat transfer from i to $i+1$) must be multiplied by the appropriate lithium coolant fraction, in this case

Table E.3.3 Geometric Parameters of Individual Flow Channels for Each Blanket Analyzed in Convection Analysis

blanket #	channel	region	D_e, (m)	A_j (m^2)	F^j_{split}
1	1	Manifold	0.474	0.225	8
	2	Blanket	0.474	0.225	8
	3	First Wall	0.032	1.13e-03	332
	1	Manifold	0.030	0.175	120
	2	Blanket Segment 2	0.020	0.116	330
	3	Blanket Segment 1	0.020	0.116	330
	4	Flow Splitter	0.121	0.699	30
	5	First Wall	3.15e-03	0.018	30
3	1	Manifold	0.360	0.135	9
	2	Blanket	0.300	0.090	9
	3	First Wall	8.00e-03	5.03e-05	270
4	1	Manifold	0.474	0.225	8
	2	Blanket	0.474	0.225	8
	3	First Wall	0.032	1.13e-03	332

0.889. And, in turn, the conduction parameter Δk_i, which should only represent conduction from structure to structure (since heat transfer from structure to coolant is accounted for with h_i), must be multiplied by the appropriate structure fraction, in this case 0.111.

References for Appendix E

[E.1] B. Malinovic, Natural Convection Characteristics of Liquid Metal Cooled Fusion Reactors, S.M. Thesis, Nuclear Engineering Department, Massachusetts Institute of Technology, 1986.

[E.2] S. Glasstone and A. Sesonske, Nuclear Reactor Engineering, 3rd Edition, p. 376, Van Nostrand Reinhold Company, New York, 1981.

[E.3] N.E. Todreas and M.S. Kazimi, Nuclear Reactor Thermal Analysis, Hemisphere, to be published 1988.

[E.4] Frank M. White, Fluid Mechanics, McGraw-Hill Book Company, New York, 1979.

[E.5] D.L. Smith et al., Blanket Comparison and Selection Study (BCSS) - Final Report, Argonne National Laboratory, ANL-84-1, September 1984.

[E.6] B. Malinovic and M. Kazimi, Passive Decay Heat Removal in Liquid-Metal Cooled Reactors, Fusion Technology 10, (3), pp. 1205-1210, November 1986.

[E.7] R.L. Miller, et. al., Advanced Tokamak Reactors Based on the Spherical Torus (ATR/ST), Los Alamos National Laboratory, LA-10740-MS, June 1986.

[E.8] John H. Lienhard, A Heat Transfer Textbook, Prentice-Hall, Inc., Englewood Cliffs, New Jersey, 1981.

F. Code Listing

F.1 Listing of THIOD

```
c       PROGRAM THIOD
c
        dimension npts(50),xzn(50),xmesh(50),dxzn(50),x(50,0:500),
       1xr(0:500),dx(0:500),tims(0:500),ptk(0:500),
       2tplt(50,0:500),iprd(0:500),aimp(0:500),bimp(0:500),cimp(0:500),
       3dimp(0:500),eimp(0:500),fimp(0:500)
        dimension tk1(50),tk2(50),rcp1(50),rcp2(50),ep(0:500),ptk1(0:500),
       1prcp1(0:500),prcp2(0:500),irad(0:500,2),
       2ptk2(0:500)
        dimension tl(50,50),xmu(50,50),a(50,50),ptl(0:500,50),uop(50),
       1pxmu(0:500,50),pa(0:500,50),nmiso(50),npniso(0:500),
       2st(0:500),puop(0:500),
       3timpl(50),tmtim(10,50),iplt(10),kk(0:500),aop(50),
       4paop(0:500),t5(0:500)
        dimension ax(50),rmax(10),sub(5,10),rk1(5),rk2(5),tmax(10)
        double precision t(0:500),dtk(0:500),mdot,pmdot(0:500),fact,
       1prcp(0:500),dt,ph(0:500),pkextra(0:500),mdss,mdcomp
```

```
      real chlen,charea,rho,cp,deltt,dlt2,dtrtio,alhs,blhs,blam,
     1bchk,pflfrac(0:500),flfrac(50)
      integer stpt(50),enpt(50),parrd
      character*15 namet
      logical wallf,conf
      real econc(100),rha,rhb,tha,thb,fac,ptin(0:500)
      character*2 ename(100),rname
      character*8 titlet(8)
c
c open input and output files
c
      call link("unit1=(max,text,create),unit2=option,unit3=qtrpr,
     1unit4=geom,unit5=params,unit6=(rdout,text,create),
     2unit8=(tptimout,text,create),unit9=(tmpout,text,create),
     6unit10=(mdotout,text,create),
     3unit11=cntl,unit12=matlib,unit13=(elconc,text,create),
     6unit7=(heatmsgs,text,create),
     4print1,read2,read3,read4,read5,print6,print7,print8,print9,
     5print10,read11,read12,print13//")
c
c set option variables
c
      wallf=.false.
      conf=.false.
      rname=' '
c ***The following lines entered by jps*****************
c
c read title and options
c
      read(2,'(8a8)') (titlet(i),i=1,8)
```

```
      write(1,104)(titlet(i),i=1,8)
      write(6,104)(titlet(i),i=1,8)
      write(8,104)(titlet(i),i=1,8)
      write(9,104)(titlet(i),i=1,8)
      write(10,104)(titlet(i),i=1,8)
      write(7,104)(titlet(i),i=1,8)
104   format(8a8,/)
      read(2,'(a15)')namet
      write(7,106) namet
106   format(" option = ",a15)
      if(namet.eq.'wall load')then
      wallf=.true.
      read(2,'(i3)')numtri
      read(2,'(e10.3)') (ax(i),i=1,numtri)
      goto 2
      end if
      if(namet.eq.'conductivity')then
      conf=.true.
      read(2,'(a10)')rname
      read(2,'(i3)')numtri
      read(2,'(f7.4)') (ax(i),i=1,numtri)
      goto 2
      end if
      numtri=1
c
c begin option loop
c
2     do 999 izq=1,numtri
c
c set all variables to zero
```

```
c
      do 19 i=1,10
19    rmax(i)=0
      eimp(0)=1.0
      fimp(0)=0.0
      dpsm=0.0
      mdot=0.0
      parrd=0
      theat=0.0
      qtot=0.0
      trad=0.0
      sgend=0.0
      rewind 3
      rewind 4
      rewind 5
      rewind 13
      rewind 11
c **************************
c
c *** read geometry indices from file GEOM ***
c
c **************************
c
      sig=5.67e-08
      dlt2=10.
      alhs=1.0
      blhs=100.0
      read(4,10) nmzone
      read(4,10) (npts(i),i=1,nmzone)
10    format(i3)
```

```
      read(4,20) (xzn(i),i=1,nmzone+1)
20    format(e10.3)
c
c *** done reading geometry indices ***
c *** now calculate geometric mesh parametes ***
c
      ntots=0
      do 30 i=1,nmzone
      ntots=ntots+npts(i)
      dxzn(i)=xzn(i+1)-xzn(i)
      xmesh(i)=dxzn(i)/npts(i)
      x(i,1)=xzn(i)+xmesh(i)/2.
      do 30 j=2,npts(i)
      x(i,j)=x(i,j-1)+xmesh(i)
30    continue
c
c *** done calculating geometric mesh params. ***
c
c *** now read time values ***
c *** these are the start time, end time and time step ***
c
      read(4,35) start,time,dt
35    format(2f9.1,f7.4)
c *** and times at which the temp. dist. will be printed and plotted ***
      read(4,10) nsols
      read(4,45) (tims(i),i=1,nsols)
45    format(f9.1)
c
c *** done reading time values ***
c
```

```
c *** now read initial conditions ***
c
        read(4,55) (t(i),i=1,ntots+1)
55      format(f7.1)
c
c *** done reading initial conditions ***
c *** now read plot points ***
c
        read(4,10) nplots
        read(4,10) (iplt(i),i=1,nplots)
c
c**********************************
c
c *** now read material properties by zone from file PARAMS ***
c *** first conductivity, then (rho x Cp) - both k and rcp are ***
c *** linear functions of temp. ie, A*T + B. Read A,B ***
c *** read one additional conductivity for Boundary Condition ***
c
c**********************************
c
        if(conf)fac=ax(izq)
c
        write(7,108)
108     format("zone",1x,"      tha     ",2x,"      thb     ",6x,
       1"       rha     ",2x,"      rhb     ",/)
        do 98 j=1,nmzone
        write(13,'(/,i3)')j
c
c now find k and (rho x Cp) for each zone - subroutine ISOTOPE
c
```

```
            call isotope(emax,ename,econc,rha,rhb,tha,thb,fac,rname)
            tk1(j)=tha
            tk2(j)=thb
            if(rha.eq.0.and.rhb.eq.0)rhb=1.0
            rcp1(j)=rha
            rcp2(j)=rhb
98          write(7,107) j,tha,thb,rha,rhb
107         format(i3,2x,e10.3,2x,e10.3,6x,e10.3,2x,e10.3)
            read(5,48)tk1(nmzone+1),tk2(nmzone+1)
48          format(2e10.3)
40          format(e10.3)
c *** read emissivity mesh points that radiate ***
c *** read number of pairs of radiating mesh points, and the pairs ***
            read(5,10) nmrads
            do 42 i=1,nmrads
            read(5,10) iprd(i)
            read(5,40) ep(iprd(i))
            read(5,46) irad(i,1),irad(i,2)
46          format(2i4)
42          continue
            ep(0)=0.0
c
c *** done reading mat. props.
c
c **********************************
c
c *** now read q-triple-prime info from file QTRPR ***
c *** first read number of isotopes in each zone ***
c *** then lambda, mu, and coefficient A for each isotope ***
c
```

```
c**********************************
c
      do 50 i=1,nmzone
      read(3,10) nmiso(i)
      read(3,41) aop(i)
      read(3,41) uop(i)
      aop(i)=aop(i)*1.0e+06
      if(nmiso(i).eq.0) go to 50
      read(3,41) (tl(i,j),j=1,nmiso(i))
      read(3,41) (xmu(i,j),j=1,nmiso(i))
      read(3,41) (a(i,j),j=1,nmiso(i))
      do 51 j=1,nmiso(i)
      a(i,j)=a(i,j)*1.0e+06
51    continue
50    continue
      read(3,48) a1,anorm
      read(3,10) ikk
      kk(ikk)=1
      read(3,41) adp1
      read(3,45) ht1
      read(3,45) ht2
41    format(e11.4)
c
c *** done reading q-triple-prime info ***
c
c *** now calculate mat. props. and qtrpr by fine mesh point ***
c *** assign mesh point values to corresponding zone values ***
c
      mm=0
      do 60 i=1,nmzone
```

```
      do 60 j=1,npts(i)
      mm=mm+1
      xr(mm)=x(i,j)
      dx(mm)=xmesh(i)
      ptk1(mm)=tk1(i)
      ptk2(mm)=tk2(i)
      prcp1(mm)=rcp1(i)
      prcp2(mm)=rcp2(i)
      paop(mm)=aop(i)
      puop(mm)=uop(i)
      do 70 l=1,nmiso(i)
      ptl(mm,l)=tl(i,l)
      pxmu(mm,l)=xmu(i,l)
      pa(mm,l)=a(i,l)
70    continue
      npniso(mm)=nmiso(i)
60    continue
      ptk1(mm+1)=tk1(nmzone+1)
      ptk2(mm+1)=tk2(nmzone+1)
      xr(ntots+1)=xzn(nmzone+1)
      if(mm.eq.ntots) go to 80
      write(6,90) mm,ntots
90    format(' mm=',i4,' ntots= ',i4)
      stop
c
c *** done calculating fine mesh data ***
c
c
c *** now start thermal calculation ****
c
```

```
c *** set time to inputted start value - fix initial conditions ***
c
80      xt=start
        do 191 i=1,ntots
        st(i)=t(i)
191     continue
        sdt=dt
        nt=1
c
        if(wallf)then
        a1=ax(izq)
        write(1,101)(a1*5)
        write(6,101)(a1*5)
        write(8,101)(a1*5)
        write(10,101)(a1*5)
        write(9,101)(a1*5)
101     format(/,' wall load =',e11.4,' MW/m2')
        goto 110
        end if
        if(conf)then
        write(1,102)rname,ax(izq)
        write(6,102)rname,ax(izq)
        write(8,102)rname,ax(izq)
        write(10,102)rname,ax(izq)
        write(9,102)rname,ax(izq)
102     format(/,' conductivity factor for ',a10,' is ',f7.4)
        goto 110
        end if

        write(1,103)
```

```
          write(6,103)
          write(8,103)
          write(10,103)
          write(9,103)
103       format(/,' Hey Man ! Nothing, like nothing varies...')
c
c
110       jr=0
          do 129 i=1,ntots
          t5(i)=t(i)
129       continue
          thet5=theat
          qtot5=qtot
          trad5=trad
          diff=abs(xt-tims(nt))
c
c *** if time is at an 'answer' time, print and plot temp. dist. ***
c *** and other output information
c
c *** The following lines inserted by John snyder at 17:13 hrs., 1 Jun '86 ***
          do 99 i=1,nplots
          if(t(iplt(i)).le.rmax(i))goto 99
          rmax(i)=t(iplt(i))
          tmax(i)=xt
99        continue
c ************************************************
c           write(*,181)xt
181       format(/,' time= ',f12.3)
          if(diff.gt.dt/2..and.sgend.ne.1.0) go to 140
          write(6,180) xt
```

```
      write(9,180) xt
180   format(//,' time= ',f9.1)
      write(9,172) ntots
172   format(' ntots= ',i4)
      do 160 i=1,ntots
      write(6,170) i,t(i)
170   format(' t(',i3,')= ',f16.11)
      write(9,171) xr(i),(t(i)-273.)
171   format(f10.5,f10.3)
160   continue
      write(6,192) qtot,theat,trad
      write(6,292) remax,mdot,dt,dpsm
      write(10,173) xt/3600.,mdot
173   format(f10.5,f10.4)
      do 294 i=1,nchns
      j1=stpt(i)
      j2=enpt(i)
      write(6,293) j1-1,ph(j1-1),j1-1,dtk(j1-1),j1,ph(j1),
     1j1,dtk(j1),j1,prcp(j1)
      write(6,293) j2,ph(j2),j2,dtk(j2),j2+1,ph(j2+1),
     1j2+1,dtk(j2+1),j2,prcp(j2)
293   format(' ph(',i3,')= ',e11.4,' dtk(',i3,')= ',e11.4,/,
     1'ph(',i3,')= ',e11.4,' dtk(',i3,')= ',e11.4,
     2' prcp(',i3,')= ',e11.4)
294   continue
292   format(' remax = ',e12.5,' mdot = ',e12.5,/,' dt = ',
     1e12.5,' dpsm= ',e12.5)
192   format(' qtot= ',e12.5,' theat= ',e12.5,' trad= ',e12.5)
      timpl(nt)=xt
      do 162 iptm=1,nplots
```

```
            tmtim(iptm,nt)=t(iplt(iptm))
162         continue
            nt=nt+1
            tnt=nt
            tnt=tnt/2.
            if(tnt.ne.int(tnt).and.sgend.ne.1.0) go to 140
            ngt=ngt+1
            do 165 i=1,ntots+1
            tplt(ngt,i)=t(i)
165         continue
            if(sgend.eq.1.0) go to 215
c
c *** done printing and plotting temps. ***
c
c *** add time step increment to time - proceed with calculation ***
c
140         xt=xt+dt
            if(xt.gt.time) sgend=1.0
126         do 131 i=1,ntots
            t(i)=t5(i)
131         continue
            qtot=qtot5
            theat=thet5
            trad=trad5
            dpsm=0.0
            jr=0
            dtx=0.0
c
c *** start spatial loop ***
c
```

```
c *** first call CONVECT to get kextra, h, and mdot
c
c *** now we want to calculate the convection-related terms,
c *** that is, mdot, ph(i-1), and ph(i) - we'll use the same
c *** values as last time unless the temperatures have changed
c *** or if we're still in the 'transient'                    ***
c
c          if(mdot has changed) call subroutine
c if mdot is still not near steady state value, we must
c call convect even if deltt has not changed.
c
          do 49 i=nchns,1,-1
          do 59 j=stpt(i),enpt(i)
          pflfrac(j)=flfrac(i)
          if(i.eq.nchns) then
          ptin(j)=tinlet
          go to 59
          endif
          jtmp=stpt(i+1)
          ptin(j)=t(jtmp)
59        continue
49        continue
          bchk=exp(-blam*xt)
          if(blam.eq.0.0.or.bchk.lt.0.0005) then
          mdss=alhs/(2.*blhs)
          mdcomp=abs(mdot-mdss)/mdss
          if(mdcomp.lt.0.05) then
          do 69 i=1,nchns
          do 79 j=stpt(i),enpt(i)
          if(dlt2.lt.t(j)) dlt2=t(j)
```

```
79      continue
69      continue
        dlt2=dlt2-tinlet
        dtrtio=abs(deltt/dlt2 - 1.)
        if(dtrtio.lt.0.01) go to 89
        end if
        end if
c
        pkextra(0)=0.0
        ph(0)=0.0
        pmdot(0)=0.0
        call convect(t,dt,xt,ntots,tinlet,charea,chlen,rho,cp,mdot,
       1pmdot,ph,pkextra,nchns,stpt,enpt,deltt,tcsig,alhs,blhs,
       2blam,flfrac,parrd,a1,remax)
c
c *** if time step was too large for CONVECT, reduce it
c
        if(tcsig.eq.2.5) go to 121
c
c *** calculate temp.-dependent conductivity ***
c
89      do 120 i=1,ntots
        ptk(i-1)=ptk1(i-1)*t(i-1)+ptk2(i-1)+pkextra(i-1)
        ptk(i)=ptk1(i)*t(i)+ptk2(i)+pkextra(i)
        ptk(i+1)=ptk1(i+1)*t(i+1)+ptk2(i+1)+pkextra(i+1)
c
c *** calculate conductivity term dk at zone interface ***
c
        dtk(i-1)=0.0
        asgn1=ptk(i-1)*ptk(i)
```

```
          if(asgn1.eq.0.) go to 201
          dtk(i-1)=(dx(i-1)+dx(i))/((dx(i-1)/ptk(i-1))+(dx(i)/ptk(i)))
          if(ph(i-1).ne.0.0) dtk(i-1)=dtk(i-1)*
         1(1.-(max(pflfrac(i),pflfrac(i-1))))
201       dtk(i)=0.0
          asgn=ptk(i)*ptk(i+1)
          if(asgn.eq.0.) go to 100
          dtk(i)=(dx(i)+dx(i+1))/((dx(i)/ptk(i))+(dx(i+1)/ptk(i+1)))
          if(ph(i).ne.0.0) dtk(i)=dtk(i)*
         1(1.-(max(pflfrac(i+1),pflfrac(i))))
c           write(6,710) i,dtk(i)
710       format(' dtk(',i3,')= ',e12.5)
c
c *** set conductivity boundary condition ***
c
100       if(asgn1.eq.0.) ph(i-1)=0.0
          if(asgn.eq.0.) ph(i)=0.0
          if(ptk(ntots+1).eq.0.0) go to 145
          dtk(ntots)=ptk(ntots+1)*(xr(ntots+1)-xr(ntots))
c           write(6,710) ntots,dtk(ntots)
c
c *** calculate temp.-dependent rho x Cp ***
145       prcp(i)=prcp1(i)*t(i)+prcp2(i)
c
c
c
c *** integrate qtriple-prime over dx and dt ***
c
231       q=0.0
          x1=xr(i)-dx(i)/2.
```

```
      x2=xr(i)+dx(i)/2.
      t1=xt
      t2=xt+dt
      do 130 l=1,npniso(i)
      coeff=pa(i,l)/(pxmu(i,l)*ptl(i,l))
      xpart=exp(-pxmu(i,l)*x2)-exp(-pxmu(i,l)*x1)
      tpart=exp(-ptl(i,l)*t2)-exp(-ptl(i,l)*t1)
      q=q+(coeff*xpart*tpart)
130   continue
c
c *** add operating heat - q" to pt. 1 and q"'(op) to whole blkt ***
c
      fht=1.-((xt-ht1)/(ht2-ht1))
      fht=min(fht,1.0)
      fht=max(fht,0.0)
      qop=(paop(i)/puop(i))*(exp(-puop(i)*x1)-exp(-puop(i)*x2))
      q=((adp1*kk(i)+qop)*dt*fht)+q
      q=q*a1/anorm
      qtot=qtot+q
c       write(6,600) i,t(i-1),t(i),t(i+1)
c600 format(' i=',i3,' t(i-1)=',e12.5,' t(i)=',e12.5,'t(i+1)=',e12.5)
c
c *** calculate qtrpr
c
      qpart=q/(prcp(i)*dx(i))
      c1p=dtk(i-1)/(prcp(i)*dx(i))
      c1p=c1p*(t(i-1)-t(i))/(xr(i)-xr(i-1))
      c2p=dtk(i)/(prcp(i)*dx(i))
      c2p=c2p*(t(i)-t(i+1))/(xr(i+1)-xr(i))
c
```

```
c *** now see if point i radiates - if not, calc. new a,b,c,d,e,f ***
c
      if(ep(i).ne.0.) go to 135
      r1p=0.0
      r2p=0.0
      go to 125
c
c *** if point i radiates, calculate temp. rise due to radiation ***
c
135   jr=jr+1
c       write(6,600) i,t(i-1),t(i),t(i+1)
      if(ep(irad(jr,1)).eq.0.) then
      epr1=0.
      go to 136
      end if
      epp1=(1./ep(irad(jr,1)))+(1./ep(i))-1.
      epr1=(1./epp1)
136   if(ep(irad(jr,2)).eq.0.) then
      epr2=0.
      go to 137
      end if
      epp2=(1./ep(irad(jr,2)))+(1./ep(i))-1.
      epr2=(1./epp2)
137   r1p=sig*epr1/(prcp(i)*dx(i))
      r1p=r1p*(t(irad(jr,1))**4.-t(i)**4.)
      r2p=sig*epr2/(prcp(i)*dx(i))
      r2p=r2p*(t(i)**4.-t(irad(jr,2))**4.)
c
c *** found radiation temp change ***
c
```

```
c *** find aimp(i),bimp(i),cimp(i), and dimp(i)
c
125     aimp(i)=dt/(dx(i)*prcp(i))*(dtk(i)/(xr(i+1)-xr(i))+ph(i))
        ovrf1=(pmdot(i)*cp*dx(i))/(charea*chlen)+
       1(dtk(i-1)/(xr(i)-xr(i-1)))+(dtk(i)/(xr(i+1)-xr(i)))+ph(i-1)+ph(i)
        bimp(i)=(dt/(prcp(i)*dx(i)))*ovrf1 + 1.
        cimp(i)=dt/(dx(i)*prcp(i))*(dtk(i-1)/(xr(i)-xr(i-1))+ph(i-1))
        dimp(i)=t(i)+(pmdot(i)*cp*ptin(i)*dt/(charea*chlen*prcp(i)))+
       1qpart + (dt*(r1p-r2p))
c
c *** find eimp(i),fimp(i) from a,b,c,d and previous values ***
c
        eimp(i)=aimp(i)/(bimp(i)-(cimp(i)*eimp(i-1)))
        fimp(i)= (dimp(i)+(cimp(i)*fimp(i-1)))/
       1(bimp(i)-(cimp(i)*eimp(i-1)))
c
c *** now end first i loop.
c
120     continue
c
c     *** now calculate t(ntots) ***
        dimp(ntots)=dimp(ntots)+aimp(ntots)*t(ntots+1)
c
        atmn=t(ntots)
        t(ntots)=(dimp(ntots)+(cimp(ntots)*fimp(ntots-1)))
       1/(bimp(ntots)-(cimp(ntots)*eimp(ntots-1)))
        theat=theat+(t(ntots)-atmn)*prcp(ntots)*dx(ntots)
        trad=trad+(dt*(r2p+c2p)*dx(ntots)*prcp(ntots))
c
c     *** start next i loop from i=ntots, find t(i) from t(i+1) and
```

```
c     *** a,b,c,d,e,f     ***
c
          do 220 i=ntots-1,1,-1
          atime=t(i)
          t(i)=(eimp(i)*t(i+1)) + fimp(i)
          tgain=(t(i)-atime)*prcp(i)*dx(i)
          theat=theat+tgain
c
c *** check time step ***
c *** if temp change is too fast, reduce time step, go back and
c *** repeat. If temp change is very slow, increase time step.
c *** otherwise, continue as is ***
c
          btim=abs(atime-t(i))
          if(btim.lt.4.) go to 122
          tcsig=2.5
122       if(tcsig.gt.2.) go to 121
          if(tcsig.eq.2.) go to 220
          dps=btim/dt
          if(dps.gt.0.05) tcsig=1.
          if(dps.gt.0.5) tcsig=2.
          if(dpsm.lt.dps) dpsm=dps
c
220       continue
c
121       dtinc=3.-tcsig
          tcsig=0.
          if(dtinc.ge.1.) go to 128
          dt=dt*dtinc
          write(6,124) btim,i,xt,dt
```

```
124     format(" btmax=",e11.4,"at i=",i3,
       1"at time= ",f12.4,", decrease dt to ",e11.4)
        xt=xt-(dt/dtinc)+dt
        if(dt.lt.1.0e-06) sgend=1.0
        go to 126
128     dt=dt*dtinc
        if(dt.gt.100.) dt=100.
c
c *** end of time step - return, add dt to time, and continue ***
c *** on to next time step ***
        go to 110
c
c *** calculation is complete - print the results ***
c
c 215 call tmpplt(tplt,xr,ntots,ngt,xzn,nmzone)
215     write(6,735) dt
735     format(' at end, dt= ',e11.4)
c         call timplt(timpl,tmtim,nt,nplots,iplt)
        write(8,755) nt
        write(10,755) nt
755     format(' nt= ',i3)
        do 740 n=1,nplots
        write(8,747) iplt(n)
747     format(//,' i= ',i4)
        do 743 m=1,nt
        if(n.eq.1) timpl(m)=timpl(m)/3600.
        tmtim(n,m)=tmtim(n,m)-273.
        write(8,171) timpl(m),tmtim(n,m)
743     continue
740     continue
```

```
c *** The following lines inserted by John Snyder at 17:21 Hrs. , 1 Jun 86
      write(1,801)time
801   format(' mesh # max temp after',
     1 f9.1,' sec',' time of max (sec)')
      do 810 i=1,nplots
810   write(1,802)iplt(i),(rmax(i)-273.),tmax(i)
802   format(i5,f21.1,f20.1)
999   continue
c ***********************************************
      stop
      end
```

```
c       Subroutine CONVECT
c           subroutine convect(t,dt,xt,ntots,tinlet,charea,chlen,rho,cp,
      1mdot,pmdot,ph,pkextra,nchns,stpt,enpt,deltt,tcsig,
      2alhs,blhs,blam,flfrac,parrd,a1,remax)
       real rho,beta,mu,tk,cp,deltt,
      1thhght,tinlet,tcsig,remax,
      2chlen,charea,chalph,chgeom,fric,frclam,frctur,
      3bmag,blam,
      4sigwall,thwall,
      5dhe(50),arch(50),flfrac(50),flspl(50),
      6grav,xt
       real renb(50),nu,pe,
      1prnb,psi,eh,em,emonu,flvel,alhs,alhs2,blhs,crhs,bfld
       integer parrd,nchns,stpt(50),enpt(50)
       double precision t(0:500),ph(0:500),mdot,pmdot(0:500),dt,
      1pkextra(0:500),kextra(50),h(50)
c
c *** see if this is first call to CONVECT; if it is, read
c *** input parameters. If not, then go straight to calculations ***
c
c *** this information assumes "all one channel" to get mdot. -
c *** later we will get information on specific channels, so we
c *** can calculate the Re (and hence h) for each channel ***
c
        grav=9.8
        if(parrd.eq.1) go to 1
        parrd=1
```

```
      write(7,30)
30    format(' reading convect info')
      read(5,2) rho,beta,mu,tk,cp
2     format(5e10.3)
      read(5,3) thhght,tinlet
3     format(2e10.3)
      read(5,4) chlen,charea,chalph,chgeom,frclam,frctur,mdot
      mdot=mdot*a1
4     format(7e10.3)
      read(5,3) bmag,blam
      read(5,3) sigwall,thwall
c
c *** now read about channels to calculate Re, h ***
c
      read(5,5) nchns
      read(5,7) (stpt(i),enpt(i),i=1,nchns)
      read(5,6) (dhe(i),arch(i),flfrac(i),flspl(i),i=1,nchns)
6     format(3e10.3,f5.0)
c
5     format(i3)
7     format(2i4)
c
c
c *** now start calcs. - find deltt ***
c
1     deltt=0.0
      remax=0.0
      do 9 i=1,nchns
      flvel=mdot/(rho*arch(i)*flspl(i))
      renb(i)=(rho*flvel*dhe(i))/mu
```

```
            if(renb(i).gt.remax) remax=renb(i)
            do 9 j=stpt(i),enpt(i)
            if(deltt.lt.t(j)) deltt=t(j)
9           continue
            deltt=deltt-tinlet
c
c find maximum Reynold's number, distinguish between laminar
c and turbulent flow ***
c
            fric=frclam/remax
            if(remax.gt.2100.) fric=frctur*(remax**(-0.25))
c
c now find mdot
c
            alhs=(rho*beta*grav*thhght*deltt)
            blhs=(sigwall*thwall*chlen)/(charea*chalph*rho)
            bfld=bmag*(exp(-1.*blam*xt))
c
            blhs=(blhs*(bfld**2.)+(fric*mdot))/2.
            clhs=(blhs-(chgeom/dt))*mdot
            if(clhs.ge.(0.5*alhs)) then
            tcsig=2.5
            go to 10
            end if
            alhs2=alhs-clhs
            brhs=blhs+(chgeom/dt)
            mdot=(-brhs+((brhs**2.)+(fric*alhs2))**0.5)/(fric/2.)
c
c
c *** calculated mdot - now calculate Pr ***
```

```
c
      prnb=(cp*mu)/tk
c
c *** now start channel loop, find renb, kextra, h for each channel ***
c
      do 19 i=1,nchns
      flvel=mdot/(rho*arch(i)*flspl(i))
      renb(i)=(rho*flvel*dhe(i))/mu
      emonu=(2.9024e-02*(renb(i)**7.6862e-01))
      em=emonu*(mu/rho)
      p1=prnb*(emonu**1.4)
      psi=1.-(1.82/p1)
      if(psi.lt.0.) psi=0.0
      eh=psi*em
      kextra(i)=(eh*rho*cp)*flfrac(i)
      pe=prnb*renb(i)
      nu=5.0 + 0.025*((psi*pe)**0.8)
c
      if(prnb.gt.0.2) then
      if(remax.lt.2100.) kextra(i)=0.0
      nu=4.364
      if(renb(i).gt.2100.) nu=0.023*(renb(i)**0.8)*(prnb**0.4)
      end if
c
      h(i)=(flfrac(i)*tk*nu)/(dhe(i)/(enpt(i)-stpt(i)+1))
19    continue
c
c *** now set point values
c
      do 10 i=1,nchns
```

```
      ph(stpt(i)-1)=h(i)
      ph(enpt(i))=h(i)
      do 10 j=stpt(i),enpt(i)
      pmdot(j)=mdot/flspl(i)
      pkextra(j)=kextra(i)
10    continue
c
      return
      end
```

```
c     Subroutine ISOTOPE
c
          subroutine isotope(emax,ename,econc,rha,rhb,tha,thb,fac,
         . rname)
          real pct(10),conc(10),numd(500),econc(100),l,rha,rhb,
         . tha,thb,fac
          integer num(10),emax,nmax
          character*2 name(500),ename(100)
          character*10 sname,tname,rname
c     unit 11 is cntl.dat
c     unit 12 is matlib.dat
c     unit 13 is elconc.dat
             emax=0
             nmax=0
             rha=0
             rhb=0
             tha=0
             thb=0
c
c read materials in zone
c then find the material in material library MATLIB, find
c k, (rho x Cp), etc. find average of these values for each zone
c
             read(11,'(i3)')numsub
             do 10 i=1,numsub
             read(11,53)sname,pct(i)
53           format(a10,f7.4)
```

```
      write(7,101)sname
101   format(' looking for',a10)
      rewind 12
1     read(12,'(a10)',end=3)tname
      if(tname.ne.sname)goto 1
      goto 2
3     write(7,100)sname
100   format(' element ',a10,' not found in matlib database...')
      goto 10
2     read(12,'(2e10.3)')ztha,zthb
      read(12,'(2e10.3)')zrha,zrhb
      if(sname.eq.rname)then
      ztha=ztha*fac
      zthb=zthb*fac
      end if
      tha=tha + ztha*pct(i)
      thb=thb + zthb*pct(i)
      rha=rha + zrha*pct(i)
      rhb=rhb + zrhb*pct(i)
      read(12,'(e10.3)')conc(i)
      read(12,'(i3)')num(i)
      do 20 j=1,num(i)
20    read(12,'(a2,e10.3)')name(j+nmax),numd(j+nmax)
      nmax=nmax+num(i)
10    continue
      do 24 i=1,100
      econc(i)=0.0
24    ename(i)=' '
      do 30 i=1,nmax
      l=i
```

```
      k=1
4     if((l/num(k)).le.1.0)goto 5
      l=l-num(k)
      k=k+1
      goto 4
5     do 40 j=1,emax
      if(ename(j).ne.name(i))goto 40
      econc(j)=econc(j) + numd(i)*pct(k)*conc(k)
      goto 30
40    continue
      emax=emax+1
      ename(emax)=name(i)
      econc(emax)=numd(i)*pct(k)*conc(k)
30    continue
      do 50 i=1,emax
      write(13,'(a2,e10.3)')ename(i),econc(i)
50    econc(i)=econc(i)/.08
      return
      end
```